

**DETECTION AND MONITORING OF DNAPLs IN THE SUBSURFACE UNDER  
TRANSIENT CONDITIONS USING CROSS WELL RADAR**

by  
MARIA FERNANDA SERRANO GUZMAN

A proposal submitted in partial fulfillment of the requirements for the degree of

Doctor of Philosophy  
in  
CIVIL ENGINEERING  
UNIVERSITY OF PUERTO RICO  
MAYAGÜEZ CAMPUS  
April, 2008

Approved by:

---

Ingrid Y. Padilla C., Ph.D.  
President, Graduate Committee

---

Date

---

Sangchul Hwang Ph. D.  
Member, Graduate Committee

---

Date

---

Rafael Rodríguez S., Ph. D.  
Member, Graduate Committee

---

Date

---

Eric Harmsen, Ph. D.  
Member, Graduate Committee

---

Date

---

Prof. Ismael Pagán Trinidad, MSc.E.  
Director, Department of Civil Engineering and Surveying

---

Date

---

Ramón Torres, Ph. D.  
Representative Graduate Studies

---

Date

## ACKNOWLEDGMENTS

First of all I would like to thank Dr. Ingrid Padilla, my advisor, for her help, support and guidance given to me both personally and academically during this work. She has been more than my professor, she has been a friend. I would also like to express appreciation to my committee members, Dr. Sangchul Hwang, Dr. Eric Harmsen, and Dr. Rafael Rodríguez, and Dr. Ivonne Santiago for their assistance. Thanks to Dr. Domingo Rodríguez and Dr. Rafael Segarra who provided me with his guidance and always believed in me.

Thanks to the friends I made during my years as a graduate student: Mrs. Melissa Herrera, Mrs. Shirley Morillo, Mrs. Perla Torres, Mrs. Marjorie Valdez, Mr. Humberto Hernández, and Mr. Gustavo Suárez, they will always be present as an important part of my joyful memories. Thanks to my friends Mrs. Cecilia Hernández and Mrs. Lara Santiago, who were always willing to help me and certainly wanted the best for me. Thanks to Mr. Diego Darío Pérez who was always giving me support when the experiment was successful and when things were not good, he always had a lovely word to move me to reach this goal. Special thanks to my son Carlos Alberto, he was my classmate and my friend, and gave me support in all the aspects of my life. Thanks to my parents, brothers and sister, and my grandmother, who always made me feel loved,

knowing that they wanted the best for me; and big thanks to them for always providing me with wise advice.

Thanks to the Civil Engineering Department at Universidad Pontificia Bolivariana at Bucaramanga (Colombia), especially gratitude to Dr. Luis F. Casas, Dr. Luis E. Aramburo, Ing. Samuel Montero, and Dr. Amparo Téllez. Thanks to the Civil Engineering Department at the University of Puerto Rico, especially gratitude to Professor Ismael Pagan, Mrs. Hilda Rojas, Mrs. Daysy Morales, Mr. Octavio Ortiz, and Mrs. Jessica Aponte, and Gordon-CenSSIS, the Bernard M. Gordon Center for Subsurface Sensing and Imaging Systems, under the Engineering Research Centers Program of the National Science Foundation (Award Number EEC-9986821) for allowing me conduct my experiments and give me financial support. Finally, and furthestmost, I would like to give special thanks to God for giving me life.

## TABLE OF CONTENT

<b>1. INTRODUCTION</b> .....	1
1.1 JUSTIFICATION .....	1
1.2 HYPOTHESIS DEVELOPMENT.....	11
1.3 OBJECTIVES .....	12
1.4 SCOPE OF EXPERIMENTAL WORK.....	13
1.5 RESEARCH SIGNIFICANCE.....	14
1.6 THESIS ORGANIZATION.....	15
<b>2. THEORETICAL BACKGROUND</b> .....	17
2.1 DENSE NON-AQUEOUS PHASE LIQUIDS .....	18
2.1.1 <i>Physico-chemical Properties of Chlorinated Solvents</i> .....	19
2.1.2 <i>Subsurface Transport of Chlorinated Solvents</i> .....	20
2.1.3 <i>DNAPL Remediation</i> .....	24
2.1.4 <i>Detection Methods</i> .....	30
2.1.4.1 <i>Borehole and soil core technologies</i> .....	31
2.1.4.2 <i>Geophysical technologies</i> .....	36
2.2 ELECTROMAGNETIC BASIS FOR CWR DETECTION.....	50
2.2.1 <i>Electromagnetic Wave Propagation</i> .....	50
2.2.2 <i>Electromagnetic Wave Propagation in Lossy Dielectric Materials</i> .....	52
2.2.3 <i>Electromagnetic Wave Propagation in Lossless or Low-loss Dielectric Materials</i> .....	55
2.3 ELECTRICAL PROPERTIES OF THE SOIL.....	60
2.3.1 <i>Methods for Determination of Dielectric Properties of Soils</i> .....	70
2.4 ANTENNAS .....	72
2.4.1 <i>Antenna Characteristics</i> .....	74
2.4.2 <i>Types of Antennas</i> .....	75
2.5 DIGITAL INTERPRETATION OF CHEMICAL MOVEMENT INTO THE SOIL .....	79
<b>3. METHODOLOGY</b> .....	81
3.1 MODELED DNAPL.....	82
3.2 SOILBED EXPERIMENTAL SETUP .....	83
3.2.1 <i>Soil Packing</i> .....	86
3.2.2 <i>Soil Characteristics</i> .....	88
3.2.3 <i>DNAPL Delivering System</i> .....	89
3.2.4 <i>Experimental Room</i> .....	90
3.3 DATA ACQUISITION SYSTEM.....	92
3.3.1 <i>Measurement Accuracy</i> .....	92
3.4 ANTENNA DESIGN AND TESTING .....	93

3.4.1 Dipole and Monopole Antenna Selection .....	94
3.4.2 Loop Antenna Response Testing .....	99
3.4.3 Boundary Conditions .....	100
3.5 DETECTION OF UNDERGROUND DNAPL AND OTHER TARGET ELEMENTS.....	101
3.5.1 Detection of Underground Target Elements .....	101
3.5.2 DNAPL Detection.....	102
3.6 DETERMINATION OF DIELECTRIC PROPERTIES .....	104
3.6.1 Two-Port Network Theory.....	105
3.6.2 S-Parameter Description .....	107
3.6.3 S-Parameters Measurements with a NA .....	111
3.6.4 Validation Method .....	111
3.6.5 SoilBed Method .....	112
3.7 DIGITAL VISUALIZATION AND IMAGE ANALYSIS .....	115
<b>4. TWO-DIMENSIONAL DETECTION OF UNDERGROUND CONTAMINATION AND BURIED OBJECTS USING CROSS-WELL RADAR</b> .....	119
4.1 ABSTRACT.....	119
4.2 INTRODUCTION .....	120
4.3 MATERIALS AND METHODS.....	124
4.3.1 <i>SoilBed Experimental Setup</i> .....	124
4.3.2 <i>Measurements of Antenna Characteristics</i> .....	126
4.3.3 <i>Antenna Response Testing</i> .....	128
4.4 EXPERIMENTAL RESULTS.....	130
4.4.1 <i>Transmission and Reflection Measurements</i> .....	130
4.4.2 <i>Data Reliability</i> .....	134
4.4.3 <i>Boundary effect in Transmission Response</i> .....	134
4.4.4 <i>Variations in Transmission and Reflection Measurements in Presence of Objects</i> .....	137
4.5 SUMMARY AND CONCLUSIONS .....	138
<b>5. BIMODAL DETECTION OF UNDERGROUND CONTAMINATION IN TWO DIMENSIONAL SYSTEMS.....</b>	140
5.1 ABSTRACT.....	140
5.2 INTRODUCTION .....	141
5.2.1 <i>Dielectric properties</i> .....	142
5.2.2 <i>Digital visualization and Image Analysis</i> .....	144
5.3 MATERIALS AND METHODS.....	145
5.3.1 <i>SoilBed Experimental Setup</i> .....	145
5.3.2 <i>Antenna Characteristics</i> .....	148
5.3.3 <i>Antenna Response Testing</i> .....	149
5.3.4 <i>Electromagnetic Modeling of 2D SoilBed</i> .....	150
5.3.5 <i>Digital Visualization and Image Analysis</i> .....	151
5.4 EXPERIMENTAL RESULTS.....	153
5.4.1 <i>Transmission and Reflection Measurements</i> .....	153
5.4.2 <i>Data Reliability</i> .....	155
5.4.3 <i>Electromagnetic Modeling of 2D SoilBed</i> .....	156

5.4.4 <i>Digital Visualization and Image Analysis</i> .....	159
5.5 SUMMARY AND CONCLUSIONS .....	164
<b>6. CROSS WELL RADAR TOMOGRAPHY</b> .....	166
6.1 ABSTRACT .....	166
6.2 INTRODUCTION .....	167
6.2.1 <i>Discretized Model for Image Reconstruction</i> .....	168
6.3 TOMOGRAM DEVELOPMENT .....	171
6.3.1 <i>Algebraic Reconstruction Technique</i> .....	175
6.3.1.1 <i>Illustrative example of the ART process</i> .....	178
6.4 APPLICATION OF SART TO SIMULATE UNDERGROUND TARGET DETECTION .....	181
6.5 SUMMARY AND CONCLUSIONS .....	183
<b>7. DNAPL DETECTION AND VISUALIZATION UNDER VARIABLE CONDITIONS: EXPERIMENTAL RESULTS</b> .....	184
7.1 MATERIALS AND METHODS.....	184
7.2 RESULTS .....	185
7.2.1 TCE and Water Infiltration in Initially-dry Soil Experiments.....	185
7.2.1.1 <i>Transmission response</i> .....	186
7.2.1.2 <i>Reflection response</i> .....	193
7.2.2 Water saturation conditions .....	196
7.2.2.1 <i>Transmission response under water saturation</i> .....	201
7.2.2.2 <i>Reflection response under water saturation</i> .....	202
7.2.2.3 <i>Electromagnetic measurements in the presence of TCE in water-saturation experiments</i> .....	206
7.3 VARIATIONS IN DIELECTRIC PERMITTIVITY.....	207
7.3.1 Variations of dielectric properties in initially dry soil experiments .....	209
7.3.2 Variations of dielectric permittivity in saturation experiments .....	216
7.4 TOMOGRAMS DURING TCE INJECTION IN DRY CONDITIONS AND SATURATED CONDITIONS .....	221
7.4.1 Tomograms for initially-dry experiments.....	222
7.4.2 Tomograms for soil under water-saturation experiments .....	231
7.4.3 Tomographic limitations.....	233
7.5 DIGITAL VISUALIZATION AND IMAGE ANALYSIS DURING TCE INJECTION IN INITIALLY-DRY AND SATURATED CONDITIONS .....	241
7.5.1 Image processing and analysis.....	242
<b>8. SUMMARY, CONCLUSIONS, AND RECOMMENDATIONS</b> .....	253
<b>9. REFERENCES</b> .....	268

## LIST OF FIGURES

Figure 2.1 DNAPL distribution in unconsolidated deposits .....	21
Figure 2.2 Electric and magnetic fields .....	51
Figure 2.3 Spectrum of the EM radiation .....	52
Figure 2.4 Raypaht loss.....	58
Figure 2.5 Wire antenna types .....	76
Figure 3.1 SoilBed prototype with a) metal mesh held by PVC fixers b) packed with dry sand. ....	85
Figure 3.2 Borehole location at soilBed setup a) number 2, b) number 3, and c) number 4 .....	87
Figure 3.3 Soil delivery guide.....	88
Figure 3.4 Granulometric distribution sandy soil .....	89
Figure 3.5 TCE injection setup : porous cup, teflon ending, tygon tubing, and fitting ....	90
Figure 3.6 Studio like room .....	91
Figure 3.7 Network Analyzer, multiport test set, and soilBed(type 2, Table 3.2).....	92
Figure 3.8 Tested a) monopole, b) dipole, c) double, and d) loop antennas.....	94
Figure 3.9 Sampling distances used for testing and selection of antenna types .....	95
Figure 3.10 Reflection response of monopole and dipole antennas .....	97
Figure 3.11 Transmission response of Monopole and Dipole Antennas .....	97
Figure 3.12 a) Materials for construction of loop antennas, and b) loop antenna .....	98
Figure 3.13 Electromagnetic boundaries conditions a) metal plate in front and back site b) metal plate in top and bottom c) metal plate inside located together the mesh. ....	100
Figure 3.14 Theoretical 2-port Network for $\mu_r$ and $\epsilon_r$ estimate.....	105
Figure 3.15 Generalized two-port network excited by voltages sources $V_1$ and $V_2$ .....	105
Figure 3.16 Real part of permeability for Teflon.....	113
Figure 3.17 Imaginary part of permeability for Teflon.....	114
Figure 3.18 Real part of permittivity for Teflon .....	114
Figure 3.19 Imaginary part or relative permittivity for Teflon .....	115
Figure 3.20 Wall opening for the camera zoom .....	116
Figure 3.21 Image acquisition and analysis system a) calibration soil cells, b) stained soil cells, and c) studio room .....	116
Figure 3.22 Image acquisition and analysis system a) calibration soil cells, b) stained soil cells, and c) studio room .....	118
Figure 4.1 Two-Dimensional flow setup .....	125
Figure 4.2 Description of coaxial cable .....	127
Figure 4.3 Location of antennas in a 2D soilBed setup (ID 3, Table 3.2) .....	128
Figure 4.4 Transmission response $S_{29}$ at the setup (ID 3, Table 3.2) .....	132
Figure 4.5 Transmission response $S_{49}$ for antennas at the setup (ID 3, Table 3.2).....	132

Figure 4.6 Reflection response at borehole 9 when receiving is at borehole 2 .....	133
Figure 4.7 Reflection response at borehole 9 when receiving antenna is at borehole 4. ....	133
Figure 4.8 Transmission response for antennas borehole 9 and 4 (ID 3, Table 3.2) .....	135
Figure 4.9 Transmission response $S_{49}$ and $S_{29}$ (ID 3, Table 3.2) .....	135
Figure 4.10 Reflection measurement $S_{29}$ .....	136
Figure 4.11 Reflection measurement $S_{49}$ .....	136
Figure 4.12 Comparison of transmission measurement $S_{49}$ without and with an object inside the soil .....	137
Figure 4.13 Comparison of reflection measurement $S_{49}$ without and with an object inside the soil.....	138
Figure 5.1 a) Two-dimensional electromagnetic and flow setup with antennas, b) parallel metal mesh, and (c), and loop antenna (soilBed ID 4, Figure 3.2). .....	146
Figure 5.2 Image acquisition and analysis system: (a) digital camera, (b) calibration soil cells, (c) stained soil cells, and (d) studio room.....	151
Figure 5.3 Transmission measurements in presence (pink line) and absence (blue line) of an object: Port 1 sends, Port 3 receives.....	153
Figure 5.4 Transmission measurements in presence (pink line) and absence (blue line) of an object: Port 1 sends, Port 4 receives.....	154
Figure 5.5 Reflection measurements in presence (pink line) and absence (blue line) of an object: Port 1 transreceiving .....	154
Figure 5.6 Transmission response for antennas in port 3 and 1 (ID 4, Table 3.2).....	155
Figure 5.7 Soil-Bed electromagnetic model for: dry sand with transmitting port at (a)14.5 and (b) 35 cm above the bottom; saturated sand on the bottom third (air-water interface at 27.3 cm) and dry sand on the top two thirds with transmitting port at (c)14.5 and (d) 35 cm above the bottom; saturated sand on the bottom half (air-water interface at 27.3 cm) and dry sand on the top half with transmitting port at (e) 14.5 and (f) 35 cm above the bottom. Receiving ports are 5 cm apart. ....	157
Figure 5.8 Image analysis for a 10 ml injection of a 5% dye concentration.....	160
Figure 5.9 Average pixel intensity in dyed soil as a function of TCE volume at 10% dye concentration.....	161
Figure 5.10 Average difference intensity( $\Delta P_i$ ) as a function of TCE volume with dye	162
Figure 5.11 Average pixel difference intensity value for same volume different dye concentration.....	163
Figure 5.12 TCE injection in the calibration cell.....	163
Figure 6.1 Ray-path coverage associated with borehole distribution .....	169
Figure 6.2 Discrete model of a region between boreholes showing a typical raypath through $I \times J$ digital image of velocity .....	172
Figure 6.3 Matrix form in ART .....	177
Figure 6.4 Discrete model of a region between boreholes showing a typical ray path through the $0 \times 4$ ( $I \times J$ ) digital image with a specific dielectric property ( $\epsilon$ ).....	179
Figure 6.5 Expanded matrix.....	180
Figure 6.6 Tomographic images of squared UTE using straight raypath SART of different grid sizes having five antennas. Red dots are used to show antenna location .....	182
Figure 7.1 Transmission measurement during TCE injection-initially dry experiments	187
Figure 7.2 Transmission measurement when receiver is in Port 5 and transmitter in Port 1-initially dry experiments.....	188

Figure 7.3 Transmission measurement when receiver is in Port 6 and transmitter in Port 1-initially dry experiments .....	189
Figure 7.4 Influence of depth in EM response receiver (Port 6)-transmitter (Port 2) initially dry experiments .....	191
Figure 7.5 Influence of depth in EM response receiver (Port 7)-transmitter (Port3) initially dry experiments .....	191
Figure 7.6 Influence of depth in EM response receiver (Port 8)-transmitter (Port4) initially dry experiments .....	192
Figure 7.7 Influence of depth in reflection response at Port 1-initially dry conditions ..	194
Figure 7.8 Influence of depth in reflection response at Port 2 initially dry experiments	195
Figure 7.9 Influence of depth in reflection response at Port 3 initially-dry experiments	195
Figure 7.10 Influence of depth in reflection response at Port 4 initially-dry experiments .....	196
Figure 7.11 Transmission measurement at receiver (Port 5) when -transmitter (Port 1) during saturation .....	197
Figure 7.12 Transmission measurement receiver (Port 6)-transmitter (Port 1) during saturation.....	198
Figure 7.13 Transmission measurement receiver (Port 7)-transmitter (Port 1) during saturation.....	198
Figure 7.14 Transmission measurement receiver (Port 8)-transmitter (Port 1) during saturation.....	199
Figure 7.15 Transmission measurement receiver (Port 6)-transmitter (Port 2) during saturation.....	199
Figure 7.16 Transmission measurement receiver (Port 7)-transmitter (Port 3) during saturation.....	200
Figure 7.17 Transmission measurement receiver (Port 8)-transmitter (Port 4) during saturation.....	200
Figure 7.18 Influence of depth in reflection response at Port 1 (at 5 cm from top) - saturated condition .....	203
Figure 7.19 Influence of depth in reflection response at Port 2 (at 10 cm from top) - saturated condition .....	204
Figure 7.20 Influence of depth in reflection response at Port 3 (at 15 cm from top) - saturated condition .....	204
Figure 7.21 Influence of depth in reflection response at Port 4 (at 20 cm from top)- saturated condition .....	205
Figure 7.22 Transmission electromagnetic response in initially-dry experiments .....	208
Figure.7.23 Reflection electromagnetic response in initially-dry experiments .....	209
Figure 7.24 Relative permittivity values for dry soil in initially-dry experiments .....	210
Figure 7.25 Relative permittivity values after 5 min TCE injection in initially-dry experiments .....	210
Figure 7.26 Relative permittivity value after 10 min TCE injection in initially-dry experiments .....	211
Figure 7.27 Relative permittivity values after 30 min TCE injection in initially-dry experiments .....	211
Figure.7.28 Relative permittivity value after 50 min TCE injection in initially-dry experiments .....	214

Figure 7.29 Relative permittivity value after 80 min TCE injection in initially-dry experiments .....	214
Figure 7.30 Relative permittivity value after 130 min TCE injection in initially-dry experiments .....	215
Figure 7.31 Relative permittivity values in dry soil prior to saturation experiments .....	218
Figure 7.32 Relative permittivity values when the tank is fifty percent saturated .....	219
Figure 7.33 Relative permittivity values when the tank is seventy five percent saturated .....	219
Figure 7.34 Relative permittivity values when tank is one hundred percent saturated ..	220
Figure 7.35 Relative permittivity values at 10 min after TCE injection in saturated soil .....	220
Figure 7.36 Relative permittivity value at 45 min after TCE injection in saturated soil	221
Figure 7.37 Results of: a) digital image, and b) tomogram of dry soil prior to injection of TCE in initially-dry experiments .....	224
Figure 7.38 Results of: a) digital image, and b) tomogram at 5 min TCE in initially-dry experiments .....	225
Figure 7.39 Results of: a) digital image, and b) tomogram at 10 min TCE in initially-dry experiments .....	226
Figure 7.40 Results of: a) digital image, and b) tomogram at 30 min TCE in initially-dry experiments .....	227
Figure 7.41 Results of: a) digital image, and b) tomogram at 130 min TCE in initially-dry experiments .....	228
Figure 7.42 Slowness distribution in initially-dry experiments.....	229
Figure 7.43 Slowness distribution at 5 min of TCE in initially-dry experiments.....	229
Figure 7.44 Slowness distribution at 10 min of TCE in initially-dry experiments.....	230
Figure 7.45 Slowness distribution at 30 min of TCE in initially-dry experiments.....	230
Figure 7.46 Slowness distribution at 130 min of TCE in initially-dry experiments.....	231
Figure 7.47 Results of a) digital image, and b) tomograms for dry soil prior to saturation experiments .....	235
Figure 7.48 Results of a) digital image, and b) tomograms for fifty percent soilBed saturation.....	236
Figure 7.49 Results of a) digital image, and b) tomograms for seventy five percent soilBed saturation.....	237
Figure 7.50 Results of a) digital image, and b) tomograms for one hundred percent soilBed saturation.....	238
Figure 7.51 Results of a) digital image, and b) tomograms at 10 min of TCE injection-saturated soil .....	239
Figure 7.52 Results of a) digital image, and b) tomograms at 45 min of TCE injection-saturated soil .....	240
Figure 7.53 a) Image analysis during initially -dry experiments .....	246
Figure 7.54 b) Histograms during initially -dry experiments .....	247
Figure 7.55 a) Image analysis during saturation process .....	248
Figure 7.56 b) Histograms during saturation process .....	249
Figure 7.57 a) Image analysis during TCE injection in saturated soil.....	250
Figure 7.58 b) Histograms during TCE injection in saturated soil.....	251
Figure 7.59 Variations in pixel intensity in dry soil .....	252

## LIST OF TABLES

Table 2.1 Electrical conductivity soil materials .....	60
Table 2.2 Real and imaginary part of dielectric permittivity .....	63
Table 2.3 Relative permittivity in soils .....	63
Table 3.1 Physical chemical properties of TCE, Sudan IV, and water .....	83
Table 3.2 SoilBeds setups .....	84
Table 3.3 Length for dipole and monopole antennas .....	96
Table 3.4 Teflon measurement dielectric properties .....	113
Table 6.1 Distance travel through raypath (0,4) .....	179
Table 7.1 Average maximum relative permittivity values estimated .....	211
Table 7.2 Average maximum relative permittivity values .....	217
Table 7.3 Average permittivity and slowness for TCE in initially dry experiments ...	223
Table 7.4 Average relative permittivity and slowness for TCE-saturated conditions .	232

## LIST OF SYMBOLS

- $\phi$ : contact angle
- $\beta$ : phase constant or wave number
- $\epsilon_r$ : relative dielectric permittivity
- $\epsilon$ : permittivity of the medium
- $\epsilon_0$ :  $8.854 \times 10^{-12}$  F/m: permittivity of free space
- $\epsilon_c$ : complex permittivity of the medium
- $\epsilon_r'$ : real part of relative permittivity
- $\epsilon_r''$ : imaginary part of relative permittivity
- $\epsilon_{r,i}^x$ : complex permittivity
- $\chi$ : empirical value
- $\epsilon_s$  is the dielectric constant of the soil particles
- $\epsilon_1$ : apparent dielectric constant for moisture content less than or equal to  $W_t$
- $\epsilon_2$ : apparent dielectric constant for moisture content greater than  $W_t$
- $\epsilon_a$ : dielectric constant of air (1)
- $\epsilon_i$ : dielectric constant of ice (3.2)
- $\epsilon_w$ : dielectric constant of pure water (81)
- $\mu_r$ : relative permeability
- $\mu$ : permeability of the medium
- $\mu_0$ :  $4\pi \times 10^{-7}$  H/m: permeability of free space

$\sigma$ : interfacial tension between NAPL and water

$\rho_n$ : density of NAPL

$\rho_b$ : bulk soil density

$\rho_s$ : particle soil density

$\rho$ : resistivity

$\lambda$ : wavelength

$v$ : speed of the wave

$\omega$ : angular frequency

$j$ :  $\sqrt{-1}$ .

$\sigma$ : electric conductivity of the medium

$\gamma^2 = j\omega\mu(\sigma + j\omega\varepsilon)$ : complex wave number or propagation constant

$\alpha$ : attenuation constant or attenuation factor

$\eta$ : intrinsic impedance

$\theta_\eta$ : phase angle of intrinsic impedance

$t$ : time

$\delta$ : skin depth

$\psi_i$ : volume fraction

$\theta$ : volumetric water content

$\phi_v$ : volumetric moisture content

$\phi$ : porosity

$\tau'$  and  $\tau''$ : empirically determined soil-type constants

$\gamma$ : fitting parameter which is related to WP.

$A_{em}$ : maximum effective aperture

$\Gamma$ : reflection coefficient

T: transmission coefficient.

$\lambda_c(w)$ : cutoff wavelength

$\lambda_{min}$ : minimum wavelength

$a_i$ : incident wave (independent) parameter

$a_{kn}$ : weighing factor expressing the influence of the properties in the  $n_{th}$  pixel on the  $k_{th}$  ray.

$b_i$ : reflected wave (dependent) parameter

$dl$ : path length increment

$d_{ij}$ : is the distance traveled by ray  $i$  in pixel  $j$

$f(x,y)$ : material parameter

$g_k$ : line integral data

$ds$ : cell-weighting factor

$f_{ij}^q$ : initial guess, projection values for one grid element

$\hat{g}$ : is the projection value

$l_{cc}$ : center conductor length

$l_{dd}$ : dielectric conductor length

$r_t$ : radius of the pore throat that the NAPL must move through to exit or enter the pore

$r_t$ : radius of the water filled pore throat that the NAPL must move through to exit or enter pore

$y_{11}, y_{12}, y_{21}, y_{22}$ : parameters obtained from measurements with VNA

$\Delta s_{ijk}$ : length of a ray segment that intercepts the pixel

$a$ : radius of the loop.

$c$ : velocity of free space ( $3 \times 10^8$  m/s)

$f$ : frequency or rate of oscillation

$g$ : gravitational constant

$ij$ : (column, row) grid of rectangular pixel elements

$i\Delta x$  and  $j\Delta y$ : pixel center

$m_k$ : measurement

$p$ : wave slowness

$q$ : is each iteration

$q_{th}$ : iteration that represents the average value of  $f(x,y)$  on the cell  $(i,j)$

$t_k$ : travel time

$w$  represents frequency dependent of the S-parameters

$\lambda$ : is the relaxation factor

$A$ : N-number of projection estimated values

$C$ : circumference

$C$ : clay content in percent of dry soil

$E$  and  $H$ : electric and magnetic field

$E_s$  and  $H_s$ : the phasor form of the time harmonic

$E$  and  $H$ , respectively

$D$ : weight projection matrix

$I$ : total number of columns in the grid

$I_1$  and  $I_2$ : input current

$IL$ : attenuation or insertion loss

$J$ : total number of rows

$K$ : dummy variable

$K_a$ : relative permittivity

$K_{th}$ : raypath

$M$ : number of pixels

$N$ : number of turns in the loop

$N$ : total number of observations

RL: return loss

$R_k$ : signal paths

$S$ :  $N$ -number vector of unknown material parameter

$S$ : sand content in percent of dry soil

$S_{11}$  and  $S_{22}$ : reflection electromagnetic measurement

$S_{12}$  and  $S_{21}$ : transmission electromagnetic measurement.

$S_{ps}$ : physical size

$V_1$  and  $V_2$ : voltage sources

$W_t$ : transition moisture content

WP: moisture content at the Wilting Point (pore water pressure 15 bars)

$Z_i$ : reference impedance

$Z_1$  and  $Z_2$ : input impedance at port 1 and 2, respectively

$Z_0$ : intrinsic impedance ( $50\Omega$ )

$Z_n$ : critical height

**LIST OF APPENDIXES**

Appendix 1 Dielectric properties flow chart and code .....	304
Appendix 2 Tomography flow chart and tomography code .....	308
Appendix 3 Image acquisition code .....	324
Appendix 4 Image processing .....	328
Appendix 5 An electromagnetic model of the Soil-Bed setup .....	333
Appendix 6 Transmission and reflection data – All antennas .....	342
Appendix 7 Statistical analysis .....	358

## **ABSTRACT**

Contamination of soils and groundwater, accidental spills, poor storage facilities, and inadequate disposal practices cause serious detriment of the environment and can pose a serious threat to human health. Common contaminants found in underground environments include many Dense Non-Aqueous Phase Liquids (DNAPLs). DNAPLs are liquids denser than water. Most DNAPLs experience only partial degradation in the subsurface, and persist for long time slowly releasing soluble organic constituents to groundwater. The most common DNAPLs are halogenated solvents, such as trichloroethylene (TCE) and tetrachloroethylene (PCE). Their heterogeneous distribution in the environments makes DNAPLs difficult to locate, characterize, and remediate. It is therefore, necessary to develop new technologies that will enhance our ability to characterize contaminated sites, locate underground contaminants, evaluate fate and transport processes, and remediate contaminated sites.

The research presented herein develops and evaluates Cross Well Radar (CWR) technologies to detect and monitor DNAPLs contamination in subsurface environments under transient flow conditions. It involves systematic development and testing of sensing system, signal management and processing; and imaging technologies. Electromagnetic and flow experiments are used in conjunction with image acquisition technologies to generate critical information and evaluate the effectiveness and reliability

of CWR systems.

A methodology has been developed to detect electromagnetic (EM) changes caused by variable spatial and temporal distribution of fluids with different EM properties. The method used a 2D flow and electromagnetic soilBed instrumented with loop antennas. Measurements show sufficient contrast between EM properties of uncontaminated and DNAPL-contaminated soil to apply CWR for contaminant detection. The contrast is dependent on water content, frequency range of analysis, fluid movement, distribution, and heterogeneities, and the presence of physical, and fluid interfacial areas.

A method was developed to estimate relative permittivity along raypath between transmitting and receiving CWR antennas from EM measurements. The method assumes lossless medium and perfectly coupled and identical radiation characteristics of the antennas. Estimates determined from water and TCE flow experiments indicate that variable and temporal distribution of fluids with different EM properties cause detectable changes in dielectric properties of the bulk soil.

A sequentially algebraic reconstruction method (SART) was developed and applied to generate tomographic images of the estimated relative permittivities. The tomograms can be used to image and visualize the presence of disturbances in the medium. The tomographic method generates acceptable tomograms of under ground target elements in soils, provided that there is sufficient density of antennas array and proper grid spacing. The codes provide a tool for optimal CWR system design and can be applied to

determine the number of antennas required for good resolution of a specific geometry in lossless medium. Generated images suggest slight variations of the tomograms after injection of TCE and water in the system. The tomographic results show changes caused by variable flow and fluid saturation and distribution conditions. The experimental resolution and potential measurement error, however, limit the asseverance of conclusive remarks in the system.

This research also developed image acquisition and processing algorithms to analyze visual images of dyed contaminants, discriminate between regions of different amounts of DNAPLs, and assess potential relationships between electromagnetic variations and the spatially-distributed DNAPL in the soil. The results indicate that the image processing and analysis techniques developed in this research are effective in detecting changes by fluid flow and distribution. Differences in color intensity in the presence of water suggest that this technique may be applicable to monitor flow and saturation. Changes on pixel intensity during dyed TCE injection also indicate its application to monitor transport and mass of TCE in the system.

The methods developed and tested in this research represent significant contributions, which move underground detection technologies closer to real applications. Recommendations addressed the limitations encountered and establish a basis for full deployment of CWR technologies for detection of underground contamination.

## RESUMEN

Contaminación de suelos y agua subterránea por derrames accidentales, deficientes sistemas de almacenamiento e inadecuadas prácticas de disposición de residuos causan deterioro al ambiente y ponen en riesgo la salud humana. Dentro de los contaminantes más comunes están los compuestos más densos que el agua, DNAPLs cuyas siglas en inglés representan a los Dense Non-Aqueous Phase Liquids. La mayoría de estos compuestos experimentan una degradación parcial en el subsuelo, y presentan una persistencia por mucho tiempo dejando cantidades residuales en los depósitos de agua subterránea. El tricloroetileno y percloroetileno (TCE y PCE, respectivamente, por sus siglas en inglés) hacen parte de los más comunes DNAPLs presentes en el ambiente. La forma heterogénea como se distribuyen estos compuestos, hacen difícil su localización, caracterización, y remediación. Por esta razón, es necesario el desarrollo de nuevas tecnologías que permitan mejorar las habilidades de caracterizar sitios contaminados, localizar la contaminación, y evaluar sistemas de disposición y tratamiento de los sitios contaminados.

Esta investigación evalúa y desarrolla la tecnología Cross Well Radar (CWR) para detectar y monitorear contaminación de DNAPLs en ambientes subterráneos bajo condiciones de flujo variable. Esto implica el desarrollo y prueba de sistemas de monitoreo y de análisis y procesamiento de señales y de imágenes. Experimentos

electromagnéticos y de flujo fueron aplicados junto con las técnicas de adquisición de imágenes para generar información que evaluara la efectividad y confiabilidad de los sistemas de CWR para detección de DNAPLs.

La metodología desarrollada permitió detectar cambios electromagnéticos causados por variaciones espaciales y temporales de los fluidos con diferentes propiedades eléctricas. En el método, se utilizó un tanque de flujo en dos dimensiones, el cual se instrumentó con antenas loop. Las medidas electromagnéticas muestran suficiente contraste, el cual depende del contenido de agua, el rango de frecuencias que se utiliza, el movimiento y distribución del fluido, y la presencia de interfaces entre los diferentes fluidos y el medio.

Se desarrolló un método para estimar permitividades relativas a lo largo de las antenas utilizadas. El método utilizado asume ausencia de pérdidas en el medio y un acoplamiento idéntico de las antenas. Así mismo, los resultados mostraron variaciones en el sistema de distribución de los fluidos con diferentes propiedades eléctricas, los cuales causan cambios en las propiedades eléctricas de la densidad bulk del suelo.

Se desarrolló un sistema de reconstrucción tomográfica con el cual se prepararon tomogramas partiendo de los valores estimados de permitividades. Los tomogramas pudieron ser usados para visualizar la presencia de perturbaciones en el medio. El método tomográfico genera tomogramas aceptables para objetos introducidos dentro del suelo, toda vez que existan suficiente densidad de antenas distribuidas con un espaciamiento apropiado. El programa desarrollado provee una herramienta apropiada

para el diseño de sistemas CWR en un medio que no tenga pérdidas. Los resultados tomográficos muestran cambios en variación de flujo y durante la saturación del suelo. La resolución experimental y los errores posibles de las medidas limitan la determinación exacta del TCE en el suelo.

Esta investigación también desarrolló un sistema de adquisición y procesamiento de imágenes para analizar los cambios en suelos no contaminados y contaminados, discriminados entre regiones con diferentes cantidades de DNAPLs. Los resultados indican que los algoritmos desarrollados son efectivos para detectar cambios de flujo en los fluidos. Las diferencias en intensidad de color en los suelos con contenido de agua indican que la técnica puede ser útil para monitorear el movimiento del flujo y la saturación del medio. Igualmente, los cambios de intensidad en los suelos con TCE indicaron que puede ser utilizada para aplicarla en determinación de la cantidad de masa de TCE.

Los métodos desarrollados y probados en esta investigación representan una contribución valiosa para los sistemas de detección del subsuelo. Se plantean recomendaciones para mejorar la técnica de CWR en experimentos futuros.

## **1. INTRODUCTION**

The growing population demand and increasing production of energy supply have caused an increase in the release of organic contaminants into the environment. Contamination of soils and groundwater by accidental spills, poor storage facilities, and inadequate disposal practices causes serious detriment of the environment and can pose a serious threat to human health. Common contaminants found in underground environments include many Dense Non-Aqueous Phase Liquids (DNAPLs), which pose particular threats because of their heterogeneous distribution and long-term perseverance in the environment. Moreover, they are difficult to locate, characterize, and remediate (NRC, 2000a). It is, therefore, necessary to develop new technologies that will enhance our ability to characterize contaminated sites, locate underground contaminants, evaluate fate and transport processes, and remediate contaminated sites.

### **1.1 JUSTIFICATION**

In the subsurface, contaminants can migrate and be entrapped as immiscible liquids, which can serve as a constant source of contamination. It is, therefore, necessary to locate and remediate these internal sources of contamination. Traditional approaches for locating and characterizing contaminated sites rely on invasive techniques that require drilling, testing, and sampling. While these techniques provide the most direct access to

the subsurface, they are generally expensive and only provide measurements at points in a three dimensional surface (NRC, 2000b). Detection of these contaminants becomes extremely difficult because of their heterogeneous distribution in subsurface environments. Measurement points in a heterogeneous distributed contaminant volume do not reflect the spatial extent of the contamination. Furthermore, invasive techniques in polluted areas can promote further spread of contaminants. Non invasive detection methods involve little or no disruption of surface materials, but they yield indirect measurements of site characteristics based on the response to artificial or natural stimuli (NRC, 2000a). This response must be interpreted to infer the characteristics (e.g., chemical constituency, porosity, structural features) of contaminated sites.

Non-invasive techniques such as electromagnetic and acoustic methods offer rapid and relatively inexpensive characterization, but they may suffer from lack of resolution and specificity. Improvement of these technologies will enhance our ability to detect and monitor plumes and sources of organic contaminants, form a better understanding of the processes affecting their fate and transport in subsurface environments, and assess remediation schemes in contaminated sites.

#### Electromagnetic Detection Methods

Non-invasive electromagnetic methods have been applied to detect contaminants in the subsurface, but depend on type and concentrations of contaminant (NRC, 2000a). Mostly these methods are applicable for electrically conductive, inorganic contaminants. Direct

detection of organic contaminants by non-invasive is considerably more challenging because of their electrically insulative properties (NRC, 2000a). Dissolved organic contaminants are nearly impossible to detect using non-invasive techniques. Some detection technologies are relying on electrically charged byproducts to detect contamination. Immiscible fluids such as gasoline and chlorinated solvents have been detected to some extent using electromagnetic (EM) methods.

Electromagnetic characterization and detection methods use the response of the media (ground) to the propagation of electromagnetic waves with electric and magnetic components. Electromagnetic waves in a lossless medium do not lose energy and are not attenuated (amplitude is not reduced). In a lossy medium, energy losses cause the wave to be attenuated. Energy loss occurs from reflection/transmission losses, scattering, and absorption losses (Reynolds, 1997). Reflection/transmission losses occur across interphases of different EM properties. Scattering results from the presence of objects with dimensions of the same order as the wavelength of the signal. Absorption, which converts EM energy into heat, is caused by the geometrical spread of the energy. The attenuation of the EM waves resulting from these energy losses is a function of the dielectric and electrical properties of the media: dielectric constant ( $\epsilon$ ), conductivity ( $\sigma$ ), and magnetic permeability ( $\mu$ ). Any variations in these properties across the media give rise to reflection of EM waves (Sharma, 1997). The greater the contrast the greater the amount reflected.

EM waves in a dielectric medium enclosed by perfectly reflection boundaries at separation distances comparable to or smaller than the wavelength of the signal are repeatedly reflected between opposite walls and trapped within the medium (Kruk, 2006). These boundaries, thus, act as waveguides, guiding the EM energy from one point to another. For a lossless dielectric, the EM waves in the waveguide can be imagined as traveling down the path in a zig-zag manner with no energy loss as the energy is guided from one point to another. The waveguide can be designed such that an EM incident will produce one diffraction order in reflection, and the energy is stored due to total internal reflection. Total internal reflection of the first order at the boundary of the waveguide and the layer material is ensured in the absence of modal dispersion, which smears out the wave. This can be accomplished if the spread-out width of the signal dictated by the thickness of the wave guide is less than half-wavelength (Bunkowski et al., 2006). The proportion of incident wave that is reflected or transmitted depends on the constitutive parameters ( $\epsilon$ ,  $\sigma$ ,  $\mu$ ), and the total electric and magnetic fields (Sadiku, 2001).

Several electromagnetic methods exploit differences in the electromagnetic properties of subsurface constituents (soil, water, air, contaminants) to detect underground contamination. These methods include: induced polarization, low frequency methods, ground penetrating radar, and cross well radar techniques.

Induced Polarization (IP) methods assess the response of the ground to an excitation and the removal of an induced electrical signal (NRC, 2000a; Reynolds, 1997). Induced Polarization (IP) methods can be used to detect electrochemical reactions of immiscible

contaminants with surrounding media. Because of IP sensitivity to clays at depth, it is sometimes difficult to determine if an IP anomaly is due to actual contamination or clay lenses. Furthermore, IP technologies are limited by lack of consistent high quality, high volume data and dissemination of computer codes (NRC, 2000a).

Low frequency electromagnetic methods operating at frequencies between 1 and 30MHz provide capabilities to measure organic contaminants, engineered structure, and buried non metallic objects (NRC, 2000a). Their resolution is, however, relatively low.

Ground Penetrating Radar uses transmitting and receiving antennas above the ground surface that transmits high-frequencies electromagnetic waves ( $10^1$ - $10^3$ MHz) into the soil. It commonly shows better resolution than lower frequency EM methods because of its smaller wavelength. When EM waves interact with an interface between two media with different resistivities and dielectric permittivities they are reflected and scattered back to the surface, where the signal is received for interpretation (NRC, 2000a). GPR detection technologies rely on the contrast between the dielectric permittivities of the soil medium, water and DNAPLs to determine water contents, and detect contamination of organic immiscible fluids (NRC, 2000a). In absence of time-dependent EM data showing dielectric permittivity contrast before and after contamination, which is a more typical situation, GPR data may reflect radar wave attenuation in regions contaminated with organic fluids. This change in character of radar reflector is not a conclusive way of determining the presence or absence of a contaminant. This change in GPR signals can lead to high degree of uncertainty (NRC, 2000a). Furthermore, the use of GPR for

detection in underground systems is limited to shallow depths.

Cross Well Radar (CWR) is similar to GPR technology in that radar waves are emitted from transmitting to receiving antennas. Unlike GPR, CWR uses greater wave frequencies (0.4 – 2.2 GHz) and the antennas are lowered into the ground. In CWR, radar waves are emitted from a transmitting antenna in one well through the ground to a receiving antenna in other wells. The ability of locating antennas at different depths may yield greater resolution at much greater depths for detection of DNAPLs in underground systems (Farid, 2004; Farid et al., 2002).

The use of cross well radar (CWR) has proven to be a reliable technology for detection of objects (such as acrylic plates) in soils under water saturated conditions (Farid, 2004; Farid et al., 2003a). These studies, however, did not address the applicability of the CWR technology for detection of heterogeneously distributed DNAPLs in unsaturated soil. Consequently, the CWR technology must be further developed and tested for gradual distribution of DNAPL in unsaturated soils. Like with GPR, detection of underground objects using CWR relies on significant contrast between the dielectric properties of the studied objects and the soil matrix.

#### Electromagnetic Properties of Soils

Differences in relative dielectric permittivity between water ( $\epsilon_r$ ) ( $\approx 80$ ), dry soil ( $\approx 3-10$ ), DNAPL ( $\approx 2.3$  to  $10.4$ ), and air (1) form the basis for CWR detection of immiscible fluids

(Farid, 2004). The dielectric constant of bulk soil is known to vary with water content (Farid, 2004; Miller et al., 2004; Carcione et al., 2003; Starr et al., 2000(a and b); Starr et al., 1999; Hipp, 1974). Generally, dielectric constant tend to increase with soil water content (Miller et al., 2004; Francisca and Rinaldi, 2003), ranging from 3-10 in dry soil values to over 40 for saturated soils, with most values ranging between 3 and 30 (Miller et al., 2004; Reynolds, 1997).

The effect of organic liquid content on dielectric constant of bulk soil depends on the value of the dry medium, and that of the organic liquid. Francisca and Rinaldi (2003) show a slight increase in dielectric permittivity as the volumetric content of an organic increased from dry conditions. This is a result of the organic liquid (dielectric constant  $\approx 2.3$ ) displacing a fluid (air) with a much smaller dielectric value (1). It is expected that organic liquids with higher permittivity values (e.g. chlorinated solvents) reflect higher contrast as a function of volumetric content. For water-saturated soils, dielectric permittivity tends to decrease as the volumetric content of the organic liquid increases (Francisca and Rinaldi, 2003). This is due to the displacement of a fluid (water) with a relatively high permittivity ( $\approx 80$ ) by one of lower value ( $\approx 2.3$ ). The effect of organic liquid content on dielectric constants in soils of varying degree of saturation depends on water content, soils properties, and dielectric properties of the liquid (Carcione et al., 2003). Dielectric constants are expected to drop significantly with decreasing water content, but increase slightly with decreasing air content.

Dielectric properties have been reported to be a function of the frequency of the emitted

radar waves (Miller et al., 2004; Francisca and Rinaldi, 2000; Hoekstra and Delaney, 1974; Hipp et al., 1974). At low frequencies (<10MHz), the dielectric constant has been reported inversely proportional to frequency (Hoekstra and Delaney, 1974), and has strong dependency with soil textural composition and water content (Srivastava and Mishra, 2004; Peplinski et al., 1995). Dielectric constant for water at higher frequencies remain relatively constant up to about 1GHz, and then decreases significantly with increasing frequency (Hoekstra and Delaney, 1974). At frequencies below 50MHz, the variations on the complex dielectric constant depends strongly on soil type (Van Dam et al, 2005a; Hoekstra and Delaney, 1974). At higher frequencies (>100MHz), the complex dielectric constant of wet soil tends to decrease (Miller et al., 2004; Francisca and Rinaldi, 2000; Hoekstra and Delaney, 1974; Hipp et al., 1974) depending on soil type, water content, and temperature.

Various methods have been devised to resolve subsurface heterogeneous in soil, utilizing both refraction and reflection of waves (Eppstein and Dougherty, 1998). Vector network analyzers (VNA) are used to measure scattering parameters (S-Parameters), and estimating transmission and reflection properties of the media along a raypath between transmitting and receiving antennas. These properties are then related to the dielectric and permeability properties along the raypath.

## Antennas

Estimation of dielectric properties between receiving and transmitting antennas require

prior knowledge of the transmission characteristics of the antennas. Antennas are dielectric structures designed to radiate or receive EM energy with directional and polarization properties, and serve as transducers between guided waves propagating in a transmission line and EM waves radiating in the surrounding medium. To minimize reflection and radiation losses at the transmission line-antenna juncture, it is necessary to have matching wave impedance in both components (transmission line and antennas). Even if these impedances are matched, antennas may have permanent radiation losses. For efficient antennas it is necessary to minimize these losses.

If antennas are electromagnetically similar and efficient, measured transmission and reflection coefficient between transmitting and receiving antennas reflect the dielectric and permeability properties of the media along a particular raypath. In CWR, it is possible to measure dielectric and permeability properties along several raypaths by positioning transmitting and receiving antennas at different locations within the medium.

### Tomographic Images

By using data from many intersecting raypaths, an image of the subsurface can be mathematically reconstructed to form a tomogram image based on measured dielectric properties. Several reconstruction algorithms have been applied to image subsurface inhomogeneities (Sharma, 1997). Most of these algorithms fall within one of two categories: discretization methods and transformation methods. Discretization methods consider the area of interest to be compressed of discrete cells (or pixels) where the

physical properties are assumed constant. Wave energy is considered to propagate in a straight-ray form through the various pixels to provide a sum or projection of all incident raypaths values within the cell. Transformation methods are based on the use of Fourier transform on continuous functions of continuous set of projections (Sharma, 1997). Both categories, discretization and transformation methods, give inexact result, and their application depends on a compromise between accuracy and computational resources. Discretization methods generally demand more computational resources than transformation methods, but they produce fewer artifacts. Reconstruction methods are less sensitive to noise and generate more accurate images in the case of incomplete data.

### Image Analysis

Analysis of images in the visible electromagnetic spectrum have been applied using dye tracers to investigate fate and transport processes in subsurface environments at small scales (Kasteel et al., 2005; Persson et al., 2005a; Persson et al., 2005b; Vanderborght et al., 2002; Stadler et al., 2000). Image analysis techniques have also been applied to estimate surface moisture (Persson et al., 2005b). These methods involve applying a diffuse light source and measuring the amount of light transmitted or reflected with a digital camera. They generate high spatial resolution data (Persson et al., 2005a). Traditionally, analysis of dye images involves separation between stained and non-stained soil. Improvement in methods and technologies has however given rise to determination of dye concentration (Persson et al., 2005a).

The research presented herein develops and evaluates Cross Well Radar (CWR) technologies to detect and monitor DNAPLs contamination in subsurface environments under transient flow conditions. It involves systematic development and testing of sensing system, signal management and processing; and imaging technologies. Electromagnetic and flow experiments are used in conjunction with image acquisition technologies to generate critical information to evaluate the effectiveness and reliability of CWR systems.

## **1.2 HYPOTHESIS DEVELOPMENT**

Based on the above discussion, it is hypothesized that:

- Sufficient contrast exists between EM properties of uncontaminated and DNAPL-contaminated soil to apply CWR for contaminant detection. It is further postulated that this contrast detection depends on water content.
- Dielectric properties along raypath between transmitting and receiving CWR antennas can be determined in a 2D electromagnetic soilBed bound by perfectly reflecting parallel surfaces.
- Spatially-distributed measurements of effective dielectric properties along raypaths in a 2D electromagnetic soilBed can be used to form tomographic images of distributed contamination under variable saturation conditions.

- Image processing and analysis of dyed-DNAPLs serve to determine amount of DNAPLs mass in a visual region.

### **1.3 OBJECTIVES**

The primary goal of this research is to develop and evaluate CWR technologies for detection and monitoring DNAPL contaminants in the unsaturated zone under variable conditions. In particular, this research addresses: (1) the applicability of dielectric contrast measurements for detection of DNAPL contamination in underground environments subjected to variable saturation conditions; (2) the applicability of 2D electromagnetic systems for measurements and imaging of dielectric properties in soils subjected to variable saturation conditions; (3) the validity of using tomographic images of dielectric properties to determine the location and extent of DNAPL contamination in the subsurface; and (4) the establishment of image analysis technologies for quantification DNAPL contamination in soils under variable saturation conditions. To meet these objectives and assess the established hypothesis several major steps were completed. These include:

- Design, construction, and development of a 2D flow and electromagnetic soilBed (soil tank) with capabilities for cross-borehole EM measurements and optical image acquisition.
- Evaluation of proper antenna type and arrangement for detection of DNAPLs in the soilBed.

- Development and execution of experimental protocols in 2D flow and EM soil systems subjected to variable saturation conditions.
- Development of computational code to determine dielectric properties from EM radar signals transmitted and received by an array of antennas.
- Development of a tomographic code to form images of spatially-distributed dielectric properties of the soil at various water and DNAPL saturation conditions.
- Development of an image acquisition and processing algorithm to visualize DNAPL extent and distribution.
- Establishment of a relationship between monitoring system for fate and transport of DNAPLs and signal received and emitted by the arrangement of chosen antennas.
- Assessment and interpretation of results in relation to extent, distribution, and movement of DNAPLs in soil environments.

#### **1.4 SCOPE OF EXPERIMENTAL WORK**

Experimental work involved taking electromagnetic measurements in a 2D flow and EM soilBed concurrently with digital images. EM measurements and digital images were collected prior to, during, and after the injection of water and/or trichloroethylene (TCE), a major underground DNAPL contaminant. EM measurements involved testing loop antennas, and measuring their transmission and reflection characteristics in the presence and absence of DNAPLs, water or underground target elements. The responses of the antennas were used to estimate spatially-distributed dielectric properties of the bulk soil.

These properties were used to produce tomograms that showed changes in the dielectric properties of the soil. During the research several antennas, analysis of mini-scale soilcells, and prototypes were made to improve the cross well radar technology.

## **1.5 RESEARCH SIGNIFICANCE**

The work conducted advances the knowledge and capabilities of methods for detection and monitoring of underground contamination, hydraulic conditions, and water infrastructure. The work has developed test beds for technology assessment of detection and monitoring methods pertinent to civil engineers. It shows that, with future development of the technologies, CWR may be applied to characterize underground contamination and moisture conditions. Development of algorithm for the interpretation of EM measurements and digital images facilitates the integration of detection technologies necessary for the enhancement of civil infrastructure and the environment.

Detection and monitoring of underground contamination and hydraulic conditions (e.g. fluid saturation) is essential for development of remedial actions in contaminated sites. As they advance, CWR and imaging technologies can be applied to spatially and temporally monitor changes in water and contaminant movement and thus develop better understanding of their fate and transport processes in the environment. Fundamental concepts of this research can also be applied for characterization of underground environments. Knowledge in the properties and conditions of underground systems place fundamental control on the fate and transport of water and contaminants and govern the selection of conceptual and predictive models. Crucial enhancement on these

technologies has been identified by the National Research Council and other governmental agencies (NRC 2000, a and b).

Detection of subsurface anomalies using non-destructive radar methods presents great potential for health assessment of aging civil infrastructure and detection of leaks from underground water distribution and sewer lines and storage tanks. The research also contributes to close the gap between technology development and its application by civil engineering domain experts. Through this integration, this research enhances the ability of civil engineers to solve civil infrastructure problems and build a better quality of life for everyone.

## **1.6 THESIS ORGANIZATION**

This dissertation works consists of several integral parts, including: design and development of experimental system and methodology to evaluate CWR technologies; performing laboratory experiments for detection and visualization of underground DNAPL and target elements; development of CWR technologies to characterize dielectric properties and construct tomographic images of these characteristics; and application of developed technologies to experimental result to detect and visualize DNAPL contamination in underground environments. These parts are organized and included in chapters, as briefly described below.

Chapter 2 describes the introductory background theory on underground contamination; DNAPLs contaminants and remediation methods; technologies for remediation and detection of subsurface contaminants; wave propagation in subsurface environments; electrical properties of soils and contaminants; measurements of electrical properties in soils; tomographic imaging of soil properties; and image processing using digital information. Chapter 3 describes the materials and methods used for the experimental work. It also describes the methodology applied to determine dielectric properties of the bulk medium from the measurements of EM wave characteristics.

Chapter 4 addresses the development of a two dimensional (2D) flow and electromagnetic setup to further assess and enhance the CWR technology for the detection of DNAPL contamination and other target elements in soil. Chapter 5 integrates CWR and image acquisition and processing technologies for bi-modal detection and monitoring of DNAPLs flow and transport in variably-saturated soils. Chapter 6 addresses the development of a physics-based tomographic model for in situ soil characterization, detection and imaging of under target elements (UTEs) in unsaturated soils by CWR. Chapter 7 describes and discusses the results on the application of CWR technologies to detect and visualize DNAPL contamination in underground environments. Chapter 8 provides a summary, conclusions, and recommendations of this experimental research.

## **2. THEORETICAL BACKGROUND**

The growing population demand and increasing production of energy supply have caused an increase in the release of organic contaminants into the environment. Contamination of soils and groundwater by accidental spills, poor storage facilities, and inadequate disposal practices causes serious detriment of the environment and can pose a serious threat to human health. Common contaminants found in underground environments include many Dense Non-Aqueous Phase Liquids (DNAPLs). These contaminants pose particular threats because of their heterogeneous distribution and long-term perseverance in the environment. Moreover, they are difficult to locate, characterize, and remediate (NRC, 2000a). It is, therefore, necessary to develop new technologies that will enhance our ability to characterize contaminated sites, locate underground contaminants, evaluate fate and transport processes, and remediate these contaminated sites.

The use of cross well radar (CWR) has proven to be a reliable technology for detection of objects (such as acrylic plates) in soils under water saturated conditions. CWR technology, however, must be further developed and tested for detection of gradual DNAPL distribution in unsaturated soils. The ultimate goal of this research is to develop and evaluate CWR technologies for detection and monitoring of DNAPL contaminants in the unsaturated zone under variable conditions. These technologies can then be applied for assessment and application of remedial technologies. This chapter addresses

background information and previous related work in DNAPL contaminants, DNAPL subsurface remediation (which can be enhanced by new detection technologies), subsurface detection methods, wave propagation theory, EM properties of bulk soil and DNAPLs, measurements of EM properties, tomographic theory, and digital image acquisition and processing.

## **2.1 DENSE NON-AQUEOUS PHASE LIQUIDS**

A dense non-aqueous phase liquid (DNAPL) is a heavier-than-water organic liquid that is immiscible with water and air. DNAPLs have been widely used in industry since the early part of the 20<sup>th</sup> century (Jackson and Dwarakanath, 1999) and their use has been widespread since the World War II (Durnford et al, 1997). Common types of DNAPLs include timber treating oils such as creosote, transformer and insulating oils containing polychlorinated biphenyls (PCBs), coal tar, and a variety of chlorinated solvents (Moran et al., 2007; Kueper et al., 2003). Chlorinated solvents such as trichloroethene (TCE), trichloroethane (TCA), tetrachloroethene (PCE), and carbon tetrachloride (CTET) form a class of DNAPLs that have been produced in large quantities throughout the world since the middle of the 20<sup>th</sup> century (Kueper et al., 2003). They have been used for chemical extraction (e.g., chloroform), refrigeration (methylene chloride), dry cleaning (e.g., TCE, PCE), metal degreasing (e.g., TCE, PCE), pharmaceutical production (e.g., CTET), and pesticide formulation.

The widespread use of DNAPLs has resulted in extensive contamination of underground environment, and are commonly found in groundwater resources (Moran et al., 2007; Brusseau et al., 2003; Sneddon et al., 2002; Jalbert and Dane, 2001). Thousands of DNAPL-impacted sites exist throughout United Kingdom, North America, Europe, and other industrialized areas of the world (Kueper et al., 2003). PCE and TCE are among the most frequently detected contaminants in United States (Moran et al., 2007). Indeed, of more than 1400 heavily contaminated sites in U.S., more than sixty percent are contaminated with TCE (Fischbein, 2005). Once these contaminants enter the subsurface environment, they can serve as a long-term source of contamination (Brusseau et al., 2000).

DNAPL enter the subsurface environment from accidental spills, poor storage facilities, and inadequate disposal practices (Oostrom et al., 2006; Kueper et al., 2003). Their movement and persistence in the environment depend on their physico-chemical properties, and the characteristics of the subsurface environments. Because the scope of this work is on TCE, this discussion will focus on relevant physico-chemical properties of chlorinated solvents.

### *2.1.1 Physico-chemical Properties of Chlorinated Solvents*

Chlorinated solvents are only slightly soluble in water (with aqueous solubility around 1,100 mg/L) and therefore exist in the subsurface as a separate fluid phase immiscible in both water and air. The density ( $\rho$ ) of most chlorinated solvents DNAPLs range from 1.1 to 1.6 g/cm<sup>3</sup> and their viscosity ( $\nu$ ) from 0.57 to 1.0 cp. (Kueper et al., 2003). Their

higher density and lower viscosity than water ( $\rho_{\text{water}}=998.2\text{kg/m}^3$  and  $v_{\text{water}}=1.00*10^{-6}\text{m}^2/\text{s}$  at  $20^\circ\text{C}$  (Todd and Mays, 2005) result in relatively rapid rates of subsurface migration as immiscible fluids. Furthermore, most chlorinated solvents are typically characterized by low sorption onto organic carbon, having low organic carbon distribution coefficients (Koc) ranging between 44 and 439 ml/g (Mackay et al., 1993). Low sorption characteristics result in low solute retardation and higher mobility relative to more sorbing compounds. High vapor pressures of chlorinated solvents give rise to vapor phase contamination in the gas phase.

### *2.1.2 Subsurface Transport of Chlorinated Solvents*

When released in sufficient quantities in the unsaturated or saturated zones chlorinated DNAPLs spread vertically or laterally in the subsurface. Their distribution can be continuous, discontinuous, or both (Oostrom et al., 2005). The movement is generally not uniform and follow preferential flow path along relatively large-size pores. DNAPLs in continuous flow strings move vertically downward, primarily by gravity, until the free phase is distributed as residual saturation in the form of mass globules or ganglia (ITRC, 2002). Residual saturation is considered immobile (Oostrom et al., 2005) and held in place by capillary forces that arise from DNAPL-water and DNAPL and surface tensions (Kueper et al., 2003). The distribution of residual saturation is not uniform and depends on porous media characteristics.

If strata of finer grains are encountered as DNAPL move downward, they may spread laterally and form pools (Figure 2.1) (ITRC, 2002). The maximum pool height formed

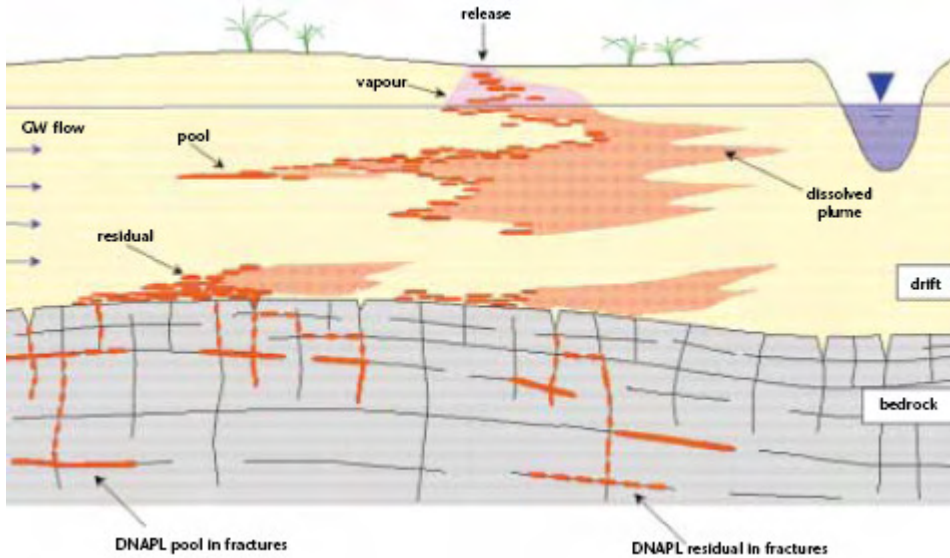


**Figure 2.1 DNAPL distribution in unconsolidated deposits**

Source: Kueper et al., 2003

before DNAPLs flow through the lower permeability zones is inversely proportional to the size of the pores and their permeability of the particular zone. The critical height ( $Z_n$ ) necessary for a DNAPL to enter a formation of pore size  $r_t$  in the unsaturated zone is given by (Bedient et al., 1997):

$$Z_n = \frac{2\sigma \cos(\phi)}{r_t g \rho_n} \quad \text{Equation 2.1}$$

where:

$\sigma$  = interfacial tension between NAPL and water

$\phi$  = contact angle

$\rho_n$  = density of NAPL

$g$  = gravitational constant

$r_t$  = radius of the pore throat that the NAPL must move through to exit or enter the pore

Larger pool heights are formed for DNAPLs with higher DNAPL-water interfacial tensions and smaller pores (i.e., finer grains with lower permeability) (Kueper et al., 2003). When vertically moving DNAPLs encounter the water table, they will accumulate until there are enough gravity forces to overcome capillary and hydrostatic forces and displace water (Bedient et al., 1997). The pressure at which water is displaced is known as the non-wetting phase entry pressure (Durnford et al., 1997). The critical height ( $Z_n$ ) required by a particular DNAPL to displace water in pores of size  $r_t$  is given by (Bedient et al., 1997):

$$Z_n = \frac{2\sigma \cos(\phi)}{r_t g(\rho_n - \rho_w)} \quad \text{Equation 2.2}$$

where:

$r_t$  = radius of the water filled pore throat that the NAPL must move through to exit or enter pore.

Fluid-fluid interactions and the presence of heterogeneous pore-size distribution may give rise to the formation of fingers, as water is displaced and DNAPLs enter below the water table (Trantham and Durnford, 1998). These fingers may move substantial distances before dissipating into the surrounding soil matrix (Jury et al., 2003). As in unsaturated media, residual DNAPL in saturated porous media forms relatively immobile discrete globules and ganglia disconnected from each other (Kueper et al., 2003). DNAPL pools also form where DNAPLs encounter finer grain media under the water table.

In unsaturated media, DNAPL globules, ganglia and pools are exposed to air. Because of the relative high vapor pressure of chlorinated solvents DNAPLs, they volatilize into the

soil-air and form a volatile plume (Pantazidou and Sitar, 1993). DNAPL globule, ganglia, and vapor can also dissolve into infiltrating water.

DNAPL globule, ganglia, and pools in saturated porous media dissolve slowly into flowing groundwater, giving rise to aqueous phase plumes. Groundwater flow through the zone contaminated by the NAPL may spread the dissolved phase beyond the boundaries of the zone containing the separate phase. The low aqueous solubility of chlorinated solvents and relative low water velocities in the subsurface result in very low removal rates of residual DNAPLs. Consequently, they act as a long-term source of contamination, and give rise to widespread contamination of ground water to unacceptable levels (Sneddon et al., 2002). Natural groundwater flow through source zones containing DNAPL globules, ganglia, and pools may therefore occupy larger aquifer volumes than the source zones, and pose greater risks to receptors and the environment (Wadley et al., 2005; Parker et al., 2003).

As groundwater flows across a source zone, DNAPLs dissolve and are generally transported downgradient with flowing groundwater. During their transport they may be dispersed, diluted, retarded, and degraded. Consequently, concentrations are highest near the source zone and decrease away in the downstream direction (Kueper et al., 2003). Contaminant concentration in wells downstream of a DNAPL source may therefore be significantly less than aqueous solubilities. Concentrations below solubility may be erroneously conceived as the absence of DNAPL source. Experience has shown that

DNAPL sources may be upstream of a monitoring well if concentrations exceed 1% of the solubility (EPA, 1992).

Moreover, the complexity and heterogeneity of fate and transport process in the subsurface makes it almost impossible to estimate the location and extend of DNAPL sources from measured concentrations in monitoring wells. If present as DNAPL mixtures (a DNAPL composed of two or more chemical compounds), the maximum potential concentration (MPC) of each component in groundwater is lower than their individual solubility. The MPC is directly proportional to the mole fraction of the particular component in the mixture (Bedient et al., 1997). As a result, the lower effective solubility is therefore not an indication that DNAPL is not present.

DNAPL contamination of soils and groundwater has detrimental effects on the environment, limits availability of water resources, and can pose a serious threat to human health. DNAPLs have been found to be toxic to mammals and other fauna (ASTDR, 2007; Moran et al., 2003). TCE has been identified as a central nervous system depressant a hepato toxin, and a carcinogen (ATDSR, 2007). PCE has been related to adverse reproductive effects on woven, liver and kidney damage, and cancer (ASTDR, 1997).

### *2.1.3 DNAPL Remediation*

Source zone remediation requires knowledge of characteristics, location, and extent, and configuration of the DNAPLs (Durnford et al., 1997). Remediation downstream of the

source zone includes aquifer restoration, plume interceptions, and monitored natural remediation (Kueper et al., 2003). Aquifer restoration seeks complete elimination of groundwater and sorbed contamination, and requires that the source zone is completely removed or isolated. Plume interception is commonly employed to limit contaminant concentration and associated risks. Monitored natural attenuation (MNA) requires good knowledge of the extent of contamination, good understanding of groundwater flow, and appropriate monitoring well network, and a large number of measurements through the year (Environment Agency, 2000).

### *Remediation Technologies*

Some technologies target DNAPL source zones, while other target the components downstream of the source zone. This section intends to provide a general overview of the various remediation technologies available for source zone remediation. Most of these technologies are also applicable to remediation of dissolved, vapor, and sorted contamination downstream of the source.

Source zones of DNAPLs may be controlled through physical containment, removal, and through in situ destruction in the contaminated zone. Often a combination of technologies is used. Removal activities must be followed by treatment and/or proper disposition of the removed contaminated medium. Ex-situ treatment technologies are beyond the scope of this work.

Source containment limits the spread of the contamination and may involve the placement of physical barriers, such as sheet piling and injection grouting, and/or hydrodynamic isolation (Wadley et al., 2005; Kueper et al., 2003; Fetter, 1999). Hydrodynamic isolation is used to isolate contaminated zone from the rest of the groundwater system. It is often combined with removal technologies, and involves the placement of extraction wells downstream of the source and injection wells up gradient from the source. The withdrawn water may be treated prior to injection, or nutrients can be added to promote bioremediation. The use of physical barriers is limited to unconsolidated technologies and requires good knowledge of the spatial extent of the DNAPL source zone and the hydrogeologic formation. Improper installation and aging of the barriers may cause leaking and containment failure. Containment technologies require extensive monitoring activities through long periods of time.

Removal of DNAPLs may be accomplished through excavation, and through fluid displacement, dissolution, or volatilization followed by liquid and/or vapor extraction (ITRC, 2000; Fetter, 1999; Fountain, 1998). Physical removal of residual and pooled DNAPLs through excavation is considered at sites where the extent of contamination is restricted to shallow unconsolidated deposits in the unsaturated zone (Kueper et al., 2003). Excavation must be done so that workers and public are not exposed and require disposal at a secure landfill or incinerator (Fetter, 1999). This method is very expensive and is limited to small-volume contamination.

DNAPL removal through fluid displacement and dissolution involve mobility and/or dissolution enhancement followed by fluid extraction, as in conventional pump and treat (Kueper et al., 2003). DNAPL direct extraction is only possible when free and/or pooled DNAPLs are present. DNAPLs can be mobilized toward extraction wells when a strong hydraulic gradient is imposed (EPA, 2004). It generally requires that extraction wells are in the zone source. Technologies designed to physically displace DNAPLs, reduce capillary forces by reducing interfacial tension between DNAPLs and groundwater using surfactants, cosolvents, or heat (Fountain, 1998). The mobilized contaminants and the contaminated groundwater are recovered from extraction wells. Technologies that enhance DNAPL dissolution involve increasing contaminant solubility through the use of chemical additives, such as surfactants and/or cosolvents, or by increasing temperature (Husser, 2003; Kueper et al., 2003; ITRC, 2000; Fountain, 1998). *In situ* flushing entails the addition of remediation fluids to the contaminated zone. These technologies can lead to an increase contaminated region, and increase contaminant loading to impermeable regions.

Technologies designed to remove DNAPLs by volatilization involve inducing flow of vapor through the unsaturated contaminated zone and the transfer of contaminants to the vapor phase (Kim et al., 2005; Fountain, 1998). Heat and steam can be used to increase the vapor pressure of the contaminants and emulsify DNAPLs. DNAPL is removed by a combination of direct volatilization from DNAPLs and volatilization from the dissolved phase. The contamination is recovered as vapor through vapor extraction wells. Soil vapor extraction (SVE) is commonly used in combination with other techniques such as

thermal, air sparging, and soil bioventing technologies. Air sparging refers to the injection of air below the water table within the DNAPL source such that contaminants partition into the rising stream of air and accelerate DNAPL dissolution (Kuerper et al., 2003). This technology may mobilize pools deeper into the subsurface and it is limited by slow diffusion of contaminants from low-permeability layers into areas with vapor exchange, vapor-phase retardation due to adsorption, limited volatility of the contaminant, and low permeability soil layers (Oostrom et al., 2006). Soil bioventing enhances *in-situ* biodegradation by addition of air. It is limited to aerobic and degradable compounds.

*In-situ* destruction of chlorinated solvents of DNAPLs may be stimulated through enhanced biodegradation, contaminant oxidation, reductive dehalogenation, and thermal decomposition. Although biodegradation of chlorinated solvents in the subsurface may occur by microorganisms that are naturally present in soil and groundwater (ESTCP, 2005), it is likely that nutrients and carbon sources may have to be added to enhance the bioremediation of chlorinated compounds. Enhance biodegradation involve the injection of nutrients and other agents to stimulate biological activity (Kueper et al., 2003). A compound may be directly biodegraded if bacteria can obtain energy from the degradation of the compound, generally when the compound acts as an electron donor in a redox reaction. Chlorinated compounds do not act as electron donors or accepters, but may be degraded cometabolically (Fountain, 1998). In cometabolic degradation, enzymes produce by the degradation of some other can from source (e.g. alcohols) induces the breakdown of the compound of interest. Biodegradation is not generally

effective in NAPLs, and require that these compounds are dissolve in groundwater to become mineralized. If injected upstream of the source zone, these agents may accelerate degradation of contaminants, and dissolution of DNAPLs.

Studies have indicated that biological activity can produce an increase in the bulk dielectric constants of the media (Schillig et al., 2007). This change in biological activity has been detected with ground penetrating radar (GPR) technologies.

Technologies involving oxidation of DNAPLs typically involve addition of oxidizer to the subsurface (Fountain, 1998). Because most chlorinated DNAPLs are relatively resistant to oxidation under naturally occurring conditions, this technology requires the addition of strong oxidizer. Common oxidants include fenton's reagent, potassium/sodium permanganate, sodium persulfate (Kueper et al., 2003), although hydrogen peroxides and ozone have also been used (ITRC, 2002). Oxidant flooding is a relatively new technology that can be applied for partial mass removal from the source zone. Screening studies and field pilot testing are necessary before considering full scale application.

Reductive dehalogenation involves the loss of halogens from the molecules as a consequence of electron transfer to the compound (Schwarzenbach et al., 2003). This reaction occurs under reducing conditions and with reductants present in anaerobic conditions. It can be mediated abiotically (e.g., using zero-valent iron), or biotically (Brown et al., 2006), and be accomplished in the aqueous, NAPL, and gas phases (Liu et al., 2001). It however requires the delivery of the reductant species.

Thermal technologies for chlorinated DNAPL remediation include flushing technologies (steam and hot water), volatilization processes (steam and electrical heating), and chemical destruction (Fountain, 1998). Most of these technologies rely on heat to vaporize and mobilize contaminants (Kueper et al., 2003). Thermal destruction heats the soil to a temperature at which the soil melt and the organic contaminants decompose if not previously volatilized (Fountain, 1998). Thermal technologies can be applied to the vadose zone and below the water table, and require soil vapor or liquid extraction systems to contain and extract the contaminants. These technologies are very expensive (energy intensive) and can carry a risk of mobilizing contamination to previously unimpacted areas (Kueper et al., 2003).

Except for excavation, most of the technologies discussed above require the delivery of flushing fluids and/or reactants to the subsurface, and the extraction of fluids (water, NAPL, gas) for contaminant removal. These technologies are affected by subsurface heterogeneities and require detailed quantitative knowledge of the geosystem properties and DNAPL mass and distribution (ITRC, 2000).

#### *2.1.4 Detection Methods*

The identification of DNAPLs in the subsurface is the first step toward remediation of an area affected by dense chlorinated contaminants (Johnson and Poeter, 2005). Given the selective and tortuous migration of DNAPLs in the subsurface, the probability of directly encountering residual or pooled DNAPL with conventional drilling programmed is very small (Kueper et al., 2003). Consequently, direct visual observations of DNAPLs do not

occur at most DNAPL sites. Instead, the presence and location of DNAPLs must be inferred using other methods. A strong need, therefore, exists for the development and integration of novel techniques, for detection and monitoring of contamination in subsurface processes.

Invasive methods using borehole sampling technologies are the most commonly used techniques for DNAPL detection and source characterization in the subsurface. These methods rely on soil and fluid sampling and analysis. Invasive point measurement may cause remobilization and further spread of DNAPLs in otherwise stable system (Sneddon et al., 2000). Several innovative technologies for characterizing the subsurface distribution have been developed (Parker et al., 2003; ITRC, 2000) and are briefly summarized below.

#### *2.1.4.1 Borehole and soil core technologies*

Invasive methods using borehole sampling technologies are the most common used techniques for DNAPL detection and source characterization in the subsurface. These methods rely on soil and fluid sampling and analysis.

Soil samples can be taken from unconsolidated deposits both above and below the water table using techniques such as hollow stem auguring and direct push technologies (Kueper et al., 2003). During borehole drilling, soil samples can be taken for visual examination and soil analysis. Visual examination may involve dye-shake tests, in which a small sample of hydrophobic dye (e.g. sudan) is mixed with the soil. If DNAPL is

present, the dye partitions into and stains the DNAPL, which is reflected as dyed globules. Other methods for soil sample analysis include heat space and fluorescence analysis. Quantitative analysis of contaminant composition is typically performed on discrete soil samples sent to analytical laboratories.

Sampling and analysis of vapors, groundwater, and DNAPLs can be done during drilling operations, and in wells. A “rule of thumb”, organic vapor measurements on the order of 1000-2000 parts per million per volume (ppmv) or higher are probably reasonable indication of the presence of DNAPL in the field (Kueper et al., 2003).

Groundwater concentrations in excess of one percent of the effective solubility of the component (e.g. TCE, CE) are also indicative of DNAPL presence. The presence of free pooled DNAPLs in wells may be determined through the use of bottom loading bailers and weighted oil-water interface probes (Kueper et al., 2003). This requires that the wells are installed in the DNAPL pool. Even in this case, it is relatively impossible to determine pool thickness and extent. It is however important to keep in mind the lack of DNAPL free product detection in wells is not indicative that DNAPL are not present in the aquifer (Pankow and Cherry, 1996).

Traditional approaches that rely on drilling, testing, and sampling for locating and characterizing DNAPL provide the most direct access to the subsurface and are required for characterization of the DNAPL (e.g., components). They are, however, expensive and only provide point measurements in a three dimensional space (NRC 2000b). The

tortuous and sparse migration of DNAPLs, combined with the fact that invasive techniques only provide access to a minute fraction of the subsurface, result in a low probability of actually encountering DNAPLs in many site investigations (Kueper et al., 2003). Furthermore, concentration analysis may not be indicative of DNAPL presence, even if present.

Direct push technology (DPT) describes a variety of methods for obtaining subsurface data in a quick, minimally invasive manner (ITRC, 2000). The tools or probes used penetrate the subsurface and are withdrawn once the required data are collected. Probes are available for directly measuring contaminant concentrations in situ and provide flexible real-time analysis. The probes allow expediting the collection of soil, groundwater, and soil gas samples for a consequent laboratory analysis. For instance, the use of piston core barrel provides excellent recovery of relatively undisturbed samples of cohesionless sandy deposits from below the water table (Parker et al., 2003). Direct push technologies are also being used in conjunction with flexible membranes fitted with absorbent liners to detect DNAPL directly (ITRC, 2000).

**Soil Probing/Cone Penetrometer-Based Technologies.** The cone penetrometer is an example of a direct push tool traditionally used in the civil engineering field for cone penetration testing (CPT) and adapted for the environmental field. In that way, standard cone penetrometers collect stratigraphic information using embedded sensors to measure cone tip pressure and sleeve friction that can be used to classify soil type (ITRC, 2000).

Several DPT configurations are available; those potentially applicable to DNAPL investigations are outlined below.

Core sampling. These devices gather core samples, which are retrieved/extracted for analysis, allow for a single sample to be gathered at a desired depth (e.g., split spoon sampler), while others allow for multiple samples to be obtained at various depths (ITRC, 2000).

Laser Induced Fluorescence. Laser induced fluorescence (LIF) is a site characterization technique for detecting petroleum products containing aromatic hydrocarbons in soil and can not be directly used to detect chlorinated solvents directly (ITRC, 2000). The sensor consists of a laser adapted to an optical detector to measure fluorescence via optical fibers. Indirectly, LIF can be used for indirect location of DNAPL source zones by identifying commingled fluorophores. In this technique, fluorescing organic matter or co-contaminants that leach preferentially into DNAPLs are used to infer the presence of DNAPLs.

Electrical Resistivity/Domain Reflectometry. These devices take advantage of the relationship between the soil dielectric constant and moisture content. The soil moisture content is determined by measuring the frequency shift of a high frequency excitation signal as it passes through the soil. The frequency shift is referred to as the resistivity. This concept is being used to characterize contaminated sites by using the difference in

electrical resistivity between contaminated and uncontaminated soils. There are a few devices that have been designed to facilitate this concept (ITRC, 2000).

*Vision Cone Penetrometer.* The vision cone penetrometer (V-CPT) consists of an electronic cone penetrometer fitted with video cameras and a lighting system that allows to visually observing the soil as the push probe is advanced (ITRC, 2000). The V-CPT system provides stratigraphic information at very high resolution. The unit can detect DNAPL globules.

Direct push technologies (DPT) allow detection *in situ*, and is generally faster and more cost effective than conventional drilling and sampling. This technology may be limited by ground and subsurface conditions (e.g., muddy conditions, uneven terrain, bedrock, clay-rich soils). Furthermore, DPT suffer from the same limitation than traditional drilling and sampling techniques in that it only provide point measurements in a three dimensional space. Moreover, these techniques may promote further spread of contaminants.

*Ribbon NAPL Sampler.* The Ribbon NAPL Sampler (RNS) is a continuous, direct sampling device that can provide detailed depth discrete mapping of NAPLs in a borehole (ITRC, 2000). This technology uses an impermeable liner and an exterior covering on the liner which reacts with pure product (e.g., LNAPL and DNAPL) to form a bright red dye stain on a white background. The reactive ribbon can then be examined for the presence and extent of layers, and even globules, of NAPL in the subsurface may

be identified by brilliant red marks on the ribbon. This technique can be deployed with DPT or traditional borehole methods and works in the vadose and saturated zones. It suffers from the same limitations as DPT and traditional drilling and sampling methods.

#### *2.1.4.2 Geophysical technologies*

Geophysical DNAPL characterization technologies employ non or semi-invasive methods of locating DNAPLs. These techniques sample a volume of the subsurface, instead of the traditional point sampling techniques, and yield indirect measurements of site characteristics. They are based on the response of the system to artificial or natural EM stimuli (NRC, 2000a). Geophysical methods are an alternative for the detection of DNAPL source zones because they avoid vertical migration, and lead to potentially more complete site characterization (ITRC, 2000). Furthermore, geophysical methods are time effective (Johnson, 2005; Johnson and Poeter, 2005) and offer a opportunity for the monitoring the site during decontamination processes (Francisca and Rinaldi, 2003).

A variety of geophysical methods allow noninvasive determination of subsurface physical and chemical properties (Carcione et al., 2003; Garambois et al., 2002; Buselli and Lu, 2001). The applicability of these technologies depends on the type of NAPL and site geology. Noninvasive technologies for DNAPL detection and characterization include induced polarization (IP), vertical induction profiling (VIP), seismic reflection, electrical resistance tomography (ERT), low frequency methods, ground penetrating radar (GPR), and cross well radar (CWR) (ITRC, 2002).

*Induced Polarization (IP)*

Induced Polarization methods assess the response of the ground to an excitation and the removal of an induced electrical signal (NRC, 2000a; Reynolds, 1997). When an applied current is switched off, the voltage decays to zero in a measurable and finite time because the ground stores charge (i.e., becomes polarized) and acts as a capacitor. When the current is switched back on, the current builds up for some time period (rise-time) to its maximum applied value (Reynolds, 1997). The voltage decay and rise time can be used to characterize the underground environment. IP measures the low-frequency capacitive behavior of the media, which is produced by the accumulation of charge across surface boundaries (NRC, 2000a). IP is present in varying degrees in all earth materials, but it manifests itself strongly when electrically conducting materials, such as metallic ores or clays, are present.

IP measurements can be made using time domain, frequency domain, phase domain and spectral methods. Time domain methods measure the voltage decay after excitation by a current pulse (Titov et al., 2004), while in the frequency domain the apparent resistivity is measured at multiple frequencies (Reynolds, 1997). In the phase domain, the spectral IP measures the phase and magnitude over a range of frequency from  $10^{-3}$  to  $4 \times 10^3$  Hz (Reynolds, 1997).

Induced polarization has been used in mineral exploration (Yang, 2002; Pelton et al., 1978), lithological discrimination, hydraulic characterization, and detection of organic contaminants (Kemna et al., 2004; Titov et al., 2004). The development of

multielectrode, automated data acquisition system and 2D and 3D inversion algorithms for resistivity image reconstruction have facilitated visualization of the subsurface resistivity distribution (Gasulla et al., 1999). Consequently, it is making possible to obtain 2D or 3D images of the polarizability of the subsurface.

Induced Polarization methods can be used to detect electrochemical reactions of immiscible contaminants with surrounding media. Because of IP sensitivity to clays at depth, it is sometimes difficult to determine if an IP anomaly is due to actual contamination or clay lenses. Furthermore, IP technologies are limited by lack of consistent high quality, high volume data and dissemination of computer codes (NRC, 2000a).

#### *Vertical Induction Profiling*

Vertical Induction Profiling (VIP), patented by Ground Truth Technology, Inc., is an electromagnetic induction process that provides information about subsurface geophysical conditions providing a three-dimensional image of subsurface resistivity (ITRC, 2000). Because hydrocarbon and DNAPL contaminants are electrical insulators and displace soil moisture, a resistivity contrast with the indigenous material can be logged by the VIP equipment (ITRC, 2000). The technology is used to provide high-resolution site characterization and DNAPL source delineation without quantified concentration data.

VIP methods use EM transmitter on the surface and a tuned receiver placed down a borehole to make a continuous vertical EM induction profile log. The transmitter component is placed at each measurement location, and an offset induction log is recorded in the nearby drill hole. The receiver in the probe moving up the drill hole measures the primary and the secondary electromagnetic fields produced at the transmitter location (ITRC, 2000). These fields are used to estimate apparent resistivity and compare directly with the physical properties of the soils. Contour maps of resistivity measurements are used to track geologic patterns and trends and to delineate the configuration of plumes (ITRC, 2000).

VIP measurements are more effective in sands, silts, clay and tills than in consolidated and unconsolidated rock. It may also be affected by metal-cased wells and by the presence of cathodic protection on pipelines and buried power lines when in close proximity to the downhole receiver (ITRC, 2000). VIP can be use to asses the presence of NAPLs, but cannot differentiate between type of contaminant (e.g., petrochemical vs. diesel fuel) (ITRC, 2000).

#### *High Resolution Seismic Reflection*

High resolution, three-dimensional seismic reflection imaging uses seismic waves to detect materials with different densities at depths of 3 to 3,000 ft. The technology basis is that when an impact is introduced at the surface, acoustic waves spread throughout the subsurface until they are bounced back (to the surface) when material with different acoustic impedance is encountered. The travel time of these acoustic waves is used to determine the depth and thickness of subsurface features. The technology does not

specifically detect DNAPLs, but it can detect fractures and channels that serve as preferred pathways for DNAPL migration (ITRC, 2000).

Seismic methods can be used to map noticeable geologic, hydrologic, and physical interfaces (Watson et al., 2001). Various methods have been devised to resolve subsurface heterogeneities utilizing both refraction and reflection of waves (Eppstein and Dougherty, 1998). Seismic refraction and reflection methods have been used successfully for mapping water tables and aquifers in unconsolidated sandy formations and defining stratigraphic boundaries, including groundwater pathways (Garambois et al., 2002).

#### *Electrical Resistance Tomography (ERT)*

Electrical resistance tomography, also known as electrical impedance tomography, is an imaging technique which uses a number of electrodes in boreholes and/or ground surface to image resistivity distribution in the underground region (Sharma, 1997). Electrical resistivity methods estimate the bulk electrical resistivity of the subsurface by measuring the voltage generated by transmission of current between electrodes implanted at the ground or in boreholes (Corwin and Lesch, 2003; Furman et al, 2003; Furman et al., 2002; NRC, 2000a). The electrical resistivity of a soil is dependent on the soil type, degree of saturation, and local geometry.

In ERT, the resistance data from multiple measurements made with overlapping electrode arrays is inverted to determine an image of the resistivity between electrodes in a two or

three dimensional distribution (Furman et al, 2003, Binley et al., 2002; ITRC, 2000). The electrical resistivity distribution can then be related to water content, concentration of electrolytic solutes, and the surface resistivity of the subsurface material.

ERT compares the electrical resistivity and phase measurements of materials in the subsurface to distinguish between contaminated and uncontaminated soil (ITRC, 2000). ERT has been applied to delineate DNAPLs in the subsurface (Chambers et al., 2004; Ramirez et al., 1996) and monitoring migration of contaminants and/or water (Liu and Yeh, 2004; Garambois et al., 2003; Benson et al., 1997). It has been applied to map leaks from underground tanks (ITRC, 2000; Benson et al., 1997), plumes of contamination, and evaluating remediation technologies (ITRC, 2000). DNAPL may be mapped, because the resistivity of ground water is less than DNAPL, and this difference can be illustrated in ERT displays. It is, however, a gross characterization technology and does not provide chemical concentration data. ERT technologies are not as effective in consolidated and unconsolidated rock, and has better results in sands, silts, clay tills, etc. (ITRC, 2000). Furthermore, this technique requires good contact between the soil and the electrodes inserted into the soil (Corwin and Lesch, 2003), and factors as depth control, and the effect of soil type need to be addresses to improve the measurement accuracy (Zhang et al., 2004).

These electrical techniques have been used for environmental purposes because of their ability to observe the change in resistivity due to migration of contaminants and/or water in the unsaturated zone (Garambois et al., 2003; Benson et al., 1997). That is attributed to

the fact that knowledge of the spatial distribution of the electrical properties of subsurface media can provide information for characterizing waste sites and monitoring flow and contaminant movement in the vadose zone (Liu and Yeh, 2004).

### *Low Frequency Methods*

Low frequency electromagnetic methods operating at frequencies between 1 and 30MHz provide capabilities to measure organic contaminants, engineered structure, and buried non metallic objects (NRC, 2000a). Their resolution is, however, relatively low.

### *Ground Penetrating Radar (GPR)*

Ground Penetrating Radar (GPR) is a high resolution geophysical technique that uses transmitting and receiving antennas above the ground surface to propagate and record high-frequency electromagnetic waves ( $10^1$ - $10^3$ MHz) into the ground (Watson et al., 2001). The propagation of the electromagnetic energy is controlled by dielectric properties in the subsurface materials (ITRC, 2000). It commonly shows better resolution than lower frequency EM methods because of its smaller wavelength. The output signal yields a trace of two-way travel time versus amplitude. The two-way trace time is the time taken by EM wave energy to travel to a boundary (i.e., zone of contrasting EM properties) and back (Peterson and Nobes, 2003). Amplitude variations in the signal trace are therefore associated with the location of EM boundaries through the two-way travel time. The signatures may be affected by soil texture and soil water content.

GPR detection and monitoring technologies, as well as other EM detection technologies, rely in the detection of contrasting EM properties of the materials present in the subsurface. Differences in dielectric properties of water ( $\approx 80$ ), dry soil ( $\approx 3-10$ ), DNAPLs ( $\approx 2.3-10.4$ ) and air (1), and other objects in the subsurface may generate reflection of EM waves at interface regions. Their presence may, therefore, appear as reflectors in a radar scan. This forms the basis for the detection of DNAPLs (Farid, 2004), buried objects (Miller et al., 2004), caves and tunnels, and subsurface heterogeneities (Clement et al., 2006; Lambot et al., 2004, Lambot et al., 2003; Sneddon et al., 2002; NRC, 2000a, Sneddon et al., 2000) using GPR technologies. Because of their importance in subsurface detection and characterization, EM properties of bulk soils and other underground components will be later discussed in a separate section.

Absorptive losses along the propagation path limit the depth of penetration of EM waves (ISTR, 2000). These losses, and consequently the depth of penetration, depend on the type of soil present, degree of saturation, size of EM heterogeneities, the EM properties of the materials present, and the frequency of characteristics of the EM wave generated by the instrument. Generally, better overall penetration is achieved in dry sandy soils; reduced penetration is common in moist, clay or conductive soils. The radar frequency selected for a particular study should provide an acceptable compromise between deeper penetration and higher resolution. High-frequency radar signals produce greater resolution but are more limited in depth of penetration (ITRC, 2000).

GPR has been used to locate and identify underground storage tanks, underground infrastructure and utilities, buried archeological artifacts, and unexploded ordnances (UXOs) such as landmines (Lambot et al., 2004 a, b, c; Miller et al., 2004; ITRC, 2000). Its potential to locate plastic-cased landmines which contain little or no metal content is much greater than metal detectors (Miller et al., 2004). GPR technologies have also been used to characterize subsurface environments and identify subsurface features, such as soil/soil, soil/rock, and unsaturated/saturated interfaces (ITRC, 2000). They have been applied to identify soil stratigraphy, provide the water content in the subsurface, follow wetting front movement, and support monitoring of contaminants (Chen et al., 2004; Lambot et al., 2003; Rucker and Ferré, 2003). Attempts have been made to correlate GPR measurements with hydrologic properties useful in the creation of fate and transport models (Lambot et al., 2004a; Garambois et al., 2002; Hubberd and Ruben, 2000). In the last few years, GPR technology has been also used to attempt to locate DNAPLs (Johnson and Poeter, 2005; ITRC, 2000; Sneddon et al., 2000; Finci et al., 1998; Brewster et al., 1995; Brewster and Annan, 1994).

GPR has a better resolution-to-cost ratio for DNAPL detection than other geophysical methods (Sneddon et al., 2000). It is, however, limited to shallow depth and relatively large continuous DNAPL contamination (pools). Furthermore, measurements are dependent on soil type and conditions. Because GPR produces indirect measurements of radar reflectors, it is not a conclusive way of determining the presence or absence of a contaminant. This change in GPR signals can lead to high degree of uncertainty (NRC,

2000a). It is, therefore, necessary to correlate measurements with existing information on subsurface conditions obtained by conventional means (ITRC, 2000).

#### *Partitioning Interwell Tracer Test (PITT)*

The partitioning tracers technology involves the injection and recovering fluids that interact with the DNAPLs (Rossabi et al., 2003). Characterizing immiscible-liquid saturation with a partitioning tracer test is accomplished by comparing the transport of a tracer that can partition into and out of immiscible liquid (partitioning tracer) to that of a nonreactive (nonpartitioning tracer) (Brusseu et al., 2003). The nonreactive or *conservative* tracers tend not to react with the NAPL and, therefore, travel unhindered through the zone of contamination. The reactive or *partitioning* tracers have an affinity for the NAPL and, therefore, attenuate (become slowed or retarded) as they travel through the contamination zone. Due to the varying natures of the two types of tracers, the time it takes for each to appear at the monitoring or extraction well will differ. The type of tracer to be used will vary depending upon the specific contaminant and zone of contamination. In the unsaturated zone, the tracers employed are gases, whereas liquid tracers are used in the saturated zone (Meinardus et al., 1998). Long-chain alcohols and fluorocarbons have been shown to work favorably in the saturated zone (Jin et al., 1995). For the vadose zone, perfluorocarbons and helium have accomplished the same favorable results (Divine et al., 2003; Brusseu et al, 2000; ITRC, 2000; Whitely et al., 1999).

Partitioning tracers have been used for detecting and quantifying DNAPL in the saturated zone, measuring trapped air saturation or water saturation (Divine et al., 2003), and also in petroleum engineering applications to determine residual oil saturation (Chen and

Knox, 1997). The petroleum industry developed in the 1970's the use of partitioning tracers to measure immiscible organic-liquid saturation in the subsurface. Brusseau et al., 2000, reported that partitioning tracer tests provided accurate estimates of the amount of chlorinated solvent saturation emplaced in sand-packed columns.

PITTs require establishing a forced gradient flow-field between the point of injection and extraction, where ground water serves as a carrier to transport tracers across the zone of investigation (ITRC, 2000). Preferential flow paths of the tracer in more conductive media may limit the technology to locate DNAPLs outside of the advective path of tracers (Rossabi et al., 2003). Contaminants located in areas of low permeability may not be accurately measured. Furthermore, complex geologic properties may limit the ability to extract and/or monitor tracers. Other limitations include: biased effects from high organic matter and its inability to quantify free-phase DNAPL. This technology also requires adequate understanding of geosystem prior to test (Oostrom et al., 2004; ITRC, 2000).

#### *Cross Well Radar (CWR)*

Cross Well Radar (CWR) is similar to GPR technology in that radar waves are emitted from transmitting to receiving antennas. Unlike GPR, CWR uses greater wave frequencies (0.4 – 2.2 GHz) and the antennas are lowered into the ground. In CWR, radar waves are emitted from a transmitting antenna in one well through the ground to a receiving antenna in other wells. The ability of locating antennas at different depths may

yield greater resolution at much greater depths for detection of DNAPLs in underground systems (Farid et al., 2002; Farid, 2004). CWR technologies rely on detecting changes in radar waves caused by subsurface heterogeneities in subsurface geology and pore fluids of different electrical properties (ITRC, 2000).

Because the electromagnetic properties of water and DNAPL differ significantly, DNAPL concentrations can be measured using CWR technologies by interpreting radar-wave attenuation in the subsurface (Kim et al., 2004; ITRC, 2000). The use of CWR has been proven to be a reliable technology for the detection of objects with similar dielectric properties as DNAPLs (such as acrylic plates) in saturated environments (Farid, 2004; Farid et al., 2003 a, b). The lower dielectric contrast between dry soil and many DNAPLs (see *Dielectric properties*) limits the technology for unsaturated environments. Its effectiveness in unsaturated media is highly dependent on soil moisture, soil mineral composition, and physicochemical properties. Generally CWR is more suitable for media that consists of a low loss, low heterogeneity material (Farid, 2004). It is less efficient in more conductive soils (e.g., clayey and saturated soils) because of greater wave attenuation. Saturated media, however, yield greater contrast detection. This technology must, therefore, be further developed and tested for heterogeneous and transient DNAPL distribution in unsaturated soils.

Applications of this technology include delineation of ore bodies (Fullagar et al., 2000), location of underground tunnels, voids, and objects (Serrano et al., 2007, 2006; Farid, 2004; Rappaport et al, 1999; Moran and Greefield, 1993), identification and mapping of

fractures in bedrock (Day-Lewis et al., 2003; Lane et al., 2003; Lane et al., 2000; Lane et al., 1999a; Lane et al., 1999b), characterization of subsurface lithology and hydrogeological properties (Jang et al., 2007; Kim et al., 2004; Binley et al., 2001; Ellifsen, 1997), delineation of flow zones and tracer movement (Lane et al., 2003; Binley et al., 2001; Lane et al., 2000; Lane et al., 1999), and characterization of subsurface contamination (ITRC, 2000; Borns et al., 1993) and remedial processes (Lane et al., 2006). Cross-hole radar surveys conducted in at field scales from a meter to 100 meters (Lane et al., 2000) in fractured and carbonated rocks (Lane et al., 1999a) have shown that CWR technologies can be used to monitor the movement of saline tracers, delineate transmissive fracture zones, and estimate formation porosity. Results were analyzed at a frequency of 100MHz. High concentration sodium chloride tracers injected into the transmissive zones increase EM attenuation observed in cross-hole radar scans as compared to the observed background attenuation (Lane et al., 2003). Inversion of observed differences creates attenuation difference tomograms. The distribution of tracers in the tomograms can be used to provide important insights into the geometry and hydraulic properties of the media. Radar transmission measurements have also been used to characterize the change in moisture content in unsaturated sand stone due to controlled saline tracer injection (Binley et al., 2001). Continual monitoring permitted determination of travel times and flow transport properties in the unsaturated zones.

Cross borehole EM imaging of a chemical and mixed waste landfill containing acids, oils, solvents, and inorganic compounds has shown the applicability of CWR technology to delineate underground contamination in an unconsolidated alluvial soil (Borns et al,

1993). Tomographic data was collected from four vertical boreholes with an approximate depth of 30 m and surface separations between 6 and 15 m. The borehole surveys used a CWR system at an operating frequency of 15MHz. The data provided information on the distribution of soil at the meter scale. The EM imaging, was able to delineate portions of chromic acid plume in areas of low soil heterogeneity. In areas of high heterogeneity, changes in soil dominated the EM image. The methods were limited to contaminated portions at high concentrations (Borns et al., 1993).

CWR technologies have proven a valuable tool for monitoring the injection and movement of biostimulants, such as vegetable oil emulsions (VOE), during bioremediation activities (Lane et al., 2006). CWR travel time data proved useful for identifying the distribution of VOE monitoring changes in groundwater chemistry caused by VOE dissolution and/or enhanced biological activity. Increased radar attenuation downgradient of injection wells reflect increased electrical conductivity from more dissolved solids produced during the biodegradation process. It was concluded that the effectiveness of the radar method to monitor the injection of enhanced remediation technologies depends on the contrast of EM properties between the injected fluid and the native pore fluid (Lane et al., 2006).

Similar to GPR, CWR technology is limited to large DNAPL concentrations (ITRC, 2000). The use of higher frequencies permits greater resolution at smaller contaminant scales than GPR, but requires smaller separation distance between transmitting and receiving antennas. A other further disadvantage of hole to hole radar is that the

boreholes must be closely spaced (a few meters to a few tens of meters, under ideal conditions), a feature rarely available at sites of practical interest (Cassiani et al., 2004). As the distance between transmitting and receiving wells increases, radar wave amplitudes become lower, creating greater difficulty in distinguishing the wave from background noise (ITRC, 2000).

## **2.2 ELECTROMAGNETIC BASIS FOR CWR DETECTION**

CWR is an electromagnetic method, which relies on the response of the media (ground) to the propagation of induced electromagnetic waves. The following section presents a brief review of fundamental concepts on electromagnetic wave propagation. It intends to provide basic EM concepts important for the application of CWR detection of subsurface DNAPL contamination. It is not intended as a detailed development of wave propagation theory.

### *2.2.1 Electromagnetic Wave Propagation*

Waves are disturbances that propagate through space and time while transporting energy. Generally, waves travel and transfer energy from one point to another, often with little or no permanent displacement of the medium particles. Fundamentally, all forms of electromagnetic energy travel at high velocity, assume the properties of the wave, and radiate outward from a source (Sadiku, 2001). Electromagnetic waves are made up of

two oscillating fields, an electric field (E) and an magnetic field (H), orthogonal to each other in a plane perpendicular to the direction of travel (Figure 2.2).

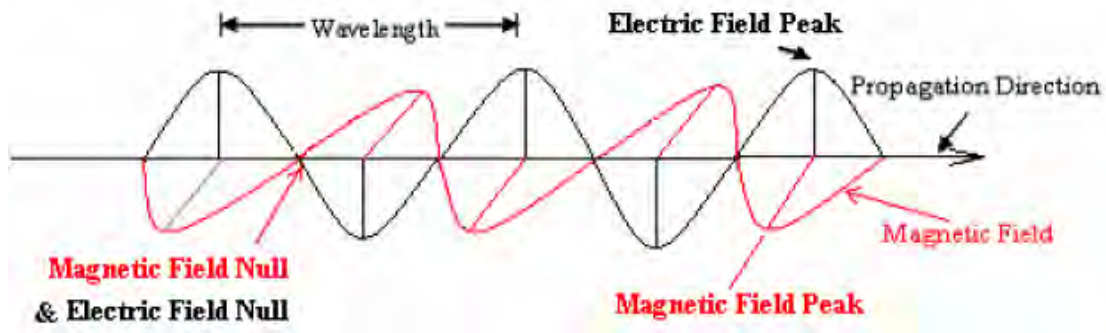


**Figure 2.2 Electric and magnetic fields**

Source: Farid, 2004.

Waves can be characterized by their frequency ( $f$ = rate of oscillation) or their wavelength ( $\lambda$ ), which is the length between two adjacent crests or troughs. Frequency is inversely related to the wavelength according to:

$$v = f * \lambda$$

**Equation 2.3**

where  $v$  is the speed of the wave. As waves move cross boundaries between different media, their speed change but their frequency remains the same. Also, note that:

$$\omega = 2\pi f$$

**Equation 2.4**

$$\beta = \frac{\omega}{v} = \frac{2\pi}{\lambda}$$

**Equation 2.5**

where:

$\omega$ : angular frequency

$\beta$ : phase constant or wave number

The behavior of the EM radiation depends on its wavelength. Higher frequencies have shorter wavelength, and lower frequencies have longer wavelength. The frequency range of the EM radiation is very wide (Figure 2.3). Radar frequencies range from the megahertz to the gigahertz scale.

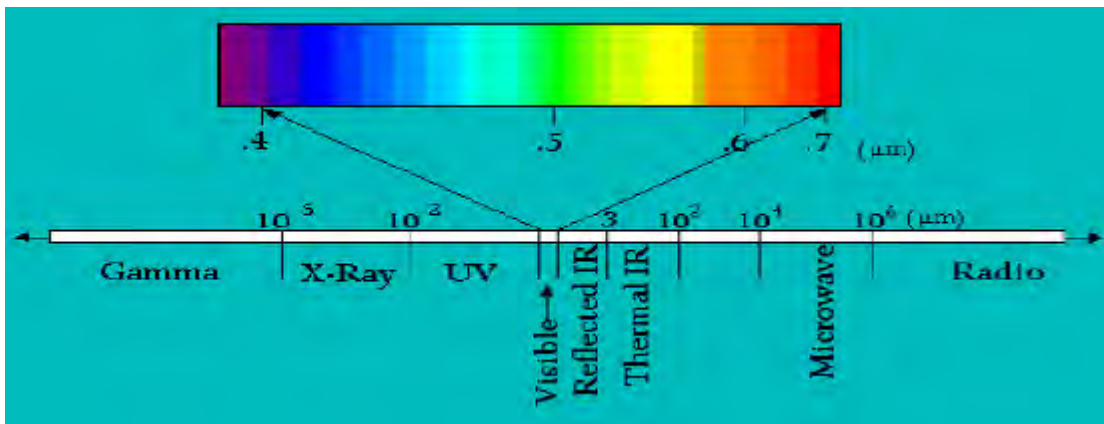


**Figure 2.3 Spectrum of the EM radiation**

Source: Farid, 2004

### 2.2.2 Electromagnetic Wave Propagation in Lossy Dielectric Materials

A lossy dielectric is a partially conducting medium, in which an EM wave losses power as it propagates due to poor conduction. In a lossy soil, waves are attenuated due to dielectric losses and the electrical conductance of the medium (Nadler et al., 2006). For a linear, isotropic, homogeneous, lossy dielectric charge-free medium where the time factor  $e^{j\omega t}$  ( $j$  is  $\sqrt{-1}$ ) is suppressed, Maxwells's Equation become:

$$\nabla \cdot \mathbf{E}_s = 0$$

**Equation 2.6**

$$\nabla \cdot \mathbf{H}_s = 0 \quad \text{Equation 2.7}$$

$$\nabla \times \mathbf{E}_s = -j\omega\mu\mathbf{H}_s \quad \text{Equation 2.8}$$

$$\nabla \times \mathbf{H}_s = (\boldsymbol{\sigma} + j\omega\boldsymbol{\epsilon})\mathbf{E}_s \quad \text{Equation 2.9}$$

where:

$\mathbf{E}_s$  and  $\mathbf{H}_s$  are the phasor form of the time harmonic E and H, respectively

j:  $\sqrt{-1}$ .

$\omega$ , angular frequency

$\boldsymbol{\sigma}$ : electric conductivity of the medium

$\boldsymbol{\epsilon}$ : dielectric permittivity of the medium

$\mu$ : magnetic permeability of the medium

Equation 2.9 can be expressed as:

$$\nabla \times \mathbf{H}_s = j\omega\boldsymbol{\epsilon} \left[ 1 - \frac{j\boldsymbol{\sigma}}{\omega\boldsymbol{\epsilon}} \right] \mathbf{E}_s = j\omega\boldsymbol{\epsilon}_c \mathbf{E}_s \quad \text{Equation 2.10}$$

where  $\boldsymbol{\epsilon}_c$  is the complex permittivity of the medium and is given by:

$$\boldsymbol{\epsilon}_c = \boldsymbol{\epsilon} \left[ 1 - \frac{j\boldsymbol{\sigma}}{\omega\boldsymbol{\epsilon}} \right] = \boldsymbol{\epsilon}' - j\boldsymbol{\epsilon}'' \quad \text{Equation 2.11}$$

and

$$\boldsymbol{\epsilon}' = \boldsymbol{\epsilon} \quad \text{Equation 2.12}$$

$$\varepsilon'' = \frac{\sigma}{\omega} \quad \text{Equation 2.13}$$

Taking the curl of both sides of Equation 2.8, the electric field may be represented as:

$$\nabla^2 \mathbf{E}_s - \gamma^2 \mathbf{E}_s = 0 \quad \text{Equation 2.14}$$

In the same way, magnetic field in equation 2.9 may be represented as:

$$\nabla^2 \mathbf{H}_s - \gamma^2 \mathbf{H}_s = 0 \quad \text{Equation 2.15}$$

where  $\gamma^2 = j\omega\mu(\sigma + j\omega\varepsilon)$ , and  $\gamma$  ( $\sqrt{j\omega\mu(\sigma + j\omega\varepsilon)}$ ) is the complex wave number or propagation constant of the medium. At low frequencies ( $f < 10^5$  Hz), the displacement currents (represented by  $\mu\varepsilon\omega^2$ ) are much smaller than the conduction currents (represented by  $j\omega\mu\sigma$ ). At high frequencies ( $f > 10$  MHz), displacement currents dominate conduction in earth materials of low conductivity ( $\sigma < 1$  mS/m) (Sharma, 1997), and the propagation of the EM field depends mainly on the permittivity of the rock (Sharma, 1997). Equation 2.14 and 2.15 are known as homogeneous vector Helmholtz's equations or simply vector wave equations (Sadiku, 2001).

Since  $\gamma$  is complex, it is expressed as:

$$\gamma = \alpha + j\beta \quad \text{Equation 2.16}$$

where:

$$\alpha = \omega \sqrt{\frac{\mu\varepsilon}{2} \left[ \sqrt{1 + \left[ \frac{\sigma}{\omega\varepsilon} \right]^2} - 1 \right]} \quad \text{Equation 2.17}$$

$$\beta = \omega \sqrt{\frac{\mu\epsilon}{2} \left[ \sqrt{1 + \left[ \frac{\sigma}{\omega\epsilon} \right]^2} + 1 \right]} \quad \text{Equation 2.18}$$

where  $\alpha$  is the attenuation constant or attenuation factor. For propagation along  $+a_z$  (Sadiku, 2001):

$$E(z, t) = E_o e^{-\alpha z} \cos(\omega t - \beta z) a_x \quad \text{Equation 2.19}$$

$$H(z, t) = \frac{E_o}{|\eta|} e^{-\alpha z} \cos(\omega t - \beta z - \theta_\eta) a_y \quad \text{Equation 2.20}$$

$$\eta = \sqrt{\frac{j\omega\mu}{\sigma + j\omega\epsilon}} \quad \text{Equation 2.21}$$

where :

$\eta$ : intrinsic impedance

$\theta_\eta$ : phase angle of intrinsic impedance

t: time

From Equation 2.19 and 2.20, it can be observed that as the wave propagates along  $a_z$ , it is attenuated in amplitude by a factor  $e^{-\alpha z}$ , hence  $\alpha$  is known as the attenuation factor (Sadiku, 2001). The quantity  $\beta$ , defined previously as phase constant or wave number, is a measure of the phase shift between  $E(z,t)$  and  $H(z,t)$ . The phase constant shows that for every wavelength of distance traveled, a wave undergoes phase change of  $2\pi$  radians.

### 2.2.3 Electromagnetic Wave Propagation in Lossless or Low-loss Dielectric Materials

For a lossless medium  $\sigma=0$ ,  $\alpha=0$ , and the wave is not attenuated and magnetic fields are in phase (Sadiku, 2001). For a low-loss dielectric medium ( $\sigma \ll \omega\epsilon$ ), the attenuation factor and wave number are approximated as:

$$\alpha \approx \frac{\sigma}{2} \sqrt{\frac{\mu}{\epsilon}} \quad \text{Equation 2.22}$$

$$\beta \approx \omega \sqrt{\mu\epsilon} \quad \text{Equation 2.23}$$

### *Skin depth or penetration depth*

The skin depth  $\delta$  is a measure of the depth to which an EM wave may penetrate the medium (Sadiku, 2001). At low frequencies, where conduction currents dominate over displacement currents,  $\delta$  is the depth at which the amplitude of the field is reduced 1/e (i.e., 37%) (Sharma, 1997). It is related to the attenuation factor by:

$$\delta = \frac{1}{\alpha} = 504 \left( \frac{\rho}{f} \right) \quad \text{Equation 2.24}$$

where:

$\rho$  ( $=1/\sigma$ ) is the resistivity in  $\Omega\text{m}$ , and  $f$  is the frequency of the EM in Hz.

At high frequencies (e.g., radar frequencies, 10-1000MHz) the displacement currents become notorious, and in a low loss medium ( $\sigma/\omega\epsilon_0\epsilon_r \ll 1$ ) the conduction currents are of small magnitude.

EM waves in a dielectric medium enclosed by perfectly reflection boundaries at separation distances comparable to or smaller than the wavelength of the signal are

repeatedly reflected between opposite walls and trapped within the medium (Kruk, 2006). These boundaries, thus, act as waveguides, guiding the EM energy from one point to another. For a lossless dielectric the EM waves in the waveguide can be imagined as traveling down the path in a zig-zag manner with no energy loss as the energy is guided from one point to another. The waveguide can be designed such that a EM incident will produce one diffraction order in reflection, and the energy is stored due to total internal reflection. Total internal reflection of the first order at the boundary of the waveguide and the layer material is ensured in the absence of modal dispersion, which smears out the wave. This can be accomplished if the spread-out width of the signal dictated by the thickness of the wave guide is less than half-wavelength (Bunkowski et al., 2006). The proportion of incident wave that is reflected or transmitted depends on the constitutive parameters ( $\epsilon$ ,  $\sigma$ ,  $\mu$ ), and the total electric and magnetic field comprise both the incident and reflected fields (Sadiku, 2001).

### ***Energy loss and attenuation***

EW waves in a lossless medium radiated by perfectly coupled antennas do not lose energy, and are, therefore, not attenuated. In subsurface environments several factors may result in a decrease in signal strength as radiowaves propagate through the media. These factors include energy losses through radiation sources (i.e., transmission lines and antenna losses), and geologic properties of the media (Figure 2.4). Energy loss occurs from reflection/transmission losses, scattering, and absorption losses (Reynolds, 1997). Reflection/transmission losses occur across interphases of different EM properties. Scattering results from the presence of objects with dimensions of the same order as the

wavelength of the signal. Absorption, which converts EM energy into heat, is caused by the geometrical spread of the energy. The attenuation of the EM waves resulting from these energy losses is a function of the dielectric and electrical properties of the media: dielectric constant ( $\epsilon$ ), conductivity ( $\sigma$ ), and magnetic permeability ( $\mu$ ). Any variations in these properties across the media give rise to reflection of EM waves (Sharma, 1997). The greater the contrast, the greater the amount reflected. The total raypath loss for a given distance of a radar system is, therefore, made up of five terms: antenna losses, transmission losses between the air-ground interface, losses caused by geometrical spreading, attenuation within the ground as a function of the material properties, and losses due to the scattering from anomalies or target elements (Reynolds, 2003).

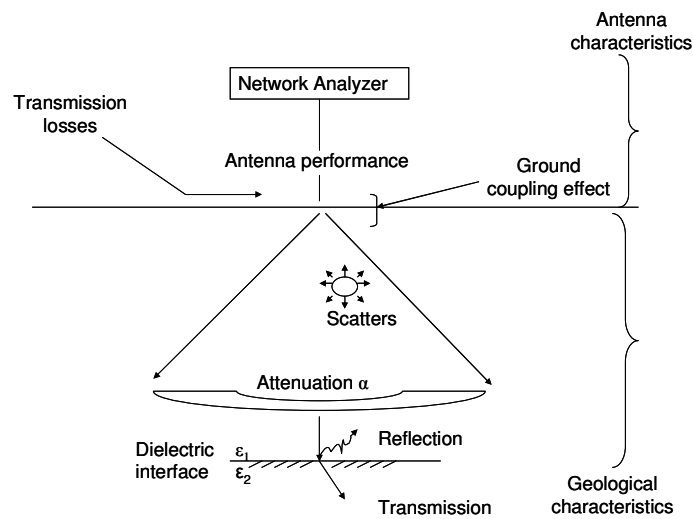


**Figure 2.4 Raypath loss**

Source: Adapted from Reynolds, 1997

In general, the speed of radio waves  $v$  in any medium, depends on the dielectric permittivity  $\epsilon_r$ , the permeability  $\mu_r$  ( $\mu_r=1$  for non magnetic materials), and the electrical conductivity  $\sigma_r$ , which are all complex and frequency dependent parameters (Garambois

et al., 2002). At the high frequencies used for radar acquisition, the EM velocities  $v$  for low-loss materials can be approximated as (Hagrey, 2007; Buyukozturk et al., 2006; Lane et al., 2003, Garambois et al. 2002: Lane et al. a and b, 1999):

$$v = \frac{c}{\sqrt{\epsilon_r \mu_r}}, \quad \text{Equation 2.25}$$

where:

$c$ : velocity of free space ( $3 \times 10^8$  m/s)

$\epsilon_r$ : denotes the relative dielectric permittivity, and is the ratio of the dielectric permittivity of the medium  $\epsilon$  and permittivity of free space ( $\epsilon_0 = 8.854 \times 10^{-12}$  F/m)

$\mu_r$ : denotes the relative permeability, and is the ratio of the permeability of the medium  $\mu$  and permeability of free space ( $\mu_0 = 4\pi \times 10^{-7}$  H/m).

Since  $\mu_r$  is close to unity in most rock materials (except strongly magnetic rocks) radar velocity is primarily controlled by  $\epsilon_r$  (Sharma, 1997). Consequently, ground radar detection relies on the contrast in radiowave velocities caused by the contrast in the relative dielectric properties of adjacent media. This approximation leads to two major assumptions;

- i) that the material is a good dielectric, i.e. the conduction current density is negligible compare to the displacement current density ( $\sigma/\omega\epsilon_0\epsilon_r \ll 1$ ), where  $\omega$  is the angular frequency, and soils with no metallic objects or no minerals present or with low clay content correspond to good dielectric.
- ii) the dispersive effects that appear through  $\epsilon$  are negligible.

### 2.3 ELECTRICAL PROPERTIES OF THE SOIL

CWR relies on detecting changes in radar waves caused by heterogeneities in subsurface geology, buried artifacts, and pure fluids of different density. The interaction of electromagnetic waves with matter depends on the electromagnetic properties of the media: dielectric permittivity ( $\epsilon$ ), magnetic permeability ( $\mu$ ), and electric conductivity ( $\sigma$ ). Table 2.1 includes values of electrical conductivity in different soils and different water content. These properties may change according with the temperature, orientation, mixture, pressure and molecular structure of the material (Agilent, 2005; Vall-Iossera et al., 2005; Hoekstra and Delaney, 1974).

**Table 2.1 Electrical Conductivity Soil Materials**

Material	Electrical conductivity $\mu\text{S/cm}$	Gravimetric water content	Author, year.
Baglio	1750 to 3560	Saturated	Crescimanno and Garofalo, 2006.
Silt loam	400 to 1250	Variable	Eigenber et al., 2006.
Perlite	50 to 400	Variable, 20% to 48%	Nadler et al., 2006.
Sandy Clay	0 300	Variable, 10 to 40%	Vall-Iossera et al., 2005.
Coalmine soils	740	Variable, 0 to 25%	Chen et al., 2004.
Sandy loam soil	550	10%	Mironov, 2004.
Sand Clay	170 180	Variable	Harmsen et al., 2003.
Silty sand	1173	Dry	Hendrick et al., 2002.
Silty clay	0.1 to 100	Variable, 3 to 25%	Hoekstra and Delaney, 1974.
Sand	90	Dry	Hipp, 1974

At the high frequencies used in radar, the propagation of EM field for earth materials of low conductivity is dependent of the dielectric permittivity and magnetic permeability.

These properties are described below.

## Dielectric permittivity

Dielectric properties depend on the polarization and dielectric relaxation characteristics of the material (Hillhorst et al., 2000). Polarization and relaxation processes are frequency dependent and can be described by the complex permittivity of the material.

A material is “dielectric” if it has the ability to store energy when an external electric field is applied (Agilent, 2005). The permittivity  $\epsilon$  describes the interaction of a material with an electric field. The relative permittivity ( $\epsilon_r$ ) is equivalent to the dielectric constant ( $k$ ) of the material, and is defined as the permittivity relative to free and is a complex function with real and imaginary components (Hilhorst, 2000; Robinson et al., 1999; Gardner et al., 1998).

$$\epsilon_r = \epsilon_r' - j\epsilon_r''$$

where:

**Equation 2.26**

$\epsilon_r'$ : real part

$\epsilon_r''$ : imaginary part

Relative permittivity is a measure of the polarizability of the material for a static field.  $\epsilon_r'$  is  $>1$  for most solids and liquids. The imaginary part of permittivity  $\epsilon_r''$  is called the loss factor (Robinson et al., 2005), and is associated with energy dissipation (Buyukozturk et al., 2006; Huisman et al., 2003) from dispersive and relaxation losses. The loss factor includes the effect of both dielectric loss and conductivity (absorption losses) (Agilent, 2005).  $\epsilon_r''$  is  $>$  than zero and usually is much smaller than  $\epsilon'$  (Buyukozturk et al., 2006;

Agilent, 2005). The ratio between the loss factor and the dielectric constant is called loss tangent ( $\tan\zeta = \epsilon_r'' / \epsilon_r'$ ). The loss tangent ( $\tan\zeta$ ) and dielectric constant are functions of measurement frequency, material homogeneity and anisotropy, moisture, and temperature in the material (Buyukozturk et al., 2006; Zwick et al., 2006; Agilent, 2005).

In both, real and imaginary part, there is characteristic frequency dependence (Logsdon, 2005; Antonik et al., 2004; Miller et al., 2004; Seyfried and Murdock, 2004; Francisca and Rinaldi, 2000; Matzler, 1998; Hallikainen et al., 1985; Hoekstra and Delaney, 1974; Hipp et al., 1974). At low frequencies (<10MHz), the dielectric constant has been reported inversely proportional (Hoekstra and Delaney, 1974) to frequency, and has strong dependency with soil textural composition and water content (Srivastava and Mishra, 2004; Peplinski et al., 1995). Dielectric constant for water at higher frequencies remain relatively constant up to about 1GHz, where it decreases significantly with increasing frequency (Hoekstra and Delaney, 1974). At frequencies below 50MHz, the variations on the complex dielectric constant depends strongly on soil type (Van Dam et al., 2005; Hoekstra and Delaney, 1974). At higher frequencies (>100MHz), the complex dielectric constant of wet soil tends to decrease (Miller et al., 2004; Francisca and Rinaldi, 2003; Hoekstra and Delaney, 1974; Hipp et al., 1974) depending on soil type, water content, and temperature.

Differences on relative dielectric permittivities for different soils depend on frequency and water content (Vall-Isoera et al., 2005; Miller et al., 2004; Francisca and Rinaldi, 2003; Robinson et al., 1999; Hoekstra and Delaney, 1974). Table 2.2 and Table 2.3 show

values of dielectric permittivity and relative dielectric permittivity in different soils. For most geologic materials the dielectric constant lies within a range of 3 to 30. Specifically, dry soils have dielectric permittivity in a range of 2 and 4, and free water has a value close to 80. That means water has a factor 20 times as large as most soil constituents (Van Dam et al., 2005 a and b).

**Table 2.2 Real and imaginary part of dielectric permittivity**

Material	Real Part Permittivity	Imaginary Part Permittivity	Frequency Range	Reference
Sandy Clay	3 to 25 4 to 30	0 to 3 0.3 to 4.5	1.2 to 2.5GHz	Vall-Iloera et al., 2005.
Sandy soil	2.62	0.039	1.4 to 18GHz	Mironov, 2004.
Soil	2.1	0.5	9.967GHz	Srivastava and Mishra, 2004.
Yeast Powder	1.2 to 1.8	Below zero	0.3MHz to 20GHz	Wosik et al., 2004.
Sand	3 to 5	0	20MHz to 1.3GHz	Francisca and Rinaldi, 2003.
Soil	6 to 11	0.9 to 3	1 to 40GHz	Tikhonov, 1994.
Sandy loam	2.8 to 3.7	0.14 to 0.22	1 to 40 GHz	Tikhonov, 1994.
Silty clay	6 to 14	0.5 to 4	$0.1 \cdot 10^9$ to $2 \cdot 10^{10}$ Hz	Hoekstra and Delaney, 1974.

**Table 2.3 Relative permittivity in soils**

Material	Relative	Frequency Range	Reference
Dry sand	2.55 2.55	100MHz 1.5 GHz	Farid, 2004.
Saturated Sand	20 20	100MHz 1.5 GHz	Farid, 2004.
Dry sand Wet sand	2.4 9	1.5 GHz	Harmsen et al., 2003.
Dry sand Sand with 25% water content	2.8 15	0.8 to 4GHz	Lambot et al., 2003.
Dry sand Dry sand	3.5 18	30MHz 3.8GHz	Hipp, 1974

The dielectric constant of bulk soil is known to vary with water content (Farid, 2004;

Miller et al., 2004; Carcione et al., 2003; Starr et al 2000(a and b); Starr et al, 1999; Hipp, 1974). Generally, dielectric constant tend to increase with soil water content (Miller et al., 2004; Francisca and Rinaldi, 2003), ranging from 3-10 in dry soil values to over 40 for saturated soils, with most values ranging between 3 and 30 (Miller et al., 2004; Reynolds, 1997).

Several models have been proposed to determine the electromagnetic properties of a soil material. Some of them are based on the volumetric fraction of the soil constituents that relate frequency dependent response to characteristic relaxation times; and others are based on the geometry and composition or physical properties of the soil components (Regalado, 2004). Certainly, there are differences on the predicted dielectric constants using different models (Vall-Iosera et al., 2005; Robinson et al., 1999).

The available methods can be grouped in (1) phenomenological (e.g., Cole-Cole and Debye), (2) volumetric, (3) empirical and semi-empirical (pedotransfer), and (4) effective medium models or approaches. The effective medium approach, or composite spheres model is only accurate for known geometries and difficult to implement for heterogeneous and multiple-phase materials. Phenomenological models, such as Cole-Cole and Debye, relate characteristics relaxation times to frequency dependent behavior of the material (Van Dam et al., 2005a). These models allow for assessment of complex dielectric properties for specific frequencies. These models, however, need recalibration for each specific material and are difficult to implement for varying soil types (Van dam et al., 2005a and b).

Volumetric models describe the dielectric properties of a soil based on the relative amount of different soils constituents and their dielectric characteristics. Electrostatically a soil medium may be considered a four-component dielectric mixture consisting of air, bulk soil, bound water and free water (Starr et al., 2000; Tikhnov, 1997; Peplinski et al., 1995; Tikhnow, 1994). The basic input parameters to all models include solid matter, pore space, and volumetric water content. Depending on the model, input variables such as organic matter and bound water may provide additional accuracy for specific conditions. Usually, frequency dependence is not taken into account (van Dam et al., 2005a). One such model, the complex refractive index (CRI) or exponential model, is one of the most popular methods (Van Dam, et al., 2005a; Hillhorst et al., 2000). The CRI model at a given frequency for a material with n components can be written as:

$$\epsilon_{r,m}^{\chi} = \sum_{i=1}^n \psi_i \epsilon_{r,i}^{\chi} \quad \text{Equation 2.27}$$

where:

$\epsilon_{r,m}^{\chi}$  is the relative permittivity in the bulk (mixed) material,

$\psi_i$  and  $\epsilon_{r,i}^{\chi}$  are the volume fraction and complex permittivity of the component i respectively, and  $\chi$  is an empirical value (assumed to be 0.5 by several authors) (Van dam et al., 2005a; Carcione et al., 2003; Lin, 2003; Starr et al., 2000 a and b). The scaling factor  $\chi$  can vary theoretically between -1 and 1, but for multiphase mixtures in soils they generally range between 0.4 and 0.8 (Van dam et al., 2005a). Several attempts have been made to give a more physical basis to the scaling factor. It has been shown that the value of  $\chi$  also (inversely) correlates with the measurement frequency (Van dam, et al., 2005a).

Recently, a new volumetric mixing equation based purely on the depolarization factors of different soil constituents has been introduced (Hillhorst et al., 2000). This model has a strong theoretical basis and tries to overcome some problems that exist in other volumetric mixing models. In this approach the measured dielectric permittivity is related to the volume-weighted sum of the permittivities of the individual material constituents. A depolarization factor is introduced to account for electric-field refractions at the material interfaces. Theoretically, the depolarization factor can be calculated for all materials but currently this is only possible for homogeneous materials with regular-shaped grains (Van dam et al., 2005a).

Empirical models are mathematical descriptions of the relationship between dielectric properties and other characteristics of a medium, especially volumetric water content and texture information (Van dam et al., 2005). There is not necessarily a physical basis for the mathematical description. Therefore, an empirical model may only be valid for the data that were used to develop the relationship. Many empirical models have originated in the field of time-domain reflectometry (TDR), and were originally used to predict the soil water content from the velocity of electromagnetic signals along TDR probes in the soil (Van dam et al., 2005a). The classic Topp-model uses a third order polynomial to describe the relation between soil volumetric water content ( $\theta$ ) and bulk or apparent relative permittivity ( $K_a$ ) for measurements taken below the relaxation frequency of water:

$$K_a = 3.03 + 9.3\theta + 146\theta^2 - 76.7\theta^3$$

**Equation 2.28**

The regression is an average of TDR measurements integrated over a frequency range of 1 MHz to 1 GHz for several soils and has proved very successful for a wide range of different soils and soil moisture conditions (Van dam et al., 2005a). Linear relationships between soil water content and  $K_a$ , which can be used to expand the Topp-model for higher water contents have also been proposed (Van dam et al., 2005a). The model functions especially good for frequencies around 100 MHz. At higher frequencies and moisture contents close to saturation ( $\theta \sim 0.4$ ) the Topp-model over-predicts the bulk relative permittivity by up to 20%. At very low water contents the Topp-model does not perform well, especially for soils with large clay content.

Other approaches relate the complex relative electrical permittivity for the bulk soil density  $\rho_b$ , particle soil density  $\rho_s$ , and water volume fraction  $\theta$  using (Miller et al., 2004):

$$\epsilon' = 1.15 \left[ 1 + \frac{\rho_b}{\rho_s} \left( (\epsilon_s)^{0.65} - 1 \right) + \theta' (\epsilon'_{f_w})^{0.65} - \theta \right]^{\frac{1}{0.65}} - 0.68 \quad \text{Equation 2.29}$$

and,

$$\epsilon'' = \left[ \theta'' (\epsilon''_{f_w})^{0.65} \right]^{\frac{1}{0.65}} \quad \text{Equation 2.30}$$

where:

$\epsilon'$  ,  $\epsilon''$ : real and imaginary part of complex relative electrical permittivity for the bulk soil

$\rho_b$  is the bulk density

$\rho_s$  is the specific density of the solid soil particles

$\theta$  water volume fraction

$\mathbf{t}'$  and  $\mathbf{t}''$  are empirically determined soil-type constants

$\epsilon'_{f_w}$  ,  $\epsilon''_{f_w}$  are the real and imaginary part of the relative dielectric constant of free water

$\epsilon_s$  is the dielectric constant of the soil particles

Harmsen and Parsiani (2003) evaluated dielectric constant considering variations in the moisture content. Parameters as soil texture, bulk and particle density, and wilting point are included in the model as is described in the following equations:

$$\epsilon_1(\theta_v) = \theta_v \epsilon_{x_1}(\theta_v) + (\phi - \theta_v) \epsilon_a + (1 - \phi) \epsilon_s, \quad \theta_v \leq W_t \quad \text{Equation 2.31}$$

With:

$$\epsilon_{x_1}(\theta_v) = \epsilon_i + (\epsilon_w - \epsilon_i) \frac{\theta_v}{W_t} \gamma \quad \text{Equation 2.32}$$

$$\gamma = -0.57WP + 0.481 \quad \text{Equation 2.33}$$

$$WP = 0.06774 - 0.00064S + 0.00478C \quad \text{Equation 2.34}$$

$$W_t = 0.49WP + 0.165 \quad \text{Equation 2.35}$$

$$\epsilon_2(\theta_v) = W_t \epsilon_{x_2} + (\theta_v - W_t) \epsilon_w + (\epsilon_w - \epsilon_i) \frac{\theta_v}{W_t} \gamma, \quad \theta_v > W_t \quad \text{Equation 2.36}$$

$$\epsilon_{x_2}(\theta_v) = \epsilon_i + (\epsilon_w - \epsilon_i) \gamma \quad \text{Equation 2.37}$$

Where:

$\phi_v$ : volumetric moisture content

$\epsilon_1$ : apparent dielectric constant for moisture content less than or equal to  $W_t$

$\epsilon_2$ : apparent dielectric constant for moisture content greater than  $W_t$

$\epsilon_a$ : dielectric constant of air (1)

$\epsilon_i$ : dielectric constant of ice (3.2)

$\epsilon_w$ : dielectric constant of pure water (81)

$\phi$ : porosity

WP: moisture content at the Wilting Point (pore water pressure 15 bars)

S: sand content in percent of dry soil

C: clay content in percent of dry soil

$W_t$ : transition moisture content

$\gamma$  : fitting parameter which is related to WP.

Additionally, the transition moisture content  $W_t$  must be determined; that is the moisture content at which dielectric constant increases steeply when increase water content. This value allows defining the moisture content/dielectric relationship within the moisture content range of 0 to 0.5 (Harmsen and Parsiani, 2003).

In addition to water content, the presence of other fluids and objects of different dielectric permittivities in soils affects their complex dielectric properties (Farid, 2004; Zhang et al., 2004; Carcione et al., 2003; Francisca and Rinaldi, 2003; Hipp et al., 1974). The effect of organic liquid content on dielectric constant of bulk soil depends on the value of the dry medium, and that of the organic liquid. Francisca and Rinaldi (2003) show a slight increase in dielectric permittivity as the volumetric content of an organic increased from dry conditions. This is a result of the organic liquid (dielectric constant ( $\approx 2.3$ ) displacing a fluid (air) with a much smaller dielectric value (1). It is expected that organic liquids with higher permittivity values (e.g. chlorinated solvents) reflect higher contrast as a function of volumetric content. For water-saturated soils, dielectric permittivity tends to decrease as the volumetric content of the organic liquid increases (Francisca and Rinaldi, 2003). This is due to the displacement of a fluid (water) with a

relatively high permittivity ( $\approx 80$ ) by one of lower value ( $\approx 2.3$ ). The effect of organic liquid content on dielectric constants in soils of varying degree of saturation depends on water content, soils properties, and dielectric properties of the liquid (Carcione et al., 2003). Dielectric constants are expected to drop significantly with decreasing water content, but increase slightly with decreasing air content. Similar to organic liquids, non-metallic objects such as landmines have dielectric values between 3 and 10, depending on their composition (Miller et al., 2004).

In addition to frequency, soil type, and fluid content, other factors, such as temperature (Seyfried and Murdock, 2004), bulk soil density (Buyukozturk et al., 2006; Miller et al., 2004), soil pore size and particle shapes influence the soil dielectric constant (Vall-Iossera et al., 2005; Zagoskin et al., 2004). It can also be significantly modified by the presence of plastic objects, metal, and salinity (Eigenber et al., 2006; Friedman, 2005; Jung et al., 2005; Miller et al., 2004).

### *2.3.1 Methods for Determination of Dielectric Properties of Soils*

Various methods have been devised to resolve subsurface heterogeneous in soil, utilizing both refraction and reflection of waves (Eppstein and Dougherty, 1998). Vector network analyzers (VNA) are used to measure scattering parameters (S-Parameters), and estimating transmission and reflection properties of the media along a raypath between transmitting and receiving antennas. These properties are then related to the dielectric and permeability properties along the raypath. More details are given on VNA methods

to determine dielectric properties in chapter 3.

Dielectric properties of soils have also been determined using time domain reflectometry (TDR) (Wakayama and Loyer, 2007; Kelleners et al., 2005; Robinson et al., 2005). TDR measurements have been widely used for monitoring soil water content and soil water salinity (Wraith et al., 2005; Zhang et al., 2004; Huisman et al., 2003; Masbruch and Ferré; Lin, 2003; Persson and Uvo, 2003; Woodhead et al., 2003; Robinson et al., 1999; Starr et al., 1999). In TDR measurements, a rising step voltage pulse is transmitted through a coaxial cable to the sample, and reflected back to the generator (Castiglione et al., 2006). Travel time of the signal can be measured from the waveform to determine the apparent dielectric constant of a soil (Lin, 2003; Persson and Wraith, 2002) and can be related to estimate the electrical conductivity (Masbruch and Ferré, 2003; Persson and Uvo, 2003). A calibrated relationship between the dielectric constant and water content is then applied to estimate soil water content. Since wave propagation in a wet soil is dispersive, it is difficult to clearly define the arrival time of the wave form (Lin, 2003). Electrical conductivity may be measured considering changes in impedance across the waveform (Wraith, 2005; Harlow et al., 2003).

#### Permeability:

Permeability  $\mu$  describes the interaction of a material with a magnetic field. The complex permeability  $\mu^*$  consists of a real part that represents the energy storage term and an imaginary part that represents the energy loss term. Relative permittivity  $\mu_r$  is the

permittivity relative to free space (Clement et al., 2006; Agilent, 2005; Lee, 2003, Clement and Knoll, 2000).

$$\mu_r^* = \frac{\mu^*}{\mu_0},$$

**Equation 2.38**

where  $\mu^*$  is the complex relative permeability and  $\mu_0$  is permeability in the free space ( $4\pi \cdot 10^{-7}$  Henry/m).

## 2.4 ANTENNAS

An antenna is a dielectric structure (as a rod or wire) for radiating or receiving radio waves with directional and polarization properties. It serves as a transitional structure between guided waves propagation in a transmission line and EM waves radiating in the surrounding medium. The transmission line may take the form of a coaxial line or a waveguide, and it is used to transport electromagnetic energy from the transmitting source to the antenna or from the antenna to the receiver (Balanis, 2005).

Beginning in the early 1960's, numerical methods were introduced that allowed analyzing and designing antennas accurately. Moreover, asymptotic methods for both low frequencies (e.g., Moment Method (MM), Finite-Difference, Finite-Element) and high frequencies (e.g., Geometrical and Physical Theories of Diffraction) were introduced, contributing significantly to get a better understanding of the antenna field.

The objective to analyze an antenna is to find the electric and magnetic fields radiated by the elements. Once this is accomplished, a number of parameters to characterize the performance of the antenna system can be found. By the other hand, to design an antenna system, the characteristics of performance are specified, and the sources to satisfy the requirements are sought (Balanis, 1992).

The space surrounding an antenna is usually subdivided into three regions: the reactive near-field region, the radiating near-field (Fresnel) region, and the far-field (Fraunhofer) region (Balanis, 2005). The reactive near-field region is defined as that region of the field immediately surrounding the antenna wherein the reactive field predominates, and is commonly taken to exist at a distance  $R < 0.62\sqrt{(D^3/\lambda)}$  from the antenna, where  $\lambda$  is the wavelength and  $D$  is the largest dimension of the antenna.

The radiating near-field (Fresnel) region is defined as that region of the field of an antenna between the reactive near-field region and the far-field region wherein radiation fields predominate and wherein the angular field distribution is dependent upon the distance from the antenna (Balanis, 2005). The radial distance  $R$  over which this region exists is  $0.62\sqrt{(D^3/\lambda)} \leq R < 2D^2/\lambda$  (provided  $D$  is large compared to the wavelength). In this region the field pattern appears as a function of the radial distance.

The far-field (Fraunhofer) region is defined as that region of the field of an antenna where the angular field distribution is essentially independent of the distance from the antenna (Balanis, 2005). In this region, the real part of the power density is dominant and

the outer boundary is ideally at infinity. The radial distance  $R$  over which this region exists is  $R \geq 2D^2/\lambda$  (provided  $D$  is large compared to the wavelength). Most antenna applications rely on radiation patterns in the far field region (Ulaby, 1997).

#### *2.4.1 Antenna Characteristics*

Important characteristics of antennas as radiator of EM energy include (Sadiku, 2001): antenna pattern, radiation intensity, directive gain, and power gain. The antenna pattern describes the three-dimensional strength of the radiation at the far field. The radiation intensity is a function of the total radiated power ( $P_{\text{rad}}$ ), and is described as  $P_{\text{rad}}/4\pi$ . The direction gain is a measure of the concentration of radiated power in particular direction, and provides information on the antenna's ability to direct radiated power in a given direction. It is usually obtained as the ratio of the radiation intensity in a given direction to the average radiation intensity. High directional gain antennas have a longer range and better signal quality, but must be aimed carefully in a particular direction. Low gain antennas have a lower range, but its orientation is inconsequential. The power gain of an antenna relates to radiation losses in the antenna. Of the total power supplied to an antenna, part is radiated into the medium ( $P_{\text{rad}}$ ), and part is dissipated as heat loss.

The power gain accounts for ohmic losses in the antenna material. It is related to the radiation efficiency of the antenna, which is defined as the ratio of the radiated power to the total power supplied.

The performance of an antenna depends on its directional radiation characteristics and its impedance. The antenna acts as an impedance to the transmission line connected to its terminal. If the transmission line is matched to the antenna impedance, part of the radiation is radiated into the medium, and part is dissipated as heat given rise to loss or ohmic resistance. To minimize reflection and radiation losses at the transmission line antenna juncture, it is necessary to have matching wave impedance in both components (transmission line and antennas). Even if these impedances are matched, antennas may have permanent radiation losses. For efficient antennas it is necessary to minimize these losses.

The radiation efficiency of the antenna is determined by the radiation and loss resistance. Radiation efficiency increases as the radiation resistance increase above the loss resistance.

#### *2.4.2 Types of Antennas*

There are various antenna types, including wire, aperture, microstrip, and array antennas (Balanis, 2005). Wire antennas are made in various shapes and sizes including loop and helix forms (Figure 2.5). Their sources of radiation are time-varying currents along the wire that give rise to the radiated electromagnetic field (Ulaby, 1997). Aperture antenna, such as the horn antenna (Figure 2.5d), works under the same principle, except that the source of radiation is the dielectric field distribution across the antenna's aperture. Aperture antennas are becoming popular because of the increasing demand for more

sophisticated forms of antennas and the use in higher frequencies. They also come on various forms, including pyramidal horn, conical horn, and rectangular waveguide.

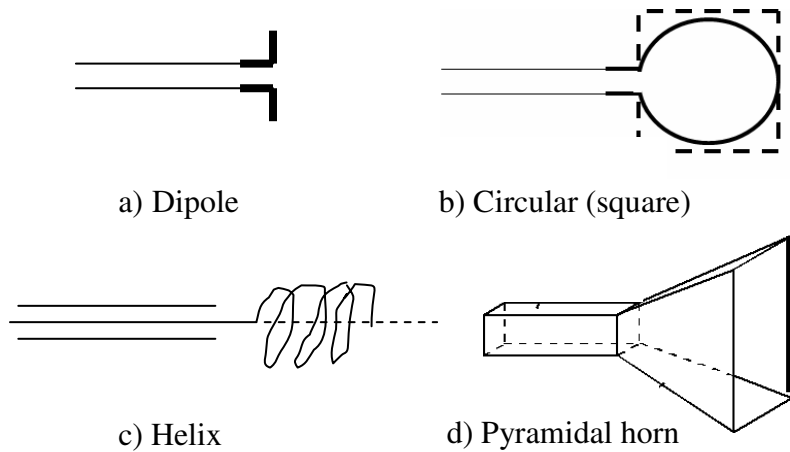


**Figure 2.5 Wire antenna types**

Source: Balanis, 2001

Microstrip antennas consist of metallic path on grounded substrate with radiating strip fed by a coaxial cable (Balanis, 2005). They have become popular for spaceborne, government, and commercial applications. Antenna arrays involve a group of radiating antennas used to produce particular radiation characteristics not achievable by single antennas. They are used to concentrate radiation patterns in the direction of interest. In this case, the radiation from the elements adds up to give a radiation maximum in a particular direction or directions, minimum in others, or otherwise as desired (Balanis, 2005).

Dipole antennas (Figure 2.5a) consist of two strength wires lying along the same axis. The wire is excited at the midpoint of a voltage source connected to the antenna via a transmission line. These antennas are also known as half-waves dipole antennas because their length  $l$  must be half the wavelength ( $l=\lambda/2$ ).

A straight-wire, quarter-wave monopole antenna consists of one-half of a dipole antenna ( $l=\lambda/4$ ) located in a conducting ground plane, perpendicular to the plane (Sadiku, 2001). It can be simply made of a coaxial cable with its shield removed at the end (Farid, 2004). A monopole antenna is commonly fed by a coaxial cable connected to antenna's base. These antennas can only radiate half of the power radiated by dipole antennas. Similar to a monopole antenna, a helicated antenna is in the form of a helix backed by a ground plane.

The role of loop, monopole, and dipole antennas on the EM wave behavior in soil and subsequent detection characteristics has been evaluated numerically (Farid et al., 2002) and experimentally. Modeling results show that both monopole and dipole antennas in a three-dimensional field can be used for detection of DNAPLs in soils. Dipole antennas can detect scattering, caused by the presence of DNAPLs, at various depths, whereas the monopole antenna can only detect at the depth of the simulated DNAPL pool. Assessment of transmission and reflection characteristics of loop and monopole antennas has shown that simple monopole antennas can couple with the soil and detect impedance differences of buried plastics and metal objects (Rappaport et al., 1999). Loop antennas showed good coupling, but lack of sensitivity for object detection.

A loop antenna consists of a conducting wire looped in multitrans around a core material. The core material can either be a ferrite bead generally small, with dimensions much smaller than  $\lambda$  (Sadiku, 2001). There are electrically small and electrically large loop

antennas. Electrically small antennas are those whose overall length (number of turns times circumference) is less than  $\lambda/10$ . Electrically large loop have circumferences of about the same length as the wavelength  $\lambda$ . Loop antennas are often used in practical applications where there is no space for straight-wire antennas.

The ohmic resistance of small loops is in general larger than the radiation resistance. Thus, they are poor radiators and their radiation efficiencies are low and greatly dependent on the ohmic resistance. The radiation resistance, and their efficiency, can be increased by increasing its perimeter and/or number of turns (Smith, 1972) (see Chapter 4). The number of turns depends on the size of the loop, with smaller loops requiring more number of loops. Another way to increase the radiation resistance and efficiency is to insert a ferrite core within its circumference (Balanis, 1992). The ferrite core increase the magnetic field and, and in turn, the radiation resistance of the loop.

The radiation efficiency of electrically small multiturn loop antennas is using an ohmic resistance which includes both the normal skin effect and the additional loss due to the proximity effect (Balanis, 2005). Moreover, the ohmic resistance of a small loop is calculated as a straight conductor equal in length to the uncoiled loop, which is adequate for the single-turn loop, but, not for the multiturn case. In a multiturn loop, the distribution of current due to the proximity effect can cause an increase in the ohmic resistance which is larger than the skin effect resistance alone. This increase in the ohmic resistance, which is normally unimportant in large antennas, greatly affects calculations of power radiated by electrically small transmitting loops (Smith, 1972).

## **2.5 DIGITAL INTERPRETATION OF CHEMICAL MOVEMENT INTO THE SOIL**

Several authors have used dye tracers to visualize preferential flow and identify transport processes at small scales (Kasteel et al., 2005; Persson, 2005a; Persson, 2005b; Persson and Uvo, 2003; Persson and Wraith, 2002; Vanderbortht et al., 2002). Dye tracers have been used in the vadose zone for investigating the effects of soil heterogeneity by visualizing spatial flow patterns at the millimeter scale (Persson et al., 2005), and quantifying infiltration and estimating the hydraulic conductivity with inverse modeling (Stadler et al., 2000). Dyes have revealed preferential flow paths, flow in fissures and worm channels, and through cracks (Persson et al., 2005). Image analysis techniques have also been applied to estimate surface moisture (Persson et al., 2005).

Image analysis techniques involve applying a diffuse light source and measuring the amount of light transmitted or reflected with a digital camera. They generate high spatial resolution data (Persson et al., 2005a). Traditionally, analysis of dye images involves separation between stained and non-stained soil. Improvement in methods and technologies has however given rise to determination of dye concentration (Persson et al., 2005a).

There are several factors that may affect the color of the dye-stained soil, including a local excitation light incidence on the soil and variations in the chemical and physical composition of the soil (Lehmann, et al., 2006; Vanderbortht et al., 2002). Furthermore,

the intensity and color temperature of the illumination incident in an irregular particle distribution leads to differences that may be seen as gradations of darkness. Consequently, corrections by geometrical distortion, inhomogeneous illumination, and differences in white standard are required. Gimmi and Ursino (2004) established a method to correct the inhomogeneity of illumination and reflection in two steps. First, the value of each pixel in the main image is normalized with image of the gray standard, taken at identical light settings. Thus, the illumination inhomogeneity is corrected. Removing reflection inhomogeneity is the second step, and is done by a bootstrap procedure, where the flat-fielded reflection image is used to estimate a second flat field.

### 3. METHODOLOGY

The primary goal of this research is to develop and evaluate CWR technologies for detection and monitoring DNAPL contaminants in unsaturated zone under variable conditions. The objectives of this research has been accomplished through a systematic methodology involving laboratory experiments in soil cells, sensing and signal processing using radar antennas, inverse modeling and imaging algorithms. Experimental work involved taking electromagnetic measurements in a 2D flow and EM soilBed concurrently with digital images.

EM measurements and digital images were collected prior to, during, and after the injection of water and/or trichloroethylene (TCE), a major underground DNAPL contaminant. EM measurements involved testing loop antennas, and measuring their transmission and reflection characteristics in the presence and absence of DNAPLs, water or underground target elements. The responses of the antennas were used to estimate spatially-distributed dielectric properties of the bulk soil. These properties were used to produce tomograms that showed changes in the dielectric properties of the soil. During the research several antennas, analysis of mini-scale soilcells, and prototypes were made to improve the cross well radar technology.

This chapter describes the materials and methods used for the experimental work. It also

describes the methodology applied to determine dielectric properties of the bulk medium from the measurements of EM wave characteristics. Descriptions of method developed to create a tomographic image of the dielectric properties is given in following sections in Chapter 6.

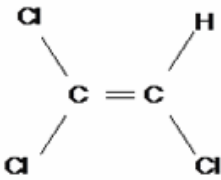
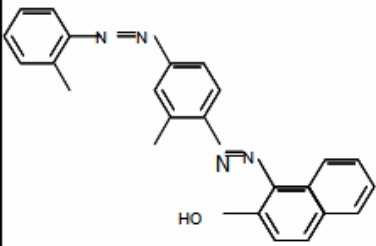
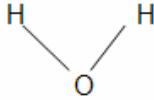
### **3.1 MODELED DNAPL**

Trichlorethylene (TCE) was selected as the target DNAPL combination in this study. The selection was based on the ubiquitousness in the environment and its physico-chemical and electromagnetic properties. TCE is one of the major contaminants in the subsurface (Moran et al., 2007; EPA, 1998). Trichloroethylene, also known as acetylene trichloride and ethinyl trichloride, is a nonpolar organic solvent, having chemical formula of  $C_2HCl_3$  (Table 3.1). It is a clear, nonflammable liquid with specific gravity greater than water and sparingly solubility in water (Table 3.1). TCE has low electric conductivity and dielectric permittivity values. Its dielectric contrast with water and soils forms the basis for detection using radar technologies.

TCE is a clear liquid that is difficult to see in soils, and must be dyed for proper visualization (Dunford et al., 1997). Consequently, Sudan IV has been chosen as a dye. Sudan IV is an insoluble organic dye (Table 3.1) which is insoluble in water but soluble in nonpolar organic solvents and fats. This solvent dye does not ionize (Dunford et al., 1997). In industrial field, it is used in coloring oils, waxes, greases, fats, hydrocarbons derivatives, polishes and acrylic emulsions (Merck, 2001). Sudan IV has been used to

dye TCE for transport visualization (Dunford et al., 1997) and TCE detection in soil samples using dye-shake test. Durnford et al., 1997, have determined that a 0.5% by weight of Sudan IV is appropriate for visualization process.

**Table 3.1 Physical chemical properties of TCE, Sudan IV, and water**

Characteristics	TCE	Sudan IV	Water <sup>*4</sup>
Appearance	Clear, colorless liquid <sup>*1, *2</sup>	Dark red powder <sup>*1*2</sup>	Clear
Odor	Chloroform-like odor <sup>*1</sup>	N/A <sup>*2</sup>	N/A
Solubility	1.100 mg/L <sup>*1</sup>	Negligible (<0.1%) <sup>*5</sup>	N/A
Specific Gravity	1.46	N/A <sup>*2</sup>	1 at 4°C
Molecular weight	131.39 AMU	380.45 AMU	18 AMU
Density	1.47 g/cm <sup>3</sup> at 20°C/4°C <sup>*1</sup>	N/A	1g/cm <sup>3</sup> at 20°
Boiling Point	87 °C (189 °F) <sup>*2</sup>	N/A <sup>*2</sup>	100°C
Melting Point	-73°C (-99 °F) <sup>*2</sup>	199 °C <sup>*2</sup>	0°C
Vapor Pressure	57.8 mmHg at 20 °C <sup>*2</sup>	N/A <sup>*2</sup>	149.4 mmHg at 0°C
Dielectric Permittivity	≈ 2.3-10.4	N/A	80
Electrical conductivity	10 <sup>-7</sup> S/m <sup>*3</sup>	Not reported	10 <sup>-5</sup> S/m distilled water 4 S/m sea water
Molecular structure			

Source:

\*<sup>1</sup>:Merk Index, 2001

\*<sup>2</sup><http://www.jtbaker.com/msds/T4940.htm>, 2005

\*<sup>3</sup>Carcioni et al. 2003

\*<sup>4</sup><http://hyperphysics.phy-astr.gsu.edu/hbase/kinetic/watvap.html#c1>, 2008

\*<sup>5</sup>Material Safety Data Sheet, J.T.Baker, 2006

### 3.2 SOILBED EXPERIMENTAL SETUP

Experimental work involved taking radar electromagnetic measurements in two-dimensional flow and EM soilBeds concurrently with digital images. SoilBeds consisted

of Plexiglas tanks packed with beach sand from Isabela, P.R. The front and rear panels of the tanks were lined with 0.3cm thick glass sheets (Valcor Samcor, PR) to avoid reactive contact between DNAPL and plexiglass. Tanks were made of transparent material to permit visual observations and digital imaging of the dyed DNAPL distribution. SoilBeds of different dimensions (Table 3.2) were used to develop packing methodology; test antenna response and EM boundary conditions; test antenna response in the presence of buried objects; and measuring spatially-distributed EM transmission and reflection characteristics of the bulk soil in the presence and absence of TCE and water. More details on the soilBed characteristics are given in following chapters describing the tests conducted and results.

**Table 3.2 SoilBeds setups**

Number ID	Dimension <sup>*1</sup>			Metal plate spacing (cm)	Borehole location and spacing (cm) <sup>*2</sup>		Applications
	L (cm)	H (cm)	W (cm)		L(x)	H(z)	
1	45.7	60.0	30.5	10.00 <sup>*3</sup>	Variable <sup>*4</sup>	10,16,12.7;15,24	Testing and selection of antenna type
2	30.0	30.0	7.0	2.20	4, 26	5,10,15,20,25	Soil packing TCE/Water detection
3	30.0	60.0	7.0	2.20	4, 26	5,10,15,20,25	Loop antenna response
4	83.0	83.0	7.0	2.20	12, 70	10,15,20,25,30, 35,40,45,50,55	2D EM Antenna testing

<sup>\*1</sup> L, H, and W are the length, height, and width dimensions, respectively

<sup>\*2</sup> Location along the length (x-axis) and height (z-axis) in soil tank assuming an origin (0.0) at the lower left corner of the tank.

<sup>\*3</sup> Metal plates were solid

<sup>\*4</sup> See selection on antenna type for spacing

The walls of the soilBed were made of lossy dielectric material. Consequently, part of the incident wave transmitted by the antennas could be directly backscattered by the walls, and then scattered by the soil itself toward the antenna (Franceschetti et al., 2003).

This requires placing perfectly reflecting boundaries in between the radiating antennas

and the soilBed walls. The spacing between the boundaries is limited by the wavelength and would require placing the boundaries close for flow experiments having no boundary effects. Consequently, metal mesh panels must be used. The mesh panels must be almost imperceptible by the soil, while maintaining a constant electromagnetic field inside the setup. This was attained by placing parallel metal meshes (InterNet, Inc., Minneapolis) to create perfect reflection boundaries along the frontal and rear walls of the soilBeds. The mesh panels minimized EM scattering by the soilBed boundaries and simplify the evaluation of EM response. The metal mesh panels (0.30cm\*0.22cm\*0.012cm, diamond-shape), were fitted with metallic frames to give them rigid support. The two parallel plates were installed vertically, and held in place by PVC fixer in all soilBeds (Figure 3.1). The fixers were selected as to avoid cause signal disturbance and should maintain the mesh plates vertically aligned without any deformation.

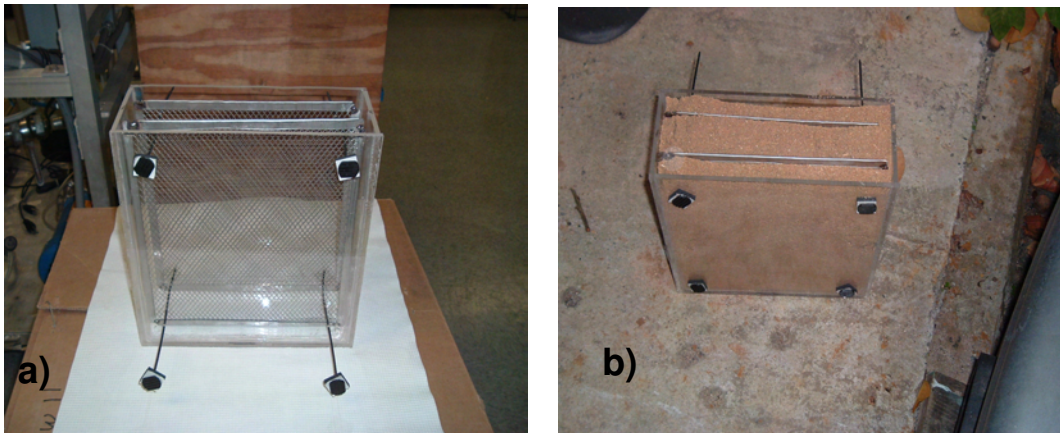


**Figure 3.1 SoilBed prototype with a) metal mesh held by PVC fixers b) packed with dry sand.**

The estimate of the separation distance between the mesh panels was based on the maximum theoretical distance that would permit perfect reflection boundaries without

modal dispersion. This distance was estimated as half the minimum wavelength ( $\lambda_{min}$ ) with the equation:

$$\lambda_{min} = \frac{c}{\sqrt{\epsilon_r} f_{max}} \quad \text{Equation 3.1}$$

where  $c$  ( $3*10^{10}$  cm/s) is the velocity of light,  $\epsilon_r$  is the dielectric relative permittivity of the media, and  $f_{max}$  is the maximum wave frequency. For a  $f_{max}$  of 1.5 GHz and a permittivity of 20 (typical for saturated sand) the separation between the metal boundaries is 2.2 cm. For unsaturated soil the  $\epsilon_r$  is lower and the separation distance can be greater.

SoilBeds were fitted with horizontal boreholes located in the lateral panels of the tanks and in between the metal plates (Figure 3.2). The boreholes were used to place the antennas in the soil. They were lined with plastic casing ( $13.53 \pm 0.1$  mm O.D.,  $9.40 \pm 0.1$  mm I.D.) to protect the antennas from soil smearing and water. The plastic casing does not affect the signal, and keep the antennas aligned. Because this casing permits insertion of the antenna, it enhances the opportunity for experimental reproducibility. The locations in the respective soilBeds are given in Table 3.2.

### 3.2.1 Soil Packing

Basic CWR technologies development for DNAPL detection requires, at the moment, homogeneous porous media. Once the technology is developed for this simpler case, further evaluation can be conducted using heterogeneous media. Extensive literature review indicates that there is little information on packing methods that can achieve reproducible and quantifiable characteristics. Many soil transport studies do not even

address or report packing methods. In general, reported soil packing of most laboratory-scale columns and tanks is performed by pouring small amounts of the soil at a time until the column or tank is filled to (sometimes) particular bulk density (Rodriguez et al., 2006). Generally, issues regarding grading of soil particles and formation of layers are obviated.

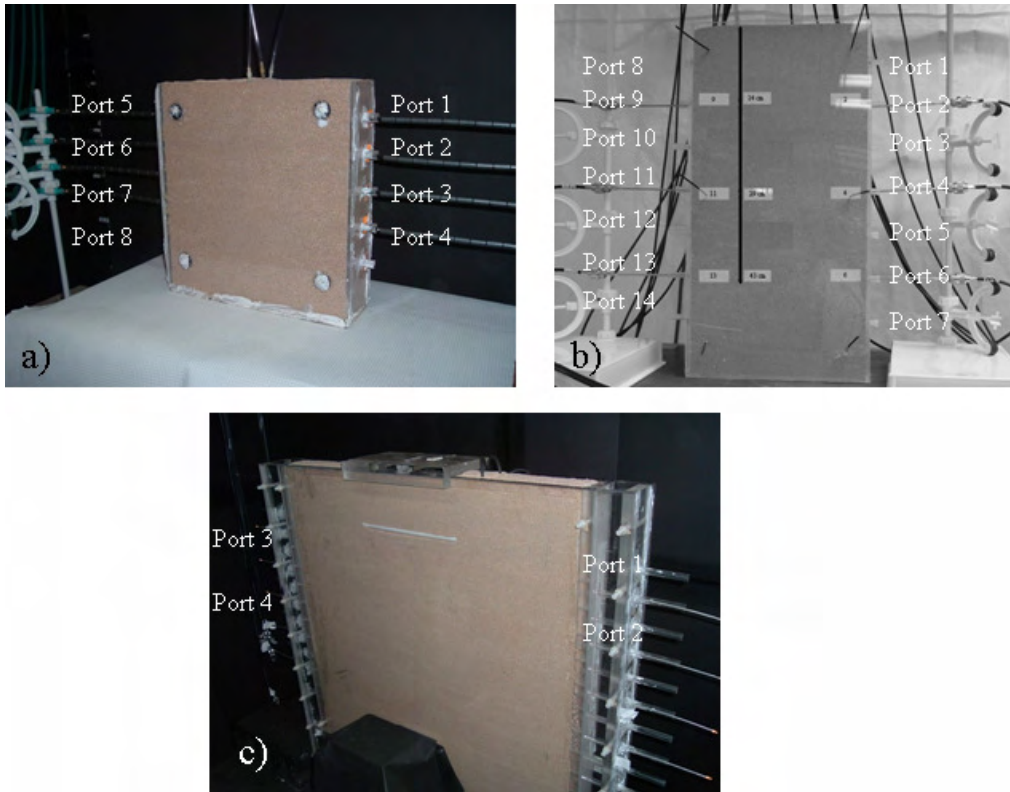


**Figure 3.2 Borehole location at soilBed setup a) number 2, b) number 3, and c) number 4**

Different methodology had to be developed in this research to attain observable homogeneous packing, avoid metal plate deformation, and maintain parallel equidistant and non-variable conditions between the metal mesh plates. The method was tested in 30 cm by 30cm soilBeds and involved delivering the sand through stain steel pipes to the top of the soil surface. The sand was delivered using a delivery guide (Figure 3.3), which

held the delivery pipes and metal plates in place while delivering the sand. The delivery was done by moving the guide sideways while transferring the sand through the pipes. The method achieved observable homogeneity, showing no particle-size gradation layering, and maintained the plates in place (aligned parallel with non-variable separation distance).



**Figure 3.3 Soil delivery guide**

### 3.2.2 Soil Characteristics

SoilBeds were packed using beach sand from Isabela, Puerto Rico. The sand mainly consists of quartz and calcite (Rodriguez et al., 2006). The particle size distribution is ranging between 25 and 60  $\mu\text{m}$  (Figure 3.4). This soil has a uniformity coefficient of 1.81 that denotes a uniform sample soil. The final density of the packed soil average was  $1.67 \text{ g/cm}^3 (\pm 0.02)$  for all packed soilBeds, yielding on average volumetric porosity of  $0.40 (\pm 0.03)$ .

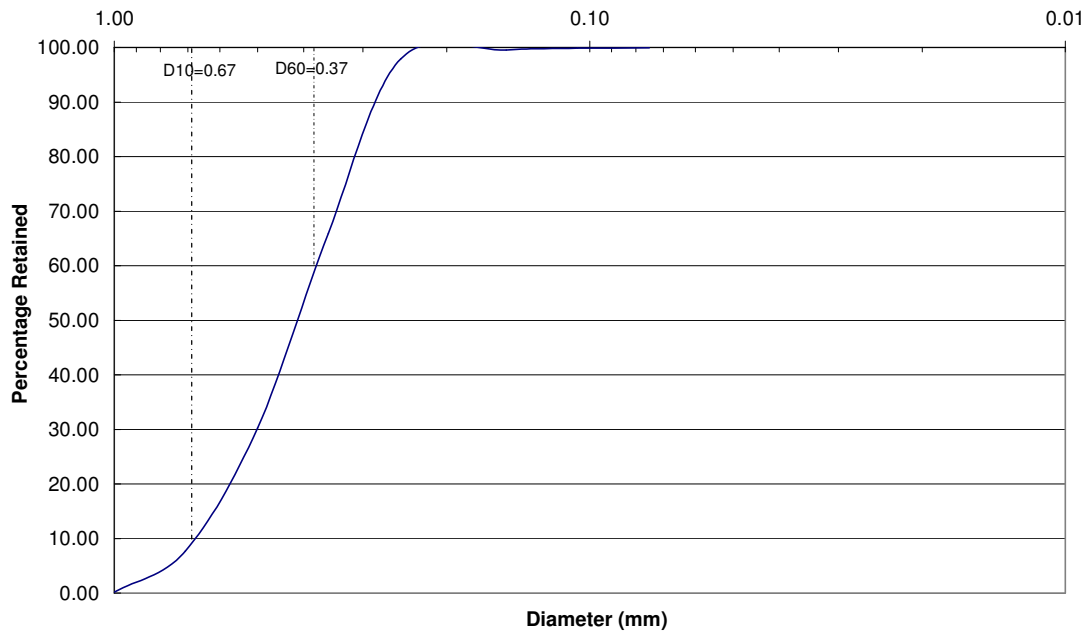


**Figure 3.4 Granulometric distribution sandy soil**

### 3.2.3 DNAPL Delivering System

Dyed TCE was injected into unsaturated and saturated soil below the surface of the soil. It was injected through hydrophobic porous tubes located at the horizontal center of the soilBed tanks. The delivery tube (Figure 3.5) consisted of Teflon porous tube (2.1336 cm O.D., 1.5748 cm I.D., Small Parts, Inc., Miramar, FL) sealed at each end with Teflon caps to induce uniform flow through out the porous tube. Thirty centimeters long tubes were used in the large soilBed (ID 4, Table 3.2), whereas three-cm long tube were used in the smaller ones (ID 2, Table 3.2). One tube was used for each compartment separated by the metal mesh plates to ensure uniform delivery along the width of the tank. The vertical location of the delivery tubes varied between tanks. It was located at 15 cm

below the soil surface in the larger soilBed (ID 4, Table 3.2) and the smaller (ID 2, Table 3.2) soilBed tank used for injecting TCE under initially-dry conditions. For the smaller soilBed tank used to inject TCE in water-saturated conditions, the delivery was located 5cm below the soil surface.

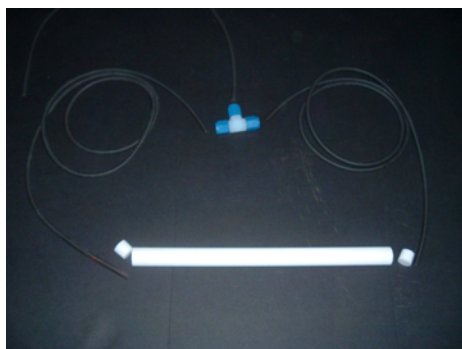


**Figure 3.5 TCE injection setup : porous cup, teflon ending, tygon tubing, and fitting**

Vyton tubing (3.2mm O.D., 1.6mm I.D., Fisher Scientific, P.R.) was inserted in the center of the delivery tubes, and connected to peristaltic pumps (Model 77200-60, Cole Parmer, Illinois) which delivered the TCE at a constant flow rate.

#### 3.2.4 Experimental Room

The experimental work was conducted in an enclosed, studio-like room (247 cm, 175 cm, 183 cm, Figure 3.6), which housed the soilBed systems. The studio-like room (SLR) located in the Environmental Engineering Laboratory (EEL) of the University of Puerto Rico, Mayaguez Campus, is equipped with a ventilation system used to remove any organic contaminants volatilizing into the atmosphere. The ventilation system consists of a bell-shape hood connected to an extraction line containing an extractor fan. The extractive line was connected to the EEL fume hood extraction line.



**Figure 3.6 Studio like room**

The SLR was built using black card board supported by an external wooden frame, and was set internally with proper illumination for image acquisition process. The illumination system consisted of a source and a background. Two illumination sources consisting of 40W fluorescent lamps were located above and in front of the targeted soilBed. The background consisted of black walls to absorb the excess of incident reflection light.

### 3.3 DATA ACQUISITION SYSTEM

Signal management and analysis were performed using a Vector Network Analyzer (8714 ET; 300 KHz to 2.2GHz) with a multiport test set (87050E) (Figure 3.7). Although three and four port vector networks analyzers (VNAs) are commercially available, the two-port VNA is most common (Lenk and Doerner, 2005).



**Figure 3.7 Network Analyzer, multiport test set, and soilBed(type 2, Table 3.2)**

Vector Network Analyzer (VNA) consists of a signal source, a receiver, and a display. The signal source launches a signal at a swept frequency range to the material under test. The signal is tuned to that frequency to measure frequency-dependent reflection and transmission characteristics of the materials (Agilent, 2005). Measurements of the reflection from and/or transmission through a material provide the information to characterize the permittivity and permeability of the material.

#### 3.3.1 Measurement Accuracy

The accuracy of the dielectric-constant measurement is critically based upon the accuracy with which the reflection and transmission coefficients can be measured. The

measurement of electromagnetic responses may contain some errors caused by system noise and environmental variations as well as certain systematic errors that are, therefore, correct (Sarabandi and Ulaby, 1988). To correct the systematic errors, the measurement system is calibrated using four independent standards whose calibration coefficients are known over the frequency range under consideration. These include through, open, short, and load. They are used singly or in combination depending on the type of calibration.

### **3.4 ANTENNA DESIGN AND TESTING**

Detection of DNAPLs in the subsurface using CWR technologies is influenced by the type and dimension of antennas used (Serrano et al., 2006). Several types of antennas were evaluated to determine the most appropriate for the soilBed system. These included monopole, dipole, double, and loop antennas (Figure 3.8). Ferrite beads were placed in the antennas to prevent bending of the cables when pushed into the soil boreholes and to absorb wave energy that could leak around the data transfer cables (Farid et al., 2003a).

Antenna testing in soilBeds incorporated parallel metal plates in the vertical position to create a 2D EM field of perfect reflection. The size and orientation of the antennas in the 2D field were, therefore, important parameters to consider. The evaluation consisted of placing the antennas in the testing soilBeds and measuring their response to an EM input. Signal management and analysis were performed using the VNA. The signal source supplied by the VNA is emitted from one antenna located in a borehole, and received by other antennas located in other boreholes. The source sends the signal at swept frequency

range between 3MHz and 2200MHz, which is the VNA range. The signal received by other antennas is analyzed at the same frequency range to detect the reflected and transmitted signals from the material (Agilent, 2005).

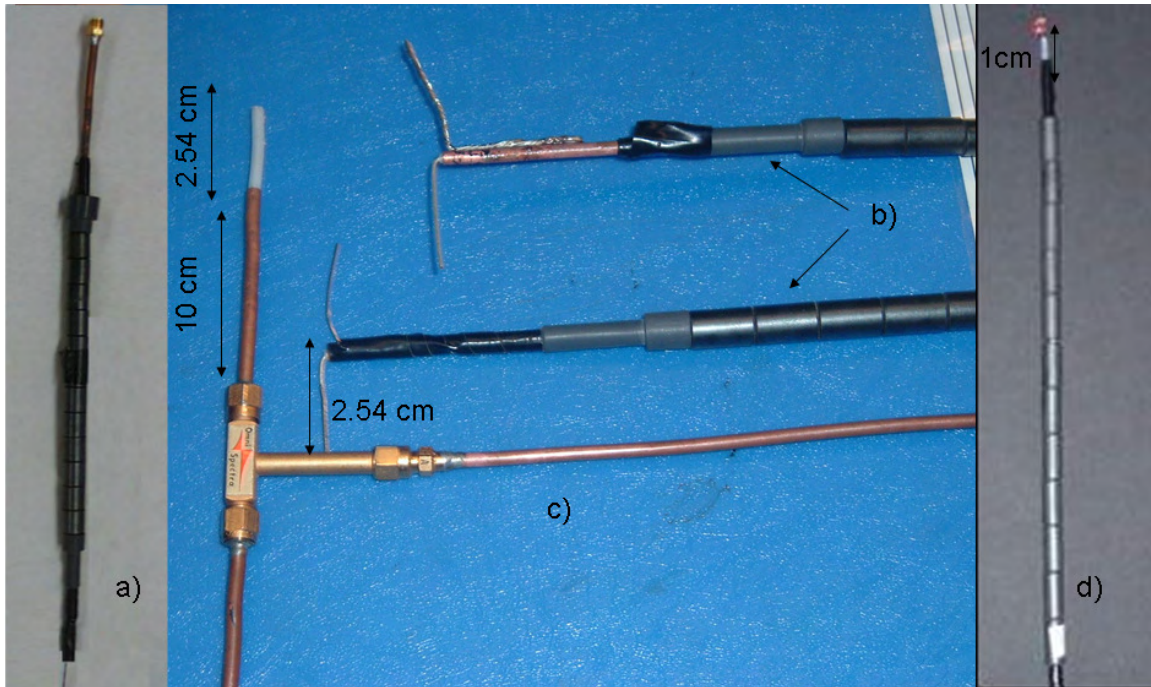


**Figure 3.8 Tested a) monopole, b) dipole, c) double, and d) loop antennas.**

#### 3.4.1 Dipole and Monopole Antenna Selection

The initial testing for selection of antenna types was conducted in a soilBed (ID 1, Table 3.2) packed with dry sand. Two solid metal plates were placed vertically and parallel to each other at a distance of 10 cm from each other to create a field of perfect reflection and accommodate the size of the antennas (Figure 3.9). The separation distance of the plates was greater than estimated for saturated soil (2.20 cm), but was estimated appropriate for unsaturated soil ( $\approx 11$  cm for  $\epsilon_r \approx 4$ ). For this testing, antennas were inserted vertically into the soil at different depth and horizontal distances in a line arrangement.

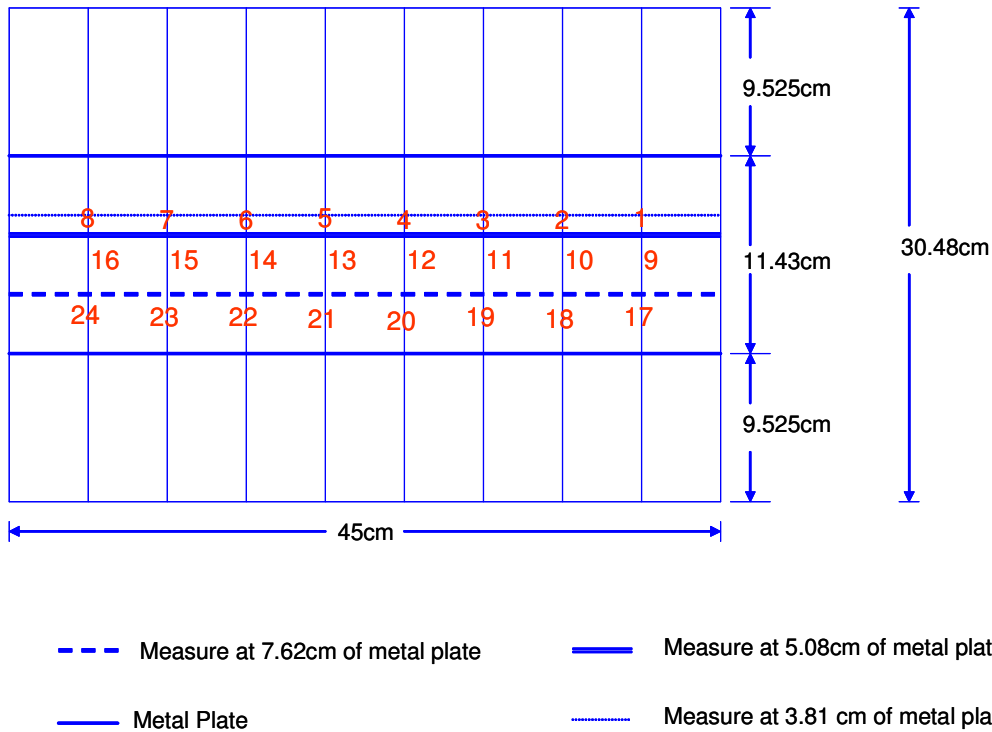


**Figure 3.9 Sampling distances used for testing and selection of antenna types**

Dipole antennas were oriented to have the dielectric field perpendicular to the perfectly reflecting boundaries. The electric field was oriented downward for the monopole antennas. Loop antennas were tested horizontally in other setups (soilBed ID 2, 3, and 4, Table 3.2).

The initial antenna testing involved inserting two antennas at a given distance (Figure 3.9) and depth and monitoring their response to EM input via a VNA. Selection was based on the decibel/frequency response for sending and receiving antennas. Only those antennas and conditions yielding a transmission range above noise level for frequencies higher than 1 GHz were considered for selection based on work presented by Farid (2004). Initial assessment indicated that the dipole antennas were responding according to the established range of frequencies and decibels, but not the monopoles antennas

(Figure 3.10 and Figure 3.11). Initial testing for selection of antennas, thus, suggested that dipole antennas performed better than monopole antennas on the configuration tested. The response of dipole antennas on the linear arrangement at different separation distances showed acceptable configuration in the linear pattern.

For the different antennas to work properly, they should conform to certain dimension specifications, which are given by the frequency used. Table 3.3 shows theoretical appropriate length for dipole and monopole antennas at radar wave frequencies. The length for dipole antennas are estimated as twice the length of the monopole antennas, whereas for the loop antennas depend on the circumference and number of turns. Theoretically, the loop antenna can be made with small circumference if the number of loops is increased (Balanis, 2005). The estimated length of the dipole and monopole antennas limited the use of these antennas in the 2D setup. Because the electric field along the length of the antennas must be perpendicular to the perfectly reflecting boundaries, the antennas must be smaller than the separation distance of the metal plates (2.2cm). It was, therefore, necessary to use loop antennas.

**Table 3.3 Length for dipole and monopole antennas**

<b>F (MHz)</b>	<b><math>\lambda</math>(m)</b>	<b><math>l_{\text{dipole}}</math>(m)</b>	<b><math>l_{\text{monopole}}</math>(m)</b>
10	30.00	15.00	7.50
100	3.00	1.50	0.75
1000	0.30	0.15	0.075
1500	0.20	0.10	0.050

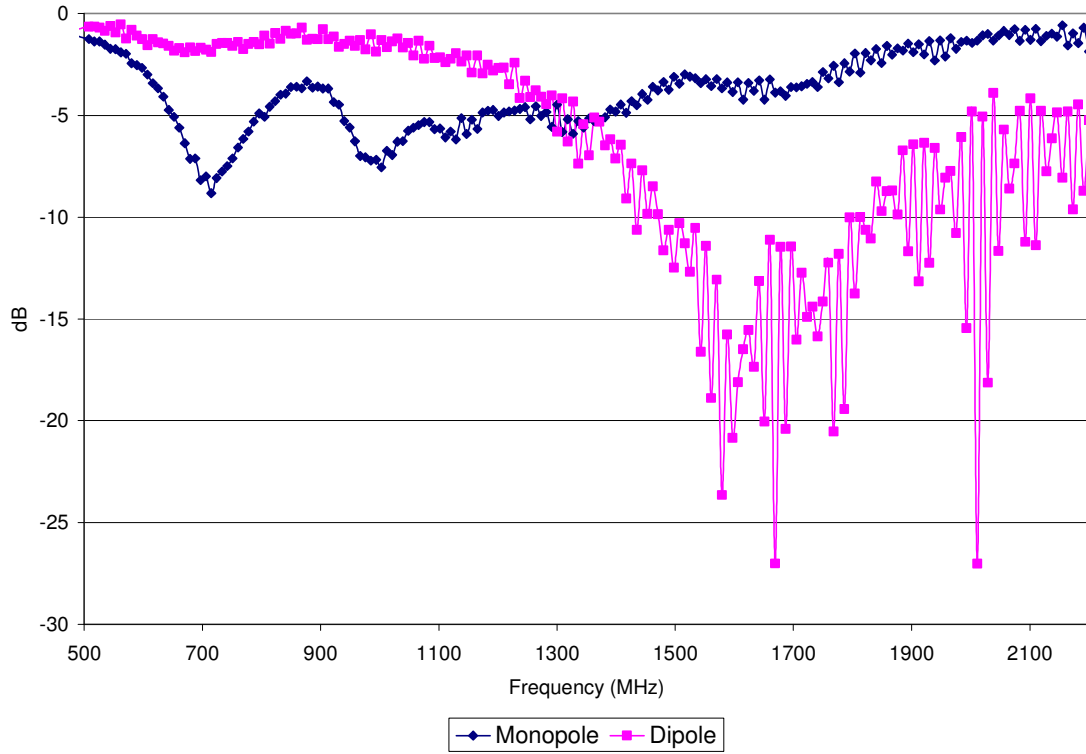


**Figure 3.10 Reflection response of monopole and dipole antennas**

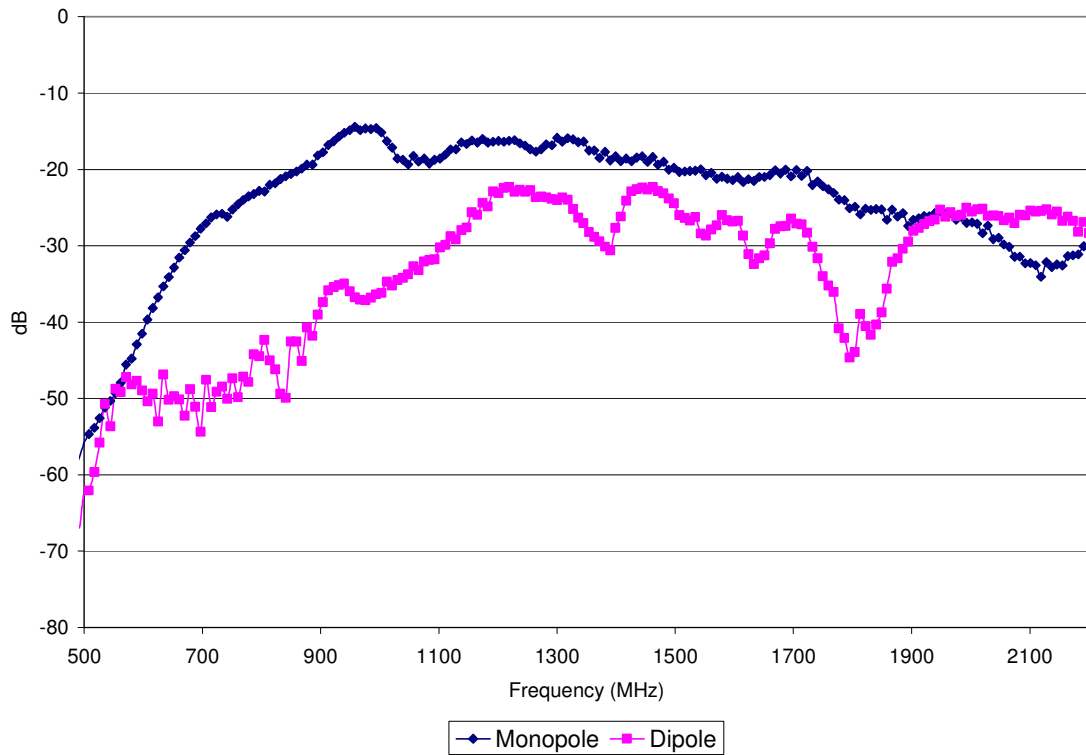


**Figure 3.11 Transmission response of Monopole and Dipole Antennas**

Small loops radiate and receive well, even in the GHz range (Balanis, 1992). They can be thought of as short magnetic dipoles. The impedance matching is, however, difficult requiring many turns and a ferrite core.

Loop antennas were built using electrical cable (0.35814cm O.D., aluminum semi-rigid bulk coaxial cable, sold in coils, Pasternack Enterprises, Irvine, California), ferrite beads and subminiature adapters (SMA) connectors (PE 4115, Pasternack Enterprises, Irvine, California) (Figure 3.12). The wire was coiled through a ferrite bead (Figure 3.12a), and welded to the center conductor and outer shield of a coaxial cable (Figure 3.12b).



**Figure 3.12 a) Materials for construction of loop antennas, and b) loop antenna**

The number of loops varied (see chapter 4 for more details). Its cylindrical diameter was 0.33 cm, and the length of the loop antenna was 24.88 cm.

The radiation resistance for this electrically small loop having a circumference ( $C$ ) of 1.0367cm and working in an ultra high frequency bands (300-2200 MHz) was estimated as (Balanis, 2005):

$$R_r = 20\pi^2 \left( \frac{C}{\lambda} \right)^4 N^2 \quad \text{Equation 3.2}$$

where  $\lambda$  is the wavelength (4.472 cm) and  $N$  is the number of turns in the loop

For a 8 loop antenna  $R_r$  was estimated as 36.49 mohms. The radiation resistance could be increased by increasing (electrically) its perimeter and/or the number of turns. The ferrite bead of very high permeability being used allowed raising the magnetic field intensity and hence the radiation resistance.

The loop antenna can be described by its maximum effective aperture  $A_{em}$  and its physical size  $S_{ps}$ . The maximum effective aperture reflects the area which when multiplied by the incident power density gives the maxim power delivered to the load, and it is described as a function of the wavelength:

$$A_{em} = \left( \frac{3\lambda^2}{8\pi} \right) \quad \text{Equation 3.3}$$

The physical size represents the cylindrical area of the loop, and it is given by:

$$S_{ps} = \pi a^2 \quad \text{Equation 3.4}$$

where  $a$  is radius of the loop.

For  $a$  loop radius of 0.165cm and a wavelength of 4.44cm ( $f=1.5\text{GHz}$ ) the  $A_{em}$  is  $2.38\text{cm}^2$  and the  $S_{ps}$  is  $8.55 \cdot 10^{-2}\text{cm}^2$ . Electrically the loop that is being tested is about 28 times larger than physical size.

### 3.4.2 Loop Antenna Response Testing

The loop antennas were tested in soilBeds ID 2, 3, and 4 (Table 3.2) packed with dry sand. The responses of the antennas were tested by placing antennas at different borehole

locations and evaluating the transmission and reflection measurements. Antennas were placed in horizontal boreholes located in the lateral walls of the soilBeds (Figure 3.2). It was important to ensure that the antenna did not touch the borehole walls. Antenna selection was based on the decibel/frequency response for sending and receiving antennas. More details on the antennas tested and their response is given in Chapter 4.

### 3.4.3 Boundary Conditions

The potential effect of the soilBeds boundary conditions response of the loop antennas was evaluated by measuring the transmission and reflection characteristics with and without the placement of soil metal plates on the top and bottom, front and back, and inside the soilBeds (ID 2, Table 3.2). Boundary condition effects were evaluated using two metal mesh panels with diamond shape openings having dimensions of 3 mm\*2.21 mm, and solid metal plates (Figure 3.13).

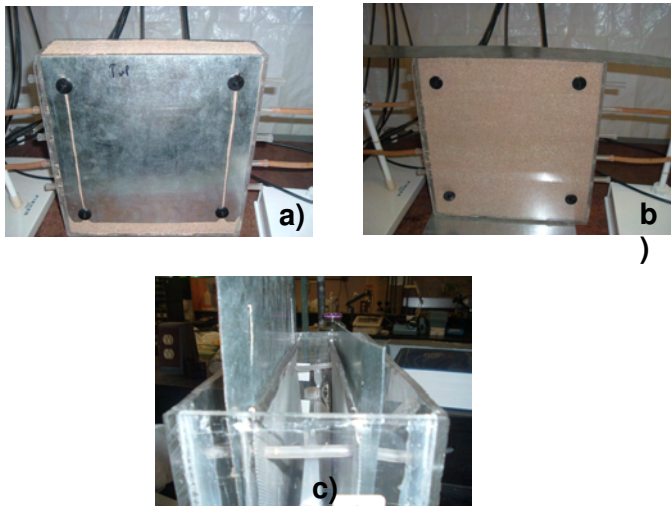


**Figure 3.13 Electromagnetic boundaries conditions a) metal plate in front and back site b) metal plate in top and bottom c) metal plate inside located together the mesh.**

### **3.5 DETECTION OF UNDERGROUND DNAPL AND OTHER TARGET ELEMENTS**

Detection of DNAPLs and other underground target elements using CWR technologies was evaluated by analyzing antenna transmission and reflection measurements across the testing soilBeds in the presence and absence of TCE or other target elements (i.e., metal and plastic bars, water).

Loop antennas were inserted 4 cm into the horizontal boreholes and connected to the VNA through a coaxial cable (10.45mm O.D., Micro-Coax, Pottstown PA). Special attention was given to avoid any contact of the antennas with the plastic boreholes walls. The VNA supplied and manage the signal source emitted and received by the antennas. The source signal was emitted through a radiating (transmitting) antenna at a swept frequency ranging between 3MHz to 2.2GHz. Receiving antennas processed the signal at the same frequency range to generate reflection and transmission measurements, which were later used to estimate dielectric properties.

#### **3.5.1 Detection of Underground Target Elements**

Detection of metal or plastic solid objects buried underground was evaluated by inserting a metal bar (2cm \* 0.5cm\*40cm) or an acrylic bar (1cm\*2cm\*40cm) across the soil surface in the horizontal center of the testing soilBed. Transmission and reflection measurements were taken prior to and after the insertion of the object and compared. The effect of the acrylic bar in antenna response was evaluated using a testing soilBed(ID 3,

Table 3.2) packed with dry sand. The response of the antennas in absence or presence of the metal bar was evaluated using the larger testing soilBed (ID 4, Table 3.2). Measurements characteristics in the presence of acrylic and metal bars are given by Serrano et al., 2006 and Serrano et al, 2007, and are presented in chapter 4 and 5, respectively.

### 3.5.2 DNAPL Detection

Experimental work to test and validate the use of CWR algorithms for detection and monitoring of DNAPLs in underground systems involved injecting a DNAPL into soilBeds (ID 2, Table 3.2) while taking EM wave propagation measurements. EM signals were transmitted and received using the previously described VNA system, and an array of 4 sets of loop antennas (Serrano et al., 2007; Serrano et al., 2006) placed in horizontal boreholes along the lateral walls of the soil

Wave propagation measurement were taken concurrently with visual images before and during the injection of trichloroethylene (TCE, a commonly found DNAPL, contaminant) dyed with Sudan IV. Initial measurements were taken in dry soil to characterize background conditions and noise. Two experimental conditions were tested: TCE injection in dry soil followed by water infiltration; and TCE injection under saturated conditions.

In the dry sand experiments TCE was injected at 15cm below the soil surface in the horizontal center of the soilBed at a rate of 0.15 ml/min for 30 minutes. Thereafter, water

was infiltrated at the surface at a rate of 10ml/min for 20 min. A sweep of EM measurements and digital pictures was taken at 5 min, 10 min, 30 min, 50 min, 80 min, and 130 min after the commencement of the TCE injection. EM measurements involved sending a EM signal from each of the antennas, while receiving in all antennas (including the radiating antenna). Measurements were made with only 1 radiating antenna at a time (i.e., one antenna send while all receive, then another send while all receive, etc). Each sweep took around 6 minutes.

For the saturated experiments the initially dry sand was water saturated from the bottom at a rate of 0.10ml/min. Digital images and EM responses were taken during the saturation period at the times when the soil tank was 50, 75, and 100 percent saturated. After saturation, but prior to TCE injection, 300 ml of water were drained to prevent water spilling during the injection. TCE was injected at 5 from the soil and water surface, respectively, at the horizontal center of the soilBed. A sweep of EM measurements and digital image acquisition was taken at the same times (from commencement of injection) as those used during TCE injection in dry sand.

Electromagnetic measurements were processed through a code developed to estimate dielectric properties a long EM raypaths (Appendix 1). These estimates were then used to develop tomographic images of the dielectric properties in the soil using a code developed for this purpose (Appendix 2). The methods used to develop these codes are described in latter sections of this document.

### 3.6 DETERMINATION OF DIELECTRIC PROPERTIES

Materials can be described electrically by their complex permittivity ( $\epsilon_r$ ) and permeability ( $\mu_r$ ) properties, which affect the response of the material to electromagnetic radiation (Feng, 2006). As EM waves travel through a media its energy is attenuated from reflection, transmission, scattering, and absorption losses (Reynolds, 1999). The attenuation of the wave is a function of  $\epsilon_r$  and  $\mu_r$ . Reflection and transmission measurements, named scattering parameters,  $S_{11}$  and  $S_{21}$  respectively, allow inferring these electromagnetic properties (Buyukoztur et al., 2006; Zwick et al., 2006; Seltman et al., 1996; Agilent, 1985). The S-parameters can be determined using a Vector Network Analyzer (VNA) connected to a physical device (i.e. an antenna), through a coaxial cable. Scattering parameters are related to the traveling waves that are scattered or reflected when a n-port network is inserted into a transmission line. These parameters are usually measured with a device imbedded between a  $50\Omega$  load and source, where there is little chance that oscillations occur (Agilent, 1995). Because the traveling EM waves do not vary in magnitude at points along lossless transmission lines, the scattering parameters can be measured using a device located at some distance ( $d$ ) from the measurement transducers, provided that the device and transducers work connected by low-loss transmission lines (Figure 3.14). Derivations of S-parameters are described in the following sections.

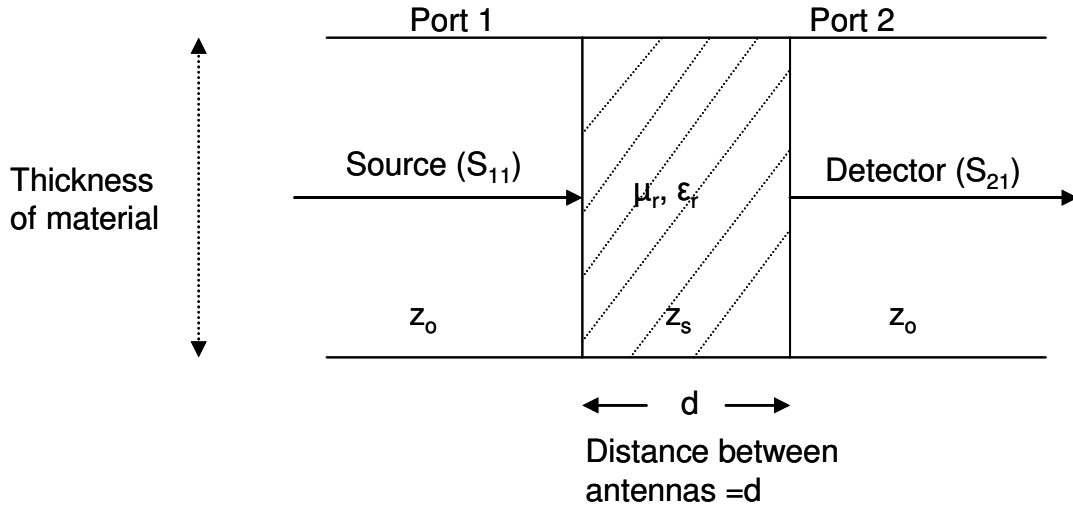


**Figure 3.14 Theoretical 2-port Network for  $\mu_r$  and  $\epsilon_r$  estimate**

Source: Adapted from Agilent, 1985.

### 3.6.1 Two-Port Network Theory

Although a NA may have any number of ports, S-parameters can be explained most easily by considering a network with only two ports, an input port and output port. To characterize the performance of two-port network, four parameters must be measured. Each parameter set is related to a set of the two variables: two represent the excitation of the network (independent variables), and the remaining represent the response of the NA to the excitation (dependent variables). Figure 3.15 shows a network excited by voltage sources  $V_1$  and  $V_2$ , the network currents  $I_1$  and  $I_2$  respectively.

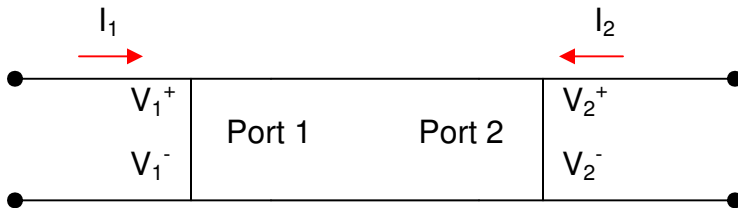


**Figure 3.15 Generalized two-port network excited by voltages sources  $V_1$  and  $V_2$**

Source: Adapted from Agilent, 1985.

Voltage sources and currents maybe related by the following equations:

$$I_1 = y_{11}V_1 + y_{12}V_2 \quad \text{Equation 3.5}$$

$$I_2 = y_{21}V_1 + y_{22}V_2 \quad \text{Equation 3.6}$$

where:

$y_{11}$ ,  $y_{12}$ ,  $y_{21}$ ,  $y_{22}$  are parameters obtained from measurements with one port of the network excited by a voltage source while the other port is short circuited (Agilent, 1995). For the 2-port network given in Figure 3.15, these parameters are estimated as the ratio of the current at one port to the voltage at the other port, with the current-port short circuited. For example,  $y_{21}$  can be estimated with the ratio of the current at port 2 to the voltage at port 1 with port 2 short circuited.

$$y_{21} = \left. \frac{I_2}{V_1} \right|_{V_2=0 \text{ (output short circuited)}} \quad \text{Equation 3.7}$$

$$y_{12} = \left. \frac{I_1}{V_2} \right|_{V_1=0 \text{ (output short circuited)}} \quad \text{Equation 3.8}$$

$$y_{11} = \left. \frac{I_1}{V_1} \right|_{V_2=0 \text{ (output short circuited)}} \quad \text{Equation 3.9}$$

$$y_{22} = \left. \frac{I_2}{V_2} \right|_{V_1=0 \text{ (output short circuited)}} \quad \text{Equation 3.10}$$

The behavior of a two-port NA can be described by two linear equations similar to Equation 3.5 and 3.6, given by:

$$\mathbf{b}_1 = \mathbf{S}_{11}\mathbf{a}_1 + \mathbf{S}_{12}\mathbf{a}_2 \quad \text{Equation 3.11}$$

$$\mathbf{b}_2 = \mathbf{S}_{21}\mathbf{a}_1 + \mathbf{S}_{22}\mathbf{a}_2 \quad \text{Equation 3.12}$$

The incident wave (independent) parameter ( $a_i$ ) is related to the reflected wave (dependent) parameter ( $b_i$ ) by the scattering parameters or S-parameters  $S_{11}$ ,  $S_{22}$ ,  $S_{21}$ , and  $S_{12}$ . The  $S_{11}$  and  $S_{22}$  represent the reflection electromagnetic measurement, whereas  $S_{12}$  and  $S_{21}$  represent the transmission electromagnetic measurement.

### 3.6.2 S-Parameter Description

Scattering parameters can be described in terms of  $a_i$  and  $b_i$  that are normalized complex voltage wave's incident on and reflected from different ports of the network analyzer. They are defined in terms of the terminal voltage  $V_i$ , the terminal current  $I_i$ , and an arbitrary reference impedance  $Z_i$ , where the asterisk denotes the complex conjugate and  $i$  represents the number of port (Agilent, 1995):

$$\mathbf{a}_i = \frac{V_i + \mathbf{Z}_i \mathbf{I}_i}{2\sqrt{|\text{Re } \mathbf{Z}_i|}} \quad \text{Equation 3.13}$$

$$\mathbf{b}_i = \frac{V_i - \mathbf{Z}_i^* \mathbf{I}_i}{2\sqrt{|\text{Re } \mathbf{Z}_i|}} \quad \text{Equation 3.14}$$

For a two-port NA, S-parameters are expressed using  $a_i$  and  $b_i$  parameters by:

$$\mathbf{S}_{11} = \frac{\mathbf{b}_1}{\mathbf{a}_1} = \frac{\frac{V_1 - \mathbf{Z}_0 \mathbf{I}_1}{2\sqrt{|\text{Re } \mathbf{Z}_0|}}}{\frac{V_1 + \mathbf{Z}_0 \mathbf{I}_1}{2\sqrt{|\text{Re } \mathbf{Z}_0|}}} = \frac{\mathbf{Z}_1 - \mathbf{Z}_0}{\mathbf{Z}_1 + \mathbf{Z}_0} \quad \text{Equation 3.15}$$

$$S_{22} = \frac{b_2}{a_2} = \frac{\frac{V_2}{I_2} - Z_0}{\frac{V_2}{I_2} + Z_0} = \frac{Z_2 - Z_0}{Z_2 + Z_0} \quad \text{Equation 3.16}$$

$$S_{21} = \frac{b_2}{a_1} = \frac{\frac{V_2}{I_2} - Z_0}{\frac{V_1}{I_1} + Z_0} = \frac{Z_2 - Z_0}{Z_1 + Z_0} \quad \text{Equation 3.17}$$

$$S_{12} = \frac{b_1}{a_2} = \frac{\frac{V_1}{I_1} - Z_0}{\frac{V_2}{I_2} + Z_0} = \frac{Z_1 - Z_0}{Z_2 + Z_0} \quad \text{Equation 3.18}$$

where  $Z_1$  and  $Z_2$  are the input impedance at port 1 and 2, respectively, and  $Z_0$  is the intrinsic impedance ( $50\Omega$ ).

S-parameters in a waveguide with separation  $d$  between ports may be related to reflection and transmission coefficients with the following equations (Agilent 1995; Baker- Jarvis et al., 1990; Agilent 1985):

$$S_{11}(w) = \frac{(1 - T^2)\Gamma}{(1 - \Gamma^2 T^2)} \quad \text{Equation 3.19}$$

$$S_{21}(w) = \frac{(1 - \Gamma^2)T}{(1 - \Gamma^2 T^2)} \quad \text{Equation 3.20}$$

where  $w$  represents frequency dependent of the S-parameters,  $\Gamma$  is the reflection coefficient, and  $T$  is the transmission coefficient.

Reflection and transmission coefficients may be related to dielectric parameters, as follows:

$$\Gamma = \frac{Z_i - Z_o}{Z_i + Z_o} = \frac{\sqrt{\frac{\mu_r}{\epsilon_r}} - 1}{\sqrt{\frac{\mu_r}{\epsilon_r}} + 1} \quad \text{Equation 3.21}$$

$$T = \exp(-j\omega\sqrt{\mu\epsilon}d) = \exp(-j\frac{\omega}{c}\sqrt{\mu_r\epsilon_r}d) \quad \text{Equation 3.22}$$

where  $\omega$  is the angular frequency,  $c$  is the velocity of light in free space,  $\epsilon_r$  is the relative permittivity,  $\epsilon_o$  is the permittivity of free space,  $\mu_r$  is the relative permeability,  $\mu_o$  is the permeability of free space,  $d$  is the length of the sample material, and  $j$  represents  $\sqrt{-1}$

Measurements of  $S_{11}(w)$  and  $S_{21}(w)$  allow estimating reflection coefficient( $\Gamma$ ) and transmission coefficient (T), and later determining the complex permittivity  $\epsilon_r$  and permeability  $\mu_r$  as follow (Clement et al., 2006; Zwick et al., 2006; Agilent, 1985):

$$K = \frac{[S_{11}^2(w) - S_{21}^2(w)] + 1}{2S_{11}(w)} \quad \text{Equation 3.23}$$

where K is a dummy variable used to estimate the reflection coefficient from measured  $S_{11}(w)$  and  $S_{21}(w)$ . It must be greater than 1. K is related to  $\Gamma$  by:

$$\Gamma = K \pm \sqrt{K^2 - 1} \quad \text{Equation 3.24}$$

The sign of the square root in Equation 24 has to be chosen such that magnitude of  $\Gamma \leq 1$  (Zwick et al., 2006). The transmission coefficient is related to  $S_{11}(w)$ ,  $S_{21}(w)$ , and  $\Gamma$  by:

$$T = \frac{[S_{11}(w) + S_{21}(w)] - \Gamma}{1 - [S_{11}(w) + S_{21}(w)]\Gamma} \quad \text{Equation 3.25}$$

The reflection and transmission coefficient are related to  $\epsilon_r$  and  $\mu_r$  by:

$$\frac{\mu_r}{\epsilon_r} = \left( \frac{1 + \Gamma}{1 - \Gamma} \right)^2 \quad \text{Equation 3.26}$$

and

$$\mu_r \epsilon_r = - \left\{ \frac{c}{\omega d} \ln \left( \frac{1}{T} \right) \right\}^2 \quad \text{Equation 3.27}$$

After solving these equations simultaneously, we can obtain:

$$\mu_r = \left\{ \frac{1}{2\pi d} \ln \left( \frac{1}{T} \right) \right\} \left( \frac{1 + \Gamma}{1 - \Gamma} \right) \frac{1}{\sqrt{\frac{1}{\lambda(w)^2} - \frac{1}{\lambda_c^2}}} \quad \text{Equation 3.28}$$

and

$$\epsilon_r = \frac{\left( \left( \frac{1}{2\pi d} \ln \left( \frac{1}{T} \right) \right)^2 - \frac{1}{\lambda_c^2} \right) \lambda(w)^2}{\mu_r} \quad \text{Equation 3.29}$$

where  $\lambda_c(w)$  is the cutoff wavelength,  $\lambda(w)$  is the wavelength that is frequency dependent

and is related to frequency ( $f$ ) and velocity of light in free space ( $c$ ) by:

$$\lambda(w) = \frac{c}{f} \quad \text{Equation 3.30}$$

### 3.6.3 S-Parameters Measurements with a NA

Vector Network Analyzer (VNA) is used to generate and receive EM waves of certain frequency characteristics. The waves are transmitted through a coaxial cable to antennas designed to radiate and receive EM energy. Once EM energy is radiated, antennas receive reflected and transmitted components, which are related to the EM properties of the medium of interest. A Matlab Code was developed using Agilent (1985) experimental data. The real (Re) and imaginary (Im) permittivity ( $\epsilon_r$ ) and permeability ( $\mu_r$ ) values are used to estimate the transmission (T) and reflection ( $\Gamma$ ) coefficients through equations:

$$\mathbf{T} = e^{-j*2*\pi*f/c*\sqrt{(\mu_r\epsilon_r*d)}} \quad \text{Equation 3.31}$$

$$\Gamma = \frac{\mu_r * \left( \sqrt{\frac{1}{\lambda^2} - \frac{1}{\lambda_{cut}^2}} \right) - 1}{\left( \frac{1}{2} \pi * d * \log\left( \frac{1}{T} \right) \right)} \quad \text{Equation 3.32}$$

$$\frac{\mu_r * \left( \sqrt{\frac{1}{\lambda^2} - \frac{1}{\lambda_{cut}^2}} \right)}{\left( \frac{1}{2} \pi * d * \log\left( \frac{1}{T} \right) \right)} + 1$$

### 3.6.4 Validation Method

Permittivity and permeability properties for Teflon were measured in coaxial and waveguide sample holders according with test reported by Agilent, 1985. The measurements were made with the HP 8510 network analyzer system consisting of the HP 8510A network analyzer, the HP 8340A synthesized sweeper, the HP 8515A S-parameter test and an HP Model 9000 Series 200 computer. A full calibration port and

averaging were used to obtain a better accuracy and repeatability of data. The method developed in the previous section was applied to determine the dielectric properties of Teflon for validation purposes. The experimental data (Table 3.4) was used to test the code estimating the dielectric properties with S-parameters (Appendix 1).

Estimated real and imaginary permeability values for Teflon (Figure 3.16 and Figure 3.17) reflect non-magnetic properties of the material. The reported value for permittivity is 2.045 (Agilent, 1985). The estimated value using the approach explained in previous sections was 2.05 (Figure 3.18 and Figure 3.19), which compares well with reported values. See Appendix 1 for details of the code.

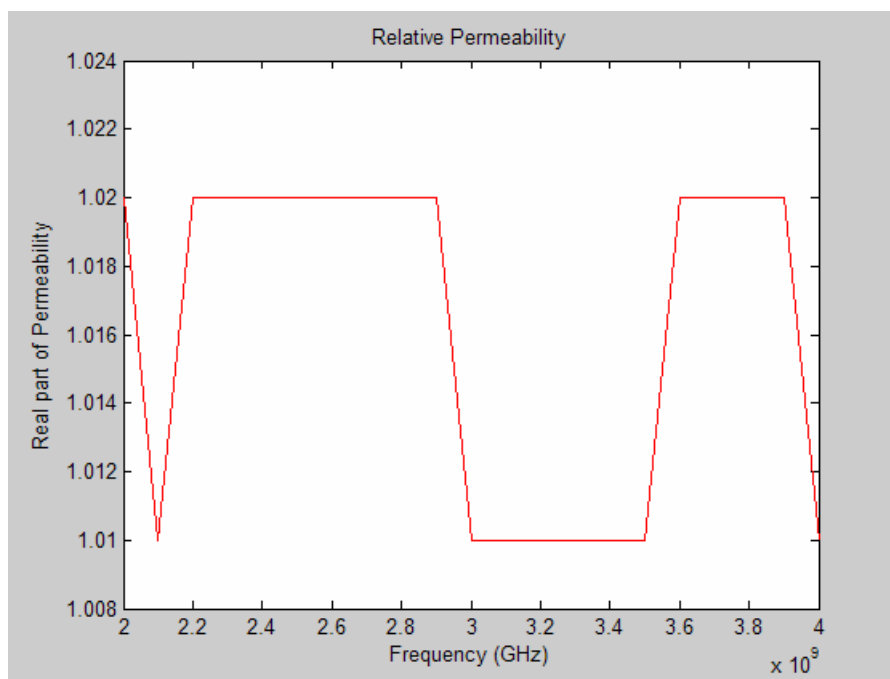
### 3.6.5 SoilBed Method

The 2D SoilBed tank works as a waveguide with two metal meshes that create perfect reflection. Scattering parameters were generated with HP 8714ET network analyzer and with an 87050E multiport test set, and data was stored in a conventional computer. After testing several antennas, (see chapter 4) loop antenna (24turns) were used. Full calibration port and averaging were used to obtain a better accuracy and repeatability of data. Once the S-parameters are determined, the code in Appendix 1 is used to estimate dielectric properties.

**Table 3.4 Teflon measurement dielectric properties**

Freq (Hz)	$\overline{\text{Re}(\epsilon_r)}$	$\overline{\text{Im}(\epsilon_r)}$	$\text{Re}(\mu_r)$	$\text{Im}(\mu_r)$
2.00E+09	2.05	0.026	1.02	0.018
2.10E+09	2.05	0.025	1.01	0.016
2.20E+09	2.05	0.027	1.02	0.016
2.30E+09	2.05	0.024	1.02	0.017
2.40E+09	2.04	0.023	1.02	0.018
2.50E+09	2.04	0.021	1.02	0.02
2.60E+09	2.04	0.019	1.02	0.022
2.70E+09	2.05	0.017	1.02	0.021
2.80E+09	2.05	0.017	1.02	0.023
2.90E+09	2.06	0.022	1.02	0.028
3.00E+09	2.05	0.017	1.01	0.021
3.10E+09	2.05	0.021	1.01	0.017
3.20E+09	2.05	0.023	1.01	0.016
3.30E+09	2.05	0.027	1.01	0.011
3.40E+09	2.04	0.027	1.01	0.011
3.50E+09	2.04	0.03	1.01	0.009
3.60E+09	2.04	0.026	1.02	0.013
3.70E+09	2.03	0.024	1.02	0.013
3.80E+09	2.03	0.019	1.02	0.018
3.90E+09	2.03	0.017	1.02	0.019
4.00E+09	2.03	0.012	1.01	0.023

Source: Agilent, 1985.

**Figure 3.16 Real part of permeability for Teflon**

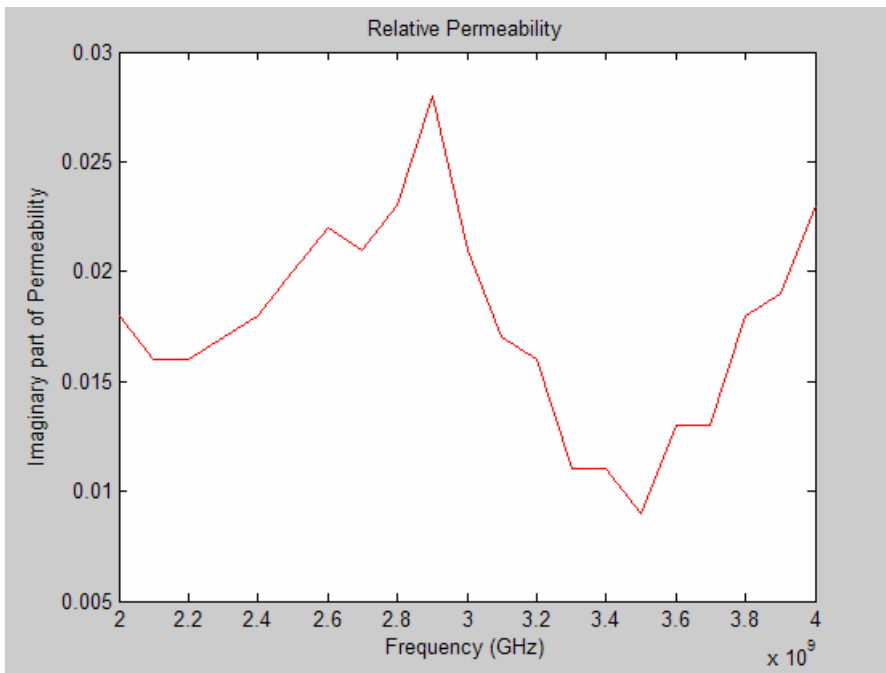


**Figure 3.17 Imaginary part of permeability for Teflon**

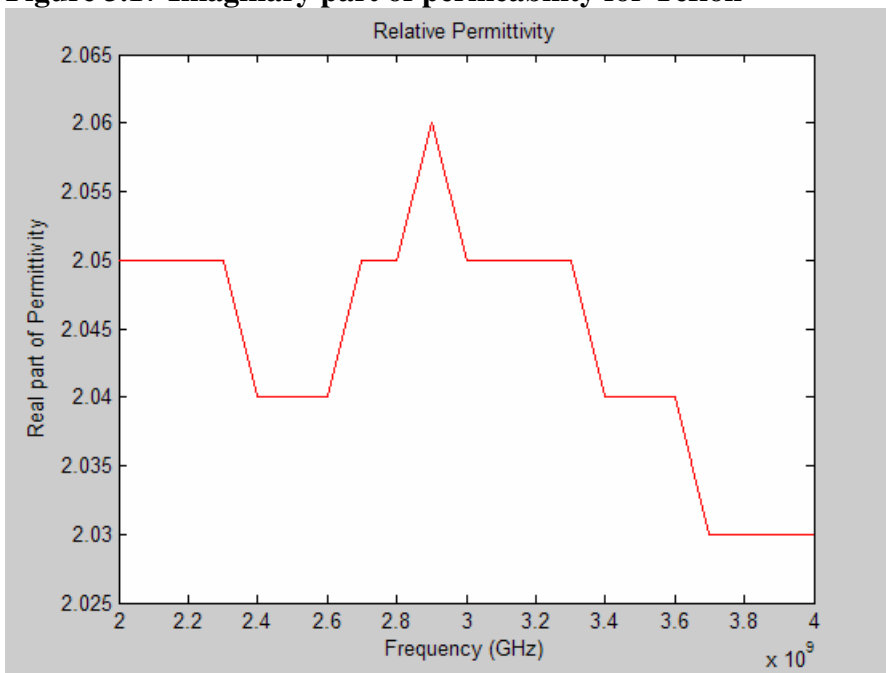


**Figure 3.18 Real part of permittivity for Teflon**

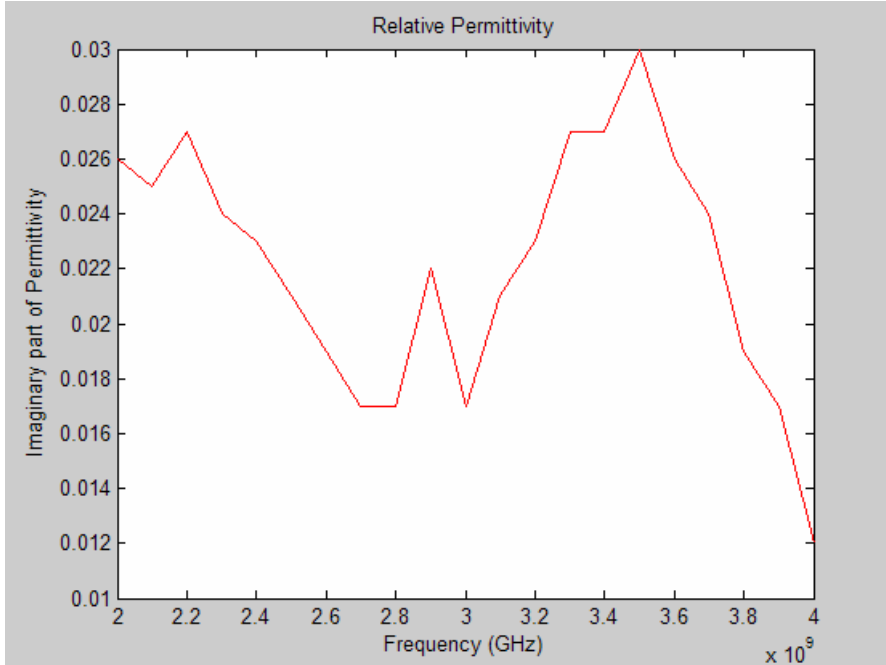


**Figure 3.19** Imaginary part or relative permittivity for Teflon

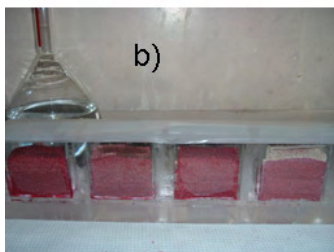
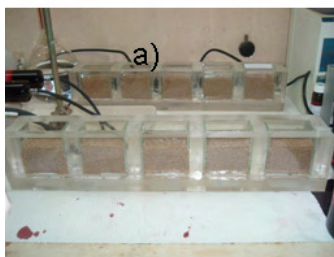
### 3.7 DIGITAL VISUALIZATION AND IMAGE ANALYSIS

Image acquisition, visualization, and analysis were applied concurrently with CWR techniques to evaluate and validate the CWR technologies for detection and monitoring of DNAPL contamination in underground environments and characterize DNAPL transport processes. It involved taking digital images of the soil beds with a chromatic digital camera with focal lenses (Sony XCD-X710CR). The camera was interfaced to a computer, which was used to manage the image acquisition and storage process. The camera (Figure 3.20) was mounted on a stainless steel tripod and placed and aligned through a focal aperture in the front wall of the studio-like room for focal view of the targeted element (e.g., soil beds, calibration cells) inside the room.



**Figure 3.20** Wall opening for the camera zoom

Proper image analysis required appropriate illumination patterns. These were attained by providing dark reflectless background and fluorescent lighting and fluorescent lighting with 40W lamps above and across the targeted element (Figure 3.21). Digital images were taken prior and during the injection and movement of Sudan IV-dyed TCE and/or water. Acquired images included a white standard required for illumination corrections. Images taken prior to injection of the fluids were used to establish a contrasting background to which later images would be compared to.



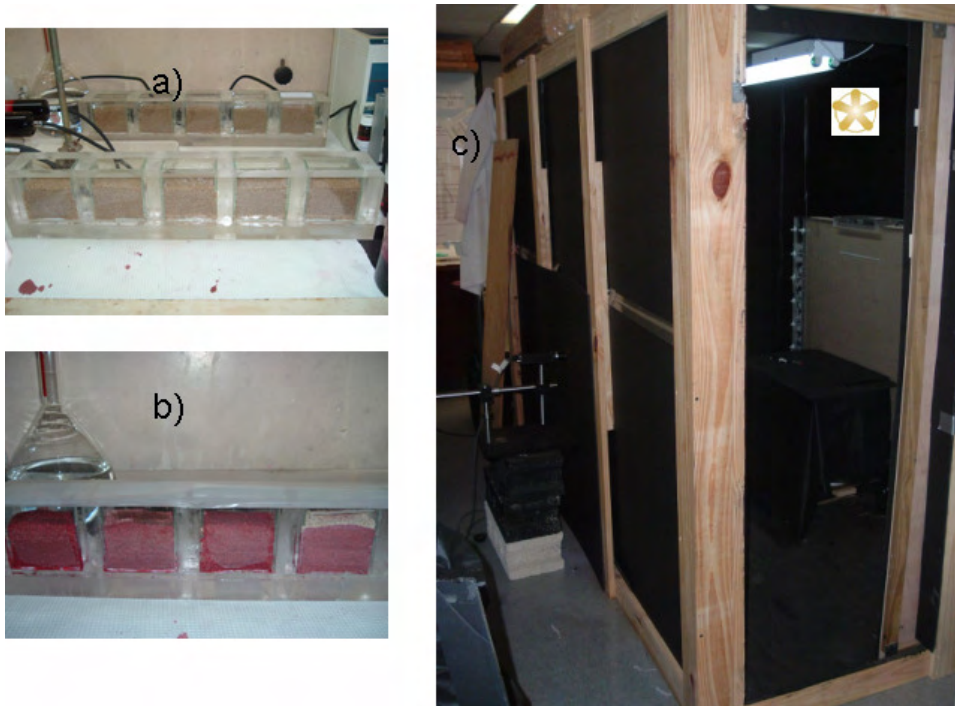
**Figure 3.21** Image acquisition and analysis system a) calibration soil cells, b) stained soil cells, and c) studio room

Image acquisition was controlled through a code developed (Appendix 3) using Matlab's Image Acquisition Toolbox. The image acquisition code was used to operate the camera, and capture and transfer the images to a computer. It considered a time-lapse effect during the acquisition velocities. The first phase was used during the injection period, which is usually the faster. The second phase was used after the injection period to monitor the 2D fluid flow. The time was adjusted according to the geometry of the targeted elements being imaged.

Image processing was done using MatLab's Image Processing Toolbox. Image analysis was conducted using a code developed in Matlab (Appendix 4) to process images of the soil without and with dyed DNAPL. The code compares pixel intensities between the initial condition before the injection of the dyed DNAPL and the condition at given times after the onset of the DNAPL injection, estimates the percent change in pixel intensities, and develops a processed image. The percent change is the difference between the initial and final conditions at a given time. The processed image is developed according to a percent-change scale, where specific pixel values are assigned to areas within predetermined percent changes: a pixel value of zero (0) is assigned to areas with less than 10% change; 85 to areas with percent changes between 10 and 20%; 120 to areas with percent changes between 20 and 50%; and 255 to areas with percent changes greater than 50%.

In order to determine the mass of DNAPL located at a particular point and space in the soil system from image analysis, it's necessary to relate pixel intensity statistics to

DNAPL mass in the system. A calibration procedure was developed by which images were taken before and after the injection of known volumes and concentrations of dyed liquids into soil calibration cells (Figure 3.22 a and b). The cells were made of the same material and packed with the same sand as the 2D soilBed. The calibration soil cells consisted of a small Plexiglas tank with five divisions lined with glass sheets: each division having dimensions of 7.62 cm \* 7.62 cm \* 1.5 cm.



**Figure 3.22 Image acquisition and analysis system a) calibration soil cells, b) stained soil cells, and c) studio room**

The calibration procedure consisted of injecting a given DNAPL volume while taking digital images. Volumes of 10, 20, 25, 35 and 40 ml were injected for sudan IV concentration of 10, 15, 20, 25, and 30 percent by weight (g/g). The known mass of dye-TCE injected was used for producing a calibration relating TCE mass and pixel intensity.

## **4. TWO-DIMENSIONAL DETECTION OF UNDERGROUND CONTAMINATION AND BURIED OBJECTS USING CROSS-WELL RADAR**

### **4.1 ABSTRACT**

Traditional approaches for locating and characterizing contaminated sites rely on invasive techniques which require drilling, testing, and sampling. These techniques provide the most direct access to the subsurface, but they are generally expensive and only provide measurements at points in a three dimensional surface. Furthermore, invasive techniques in polluted areas can promote further spread of contaminants. Development of non-invasive techniques that offer rapid and relatively inexpensive characterization is, therefore, necessary to detect and monitor plumes and sources of contaminants. Non-invasive techniques are also required for locating buried objects, such as landmines and unexploded ordnances.

The use of cross well radar (CWR) as a non-invasive technique that has proven to be a reliable technology for detection of target objects that exhibit significant contrast of dielectric properties in saturated soils. Its application to detection of heterogeneously distributed phases in unsaturated soils under variable flow conditions has yet to be developed.

This chapter addresses the development of a 2D flow and electromagnetic (EM) soilBed setup to further assess and enhance CWR technology for the detection of Dense Non-Aqueous Phase Liquids (DNAPLs) contamination and other target elements in variably-saturated soils subjected to transient flow conditions. Loop antennas have been developed and tested for this purpose. Transmission and reflection measurements are evaluated to determine the antenna's reliability and optimize their performance in the 2D electromagnetic field. The measurements indicate that a 2D EM boundary condition may be imposed by placing two parallel perfectly-reflecting metal plates along one of the dimensions of the soilBed setup. Transmission and reflection characteristics of the antennas vary with their method of construction. Results show a reliable and reproducible response from the loop antennas, but suggest some wave leakage and indicate that their design must be optimized.

Measured variations in the transmission and reflection in the presence and absence of a buried object suggest that the 2D EM soilBed setup using loop antennas can be applied to detect target elements in subsurface environments subjected to flow conditions. Future work addresses the assessment of CWR technology as a non-invasive method for detection and monitoring of heterogeneously-distributed target objects in subsurface environments.

## **4.2 INTRODUCTION**

Contamination of soils and groundwater by accidental spills, poor storage facilities and inadequate disposal practices causes serious detriment of the environment and can pose a

serious threat to human health. Common contaminants found in underground environments include many Dense Non-Aqueous Phase Liquids (DNAPLs), which are of great concerns because of their heterogeneous distribution and long-term perseverance in the environment. DNAPLs travel as dissolved solute, vapors, and immiscible liquids depending on the chemical properties, total mass present in the system, and soil and environmental conditions. While migrating as immiscible liquids, they are entrapped in different pores resulting in a heterogeneous distribution (Guilbeault et al., 2005). DNAPL contamination is therefore difficult to locate, characterize, and remediate (NRC, 2000a).

Traditional approaches for locating and characterizing contaminated sites rely on invasive techniques, which require drilling, testing, and sampling. While these techniques provide the most direct access to the subsurface, they are generally expensive and only provide measurements at points in a three dimensional surface (NRC, 2000b). Furthermore, invasive techniques in polluted areas can promote further spread of contaminants. Development of non-invasive techniques that offer rapid and relatively inexpensive characterization is, therefore, necessary to detect and monitor plumes and sources of contaminants. Non-invasive techniques are also required for locating buried objects, such as landmines and unexploded ordnances.

Non-invasive methods involve little or no disruption of surface materials, but they yield indirect measurements of site characteristics based on the response to artificial or natural stimuli (NRC, 2000b). This response must be interpreted in order be able to infer the characteristics (e.g., chemical constituency, porosity, structural features) of contaminated

sites. A large suite of non-invasive methods can be used for site characterization. The capacity of these methods to resolve contaminant characterization is, however limited. Although non-invasive techniques such as electromagnetic and acoustic methods offer rapid and relatively inexpensive characterization, they may suffer from lack of resolution and specificity (NRC, 2000b).

Cross well radar (CWR) is a relatively new technology that can serve as a non-invasive method with minimal soil disruption (Farid, 2004). It involves placing antennas into distant boreholes and emitting radar waves from the transmitting antennas in one borehole, through the soil, to the receiving antennas in other locations. The propagation characteristics of the waves depend on the materials present under the ground surface (e.g., soil, water, air, NAPL, landmines). Because the electromagnetic properties of air, water, DNAPLs, and other objects differ significantly from each other, their presence causes differences in the wave propagation properties in the soil (Farid et al., 2003b).

The propagation of the electromagnetic waves in subsurface environment can be assessed by measuring wave transmission, reflection and attenuation characteristics of the media. These characteristics depend on complex dielectric properties (i.e., dielectric permittivity) of the soil (Dong-Ho and Li, 2001; Sarabandi et al., 1988; Hallikainen et al. 1985; Hoekstra and Delaney, 1974) and vary with soil type, moisture content, temperature (Antonyk et al., 2004), and the presence of other fluid and objects. Dielectric permittivity of soil may be characterized through the use of reflection and transmission coefficients measured with CWR antennas. The values of these coefficients depend on

the frequency range of the electromagnetic field (Lambot et al., 2006; Lambot et al., 2004 a and b).

Proper measurements of reflection and transmission coefficients require accurate radiation characteristics of the antennas. These characteristics, however, depend on the type and assembly of the antenna and it is necessary to evaluate and validate their behavior in the soil. This behavior can be analyzed with the use of decibel (dB) versus frequency response data (Farid et al., 2003a; Lacko et al., 2003). Once characterized, antenna transmission and reflection responses can be analyzed in the absence and presence of target elements (e.g., DNAPL, landmines) to evaluate the contrast in dielectric properties.

This work addresses the development of a two dimensional (2D) flow and electromagnetic setup to further assess and enhance the CWR technology for the detection of DNAPL contamination and other target elements in soil. Because of the complexities associated with DNAPL flow and electromagnetic field in a spatially-constrained environment, it is necessary to determine the type, configuration, and arrangement of antennas and boundary conditions in the soilBed that will effectively serve for this detection. The feasibility of using loop antennas to measure reflection and transmission response in the absence and presence of objects in a dry soil is evaluated.

## 4.3 MATERIALS AND METHODS

### 4.3.1 *SoilBed Experimental Setup*

The use of CWR technology to detect underground DNAPLs is tested and validated using a laboratory-scale 2D soilBed setup, which minimize the generation of DNAPL contaminated soil and establish a controlled flow system. For a 2D electromagnetic field and DNAPL flow system, two perfectly reflecting plates (Figure 4.1) must be incorporated in the soilBed perpendicular to the transmitting signal but parallel to water and DNAPL flow lines. Metal mesh plates can create a 2D permanent electromagnetic field of perfect reflection, while maintaining 2D flow in the system.

The soilBed design (Figure 4.1) consists of a Plexiglass tank with a length and height of 100 cm each and a width of 7 cm. Plexiglass is used because allows for visual validation of dyed DNAPL distribution. It is warned, however, that for TCE the Plexiglas must be lined with glass sheets in the interior to avoid reaction with Plexiglass walls. The tank incorporates lateral compartments which allow the establishment of constant-head flow boundary conditions in the soil tank.

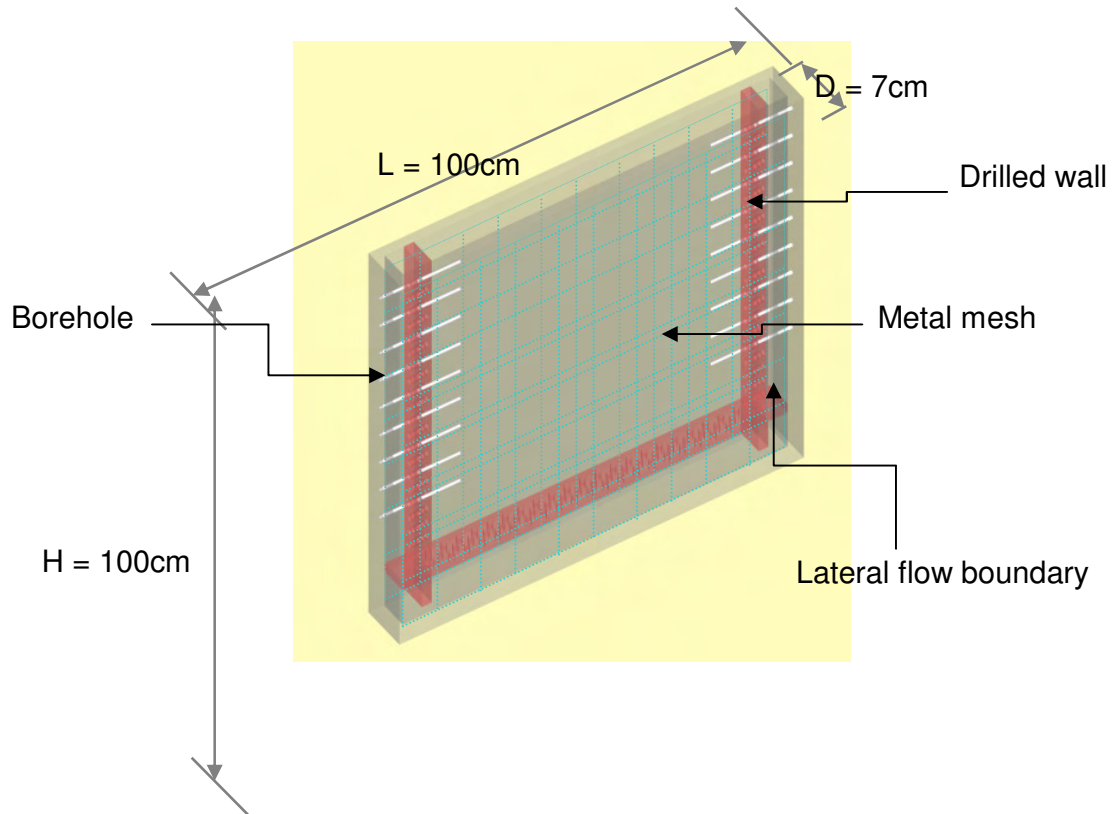


**Figure 4.1 Two-Dimensional flow setup**

The soilBed incorporates two vertical metal meshes centered in the tank and placed 2.2 cm apart. The proposed separation in the mesh had been calculated as half the minimum wavelength ( $\lambda_{min}$ ) with the equation:

$$\lambda_{min} = \frac{c}{\sqrt{\epsilon_r} f_{max}}$$

**Equation 4.1**

where  $c$  is the velocity of light,  $\epsilon_r$  is the dielectric relative permittivity of the media and  $f_{max}$  is the maximum wave frequency. A  $f_{max}$  of 1.5 GHz and a permittivity of 20, which is typical of saturated sand (Farid, 2004), is used to estimate the minimum distance required.

Antennas are inserted into the soil through horizontal boreholes lined located in the lateral panels of the tank and in between the metal plates. The boreholes are lined with

plastic ( $13.53 \pm 0.1$  mm O.D.,  $9.40 \pm 0.1$  mm I.D.) to protect the antennas from soil smearing and water. The plastic casing does not affect the signal, and keep the antennas aligned. Because this casing permits repeatable insertion of the antenna, it enhances the opportunity for experimental reproducibility. Each lateral panel holds 10 boreholes with 5 cm spacing, starting at 20 cm from the bottom of the soil tank.

SoilBed prototypes built in Plexiglass have been used to evaluate the effect of boundary conditions and antenna locations on the transmission and reflection measurement. These prototypes are scalable models of the developed 2D flow soilBed.

#### *4.3.2 Measurements of Antenna Characteristics*

Preliminary tests of different antennas suggest that loop antennas are the most appropriate for the 2D systems because of the constraints in the minimum wavelength size and electromagnetic field orientation for 2D electromagnetic conditions. The loop antennas are built using electrical cable, ferrite beads, and small miniature adapters (SMA) connector (Pasternack Enterprises, LLC, PE 4115). Ferrites beads are used to avoid antenna deflection during installation and minimize effects in transmission and reflection measurements. In each one of the antennas, the small loop antenna is welded to the center conductor ( $I_{cc}$ , Figure 4.2) and an outer shield (Figure 4.2).

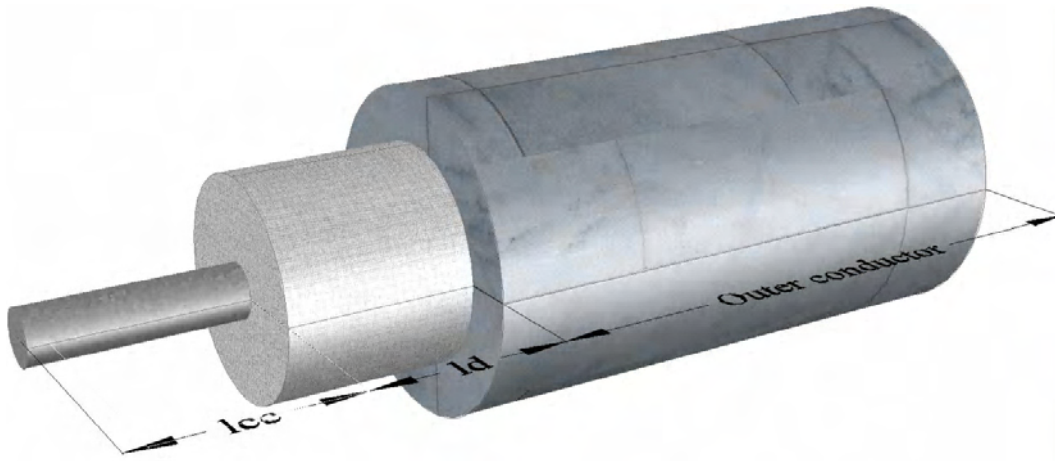


**Figure 4.2 Description of coaxial cable**

Four types of antennas (A, B, C and D) were tested in sandy soil under dry conditions in the 2D prototype setups (Figure 4.3). The antennas were constructed as follows:

- Antenna A: loop antenna with 8 turns in the helicoidal ferrite material. The center conductor is exposed 25.4 mm and covered with a shrink tubing to prevent energy leaks.
- Antenna B: loop antenna with 8 turns in the helicoidal ferrite material. The center conductor is exposed 25.4 mm and covered with electrical tape to prevent energy leaks.
- Antenna C: loop antenna with 16 turns in the helicoidal ferrite material. The center conductor is exposed 25.4 mm, and covered with electrical tape to prevent energy leaks.
- Antenna D: loop antenna with 8 turns in the helicoidal ferrite material. The dielectric ( $l_d$ , Figure 4.2) is exposed 10 mm and center conductor is exposed 5mm.

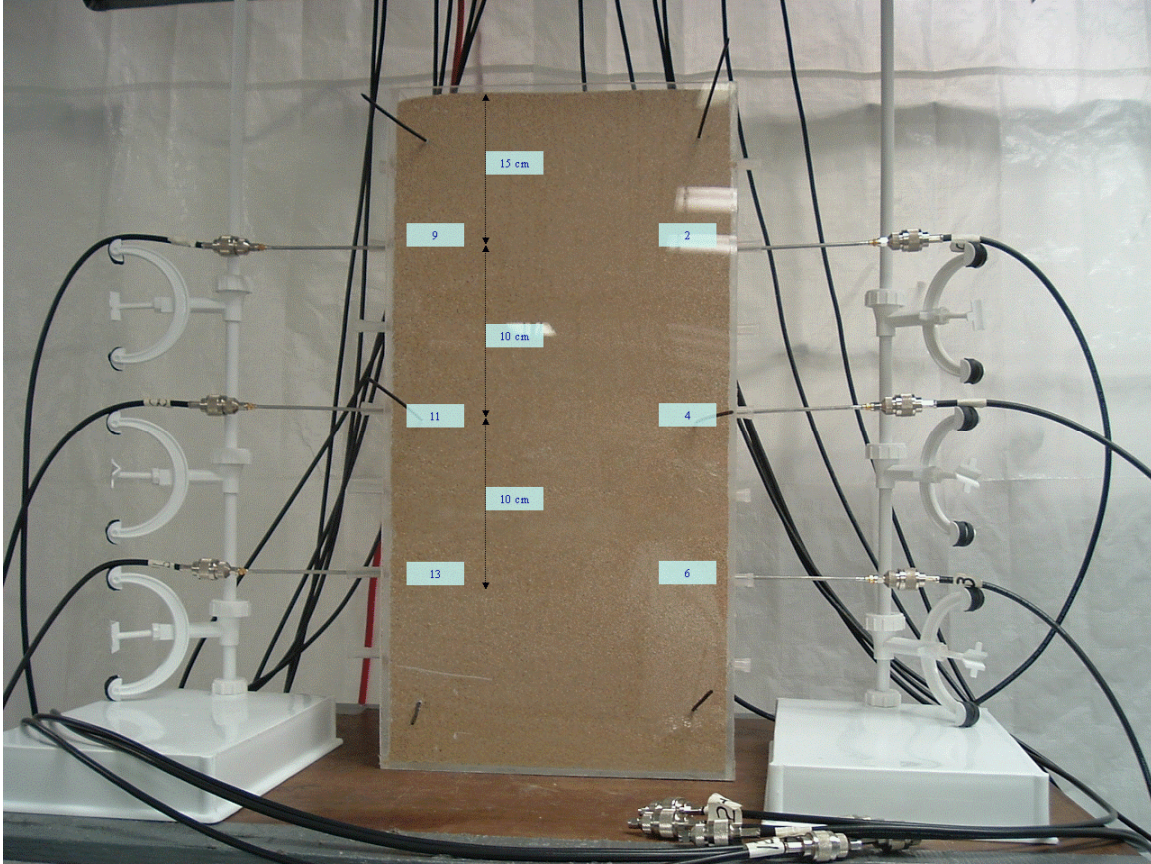


**Figure 4.3 Location of antennas in a 2D soilBed setup (ID 3, Table 3.2)**

#### *4.3.3 Antenna Response Testing*

The responses of the antennas are tested by placing antennas at different borehole port locations (Figure 4.3) in the soilBeds, and evaluating the transmission and reflection measurements (Agilent, 1997). These measurements are given by the notation  $S_{RS}$ , in which R and S refers to the antenna receiving and sending the signal, respectively. Reflection measurements ( $S_{11}$  and  $S_{22}$ ) reflect the response of the same antenna that is sending (transmitting) the signal. Transmission measurements ( $S_{21}$  and  $S_{12}$ ) reflect the response of one antenna to the signal sent (transmitted) by another antenna, thus require two antennas. The measurement response is often presented in decibel (dB), which is

defined as the logarithmic ratio of the received or transmitted signal voltage to the incident signal voltage. For reflection measurements, this logarithmic term is expressed as the return loss (RL) (Agilent, 2007):

$$RL = -20 \log \left( \frac{V_{reflected}}{V_{incident}} \right) \quad \text{Equation 4.2}$$

It represents the number of decibels that the reflected signal is below the incident signal. It is always a positive number, which varies between infinity (infinite reflection) and zero (no reflection). For transmission measurements the logarithmic term is expressed as the attenuation or insertion loss (IL):

$$IL = -20 \log \left( \frac{V_{transmitted}}{V_{incident}} \right) \quad \text{Equation 4.1}$$

Ranges of return and insertion losses are not directly reported in the literature. Return losses should be greater than zero so that some incident voltage is transmitted through the medium being evaluated. Farid (2004) considered RL values above 4 as acceptable. Insertion losses, on the other hand, should be above the noise level of the instrument. This level is about 60 dB for our instrument. Farid (2004) considered IL values between 20 and 60 to be within an acceptable range. The instrument and values reported by Farid (2004) were used for the initial assessment of antenna types (Chapter 3).

The responses of the antennas were evaluated for different types of antennas, effect of external boundaries, and presence of acrylic objects. The effect of antenna types on the transmission and reflection responses were evaluated in soilBed number 3 (Table 3.2) with imbedded parallel mesh plates. The influence of external boundaries on the

response of the antennas was assessed by measuring transmission and reflection characteristics with and without placement of solid metal plates on the external walls of soilBed number 1 (Table 3.2) having imbedded parallel metal mesh plates. Antenna response in the presence of a target element (plexiglass bar) was compared to the response without it (soilBed number 3, Table 3.2). For this test, plexiglass bar (1.5 cm wide, 0.10 cm thick) was inserted 30 cm below the soil surface at the horizontal center of the tank. Signal management and analysis were performed using a Multivector Analyzer (Agilent, Model 8714ET).

## **4.4 EXPERIMENTAL RESULTS**

### *4.4.1 Transmission and Reflection Measurements*

Transmission (Figure 4.4 to Figure 4.5) and reflection (Figure 4.6 to Figure 4.7) measurement show that the response from the loop antenna varies depending on their construction. The transmission of data in most antennas falls above 60 dB for a frequency range between 800 and 1500 MHz. These results indicate that the data is within acceptable noise limits for the network analyzer used. The range of values obtained, however, suggest some wave leakage around the antennas. Transmission measurements for the  $S_{49}$  antennas (Figure 4.5) fall closer to noise level than those for the  $S_{29}$  antennas (Figure 4.4). That is explained by the greater separation distance between transmitting and receiving antennas. As the wave propagates to greater distance, there are greater reflection/transmission energy losses caused by soil heterogeneities in the dry

sand. Greater absorption energy losses, however, may result in greater overall transmission losses for saturated conditions.

Comparison of the transmission response measured for different types of antennas in the same location (Figure 4.3) indicate that the transmission characteristics of the antennas are very sensitive to their method of construction (Figure 4.4 and Figure 4.5). Above 800MHz, antenna A, covered with heat shrink tube shows the greatest insertion losses, whereas antenna C (16-loop) shows the least up to 1400MHz. Better transmission response of antenna C in this frequency range suggests a potential for improving detection capabilities with antennas having higher number of loops.

The reflection data shows similar trends with respect to frequency, for all antenna types except for antenna C. For frequencies above 800MHz, return losses increase with increasing frequency up to 1400MHz. Above this frequency, return losses tend to decrease with increasing frequency. Antenna C, however, shows large reflection fluctuations across frequencies, indicating unstable behavior with respect to frequency. Greater return losses are observed with the 8-loop antenna with partly exposed dielectric and center conductor (antenna D). Lower return losses are observed for the 8-loop antenna with greater exposure of the center conductor, covered dielectric, and electric tape as wrapping material (Antenna B). The lower return losses of antenna B and greater variability of antenna C may be indicative of “wave leakage”. Because of the higher return losses observed for antenna D, this antenna was selected for further testing of response reliability, effects of external boundaries, and target element detection.

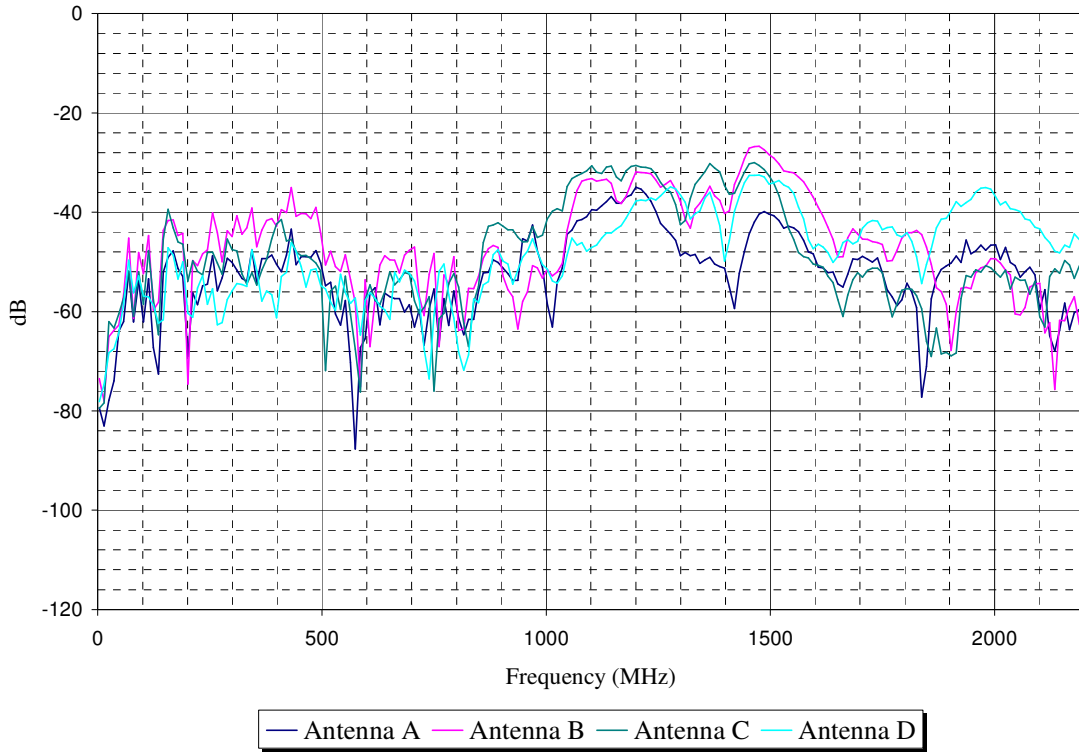


Figure 4.4 Transmission response  $S_{29}$  at the setup (ID 3, Table 3.2)

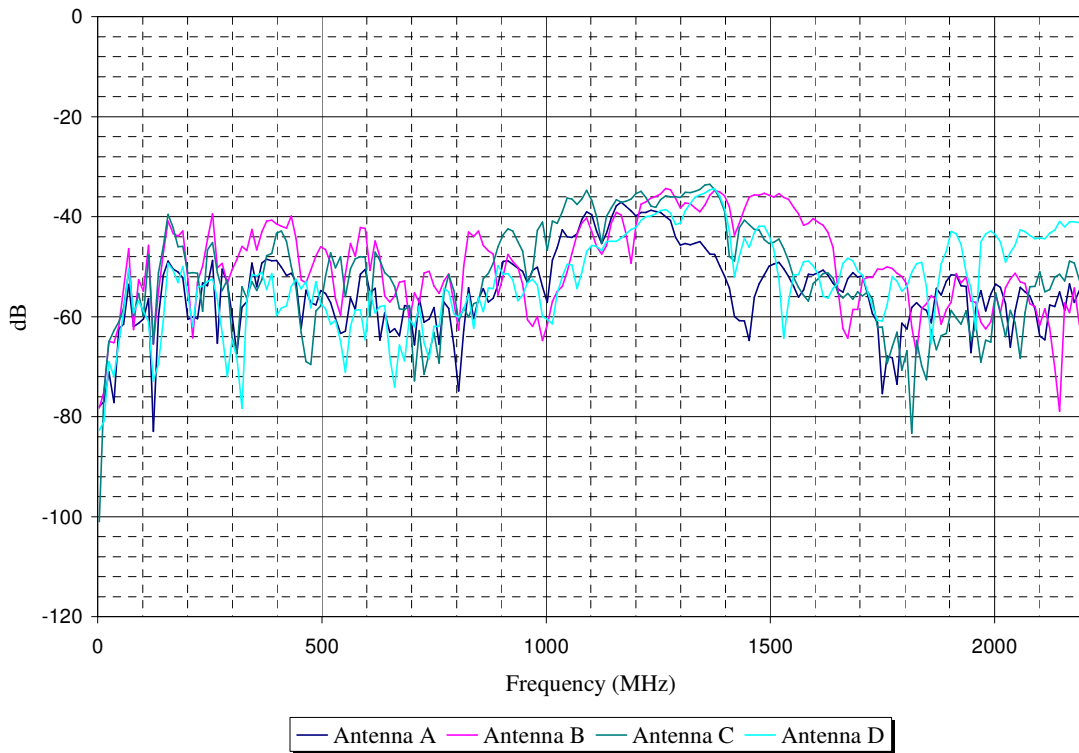
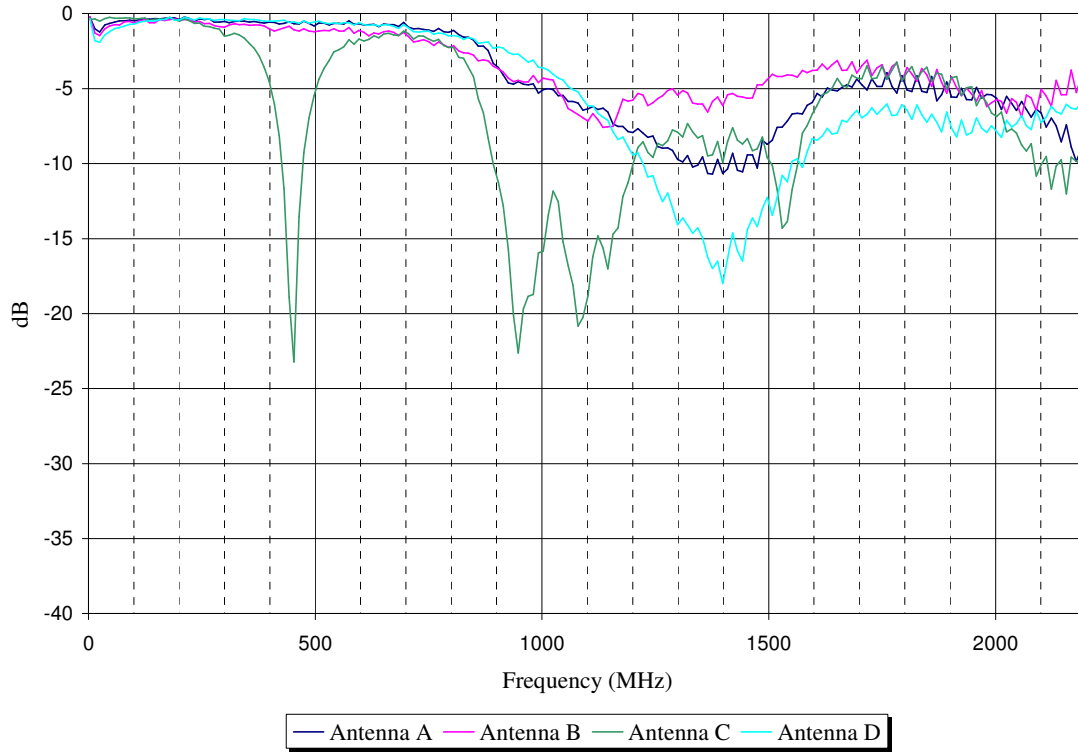
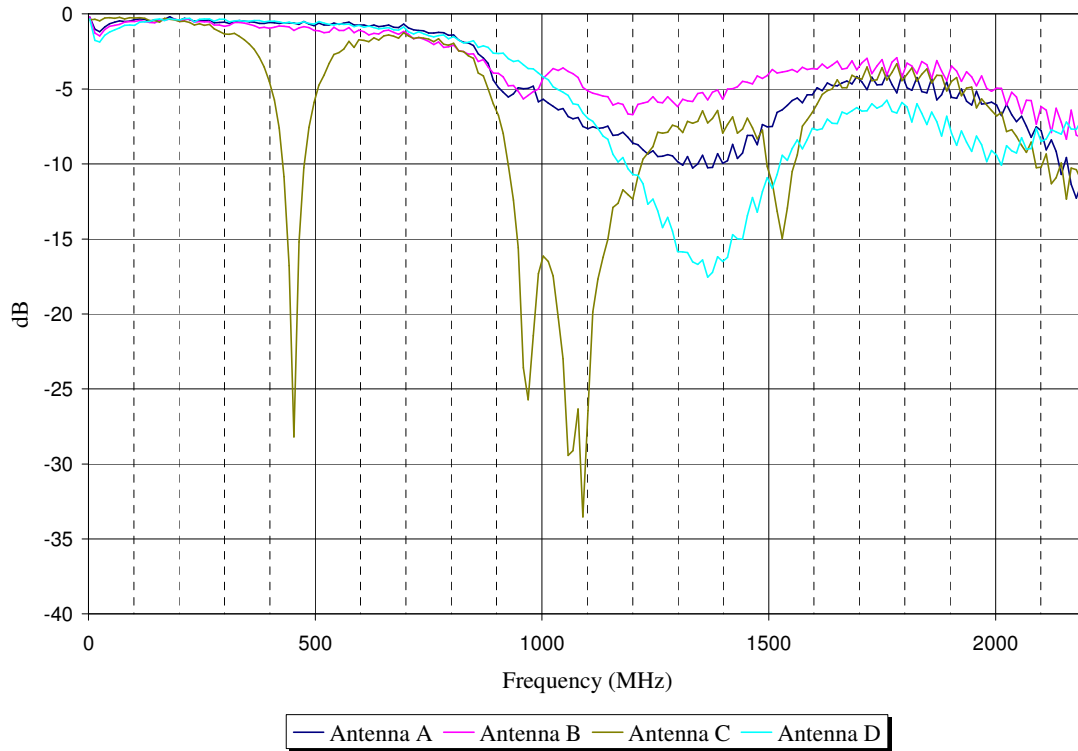


Figure 4.5 Transmission response  $S_{49}$  for antennas at the setup (ID 3, Table 3.2)



**Figure 4.6 Reflection response at borehole 9 when receiving is at borehole 2**



**Figure 4.7 Reflection response at borehole 9 when receiving antenna is at borehole 4**

#### *4.4.2 Data Reliability*

The ability of collecting reproducible data is really important to enhance CWR as a detection technique. The EM measurements have to be valid, reproducible and repeatable. That involves the development of reliable and scalable laboratory measurements. As a general CWR test procedure, transmitting and receiving antennas are placed in the soil at borehole locations (Figure 4.3) and EM measurements are then collected and stored.

Figure 4.8 shows the transmission response of antenna 2 (Figure 4.3, borehole 4) when antenna 1 (Figure 4.3, borehole 9) was transmitting ( $S_{21}$ ), and viceversa ( $S_{12}$ ). The results show response above 60dB for frequencies above 800MHz. Transmission measurement of antenna pairs ( $S_{21}$ : Transmitter 1 and Receiver 2) are, therefore, considered reliable. All other antennas pair measurements show similar results.

#### *4.4.3 Boundary effect in Transmission Response*

Transmission (Figure 4.9) and reflection (Figure 4.10 and Figure 4.12) measurement taken with and without a metal plate on the top of the 2D soilBed prototype (Figure 4.3) indicates that external boundaries do not affect the antenna response significantly. These results suggest that the boundaries are sufficiently distant from the measurement points.

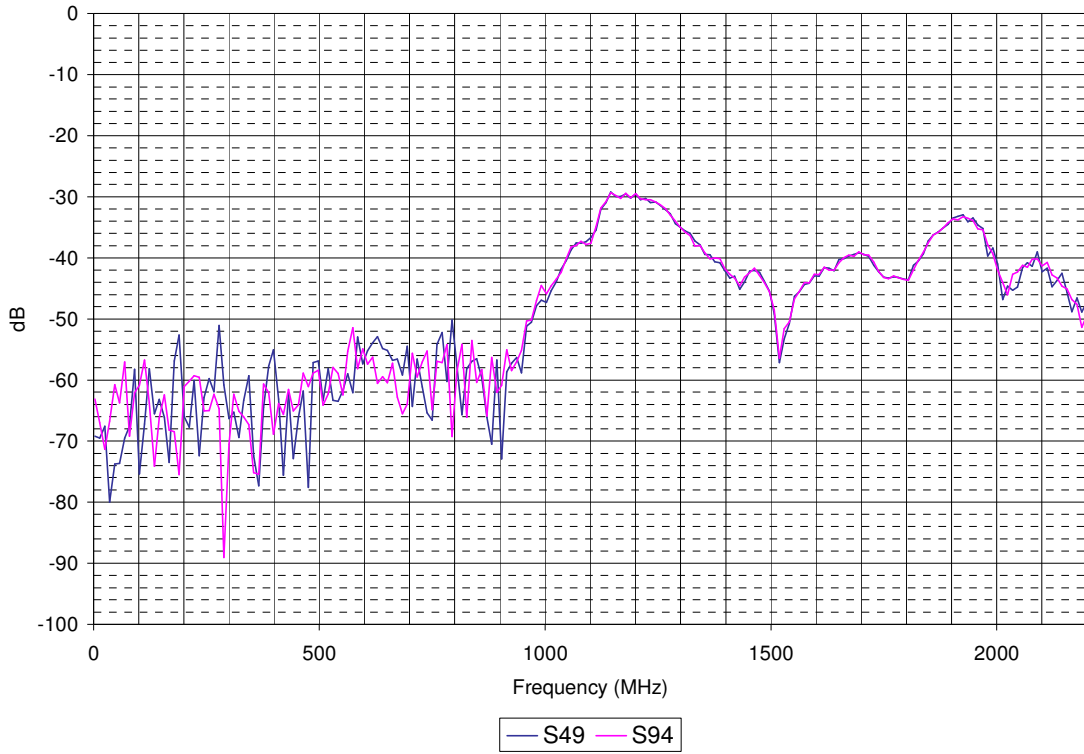


Figure 4.8 Transmission response for antennas borehole 9 and 4 (ID 3, Table 3.2)

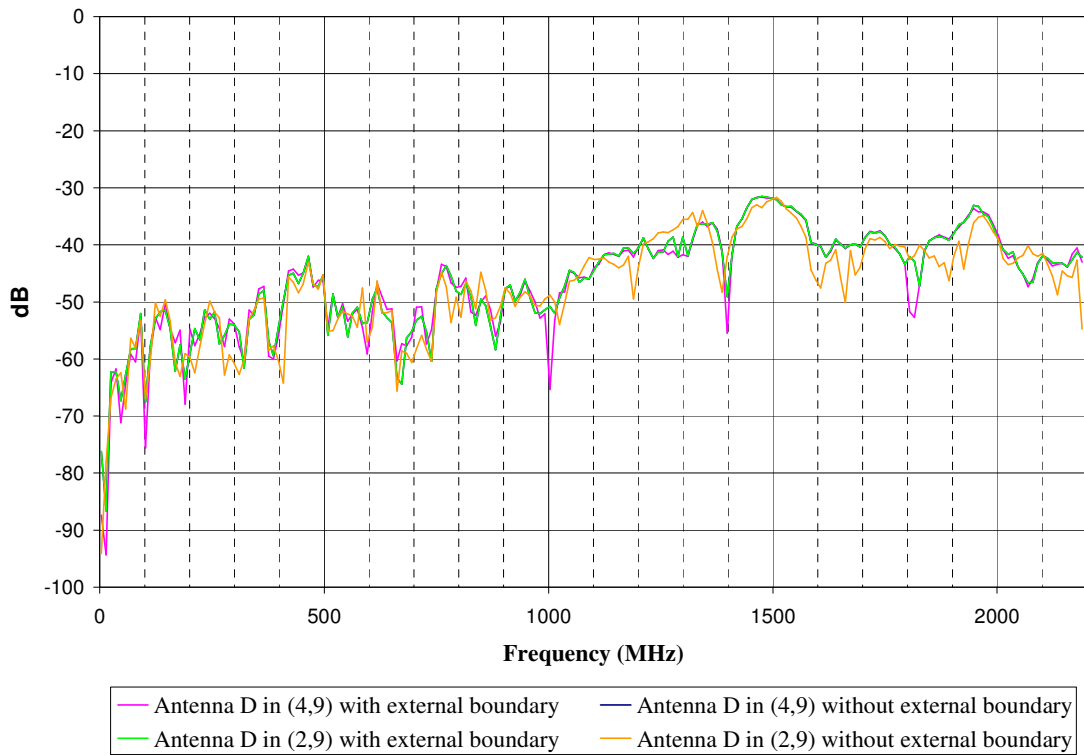
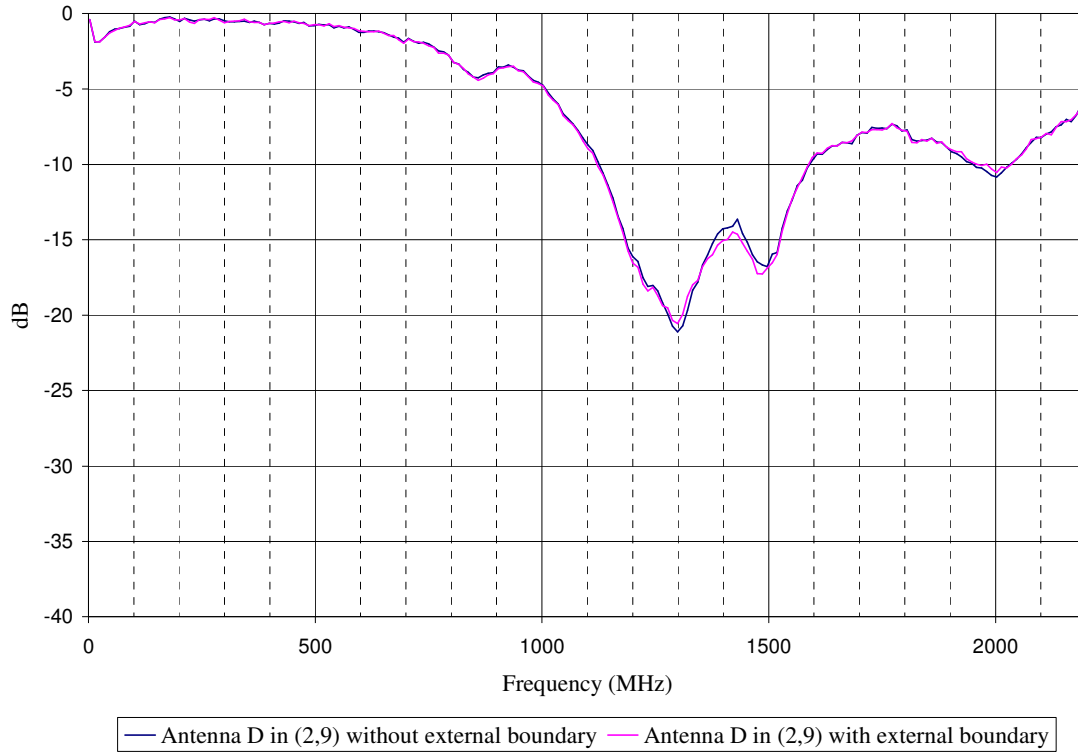
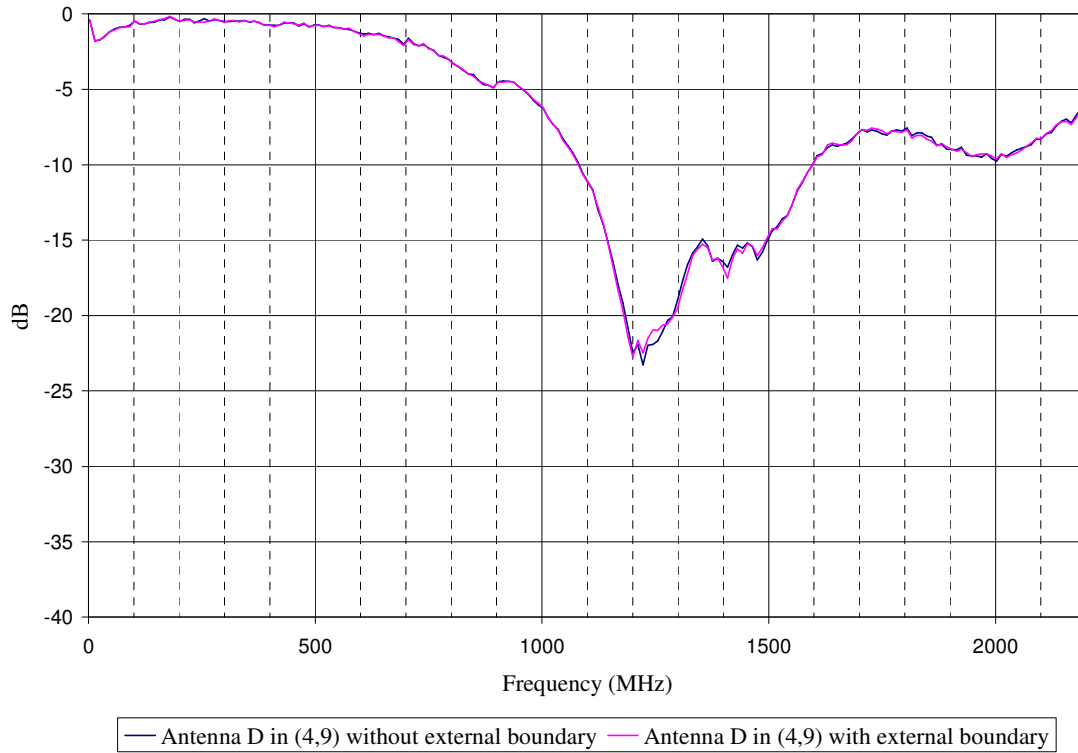


Figure 4.9 Transmission response  $S_{49}$  and  $S_{29}$  (ID 3, Table 3.2)



**Figure 4.10 Reflection measurement  $S_{29}$**



**Figure 4.11 Reflection measurement  $S_{49}$**

#### 4.4.4 Variations in Transmission and Reflection Measurements in Presence of Objects

Comparison of transmission (Figure 4.12) and reflection (Figure 4.13) measurements in the absence and presence of a target element (acrylic bar) indicates that the presence of the object in the soil causes a slight disturbance in the electrical properties. In the presence of an acrylic object, measurements are above the noise level frequencies higher than 1000MHz. The presence of the objects resulted in similar insertion losses as in its absence, but with a smoother response with respect to frequency

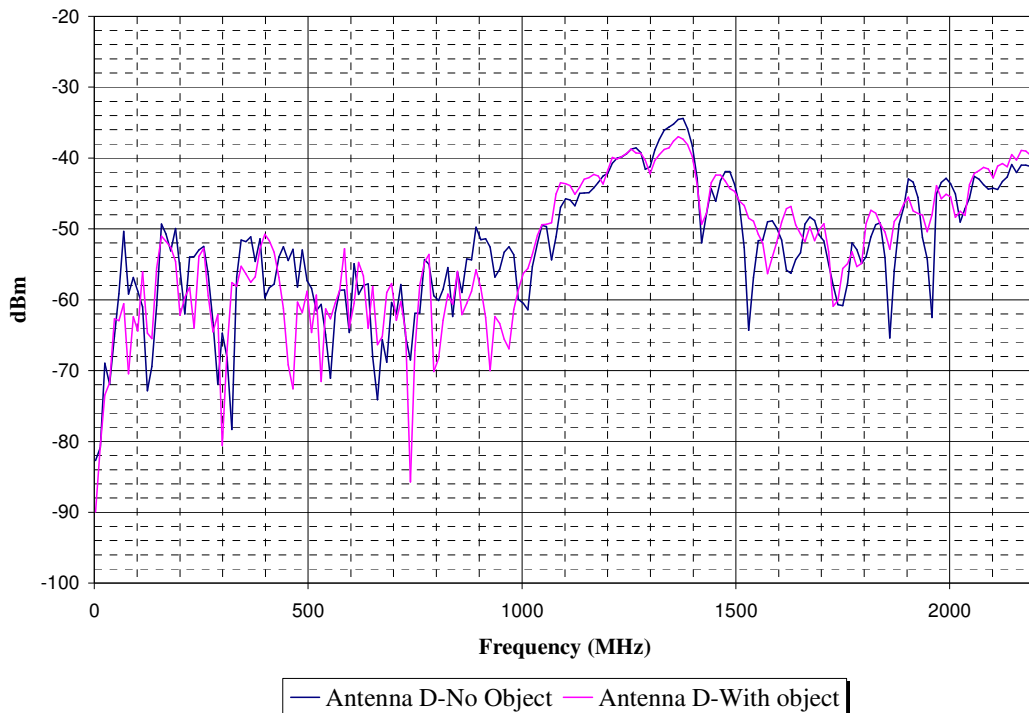


**Figure 4.12 Comparison of transmission measurement  $S_{49}$  without and with an object inside the soil**

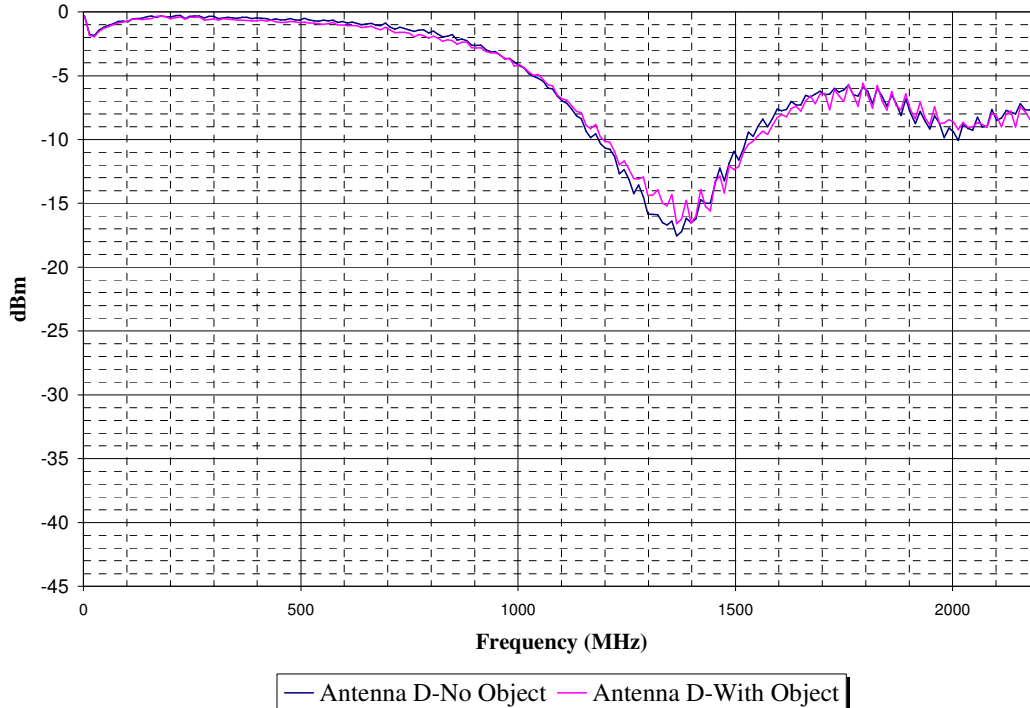


**Figure 4.13 Comparison of reflection measurement  $S_{49}$  without and with an object inside the soil**

#### 4.5 SUMMARY AND CONCLUSIONS

A two-dimensional flow and electromagnetic soilBed setup has been developed and tested to advance CWR technologies for underground detection and characterization. Preliminary results suggest that the 2D setup may be applied to detect target elements such as DNAPL contamination and buried explosives.

Transmission and reflection measurements indicate that the 2D setup and loop antennas used are reliable, but the antennas response varies with method of construction. Transmission measurements show that the antennas have some wave leakage, and

indicate that their design must be optimized. Ferrite beads have been used to minimize wave leakage.

The separation distance between transmitting and receiving antennas also influence the transmission response of the antennas. Generally, greater separation distances result in greater insertion losses. This is attributed to greater reflection/transmission energy losses cause by heterogeneities as the wave propagates to greater distances in the dry sand.

Measured variations in the transmission and reflection in the presence and absence of a buried object suggest that the 2D EM soilBed setup using loop antennas can be applied to detect target elements in subsurface.

## **5. BIMODAL DETECTION OF UNDERGROUND CONTAMINATION IN TWO DIMENSIONAL SYSTEMS**

### **5.1 ABSTRACT**

Widespread contamination of underground environments with dense non-aqueous phase liquids (DNAPLs) is of great concern to the public, military, and industrial sectors. Proper management of contaminated sites requires detection and monitoring of the contaminants, and accurate knowledge of their transport behavior in underground environments. Over the last years we have done great efforts to develop and integrate technologies that serve to locate contamination and monitor transport mechanism underground. In this paper, we describe a two-dimensional multiphase flow experiment to develop and evaluate two modes of concurrent detection and monitoring technologies: Cross Well Radar (CWR) and Image Analysis (IA). Loop antennas preset at specific locations in the tank are used to evaluate wave scattering properties of the soil under different conditions, while color images are acquired.

The electromagnetic response in the CWR antennas and IA are used concurrently to assess any relationship between electrical soil properties variations and changes spatial and temporal mass of water and contaminants. The technologies used in this research are both in development, but they can be successful tools for the detection, monitoring and

imaging of underground contaminants and process. Once developed, the technology may be applied for detecting and monitoring other buried objects.

## **5.2 INTRODUCTION**

Widespread contamination of underground environments with dense non-aqueous phase liquids (DNAPLs) is of great concern to the public, military, and industrial sectors. Proper management of contaminated sites requires detection and monitoring of the contaminants, and accurate knowledge of their transport behavior in underground environments. Traditional approaches for locating and characterizing contaminated sites rely on invasive techniques, which can promote further spread. A strong need, thus, exists for the development and integration of novel non-invasive technologies, which allow detection and monitoring of heterogeneously-distributed contaminants in subsurface environments. These technologies have potential applications for locating buried objects, such as landmines and unexploded ordnances.

The use of cross well radar (CWR) as a non-invasive technique has proven to be a reliable technology for detection of target objects that exhibit significant contrast of dielectric properties in saturated soils (Farid et al., 2003b). Its application for detection of heterogeneously-distributed phases in unsaturated soils under variable flow conditions has yet to be developed. Preliminary evaluation in no-flow 2D-SoilBed prototypes indicates that CWR technologies may be applied in unsaturated soil to detect target elements (Serrano et al., 2006). Its application in flow systems at larger scales has yet to be developed.

Image acquisition and analysis technologies have been applied to characterize soil properties, flow conditions, and the transport dissolved tracers in soils (Persson 2005a, Persson et al., 2005; Fox and Metla, 2005, Gimmi and Ursino, 2005; Kasteel et al., 2005). These studies, however, have not addressed transport of multi-phase flow of non-aqueous phase liquids in the unsaturated zone. Nor have they addressed the use of bimodal detection and monitoring techniques.

This research addresses the development of a 2D flow and electromagnetic (EM) soilBed systems, which integrates CWR and image acquisition and processing technologies for bi-modal detection and monitoring of DNAPLs flow and transport in variably-saturated soils. The feasibility of using loop antennas to measure reflection and transmission response in the absence and presence of objects in a dry soil is evaluated. The applicability of an EM model (Certuche and Rodriguez, 2007) to represent the EM conditions imposed in the 2D soilBed is assessed (Appendix 5). The section also presents a methodology developed to determine spatial DNAPL mass from image analysis.

### *5.2.1 Dielectric properties*

Cross well radar technologies are based on measurements and analysis of propagation characteristics of electromagnetic waves (EW). When an electromagnetic impulse travels through a wave-guide embedded in a soil, the amplitude of the waves is attenuated due to dielectric losses and the electrical conductance of the medium (Nadler et al., 2006). The properties of EW propagation through the soil matrix have been used to infer important

soil properties, including: porosity, volumetric water content, and the interaction of distinct phases in soils (Miller et al., 2004; Lee, 2003).

Differences in apparent dielectric constants of soil ( $\approx 4$ ), air ( $\approx 1$ ), water ( $\approx 80$ ) have been used as the basis of in situ determination soil water content in soil by time domain reflectometry (Starr et al., 2000). The same principle may be applied for contaminants with contrasting dielectric properties, such as DNAPLs. Dielectric properties have received increasing attention along with the use of electromagnetic (EM) waves (Buyukozturk et al., 2006). EW technologies may, therefore, be applicable for detection and monitoring of contaminant plumes. (Francisca and Rinaldi, 2003).

Dielectric properties of soils are frequency dependent (Agilent, 2005; Vall-I-Iossera et al., 2005; Hoekstra and Delaney, 1974). They have been studied from frequencies of 108Hz to more than 26GHz (Srivastava and Mishra, 2004). At low frequency, the dielectric constants of soil have shown to be inversely proportional to frequency (Hoekstra and Delaney, 1974), and a strong dependency on soil textural composition and water content (Srivastava and Mishra, 2004; Peplinski et al., 1995).

Measurements of soil dielectrical properties for determination of soil properties and conditions may be accomplished through several techniques (Hilhorst et al., 2000). Mainly, these techniques fall into those which utilize transmission through a sample and reflection through a sample (Curtis and Coe, 1963), and those which use both,

transmission and reflection measurements, through a sample (Sarabandi and Ulaby, 1988).

### *5.2.2 Digital visualization and Image Analysis*

Acquisition and analysis of soil images involves taking and analyzing images of soils under different conditions. Image analysis (IA) of dye tracers in unsaturated soil has been applied to investigate the effects of soil heterogeneities on flow and transport by visualizing spatial flow patterns at the millimeter scale (Persson et al., 2005). IA has also been applied to: quantify infiltration and estimate soil hydraulic conductivities; characterize preferential flow; and identify transport processes (Persson et al., 2005; Persson, 2005a,b; Vanderborht et al., 2002; Stadler et al., 2000).

Traditionally, IA of dye images involves separation between stained and nonstained soil. The image color is influenced by dye concentration and illumination parameters, including light intensity and color temperature. The images obtained with the camera may, therefore, be affected by local excitation of the incidence light on the soil, and variations in the chemical and physical composition of the soil (Lehmann, et al., 2006; Vanderborht et al., 2002). The intensity and color temperature of the incident illumination in an irregular particle distribution leads to differences that may be seen as gradations of darkness. Moreover, spatial difference on local light absorption by the soil may be interpreted as gradations of soil color (Vanderborht et al., 2002). Consequently, corrections by geometrical distortion, inhomogeneous illumination, and differences in white standard are required.

### 5.3 MATERIALS AND METHODS

This research addresses the development of a 2D flow and electromagnetic (EM) soilBed systems, which integrates CWR and image acquisition and processing technologies for bi-modal detection and monitoring of DNAPLs flow and transport in variably-saturated soils.

#### *5.3.1 SoilBed Experimental Setup*

The use of CWR technology to detect underground DNAPLs is tested and validated using a laboratory-scale 2D soilBed setup built in plexiglass (83 cm \* 83 cm \* 7cm, Figure 5.1). The soilBed was built in translucent plexiglass to allow visualization of the dyed DNAPL movement during the experiments. Because of the potential reactivity of the TCE with plexiglass, glass sheets were attached to the interior of the front and back panels to protect the plexiglass from direct contact with the TCE.

The soilBed (ID 4, Table 3.2) incorporates two metal mesh plates (diamond-shape, opening size of 0.30 cm by 0.22 cm) in the center of the tank with a separation of 2.2 cm (Figure 5.1b). The plates are perpendicular to the transmitting signal but parallel to water and DNAPL flow lines, creating a 2D permanent electromagnetic field of perfect reflection, while maintaining 2D flow in the system.

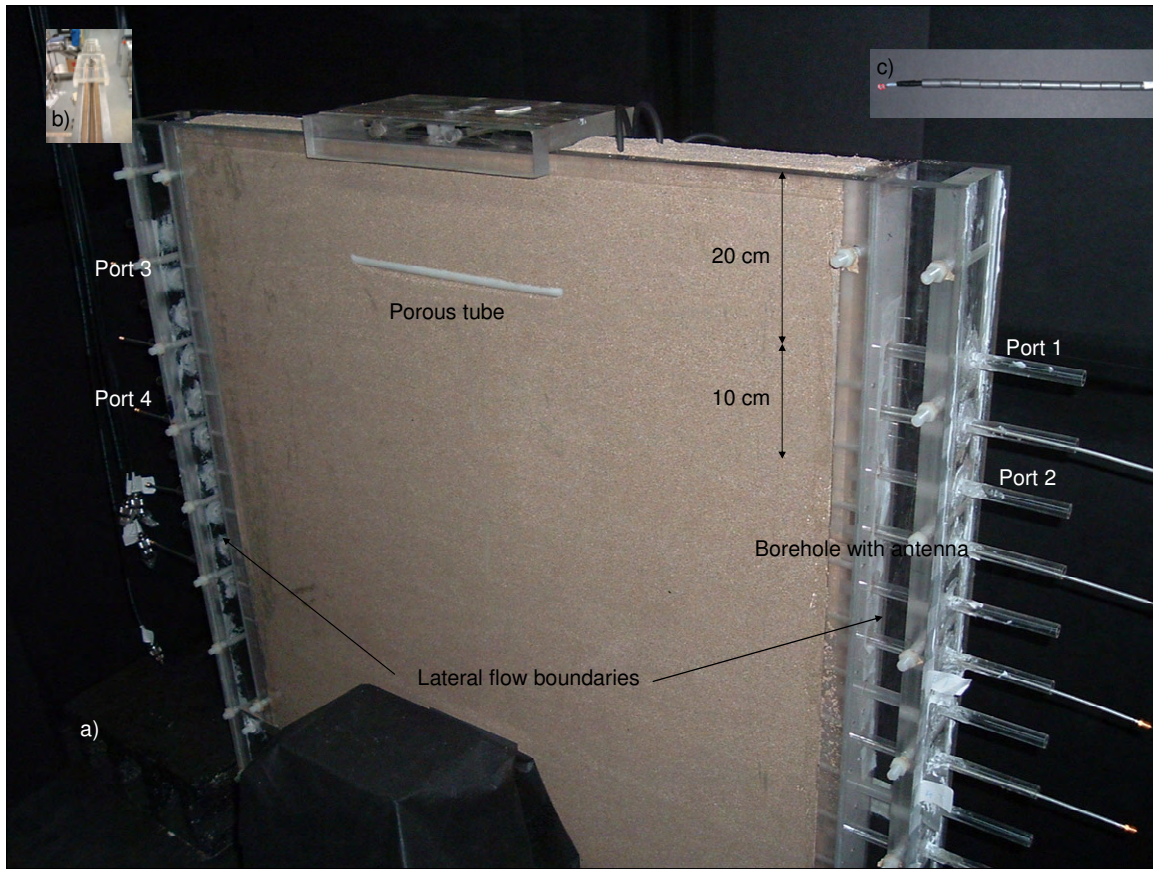


**Figure 5.1 a) Two-dimensional electromagnetic and flow setup with antennas, b) parallel metal mesh, and (c), and loop antenna (soilBed ID 4, Figure 3.2).**

Two vertical compartments (Figure 5.1a) provide lateral flow boundaries of the sand-filled compartment. The lateral inner wall for each compartment is perforated and covered with a nylon mesh. These compartments serve to support the soil, and provide for constant head reservoirs to control the water table in the soilBed. A bottom compartment, which is also perforated and nylon-mesh lined on the inner wall, serves as a constant flux boundary condition.

The soilBed was packed using silicate sand from Isabela, PR. The particle size distribution of sand is ranging between 25 and 60 mm. Sand packing was done by adding 1-cm layers through three tremie pipes, one at each mesh-separated compartment. The

final density of the packed soil is  $1.67 \text{ g cm}^{-3}$ , yielding an average volumetric porosity of 0.40.

TCE enters the soil through three hydrophobic porous tubes (30 cm L, 2.10 cm OD), simulating DNAPL leaking tanks. The porous tubes, which are sealed at the ends with Teflon caps, are used to attain even distribution. The tubes are stacked parallel to each other across the width and centered along the length of the soilBed 13.50 cm below the soil surface (Figure 5.1b). TCE is injected into the 3 tubes through Viton® tubing using peristaltic pumps.

Antennas are inserted into the soil through horizontal boreholes located at the lateral panels of the tank and in between the metal plates. The boreholes are lined with plastic casing to maintain the borehole structure and provide access to move the antennas in and out the soil. The plastic casing has been shown to enhance the antennas response in the soil (Farid, 2004).

SoilBed prototypes have been used to evaluate the effect of boundary conditions and antenna locations on the transmission and reflection measurement (Serrano et al., 2006). These electromagnetic measurements have shown that external boundaries do not affect the antenna response.

### 5.3.2 *Antenna Characteristics*

Because of the complexities associated with DNAPL flow and electromagnetic field in a spatially-constrained environment, it is necessary to determine the type, configuration, and arrangement of antennas and boundary conditions in the soil bed that will effectively serve for this detection. Electromagnetic models may be applied to characterize the behavior of the system under given conditions. The use of models, however, require conceptualization of the principal features, characterization of these features using input parameters which are often unknown, and solution of system's governing equations commonly applied under several assumptions. Consequently, model results may be affected by these assumptions and unknowns.

Preliminary tests of different antennas suggest that loop antennas are the most appropriate for the 2D systems because of the constraints in the minimum wavelength and electromagnetic field orientation for 2D electromagnetic conditions (Serrano et al, 2006). The loop antennas are built using electrical cable, ferrite beads, and small miniature adapters (SMA) connector (Pasternack Enterprises, LLC, PE 4115). Ferrite beads are used to avoid antenna deflection during installation and minimize loss in transmission and reflection measurements. Loop antennas having 8 and 16 loops and different construction modes have been tested previously (Serrano et al., 2006). It was concluded that their design and construction had to be optimized. Loop antennas having 24 turns in the helicoidal ferrite material (I.D.=0.330 cm) were built and used for the work presented in this section. A greater number of loops were used to increase the length of the antenna (24.88 cm). The center conductor is exposed 5 mm while the dielectric is exposed 10

mm. Part of the outer conductor (25.4 mm of the shield) is covered with electrical tape to prevent energy leaks, and the rest of the antenna is surrounded by ferrite beads (Figure 5.1c).

### *5.3.3 Antenna Response Testing*

The response of the antennas is tested by placing antennas at different port locations (Figure 5.1a) and evaluating the transmission and reflection measurements. Signal management and analysis are performed using a Multivector Network Analyzer (Agilent, Model 8714ET). A signal source supplied by the Network Analyzer is emitted from one antenna located in a borehole, and received by other antennas located in other boreholes. The source sends the signal at a swept frequency range between 500 and 1000 MHz, which is appropriate for a sandy soil. The signal received by other antennas is analyzed at the same frequency range to detect the reflected and transmitted signals from the material (Agilent, 2005). Reflection from and/or transmission measurements provide information to characterize the permittivity and permeability of the material. The ability of the electromagnetic system to detect buried objects in the 2D EM/Flow system were tested by introducing a metal bar (2.54 cm wide, 1 cm thick) 30 cm into the soil in the horizontal center of the soilBed (Figure 5.1) and comparing the response of the antenna in the absence and presence of the target element.

#### *5.3.4 Electromagnetic Modeling of 2D SoilBed*

An electromagnetic numerical model of the soilBed setup was developed by Certuche and Rodriguez (2007) to evaluate the wave propagation characteristics of the soilBed when media of contrasting permittivities and conductivities are present at different locations. The applicability of this model to represent the EM conditions in the 2D soilBed was assessed.

EM model was developed using Ansoft's HFSS finite-element based electromagnetic simulator. The soil region was modeled by a box (82 cm x 2 cm x 82 cm) of lossy dielectric material. The soil-box walls parallel to the xz-plane were set as perfect conductor to simulate the conducting mesh in the experimental setup. Above and below the soil box, the system was simulated as air volumes (82 cm x 2 cm x 25 cm) to provide a proper termination of the computational space. All external walls of the air boxes were set as radiating boundaries. Six wave-ports were placed on the walls parallel to the yz-plane, one transmitting on the right wall, and five receiving on the left wall. The position of the transmitting port was varied to look at the wave patterns in the soil, and the scattering parameters between wave-ports. The transmitting port is Port 1, receiving ports are numbered from bottom to top; the bottom port is Port 2, and the top port is Port 6. All simulations were performed at 600 MHz.

Three cases were simulated: Case I- soil in the soil box was assumed to be dry sand, with relative electrical permittivity of 2.55, and conductivity of 0.003 S/m; Case II- bottom third of the soil region was water saturated (air-water interface at 27.3 cm from the sand

bottom); Case III- the soil region was split into two equal boxes having saturated (bottom) and dry (top) sand (air-water interface at 41 cm from the sand bottom). Models for case II and III assumes a relative electrical permittivity of 20 and an electrical conductivity of 0.03 S/m for the saturated sand.

### 5.3.5 Digital Visualization and Image Analysis

Image acquisition, visualization, and analysis are applied concurrently with CWR techniques to evaluate and validate the CWR technologies for detection and monitoring of DNAPL contamination in underground environments, and characterize DNAPL transport processes. The image acquisition and analysis system integrates the soilBed and a digital camera interfaced to a computer, enclosed in a studio-like room set with proper lighting (Figure 5.2).



**Figure 5.2 Image acquisition and analysis system: (a) digital camera, (b) calibration soil cells, (c) stained soil cells, and (d) studio room**

Digital images were taken during the injection and movement of TCE dyed with Sudan IV in the soilBed. MatLab Image Acquisition Toolbox was used to control the camera, and capture and transfers the images to the computer (Appendix 3). Image processing was done using MatLab's Image Processing Toolbox. Image analysis was conducted using a code developed in Matlab (Appendix 4) to process images of the soil without and with dyed DNAPL. The code compares pixel intensities between the initial condition before the injection of the dyed DNAPL and the condition at given times after the onset of the DNAPL injection, estimates the percent change in pixel intensities, and develops a processed image. The percent change is the difference between the initial and final conditions at a given time. The processed image is developed according to a percent-change scale, where specific pixel values are assigned to areas within predetermined percent changes: a pixel value of zero (0) is assigned to areas with less than 10% change; 85 to areas with percent changes between 10 and 20%; 120 to areas with percent changes between 20 and 50%; and 255 to areas with percent changes greater than 50%.

In order to determine the mass of DNPL located at a particular point and space in the soil system from image analysis, it's necessary to relate pixel intensity statistics to DNAPL mass in the system. A calibration procedure was developed where images are taken before and after the injection of known volumes and concentrations of dyed liquids into soil calibration cells (Figure 5.2b and c). The cells are made of the same material and packed with the same sand and bulk density as the 2D soilBed.

## 5.4 EXPERIMENTAL RESULTS

### 5.4.1 Transmission and Reflection Measurements

Transmission (Figure 5.3 and Figure 5.4) and reflection (Figure 5.5) measurements show that the responses from the loop antennas are above noise level (60dB) in the frequency range between 500 and 1000MHz. Comparison of transmission and reflection measurements in the absence and presence of a target element (metal bar) indicates that the presence of the object in the soil causes a slight disturbance in the electrical properties. Transmission measurements for greater raypath distances (Figure 5.4) reflect measurements closer to noise level of the instrument than closer measurements. This is due to greater energy losses as wave travel to greater distances.

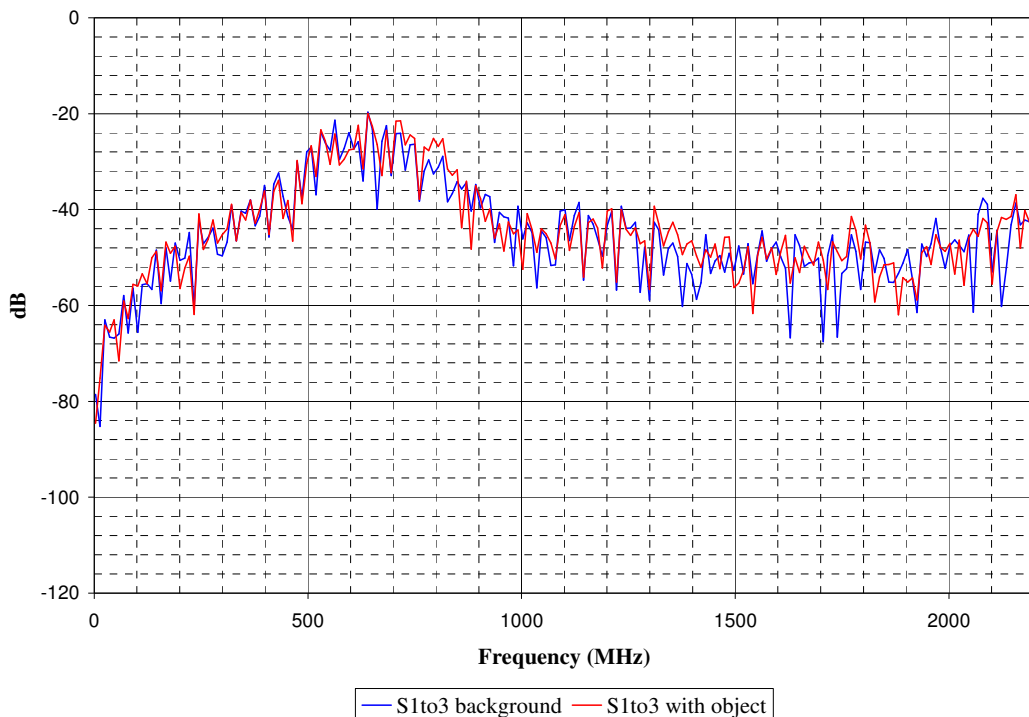


**Figure 5.3 Transmission measurements in presence (pink line) and absence (blue line) of an object: Port 1 sends, Port 3 receives**

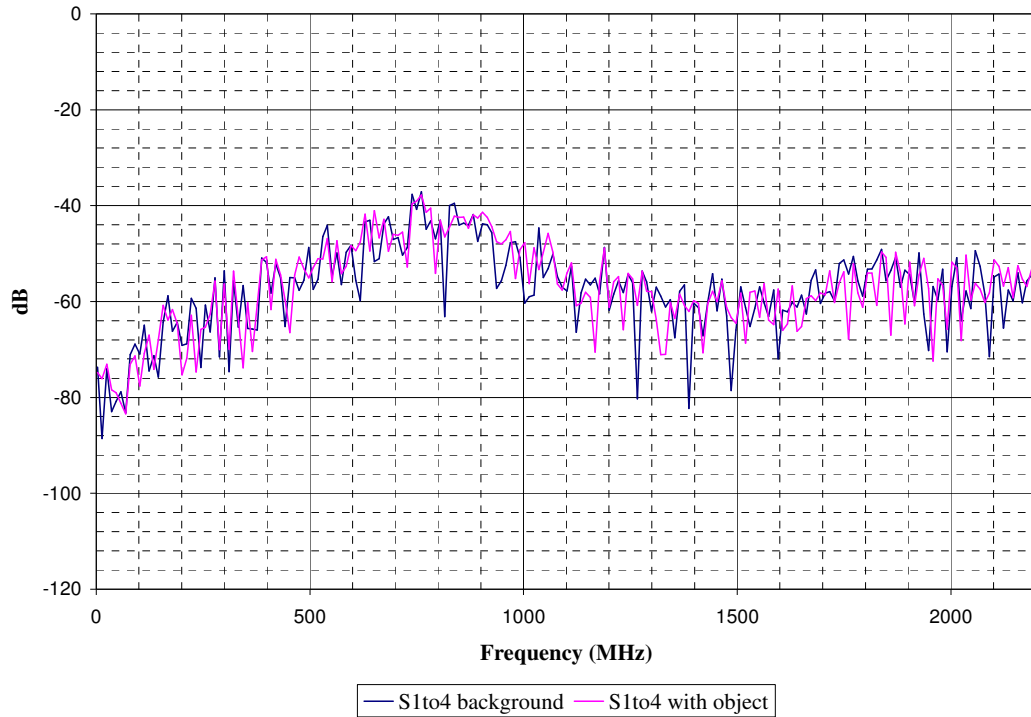


**Figure 5.4 Transmission measurements in presence (pink line) and absence (blue line) of an object: Port 1 sends, Port 4 receives**

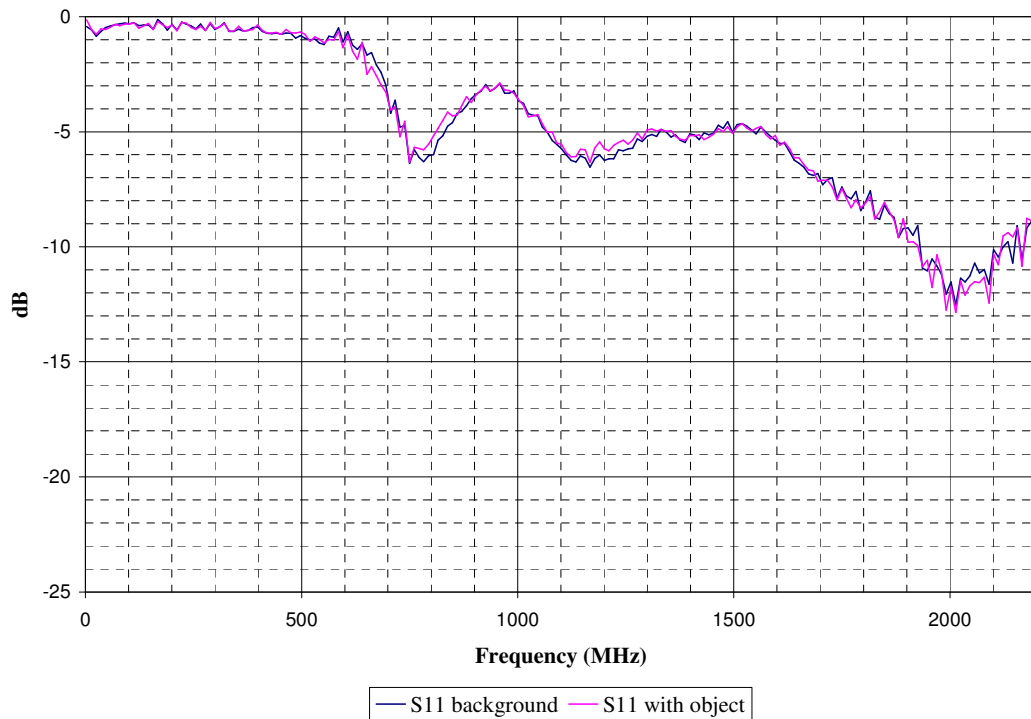


**Figure 5.5 Reflection measurements in presence (pink line) and absence (blue line) of an object: Port 1 transreceiving**

### 5.4.2 Data Reliability

The ability of collecting reproducible data is really important to enhance CWR as a detection technique. The EM measurements have to be valid, reproducible and repeatable. That involves the development of reliable and scalable laboratory measurements. As a general CWR test procedure, transmitting and receiving antennas are placed in the soil at borehole locations (Figure 5.1) and EM measurements are then collected and stored. Figure 5.6 shows the transmission response of antenna 3 (Figure 5.1) when antenna 1 (Figure 5.1) was transmitting ( $S_{31}$ ), and viceversa ( $S_{13}$ ). The results show response above 60dB for frequencies above 500MHz, and the transmission measurement of antenna pairs ( $S_{31}$ : Transmitter 1 and Receiver 3) are considered reliable. All other antennas pair measurements show similar results. Differences between  $S_{31}$  and  $S_{13}$  are attributed to differences in antenna's construction.

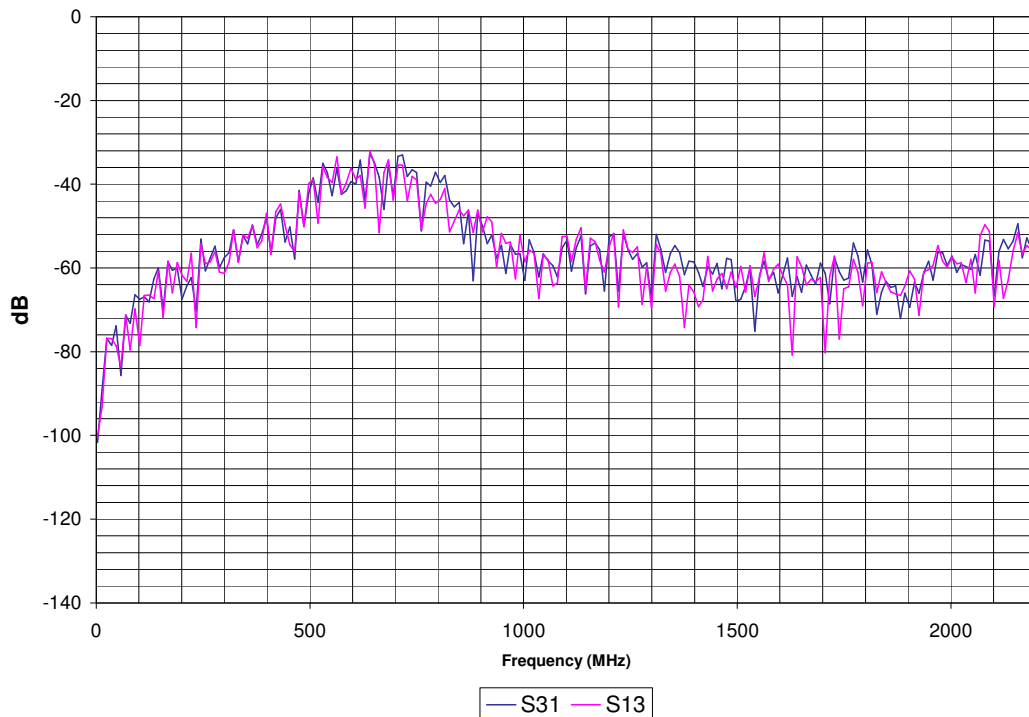


**Figure 5.6 Transmission response for antennas in port 3 and 1 (ID 4, Table 3.2)**

### *5.4.3 Electromagnetic Modeling of 2D SoilBed*

An electromagnetic numerical model of the 2D soilBed system was developed by Certuche and Rodriguez (2007) and used to simulate wave propagation characteristics of the soilBed media in the presence of contrasting permittivity and conductivity media. The model simulated energy fields and wave propagation characteristics in the soil from transmitting antennas at 14.5 and 35 cm from the bottom for the three simulated cases (Figure 5.7). Results indicate that the loss tangents at 600 MHz for dry (case I) and wet (Case II) sand were 0.035 and 0.045, respectively, indicating good dielectric properties.

In the case of the dry sand (Case I), the wave propagates radially from the transmitting port and forms a partial standing-wave pattern because of the air-soil interface (Figure 5.7a and b). The much smaller energy levels outside the soil than inside the soil box confirm that the perfectly conducting walls provide a parallel-plate waveguide structure. The wave propagation from 35 cm shows a more symmetric field distribution because of its position at equal distances from the top and bottom boundaries. Scattering parameters for all receiving ports with respect to Port 1 are lower than -100 dB, ranging between -110 and -110 dB, when the transmitting ports is located at 14.5 cm, but higher (range between -150 and -100 dB) when transmitting at 35 cm.

In Case II, the transmitting antennas located at 14.5 and 35 cm in Case II are below and above the saturated-sand/dry-sand interface (at 27 cm), respectively. The x-direction wave propagation in this case shows shorter wavelength and energy concentration in the

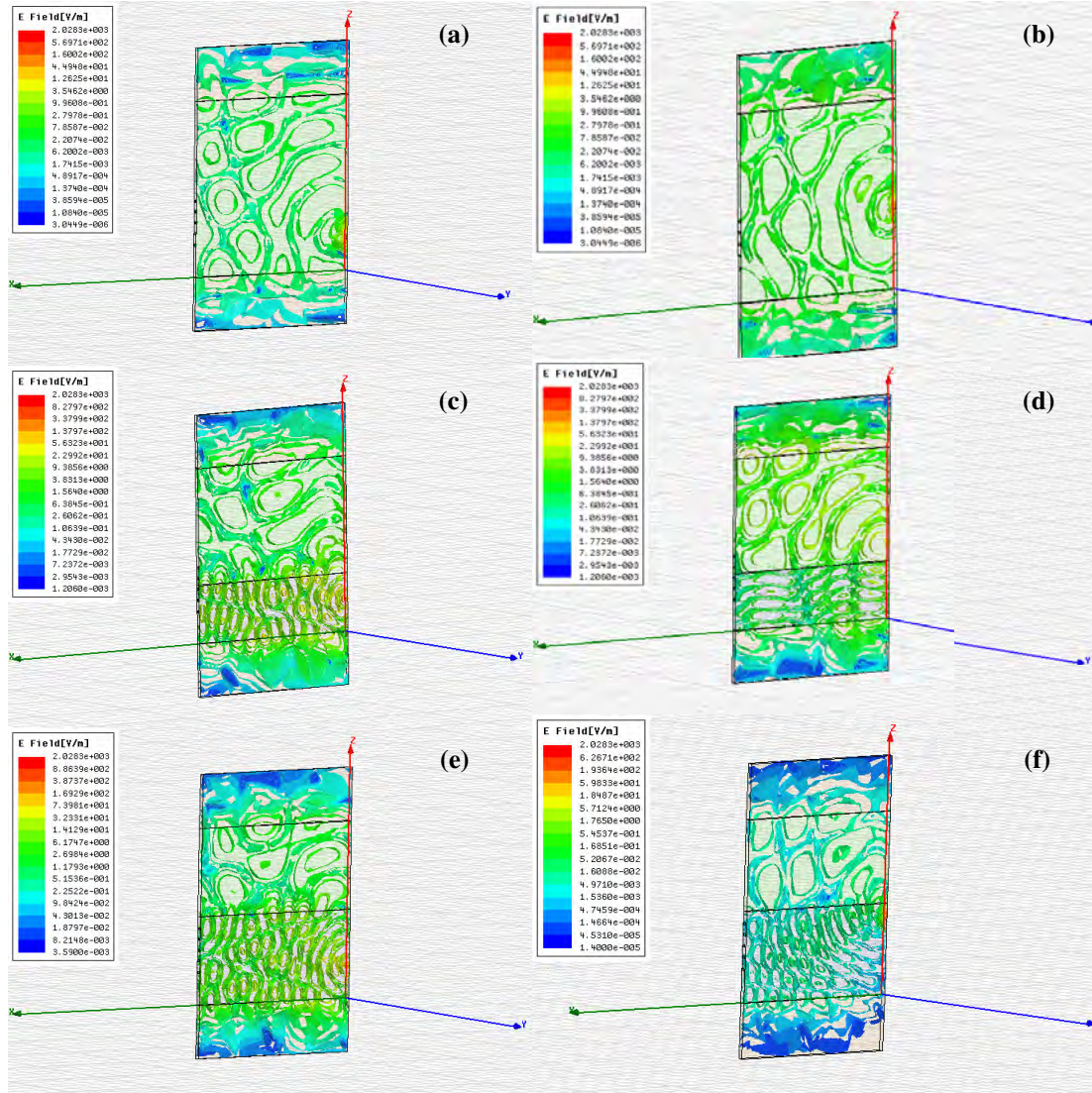


**Figure 5.7 Soil-Bed electromagnetic model for: dry sand with transmitting port at (a)14.5 and (b) 35 cm above the bottom; saturated sand on the bottom third (air-water interface at 27.3 cm) and dry sand on the top two thirds with transmitting port at (c)14.5 and (d) 35 cm above the bottom; saturated sand on the bottom half (air-water interface at 27.3 cm) and dry sand on the top half with transmitting port at (e) 14.5 and (f) 35 cm above the bottom. Receiving ports are 5 cm apart.**

saturated sand region (Figure 5.7c and d). Note that the wave in the saturated soil region propagates almost downwards (in the  $-z$ -direction). The scattering parameters are higher than the scattering parameters for dry sand (Case I), ranging between -65 and -115 dB and -70 and -130 dB when transmitting at 14.5 and 35 cm, respectively. This is caused a

by standing wave patterns created by the addition of the dry/saturated interface in the sand.

In Case III, the transmitting antennas at 14.5 and 35 cm are both located in the saturated zone below the air-water interface. Energy fields show that the wave propagates almost horizontally when the transmitting port is at 14.5 cm (Figure 5.7e), whereas it propagates at an angle of about 30 degrees from the horizontal when the port is located at 35 cm (Figure 5.7f) above the soil bottom. This is caused by the proximity of the air-water interface to the port located at 35 cm. As a result, much lower scattering parameters are estimated for the transmitting port at 35 cm (between -150 and -170 dB), than for the ports at 14.5 cm (between -45 and -105 dB) above the bottom of the sand.

In all cases the model yield scattering parameters values which are acceptable for modeling purposes, but below the measurement error level for the VNA used in this research. Consequently, they can not be verified experimentally. They do indicate that the amount of energy received by the receiving antennas at the longitudinal distance across the soilBed is relatively low. These results suggest that the antennas may be too far away for the power provided. The model supports that the 2D soilBed indeed acts as a waveguide, and further indicates the potential effect of air/water interfaces on EM wave propagation.

#### *5.4.4 Digital Visualization and Image Analysis*

Image processing algorithms were developed to analyze visual images of dyed contaminants, discriminate between regions of different amounts of DNAPLs, and assess potential relationships between electromagnetic variations and the spatially-distributed DNAPL in the soil.

Figure 5.8 shows the distribution of pixel values at 0, 5, 10, 20, and 50 minutes after onset of injection, the percent change in pixel intensities, the processed image, and histograms of difference in pixel intensity between images taken before injection and after given injection times for a 10 ml injection of a 5% dye concentration. Histograms at early times (5, 10 minutes) show a small distribution on pixel intensity difference, corresponding to a small amount of dyed contaminants after onset of injection. Higher distribution is observed on histograms at later times, indicating greater percentage of dyed contaminant.

Distribution of DNAPL in the 2D soilBed is determined from image analysis based on a calibration that relates pixel intensity to DNAPL mass. The calibration is conducted by injecting known volumes and concentrations of DNAPL into calibration soil cells (Figure 5.2b) while taking digital images. As expected, average pixel intensity values in dyed soil decreased as the amount of TCE increased in a given area (Figure 5.9), indicating darker pixels with higher TCE volume.

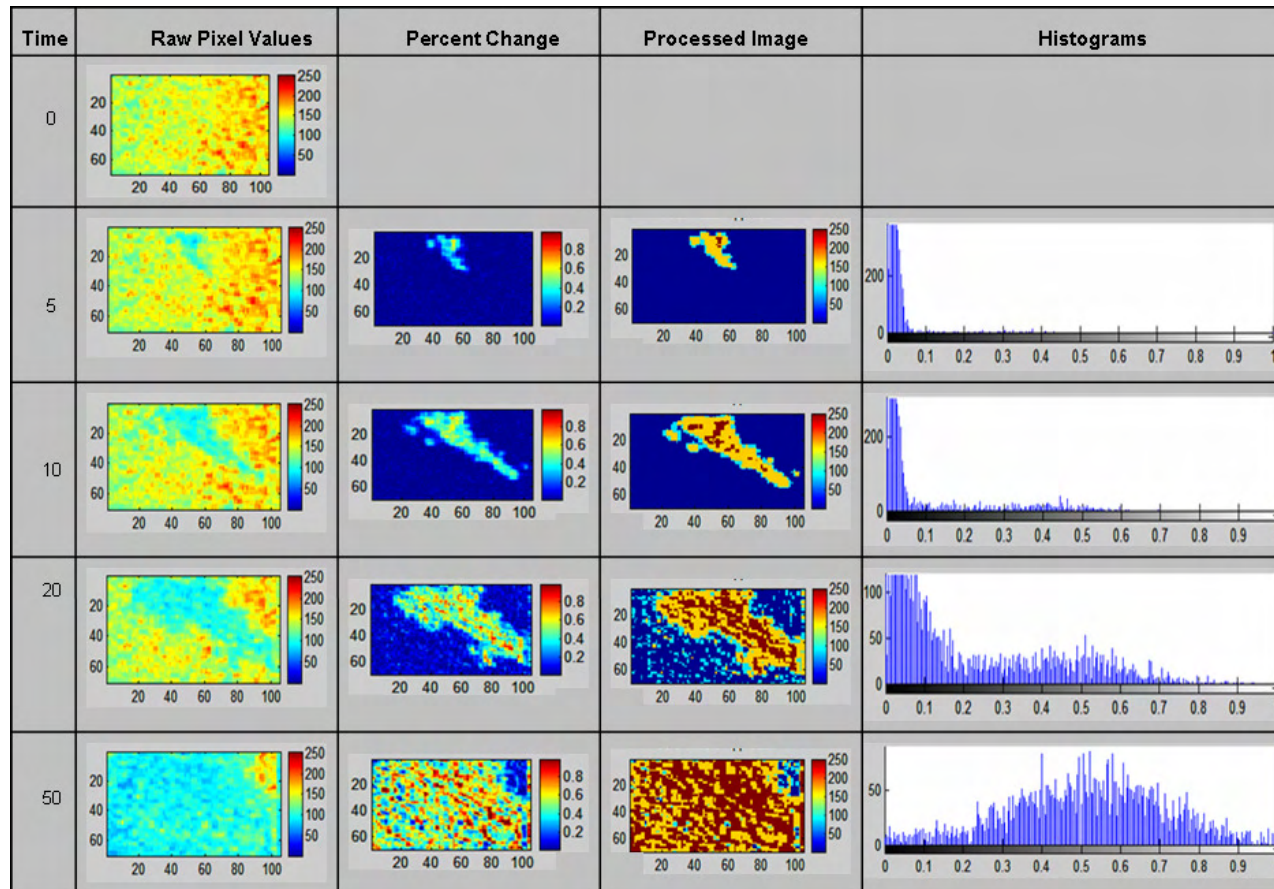
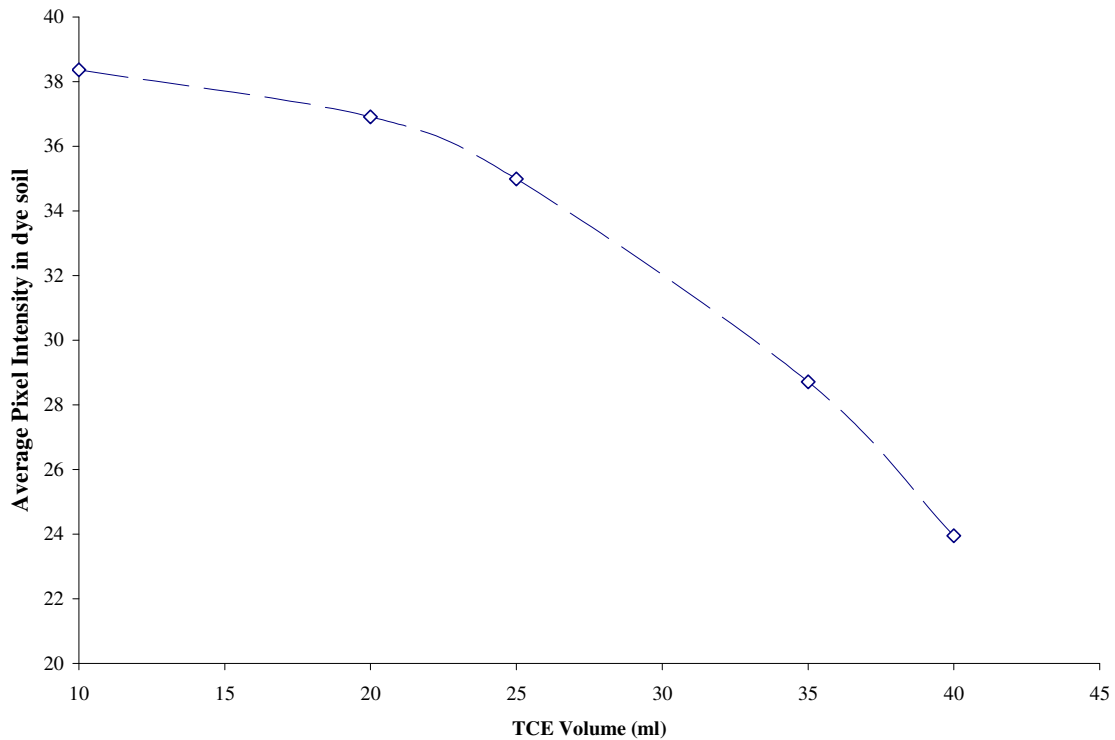


Figure 5.8 Image analysis for a 10 ml injection of a 5% dye concentration



**Figure 5.9 Average pixel intensity in dyed soil as a function of TCE volume at 10% dye concentration**

Analysis of this data shows that the differences between image intensity ( $\Delta P_i$ ) values before and after injection are strongly related to volume of dyed DNAPL, but slightly related to dye concentrations (Figure 5.10). Intensity difference is used for calibration purposes to correct for background differences. Generally,  $\Delta P_i$  increases as TCE volume increases for a given dye concentration (Figure 5.10) and for all average concentration of a given volume (Figure 5.11). This is indicating that higher intensity differences exist between images of TCE-contaminated soil and soil background as more TCE enters the system. Average pixel intensity can be, therefore, used to determine the TCE mass of the sampled volume (Figure 5.12). Differences in pixel intensities before and after TCE

injections show no observable tendency in function of dye concentrations. This is attributed to lower sensitivity to changes at the low pixel-intensity values (dark tones). The data indicates that pixel intensity is a function of TCE volume, but not dye concentration.

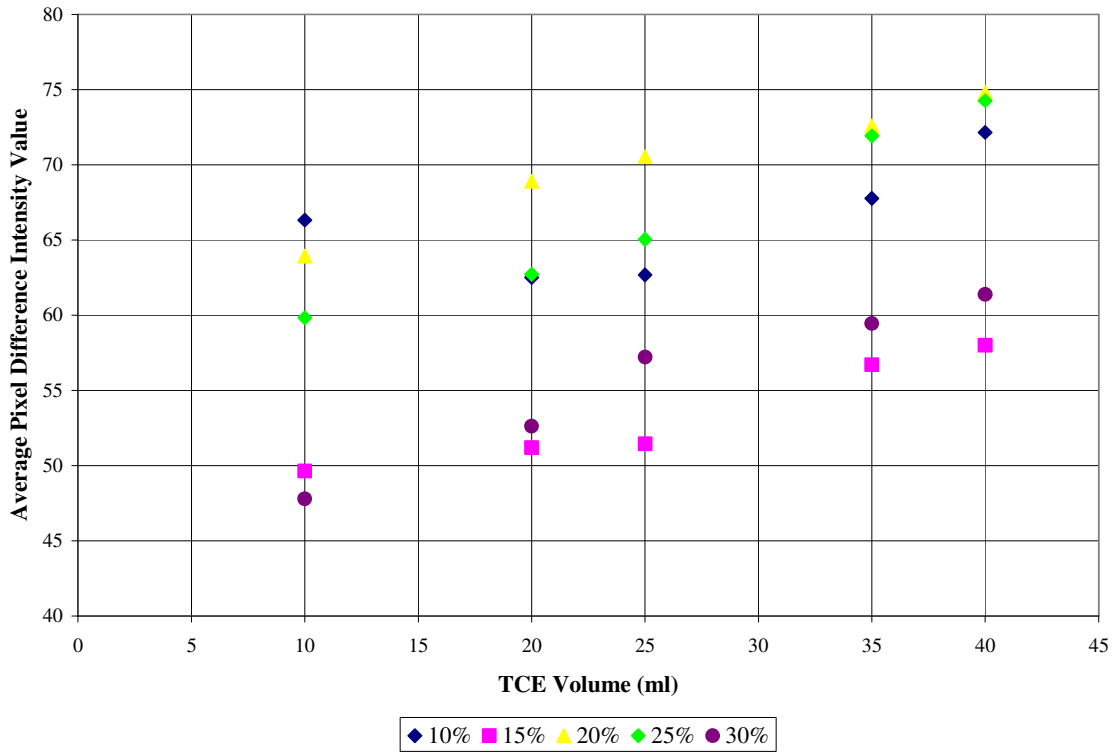


**Figure 5.10** Average difference intensity( $\Delta P_i$ ) as a function of TCE volume with dye

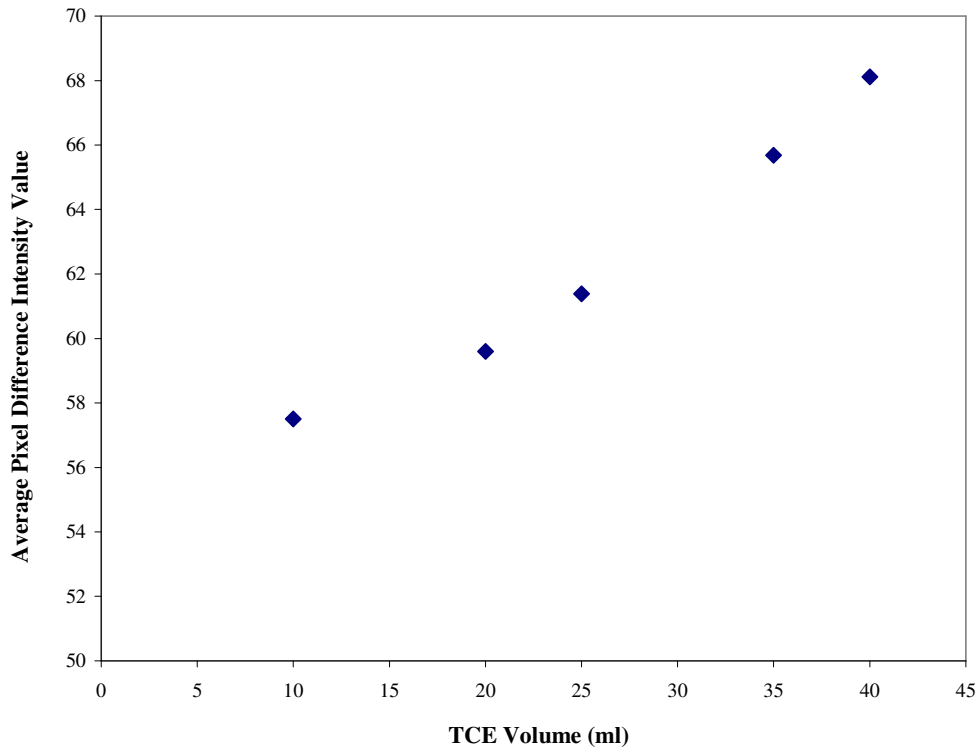


**Figure 5.11** Average pixel difference intensity value for same volume different dye concentration

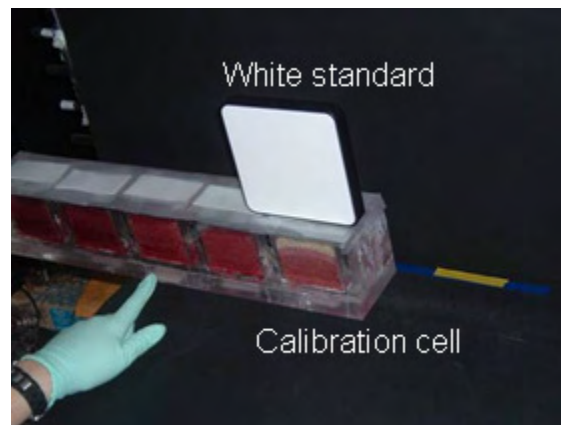


**Figure 5.12** TCE injection in the calibration cell

## 5.5 SUMMARY AND CONCLUSIONS

A two-dimensional flow and electromagnetic soilBed setup has been developed and tested for concurrent application of bi-modal detection and monitoring technologies: Cross Well Radar (CWR) and Image Analysis (IA). CWR technologies are used for underground detection and characterization. IA is used to validate CWR technologies and to characterize DNPL transport processes in underground environments. The 2D soilBed system integrates loops antennas placed in horizontal boreholes for transmission and reflection measurements within the soil, and a digital image acquisition and analysis system. The image system has been developed to acquire and analyze color images of moving dyed DNAPL while electromagnetic transmission and reflection measurements are being taken.

Preliminary results suggest that the 2D setup may be applied to detect target elements such as DNAPL contamination and buried explosives. Transmission and reflection measurements indicate that the 2D setup and loop antennas used are reliable for a larger-size soilBed, but indicate that their design must be optimized. Numerical modeling of the 2D electromagnetic field under different water content conditions shows significant variations in the wave propagation near boundaries of contrasting conductivities and permittivities. Experimental and numerical results indicate that the signal provided may have to be amplified or antennas located closer together to improve measurement resolution.

Image processing algorithms have been developed to analyze visual images of dyed contaminants and discriminate between regions of different amounts of DNAPLs. Calibrations techniques have been applied to determine amount of DNAPL from pixel intensity measurements. It is deduced that IA technologies can be applied concurrently with CWR techniques to assess the validity of CWR for DNAPL detection.

## **6. CROSS WELL RADAR TOMOGRAPHY**

### **6.1 ABSTRACT**

Severe environmental, health, and national security impacts posed by underground contamination and buried explosive devices have created the need to develop cost effective technology to detect and monitor underground target elements (UTE). Cross well radar (CWR) has been applied for detection of target objects that exhibit significant contrast of dielectric properties in soils. Its application for detection of single or distributed elements in heterogeneous underground conditions has yet to be developed.

This section addresses the development of a physics-based tomographic model (Appendix 2) for in situ soil characterization, detection and imaging of UTEs in unsaturated soils by CWR. Experimental work involves transmitting and receiving electromagnetic (EM) signals by an array of antennas in 2D SoilBED subject to variable water content conditions. The EM response is analyzed using a Matlab Code, which uses S-parameters generated by the network analyzer to estimate the dielectrical permittivities of the medium along raypaths. The permittivity estimates are used to create a tomogram of the soil and its characteristics. Tomograms are generated using algebraic reconstruction techniques (ART), with enhance convergence parameters.

Embedded UTEs are distinguished through comparative simulations of tomographic dielectric properties. Preliminary results indicate that good tomograms can be generated using an array of 5 antennas on each side of a 30 cm x 30 cm two-dimensional setup, and an array of 17 antennas for a 90 cm 90 cm two-dimensional setup.

## **6.2 INTRODUCTION**

“Tomography” comes from the Greek “tomos”, which means slice. Tomography involves reconstructing a cross section of an object using measurements of their spatial and temporal response to particular energy input(s). Many types of energy sources can be applied (e.g., electromagnetic, hydraulic, seismic). Tomographic imaging has been used to characterize subsurface systems and detect objects under the surface in many applications: astronomy, medicine, mining (Jackson and Tweeton, 1994; Dines and Lytle, 1979), geologic characterization (Hagrey, 2007; Peterson et al., 1985), and fluid monitoring (Lane et al., 2003). It has been used in many geophysical and geological field investigations (Hanafy and Hagrey, 2006).

Geophysical tomography differs from medical tomography both in physical scale and scanning geometry characteristics. Geophysical applications test on a larger physical scale than medical applications, and consequently, require lower frequencies to achieve sufficient received-signal levels over practical distances. Spatial resolution in images reconstructed from geophysical measurements may be displayed in centimeters to meters while medical images are in millimeters (Dines and Lytle, 1979).

Researches have already applied tomography technology in mapping underground resources using cross borehole imaging and cross-sectional imaging for nondestructive testing (Gu et al., 2006; Feng et al., 2003; Lane et al., 2003; Sneddon et al., 2002; Clement and Knoll, 2000; Vertiy et al., 2000; Ladas and Devaney, 1992; Middleton and Harman, 1992; Zhu and McMechan, 1989; McMechan et al., 1987). Tomography has become an important method in hydrological environmental and in engineering works. The resolution depends on the source and receivers used, and on the spacing between boreholes (Gu et al., 2006). Tomography includes three basic steps: data acquisition, data processing, and image interpretation. Thus care must be taken in preparing a data acquisition system that gives the efficiency of laboratory or field work and image quality.

### *6.2.1 Discretized Model for Image Reconstruction*

Tomographic imaging is the reconstruction of an image from its projections, where the projection is the information derived from the transmitted energies, when an object is illuminated from a particular angle (Kak and Slaney, 2001). Travel times between a fixed transmitter source and one of an array of receiver positions (Figure 6.1) reflect the average velocity along a particular raypath. Each travel time ( $t_k$ ) represents a line integral of the wave slowness  $p$  (inverse of velocity  $v$ ) along the corresponding ray path from a transmitter  $T$  to a receiver  $R$  (Jackson and Tweeton, 1994; Censor, 1983, Dines and Lytle, 1979). Travel time can be described as:

$$t_k = \int_T^R \frac{1}{v} \bullet dl = \int_T^R p \bullet dl$$

**Equation 6.1**

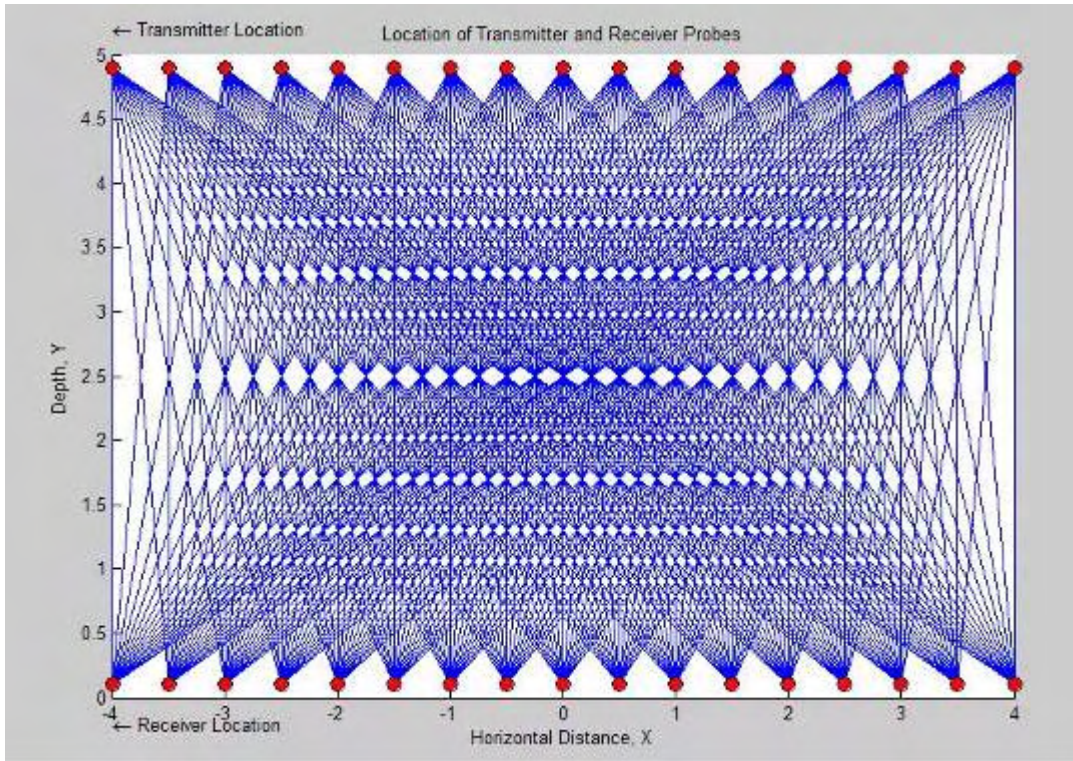


**Figure 6.1 Ray-path coverage associated with borehole distribution**

where  $dl$  is the path length increment and  $p$  is the slowness (the inverse of velocity  $v$ ).

In current geophysical applications the total length of individual rays may range from 1m to 1 Km, depending on the characteristics of the soil medium and capabilities of source and receivers (Dines and Lytle, 1979). The testing region is represented by a two-dimensional area where the distribution of velocity is calculated, and the slowness is estimated along raypaths.

It is assumed that the raypaths are approximately straight, and that the travel times between source and receiver have a constant velocity along the path. Raypaths are approximately straight if the refractive-index changes are sufficiently small. If there is

significant refraction and straight rays are assumed, the reconstructed pictures will have distortions. The straight-ray optical model may be assumed when the separation distance between source and receiver is larger than  $\lambda/2\pi$ , and when  $\lambda$  is less than  $\pi$  (Dines, 1979).

A simple approach for tomographic imaging assumes that there is a cross section of an array of unknowns, and then setting up algebraic equations for the unknowns in terms of the measured projection data. Tomographic imaging is based on matrix inversion. Although this method lacks of accuracy and the speed of implementation, it is particularly useful in situations where it is not possible to measure a large number of projections, or the projections are not uniformly distributed over 180 or 360 degrees (i.e. cross-borehole measurements). In addition, algebraic techniques are also useful when the energy propagation paths between the source and receiver positions are subject to ray bending on account of refraction, or when the energy propagation undergoes attenuation along raypath (Kak and Slaney, 2001).

There are two broad methods for reconstructing the slowness distribution  $p(x,z)$  from its line integrals: transformation methods and discretization methods. Transformation methods are based on the use of Fourier transform on continuous functions of continuous set of projections. Discretization methods, consider the area of interest to be compressed of discrete cells (or pixels) where the physical properties are assumed constant. Wave energy is considered to propagate in straight-ray form through the various pixels to provide a sum or projection of all incident raypaths values within the cell. Discretization

methods approximates the continuous function  $p(x,z)$  as a set of discrete elements or pixels (Gu et al., 2006; Jackson and Tweeton, 1994; McMechan et al., 1987; Censor, 1983). The series expansion approach differs fundamentally from the transform methods because the problem is discretized at the beginning. Both categories, transform methods and discretization methods, give inexact result, and their application depends on a compromise between accuracy and computational resources. Discretization methods generally demand more computational resources than transform methods, but they produce fewer artifacts<sup>1</sup>. Discretization reconstruction methods are less sensitive to noise and generate more accurate images in the case of incomplete data<sup>1</sup>.

### **6.3 TOMOGRAM DEVELOPMENT**

1

Tomograms are prepared using the permittivity estimates of all raypaths between transmitting and receiving antennas. Permittivity estimates are generated using the real and imaginary part of the S-Parameters obtained from the network analyzer EM response measurements (See chapter 3). These properties are estimated at different frequency for each raypath between transmitting and receiving antennas, and are later used to build tomograms of the soil properties.

Tomographic images of estimated dielectric permittivity are developed using algebraic reconstruction techniques (ART). ART assumes straight rays (Middleton and Harman, 1992; Peterson et al., 1985), and reconstructs an object by a sequence of alternating projections and correcting back projections (Mueller and Yagel, 1999). In this method an

---

<sup>1</sup> .<http://en.wikipedia.org/wiki/ART>, Accesed: February, 2008.

initial “guessed” projection is made, checked against measured data, and corrected until results are satisfactory. Simultaneous ART (SART) corrects the projection after the whole object (antenna array) has been projected (Mueller and Yogel, 1999).

In ART, the area of interest is distributed in a cartesian grid (Censor, 1983) into a series of cells (Figure 6.2), which are crossed by raypaths between transmitting and receiving antennas. Each particular raypath is characterized by a measured travel time, which reflects the average velocity along the raypath between transmitter and receiver (T and R, respectively, in Figure 6.2). In the discrete form, travel time may be expressed as:

$$t_k = \sum_{j=1}^M p_j d_{ij}, \quad i = 1 : N$$

Equation 6.2

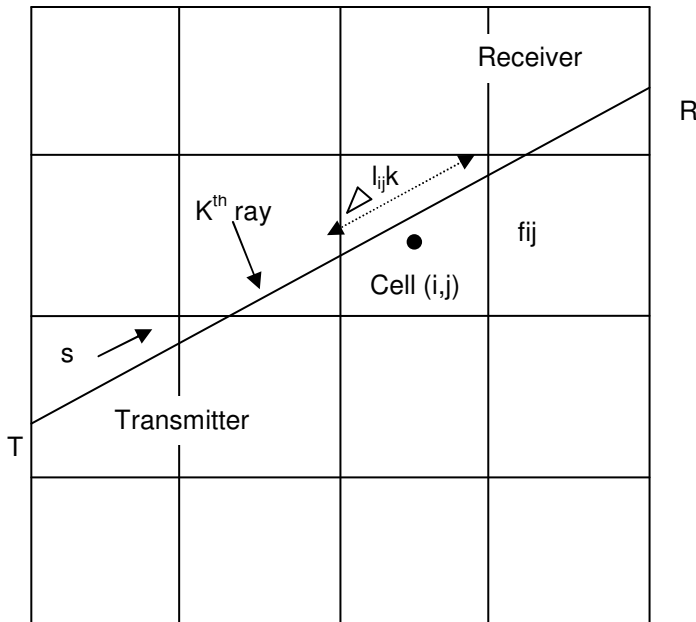


**Figure 6.2 Discrete model of a region between boreholes showing a typical raypath through IxJ digital image of velocity**

Where  $p$  is the wave slowness (inverse of velocity),  $M$  is the number of pixels,  $N$  is the total number of observations, and  $d_{ij}$  is the distance traveled by ray  $i$  in pixel  $j$ . It is assumed that velocity in each cell is constant (Gu et al., 2006; Dines and Lytle, 1979).

The basic aim of ART is to image a material parameter  $f(x,y)$  (e.g., permittivity) from line-integral data  $g_k$  collected for  $R_k$  signal paths :

$$\mathbf{g}_k = \int_{R_k} \mathbf{f}(x,y) ds \quad \text{Equation 6.1}$$

where  $ds$  represents a cell-weighting factor expressing the influence of the property in the  $ij$  pixel on the  $K_{th}$  ray. In our case, it corresponds to the length of the ray segment in the specific cell  $ij$ .

The algorithm for reconstruction begins with an initial guess of  $f_{ij}^q$  for every pixel in a Cartesian grid and estimates the projection value  $\hat{\mathbf{g}}$  at the end of each raypath:

$$\hat{\mathbf{g}} = \sum_i^I \sum_j^J \mathbf{f}_{ij}^q \Delta s_{ijk} \quad \text{Equation 6.4}$$

where  $f_{ij}^q$  indicates the estimated value after  $q_{th}$  iteration and represents the average value of  $f(x,y)$  on the cell  $(i,j)$ ,  $\Delta s_{ijk}$  is the length of a ray segment that intercepts the pixel, and  $I$  is the total number of columns in the grid and  $J$  is the total number of rows. The length  $\Delta s_{ijk}$  is set to zero for this  $i$  and  $j$  values for which the associated cell is not intercepted by the ray  $R_k$ . Commonly,  $k$  is not equal to  $q$  because the total set of rays must be examined several times before a final estimate of  $\Delta f_{ij}^q$  is obtained.

Iterations are evaluated after each raypath until the difference error between measured and estimated values is minimized. In our case, we wish to determine a set of correction due to the  $k_{th}$  ray,  $\Delta f_{ijk}^q$ , so there will be a zero error for the  $k_{th}$  path with a difference error,  $\Delta g_k$ , in data fit between measured value and estimated value:

$$\Delta g_k = (g_k - \hat{g}_k) = \sum_i^I \sum_j^J \Delta f_{ij}^q \Delta s_{ijk} \quad \text{Equation 6.5}$$

Measured values in the 2D experimental system represent the travel time ( $t_k$ ) along each raypath  $k$ . It is determined from the wave slowness ( $p$ ) properties of the material along corresponding raypath:

$$t_k = \sum_i^I \sum_j^J p_{ij} \Delta s_{ijk} = \sum_{n=1}^M p_n \Delta s_{nk} \quad \text{Equation 6.6}$$

The wave slowness ( $p$ ) is the inverse of wave velocity ( $v$ ), which for non-magnetic ( $\mu_r=1$ ) and non-conductive ( $\sigma/\omega\epsilon_r \ll 1$ ) media (Hagrey, 2007; Buyukozturk et al., 2006; Lane et al., 2003) is related to the relative dielectric permittivity ( $\epsilon_r$ ) and the vacuum velocity ( $c=0.3\text{mns}^{-1}$ ):

$$p \approx \frac{1}{v} = \frac{\sqrt{\epsilon_r}}{c} \quad \text{Equation 6.7}$$

Travel time is, thus, related to  $\epsilon_r$  by:

$$t_k = \sum_{n=1}^M \frac{\sqrt{\epsilon_{rk}}}{c} \Delta s_{nk} \quad \text{Equation 6.8}$$

The  $\epsilon_r$  values used are those estimated along a T-R raypath from S-parameter measurements (see chapter 3).

### 6.3.1 Algebraic Reconstruction Technique

Algebraic Reconstruction Technique (ART) was first published as a reconstruction algorithm in 1970 and was later recognized to be identical with Kaczmarz's algorithm for solving systems of linear equations (Censor, 1983). These algorithms work the integral equation in matrix form and apply using relaxation techniques. These methods assume straight rays (Middleton and Harman, 1992; Peterson et al., 1985).

The elementary ART algorithm is based in a rectangular Cartesian plane that is uniformly discretized into an  $ij$  (column, row) grid of rectangular pixel elements. The pixel discretization scheme samples  $f(x,y)$  at pixel center  $i\Delta x$  and  $j\Delta y$ , and therefore,  $f(x,y)$  is approximated by (Middleton and Harman, 1992):

$$i\Delta x - \frac{i\Delta x}{2} \leq x \leq \Delta x + \frac{i\Delta x}{2} \quad \text{Equation 6.2}$$

$$i\Delta y - \frac{i\Delta y}{2} \leq y \leq \Delta y + \frac{i\Delta y}{2} \quad \text{Equation 6.10}$$

$$f(x, y) = p_{ij} = f(i\Delta x, j\Delta y) \quad \text{Equation 6.11}$$

where:  $1 \leq i \leq I$ ,  $1 \leq j \leq J$ ,  $I$  is the number of columns and  $j$  is the number of rows.

The interaction of  $p_{ij}$  with the  $k_{th}$  ray is such that a measurement  $m_k$  at the receiver of the  $k_{th}$  ray is a numerical approximation of the line integral along the ray. The measurement  $m_k$  can be expressed in the same form of travel time equation expressed previously as:

$$m_k = \sum p_n a_{kn} \quad \text{Equation 6.12}$$

where  $n$  is a single index identifier for pixel element locations in the grid such that:

$$n = (j-1)I + i, \quad 1 \leq n \leq (N = IJ)$$

**Equation 6.13**

The  $a_{kn}$  is a weighing factor expressing the influence of the properties in the  $n^{\text{th}}$  pixel on the  $k^{\text{th}}$  ray. In this case,  $a_{kn}$  is the length of the intersection of the  $k^{\text{th}}$  ray with the  $n^{\text{th}}$  pixel.

The projection values  $f_{ij}^q$ , for one grid element crossed by raypaths at pixel  $n=1:M$  is estimated at each iteration  $q$  as (Kak and Slaney, 2001; Mueller and Yagel, 1999; Nugroho and Wu, 1999).

$$f_n^{(q)} = f_n^{(q-1)} + \lambda \left[ \frac{p_k - \sum_{l=1}^M a_{kl} f_n^{(q-1)}}{\sum_{l=1}^M a_{kl}} \right] a_{kn} \quad \text{Equation 6.14}$$

where  $\lambda$  is the relaxation factor, typically chosen within the interval between 0 and 1, but usually much less than 1 to provide correction overshoot (Mueller et al., 1999),  $a_{kl}$  is weighting factor for  $l$  with the incidence of  $k^{\text{th}}$  raypath.

Normally, CWR uses multiple measurements  $m_k$ , thus, Equation 6.12 can be expressed in matrix forms including many different ray paths ( $1 \leq k \leq N$ ) as:

$$A = D \cdot S$$

**Equation 6.15**

where  $A$  is a  $N$ -number of projection estimated values,  $D$  is the weight projection matrix ( $N \times M$ ) of elements  $a_{kn}$  named “projection matrix”, and  $S$  is a  $N$ -number vector of unknown material parameter,  $M$  is the total number of pixels (Middleton and Harman,

1992). This matrix form represents the basis for ART, which assumes that the cross section of the image consist of an array of unknown (given by S) that can be determined by setting up algebraic equations for the unknowns in terms of the measured projection data (A). The equation system for ART, as provided by Equation 6.15, is illustrated in Figure 6.3:

	Weight Projection Matrix (D)								
Ray path	cell 1	cell 2	cell 3		cell MxN		(S)		(A)
1	$D_{1,1}$	0	$D_{1,3}$		$D_{1,MxN}$		$S_1$		$A_1$
2	$D_{2,1}$	0	0		$D_{2,MxN}$		$S_2$		$A_2$
3	$D_{3,1}$	$D_{3,2}$	0		$D_{3,MxN}$		$S_3$		$A_3$
...	0	0	$D_{4,3}$	...	$D_{4,MxN}$		$S_4$		$A_4$
...	0	0	$D_{5,3}$		...	*	...	=	...
...	$D_{8,1}$	0	0		...		...		...
N-1	0	0	0		$D_{N-1,MxN}$		$S_{N-1}$		$A_{N-1,MxN}$
N	0	0	0		$D_{N,MxN}$		$S_N$		$A_{N,MxN}$

**Figure 6.3 Matrix form in ART**

The estimation of the unknowns (and image projections) in ART is performed through an iterative process, in which: (i) an initial guess of the unknown is guessed; (ii) a projection value is calculated on the first line (raypath); (iii) the projection value is checked against the measure data; (iv) the projection values are corrected; (v) corrected projection values are reprojected on the second line (raypath),and (vi) steps (iv) through (v) are repeated by projecting back into previous lines, correcting and reprojecting into next line until errors between estimated and measure values are minimized (Kak and Slaney, 2001).

For a large number of grids and projections, computation speed and space may be a problem. This problem can be solved by making approximations of the weighting

coefficients (Kak and Slaney, 2001). These approximations may, however, introduce “noise”. The noise can be reduced by using a relaxation factor less than 1. In our case, the relaxation factor used was 0.1.

Simultaneous algebraic reconstruction technique (SART) is an ART-type technique in which, instead of sequentially updating pixel on a ray-by-ray basis, the average correction generated by all rays in a projection is simultaneously applied to a pixel (Kak and Slaney, 2001; Mueller and Yagel, 1999). SART has proven to yield superior results than basic ART, but is usually at the expense of slower convergence. The SART correction equation is given as:

$$f_n^{(q)} = f_n^{(q-1)} + \lambda \sum_k \left[ \frac{p_k - \sum_{l=1}^M a_{kl} f_n^{(q-1)}}{\sum_{l=1}^M a_{kl}} \right] a_{kn} \quad \text{Equation 6.16}$$

where the summation with respect to  $k$  is over the rays intersecting the  $n_{\text{th}}$  image element (pixel) for a given scan direction (Kak and Slaney, 2001).

### 6.3.1.1 Illustrative example of the ART process

An illustrative example of the process applied to develop tomographic images from ray-based data is provided below. The example discretizes an area into a grid containing 25 cells (5 rows by 5 columns), having four ray paths (Figure 6.4). This ray path travels from point 0 to 4 and the properties estimated in this ray are affecting the cells registered

in Table 6.1 thus, the rest of cells will have a value of 0 in the soil properties because there are not distances of the ray path affecting them. In this manner, each  $d_{ij}$  represents the contribution of the  $j_{th}$  cell to the  $i_{th}$  total ray.

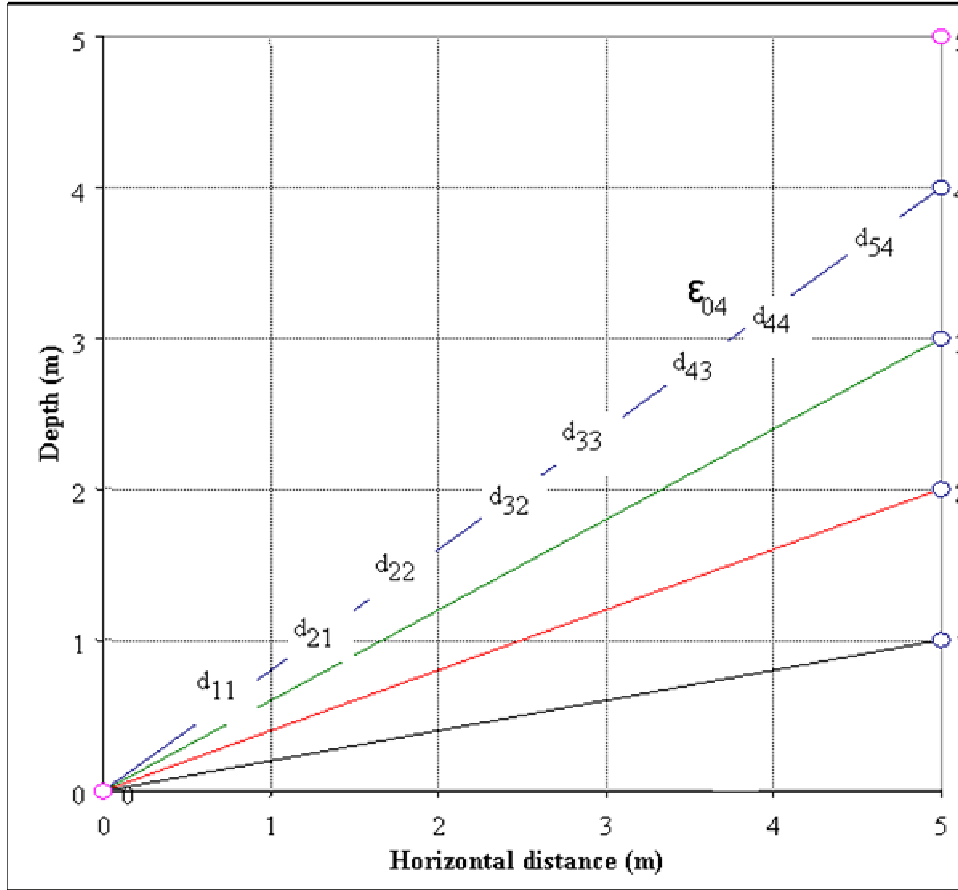


**Figure 6.4** Discrete model of a region between boreholes showing a typical ray path through the  $0 \times 4$  ( $I \times J$ ) digital image with a specific dielectric property ( $\epsilon$ )

**Table 6.1** Distance travel through raypath (0,4)

Cell(x,y)	Distance ( $d_{ij}$ )	Soil Property
(1,1)	$d_1$	$\epsilon_{04}$
(2,1)	$d_2$	$\epsilon_{04}$
(2,2)	$d_3$	$\epsilon_{04}$
(3,2)	$d_4$	$\epsilon_{04}$
(3,3)	$d_5$	$\epsilon_{04}$
(4,3)	$d_6$	$\epsilon_{04}$
(4,4)	$d_7$	$\epsilon_{04}$
(5,4)	$d_8$	$\epsilon_{04}$

Total distance of ray path (0,4) may be estimated with:

$$D_{04} = \sum_{i=1}^{i=8} di \tag{Equation 6.17}$$

For a raypath, Equation 6.2 is expanded:

$$t_k = \sum_{n=1}^{25} \frac{\Delta s_{kn}}{v_n} = \sum_{j=1}^{25} \frac{d_{kn}}{v_n} = \sum_{j=1}^{25} \frac{\sqrt{\epsilon_{rn}} d_{kn}}{c} = d_{kn} E_n \tag{Equation 6.3}$$

where  $E_r = \frac{\sqrt{\epsilon_{rn}}}{c}$  and k=1:4. A similar expansion is determined for each raypath in the grid to generate the matrix forms (Equation 6.14) used in the reconstructive process:

$$E_1 d_{11} + E_2 d_{12} + E_3 d_{13} + \dots + E_{25} d_{1,25} = t_01$$

$$E_1 d_{21} + E_2 d_{22} + E_3 d_{23} + \dots + E_{25} d_{2,25} = t_02$$

$$E_1 d_{31} + E_2 d_{32} + E_3 d_{33} + \dots + E_{25} d_{3,25} = t_03$$

$$E_1 d_{41} + E_2 d_{42} + E_3 d_{43} + \dots + E_{25} d_{4,25} = t_04$$

which can be shown in Figure 6.5.

$D_{1,1}$	$D_{1,2}$	$D_{1,3}$	. . .	$D_{1,25}$	*	E1	=	$t_1$
$D_{2,1}$	$D_{2,2}$	$D_{2,3}$	. . .	$D_{2,25}$		E2		$t_2$
$D_{3,1}$	$D_{3,2}$	$D_{3,3}$	. . .	$D_{3,25}$		E3		$t_3$
$D_{4,1}$	$D_{4,2}$	$D_{4,3}$	. . .	$D_{4,25}$		E4		$t_4$

**Figure 6.5 Expanded matrix**

In this case, the expansion has been defined for k=4 because in this example there are four raypaths in the grid, and there are 25 different properties of the soil because this is

the number of cells. Once the permittivity's values are determined the tomogram may be developed.

#### **6.4 APPLICATION OF SART TO SIMULATE UNDERGROUND TARGET DETECTION**

The developed TOMOGRAPHY code (Appendix 2) was applied to locate and estimate the shape of a simulated squared target element buried underground. The squared target element was assumed to have a constant permittivity of 4. The background permittivity (e.g.,  $\epsilon_{r \text{ soil}}$  assumed as 2) was assumed spatially constant (i.e., constant velocity). The simulation was done considering 30 cm\*30 cm soilBed setup having lateral arrays of 5 antennas on each side with a separation of 5 cm. Simulations were performed using different grid sizes (Figure 6.6). The raypaths used were traced through the target and 0.1 was used as relaxation factor. The developed code allows determining the required number of antennas to get a better resolution in tomogram according with the geometry of the system and with the size of the target. The results indicate that an array of at least 5 antennas in each side is required for proper resolution of tomograms in a 2D soilBed of 30cm \* 30 cm.

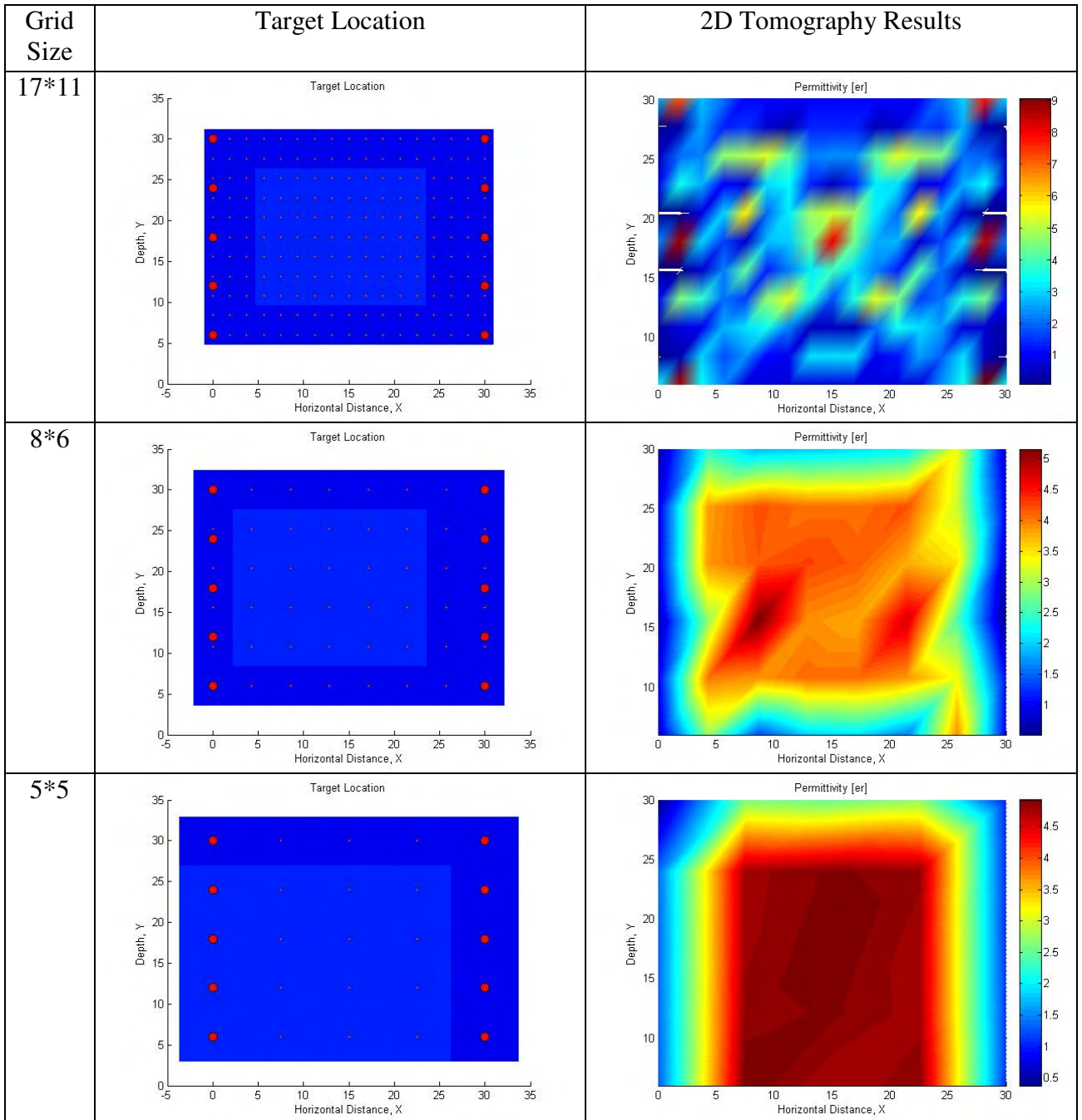


**Figure 6.6 Tomographic images of squared UTE using straight raypath SART of different grid sizes having five antennas. Red dots are used to show antenna location**

## 6.5 SUMMARY AND CONCLUSIONS

A Tomography code was developed to generate tomographic images using the permittivity estimates of all raypaths between transmitting and receiving antennas. The code uses simultaneous algebraic reconstruction techniques (SART) to develop the tomographic images. The code assumes straight raypaths, and may lose resolution if raypaths are bent due to spatially varying velocity profiles.

The developed Tomography code generates acceptable tomograms of UTEs in soils, provided that there is sufficient density of antennas arrays, and proper grid spacing. The codes, thus, provides an excellent tool for optimal CWR system design and can be applied to determine the number of antennas required for good resolution of a specific geometry. Simulations of squared UTE using the code indicate that an array of 5 antennas on each side is required for proper resolution of tomograms in a 2D SoilBed having dimensions of 30 cm x 30 cm. For an array of 5 antennas in each side, the best resolution is obtained with a grid size of 8\*6.

## **7. DNAPL DETECTION AND VISUALIZATION UNDER VARIABLE CONDITIONS: EXPERIMENTAL RESULTS**

CWR and image acquisition and processing technologies were applied during TCE injection in a 2D soilBed to assess their applicability for DNAPL detection and monitoring in subsurface environments. The technologies were applied under different water saturation to determine their applicability under variable conditions.

### **7.1 MATERIALS AND METHODS**

The experiments involved injecting dyed TCE into previously developed 2D soilBeds (ID 2, Table 3.2, Figure 3.2a) while taking electromagnetic measurements and digital images. The electromagnetic measurements relied on the use of previously-developed loop antennas distributed horizontally along the soilBed lateral panels according to previous work (Chapters 4 and 5).

Two sets of TCE injection experiments were conducted: TCE injection in dry soil followed by water infiltration, and TCE injection under saturated conditions. They are described in Chapter 3 and briefly summarized in here. In the dry sand experiments, dyed TCE was injected below the soil surface for a 30-minutes period, followed by 20-minutes water infiltration period. A sweep of EM measurements and digital images were taken before, during, and after TCE and water infiltration periods. EM measurements

involved sending a EM signal from each of the antennas, while receiving in all antennas (including the radiating antenna). Measurements were made with only one radiating antenna at a time (i.e., one antenna send while all receive, then another send while all receive, etc.). The saturated experiments were conducted after slowly saturating the sand from the bottom of the tank. Digital images and EM responses were taken during the saturation period at the times when the soil tank was saturated. TCE was injected for 30-minute period under the water table, and a sweep of EM measurements and digital images were taken.

A CWR technology developed to estimate dielectric permittivities along raypaths (Chapter 3) was applied to determine dielectric properties of the medium, before, during, and after the injection of TCE. These properties were then used to develop tomographic images of the mediums using SART (Chapter 6). The CWR-based tomographic images were then compared to digital images obtaining through image acquisition, processing, and analysis techniques (described in Chapter 4).

## **7.2 RESULTS**

The experimental results vary according to the water saturation conditions in the 2D soilBeds. Results are, therefore, presented for the initially-dry experiments, and then for the saturated experiments.

### **7.2.1 TCE and Water Infiltration in Initially-dry Soil Experiments**

Transmission and reflection measurements are shown (Figure 7.1 to 7.10) according to the temporal measurement relative to the temporal onset of the TCE and water injection and infiltration. The legend in the figures is shown as:  $S_{iTojStatus}$ , where  $i$  and  $j$  represent the transmitting and receiving antennas, and status represent TCE injection and water infiltration status:

- “N” represents measurements taken before TCE injection in dry soil
- $S_{iTojTCE5}$ ,  $S_{iTojTCE10}$ , and  $S_{iTojTCE30}$  represent measurements taken after 5, 10, and 30 minutes of TCE injection, respectively.
- $S_{iTojTCEW12}$ ,  $S_{iTojTCEW30}$ ,  $S_{iTojTCEW50}$  represent measurements taken 20, 50, and 100 minutes, respectively after TCE injection was halted and water infiltration was started (i.e., 50, 80, 130 minutes after commencement of TCE injection).

#### *7.2.1.1 Transmission response*

Transmission measurements before and during TCE injection in initially-dry soil indicate that changes in the electromagnetic properties of the soil as TCE is injected depends on frequency (Figure 7.1). Very little differences are seen between measurements taken before and after injection below about 1000 MHz. At higher frequencies, the presence of the TCE depresses transmission measurements below the measurements taken prior to the injection for most of the frequencies sampled up to about 1800 MHz. This is indicative of greater attenuation (insertion losses) caused by the presence of TCE. For frequencies above 1600 MHz greater attenuation losses are observed as TCE injected volume increases. Significant attenuation losses are observed for frequencies higher than 1700 MHz. Greater losses at a lower frequency range (between 1650 and 1775 MHz) are

observed for the measurements with the greatest TCE volume. Greatest rapid losses were seen at a higher frequency range during the initial TCE injection and for the No- TCE condition prior to injection ( $\approx 1700-1900\text{MHz}$ ). It is possible that the decrease in transmission losses are caused by molecularly- based conduction losses at this frequency range. At frequencies between about 1900 and 2000 MHz, attenuation losses are greater for the dry soil than the TCE-containing soil, suggesting electrical insulation characteristics of TCE at these frequencies.

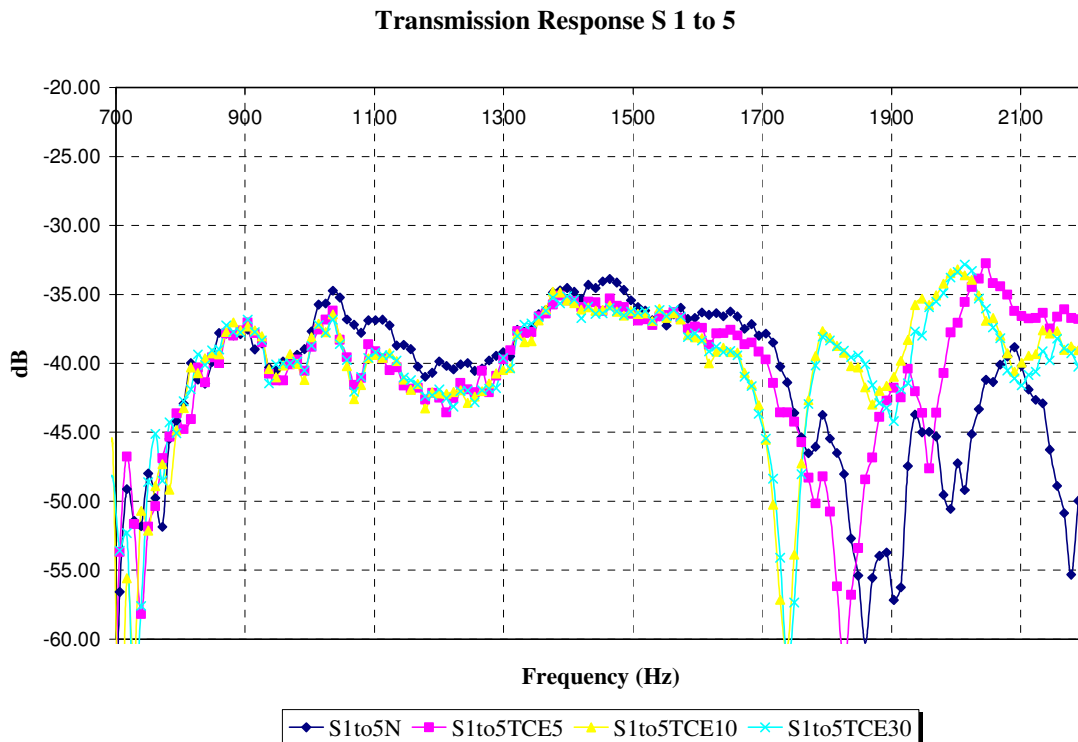


**Figure 7.1** Transmission measurement during TCE injection-initially dry experiments

As water infiltrates in the presence of TCE there are frequency-dependent changes in the EM behavior of the soil (Figure 7.2) at low frequencies (below 900 MHz). The presence of water seems to induce lower attenuation losses, as seen by the higher dB response. At this range, greater volume of water reflects lower losses. At higher frequencies, the

presence of water induces greater attenuation losses, resulting in lower dB measurements. This is attributed to the greater losses due to absorption and conduction. Greater losses are observed for greater volume of infiltrated water for frequencies between about 1000 and 1400 MHz. The losses are not as significant, however, as when water is initially infiltrating into the soil. Significant attenuation losses in the initial presence of infiltrated water are for a frequency range between 1600 and 1700 MHz.

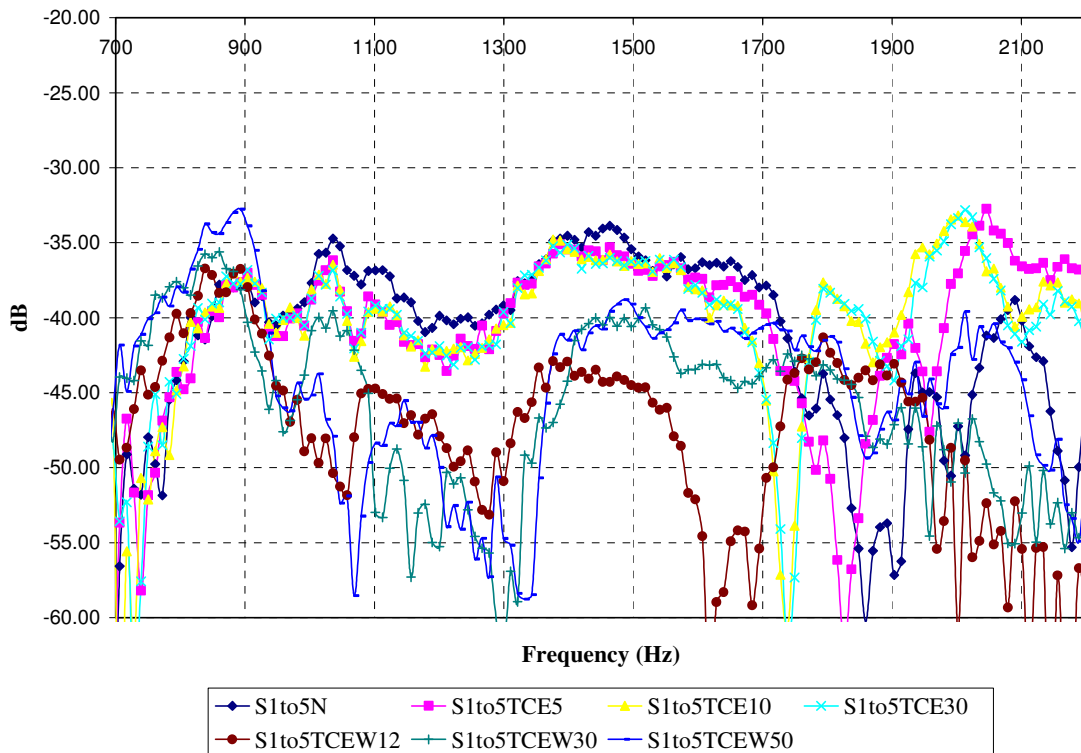


**Figure 7.2 Transmission measurement when receiver is in Port 5 and transmitter in Port 1-initially dry experiments**

The influence of raypath distance in the EM behavior of the bulk soil as TCE and water enter the system can be seen by comparing Figure 7.2 and Figure 7.3. The raypath distance from Port 1 to 6 is farther than that to Port 5. As a result there are greater

attenuation losses as the wave continue to sample the medium for longer distances. Note that the majority of the S1to5 values fall between -30 and -45 (except for frequencies higher than 1700 MHz) during the TCE injection period (Figure 7.1) and between -35 and -55dB in the presence of water (Figure 7.2). These values are reduced at Port 6, reflecting the greater attenuation losses at greater distances. The transmission results are also smoother with peak losses around 1300 MHz and between 1600 and 1700 MHz.

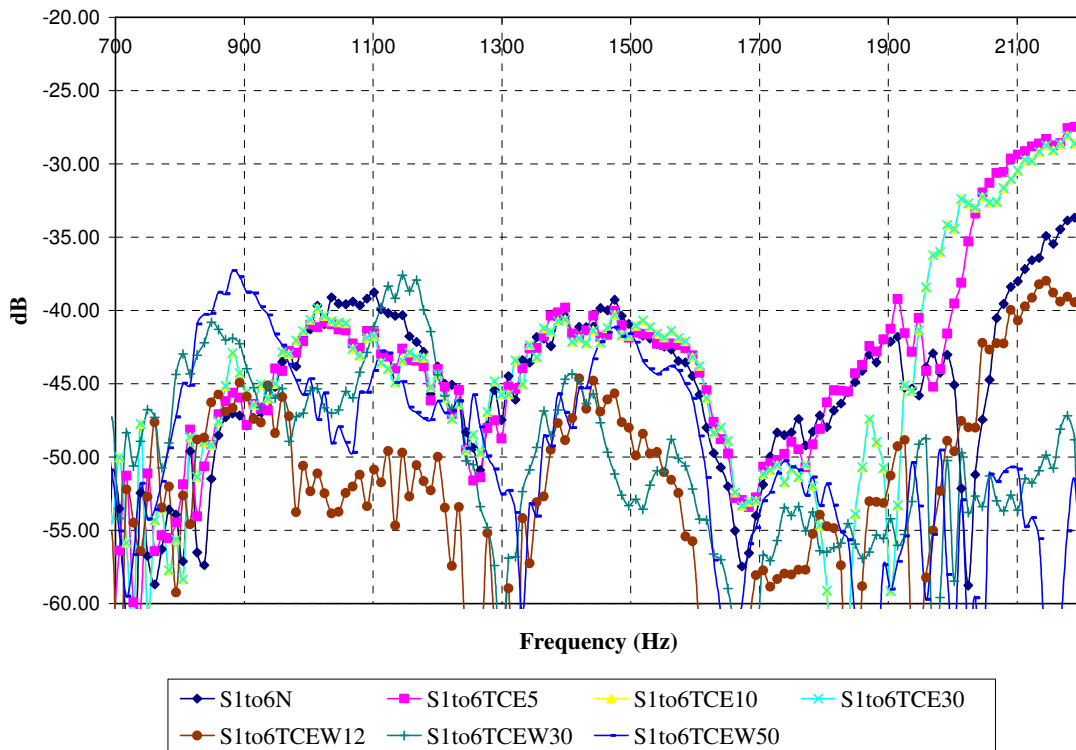


**Figure 7.3 Transmission measurement when receiver is in Port 6 and transmitter in Port 1-initially dry experiments**

#### 7.2.1.1.1 Effect of depth-dependent fluid distribution on electromagnetic response

Comparison of antenna transmission response along horizontal raypaths at 5, 10, 15, and 20 cm depth (Figures 7.2, 7.4, 7.5 and 7.6, respectively) show frequency-dependent variations in EM transmission properties. These variations are attributed to differences in

fluid distribution, heterogeneities, and potential boundaries effect. Although, it is difficult to describe and explain every variation, several frequency dependent trends can be established. Attenuations losses for soil and TCE-soil medium tend to decrease with higher frequencies for frequencies up to about 1100 MHz. After this frequency, attenuations losses remain relatively constant ( $\pm 10dB$ ) up to 1700 MHz (except for measurements at 10 cm depth). At higher frequencies, attenuation losses increase sharply and then decrease with frequency. Greater increase (sharper downward peak) is observed for measurements closer to the soil-atmospheric surfaces (Figure 7.2). No major differences are observed between measurements taken before or during TCE injection for depths other than 5 cm (closest to the surface) for frequencies below 1700 MHz. Differences between the transmission response before and after water infiltration at early infiltration times (20 min after infiltration onset) is greater near the surface, where water is infiltrating, than at deeper depths. For measurements taken after water infiltration, there is a sharp change in response at about 1900 and 2100 MHz, and the changes seem to be greater for greater volume of infiltrated water.

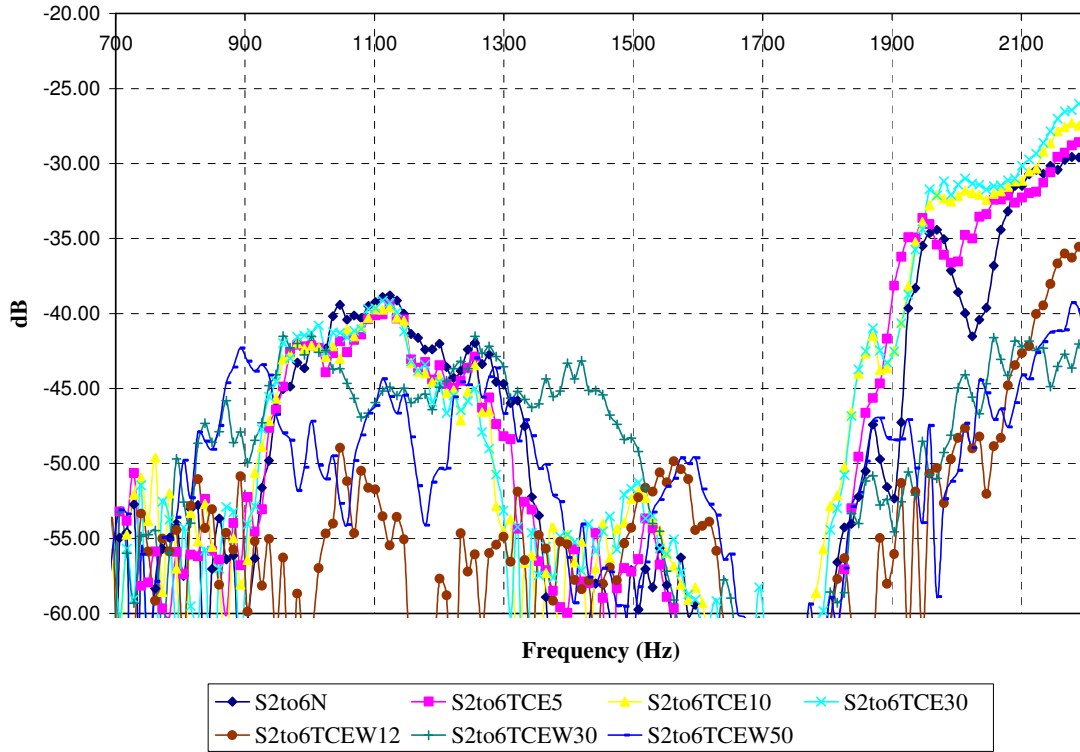


**Figure 7.4 Influence of depth in EM response receiver (Port 6)-transmitter (Port 2) initially dry experiments**

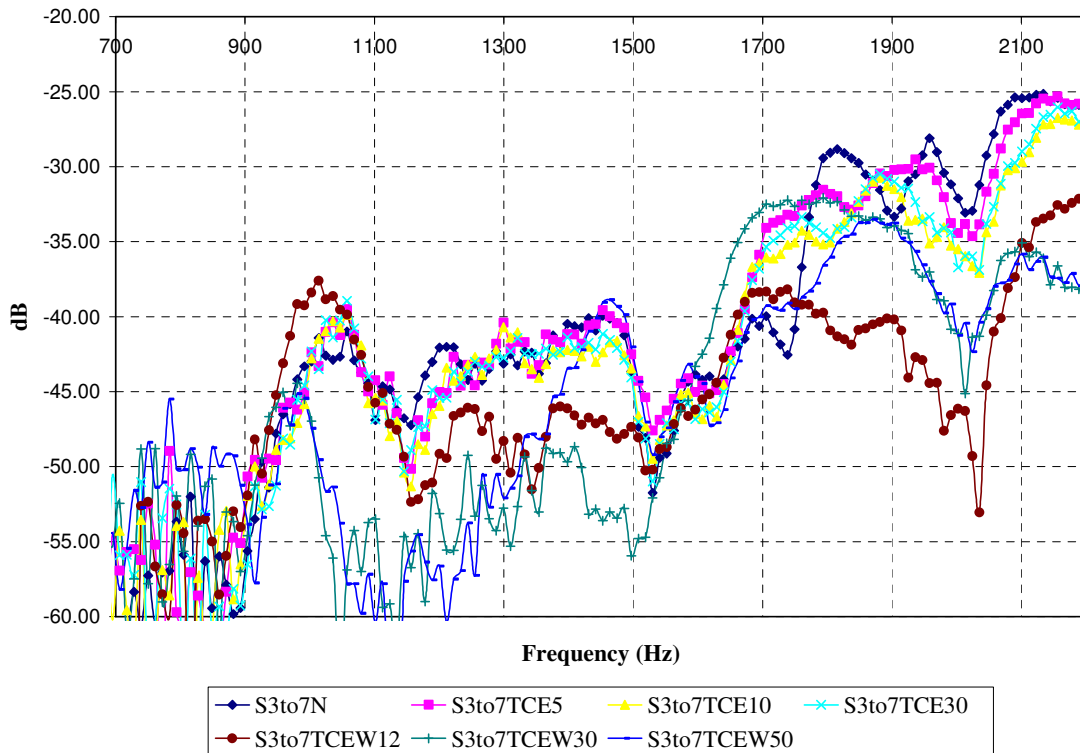


**Figure 7.5 Influence of depth in EM response receiver (Port 7)-transmitter (Port3) initially dry experiments**

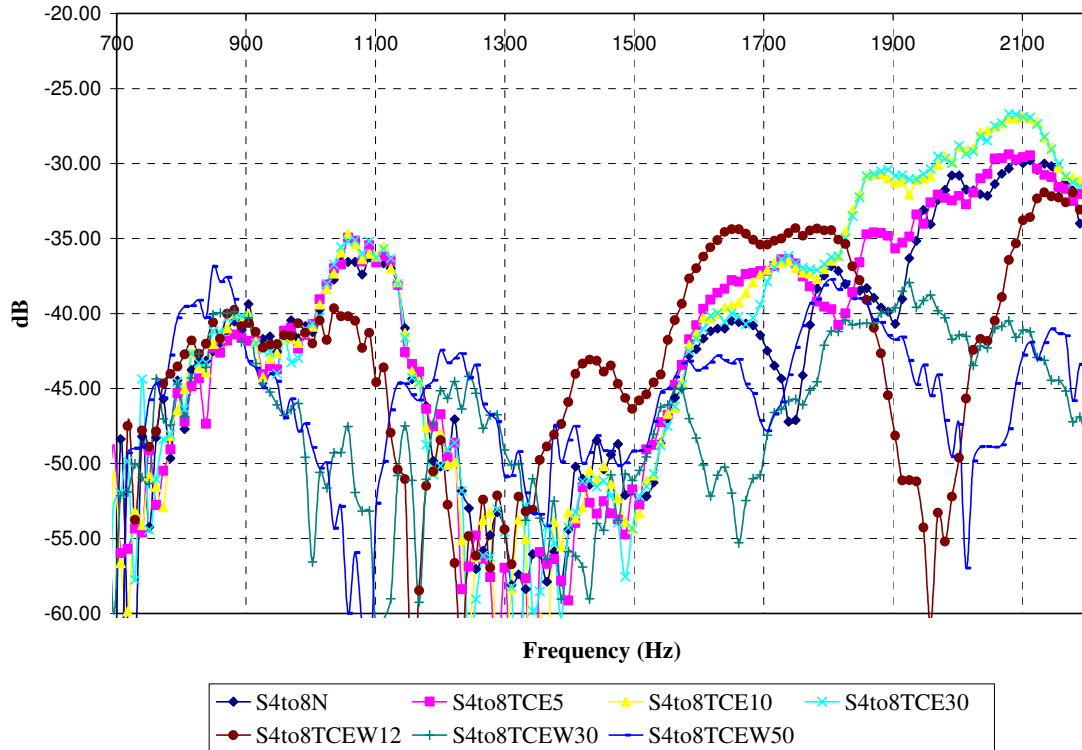


**Figure 7.6 Influence of depth in EM response receiver (Port 8)-transmitter (Port 4) initially dry experiments**

The following inferences are made from the results on the TCE and water infiltration experiments over initially-dry soil:

- The EM response along a raypath is influenced by soil-medium properties away from that raypath. For instance, response variations are observed during TCE injection at 5 cm, even though the injection is below this depth. This is attributed to wave scattering behavior.
- Transmission losses are generally greater along 10 cm depth raypath. This is potentially due to heterogeneities incorporated by the soil and the TCE injection system, although some losses may be caused by antenna transmission and receiving differences.

- Measurements at 5 and 20 cm may be influenced by the proximity to the air-soil and soil-soilBed bottom boundaries, respectively.
- Differences between transmission measurements prior to and after onset of water infiltration are caused by the presence of water which increases the transmission losses. Greater differences are observed when greater water volume has infiltrated, but are observed at early infiltration times near the surface. This is due to the infiltration lag-time (which increases with depth).
- Differential response at frequencies higher than 1700 MHz may be inversely related to volume of water infiltrated: that is the greater the volume of water infiltrated at a particular depth the lower the sharp changes. This is observed at higher depths, which show greater sharp changes in transmission properties between 1900-2100 MHz at early infiltration times. Also these changes are greater for deeper depths, where water has not reached at the time of measurements.
- Transmission response along raypath is influenced by flow heterogeneity, which possibly causes bending of the raypath.

#### *7.2.1.2 Reflection response*

Reflection response during TCE and water infiltration in initially-dry soil return losses about the same for each antenna independently of the condition in the soil (Figure 7.7 to Figure 7.10). Slight differences are observed in measurements taken before and after TCE and water injection for frequencies higher than 2000 MHz. This may be caused by

(medium-dependent) variation in antenna radiation properties and energy losses at the higher frequencies.

Differences in reflection measurements response is observed between antennas, suggesting different radiation characteristics of the antennas. Reflection loss at top and bottom about the same range (Figure 7.7 to Figure 7.10) suggest effects due to proximity to external boundaries. Maximum return losses (or lowest reflection) characteristics seem to be dependent on antennas and depth.

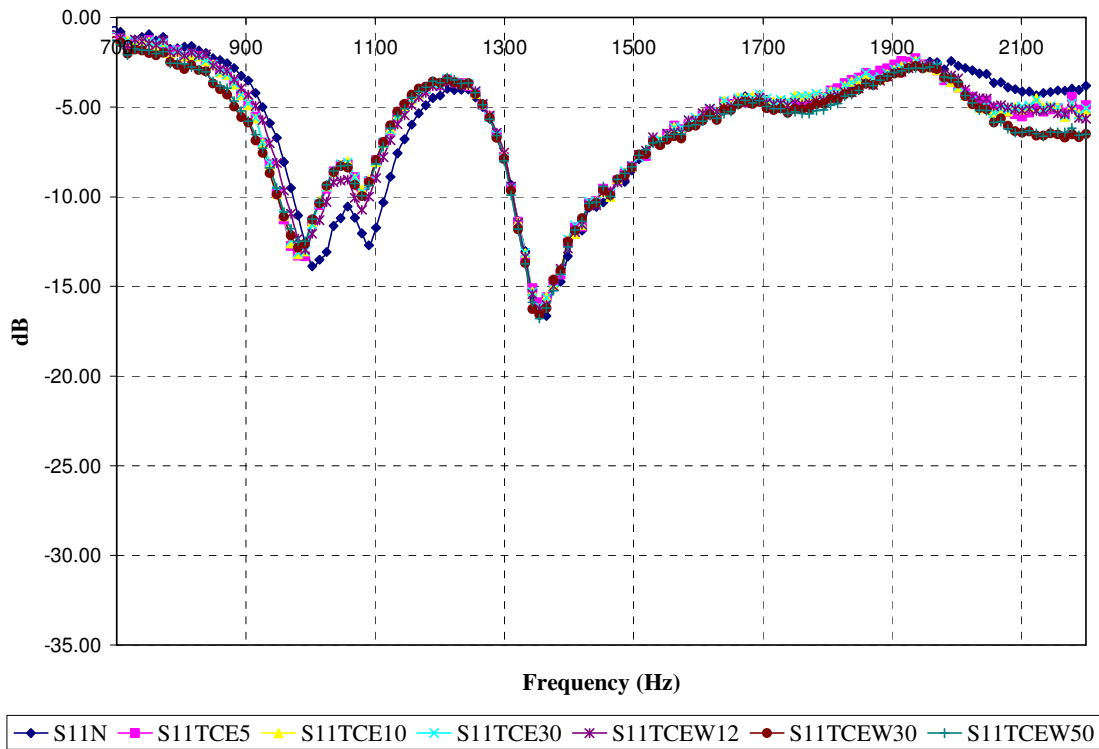


**Figure 7.7 Influence of depth in reflection response at Port 1-initially dry conditions**

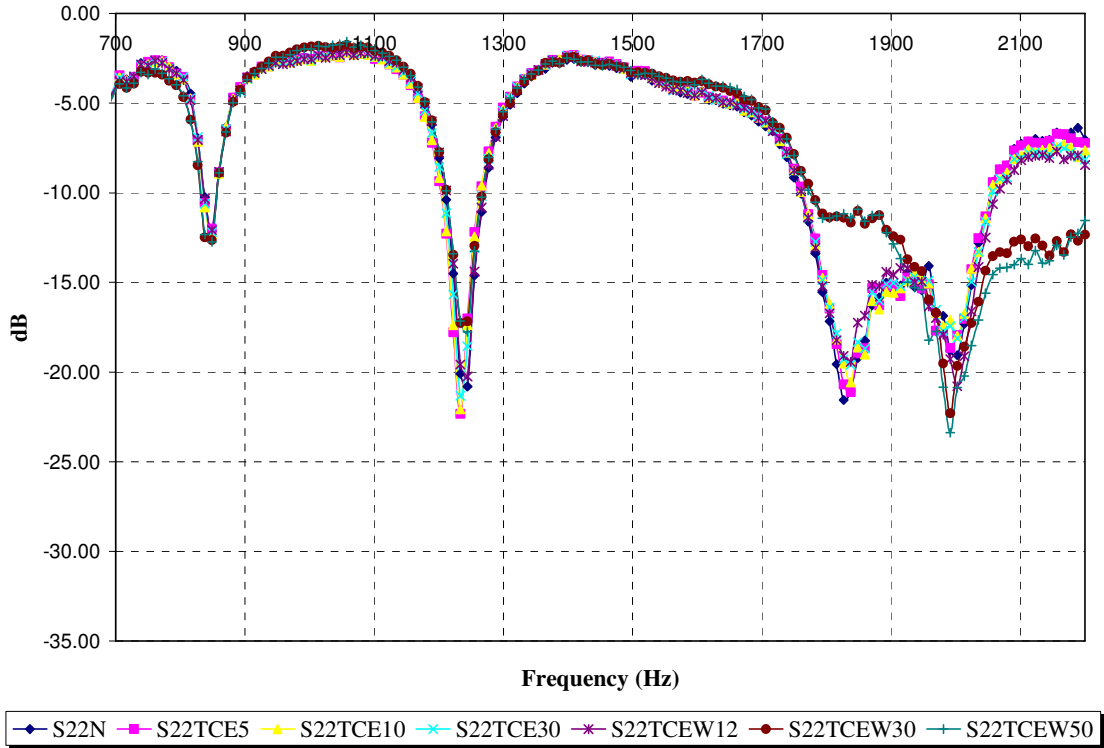


**Figure 7.8 Influence of depth in reflection response at Port 2 initially dry experiments**

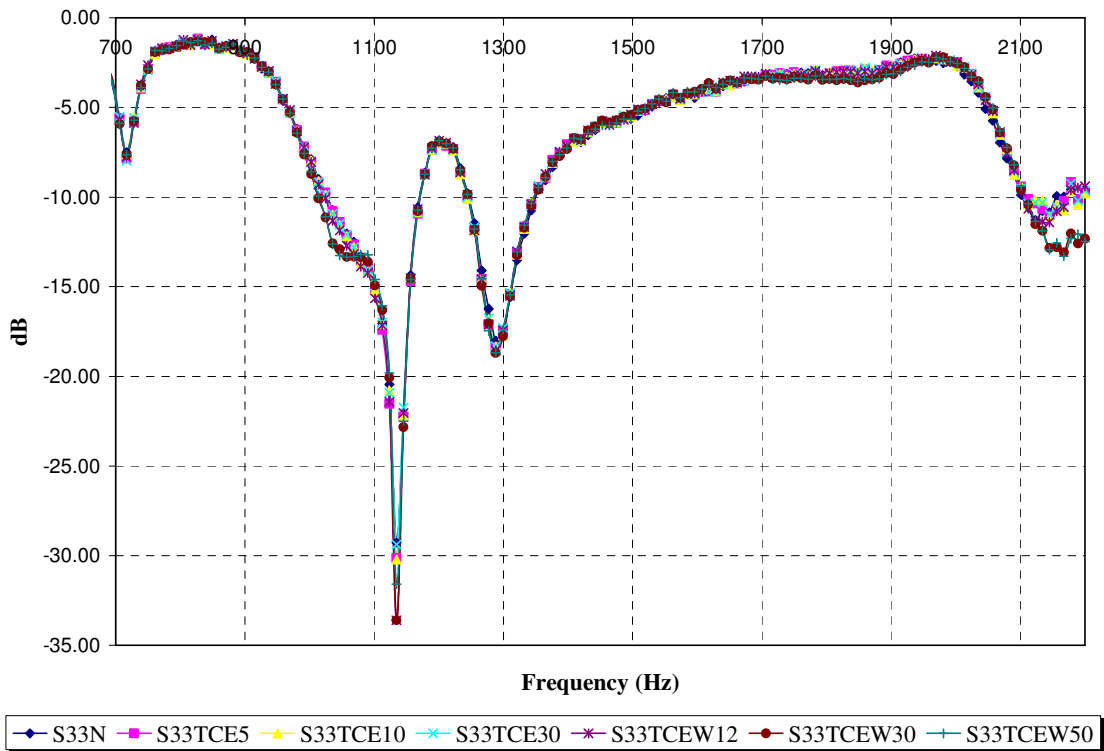


**Figure 7.9 Influence of depth in reflection response at Port 3 initially-dry experiments**

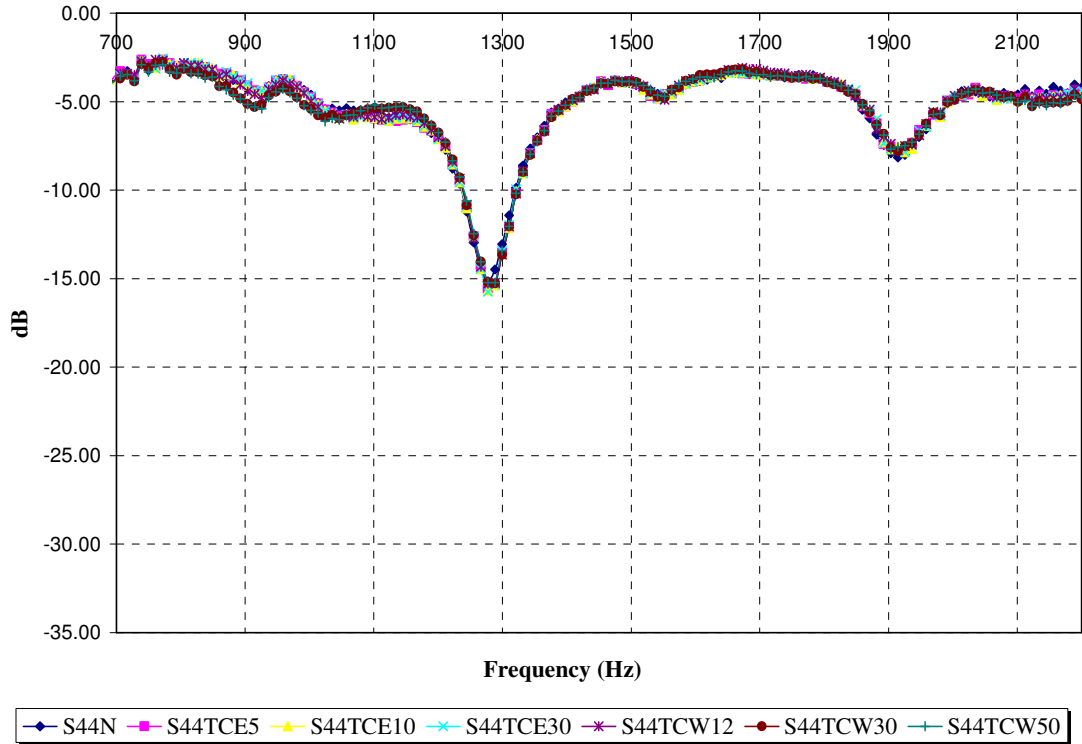


**Figure 7.10 Influence of depth in reflection response at Port 4 initially-dry experiments**

### 7.2.2 Water saturation conditions

Transmission measurements for soilBed saturation experiments are shown in Figure 7.11 to Figure 7.17. These experiments were conducted in a different soilBed than those for the initially-dry experiments, and show slightly different dry condition results. The results are presented according to the soilBed saturation degree (e.g. 25, 50, 75%) and time after onset of TCE injection. The legend in the figures is shown as:  $S_{iTojStatus}$ , where  $i$  and  $j$  represent the transmitting and receiving antennas and status represent the saturation and TCE injection status:

- “N” represents measurements taken prior to saturation
- “half” represents measurements taken when the soilBed was 50% saturated (from the bottom)

- “quarter” represents measurements taken when the soilBed was 75% saturated
- “wet” represents measurements taken when the soilBed was 100% saturated
- “10min” represents measurements taken after 10 min onset TCE injection
- “45min” represents measurements taken after 45 min onset TCE injection

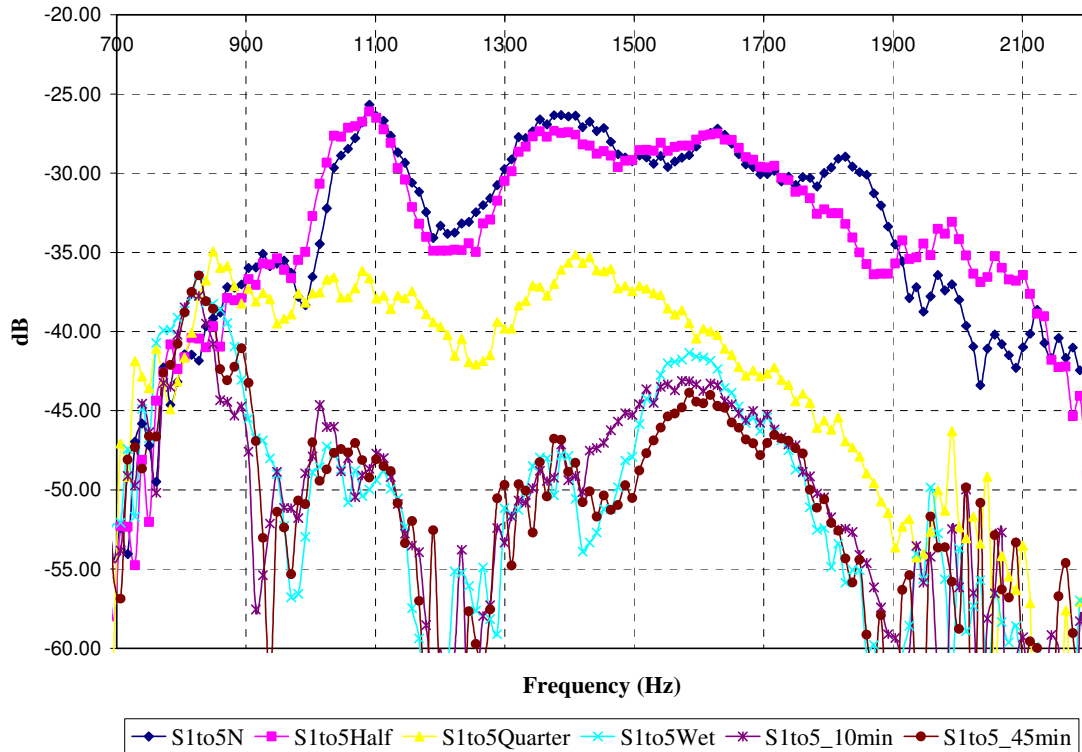


**Figure 7.11 Transmission measurement at receiver (Port 5) when -transmitter (Port 1) during saturation**

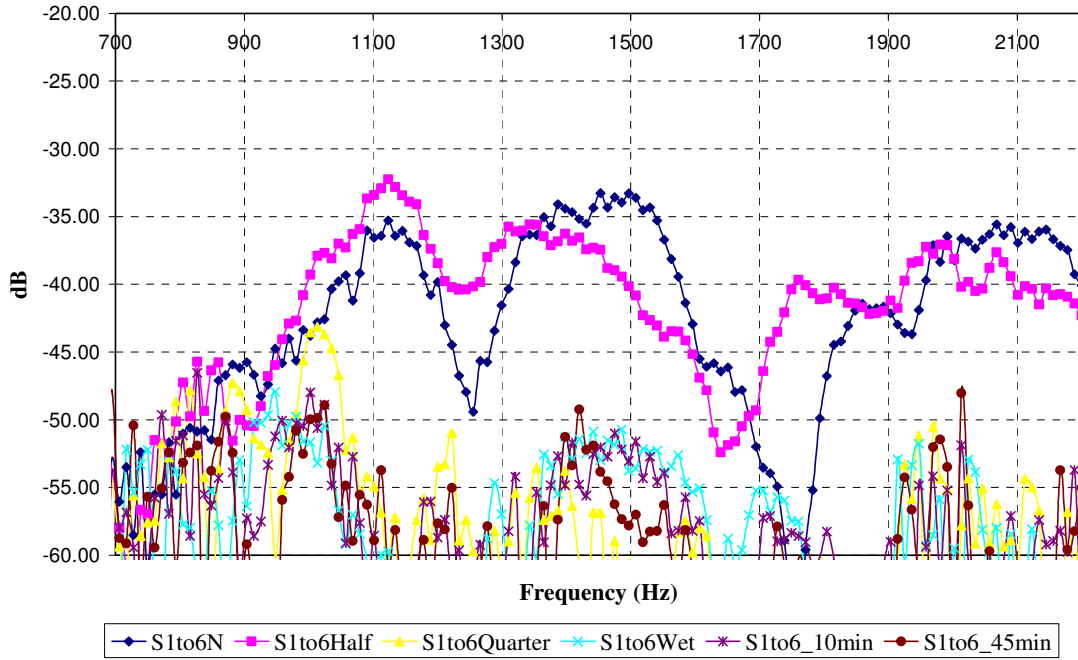


**Figure 7.12 Transmission measurement receiver (Port 6)-transmitter (Port 1) during saturation**

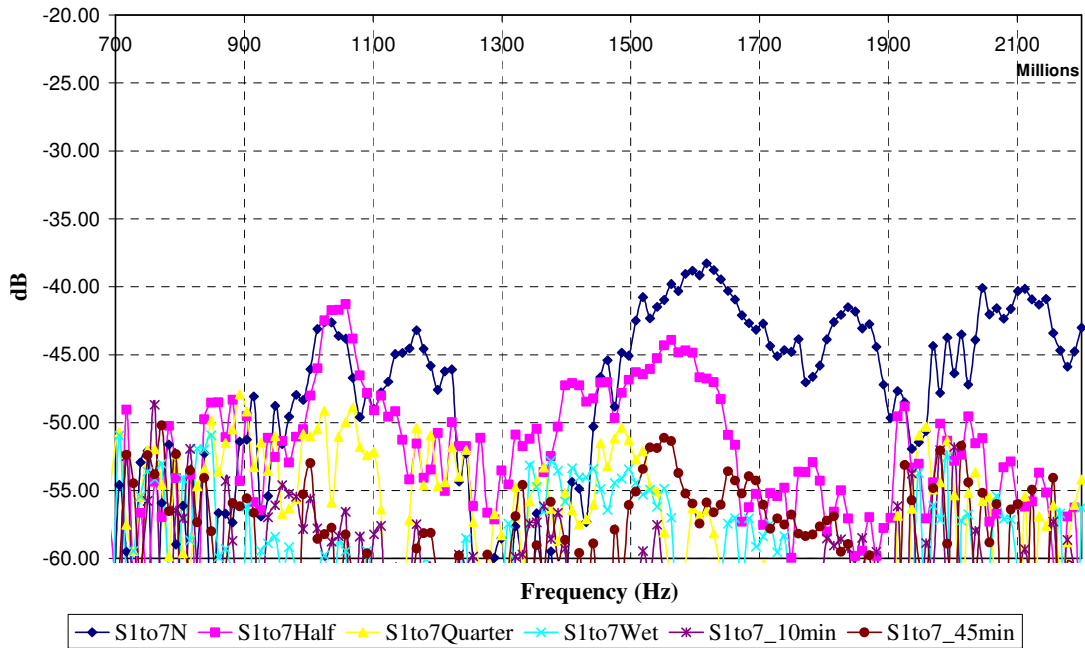


**Figure 7.13 Transmission measurement receiver (Port 7)-transmitter (Port 1) during saturation**

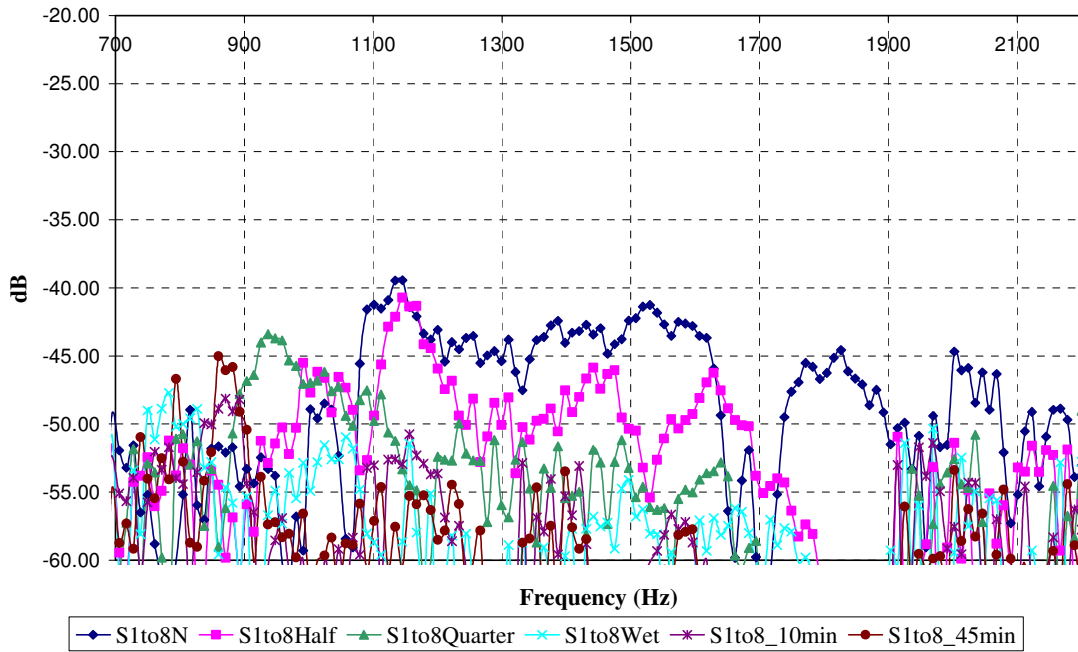


**Figure 7.14 Transmission measurement receiver (Port 8)-transmitter (Port 1) during saturation**

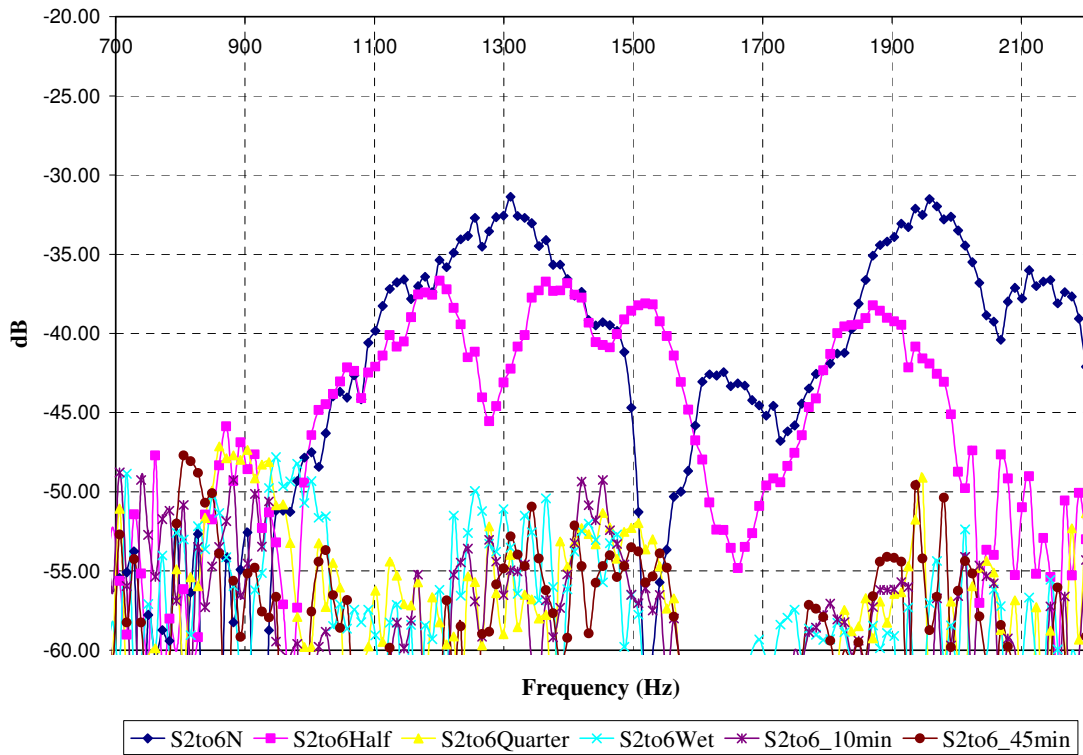


**Figure 7.15 Transmission measurement receiver (Port 6)-transmitter (Port 2) during saturation**

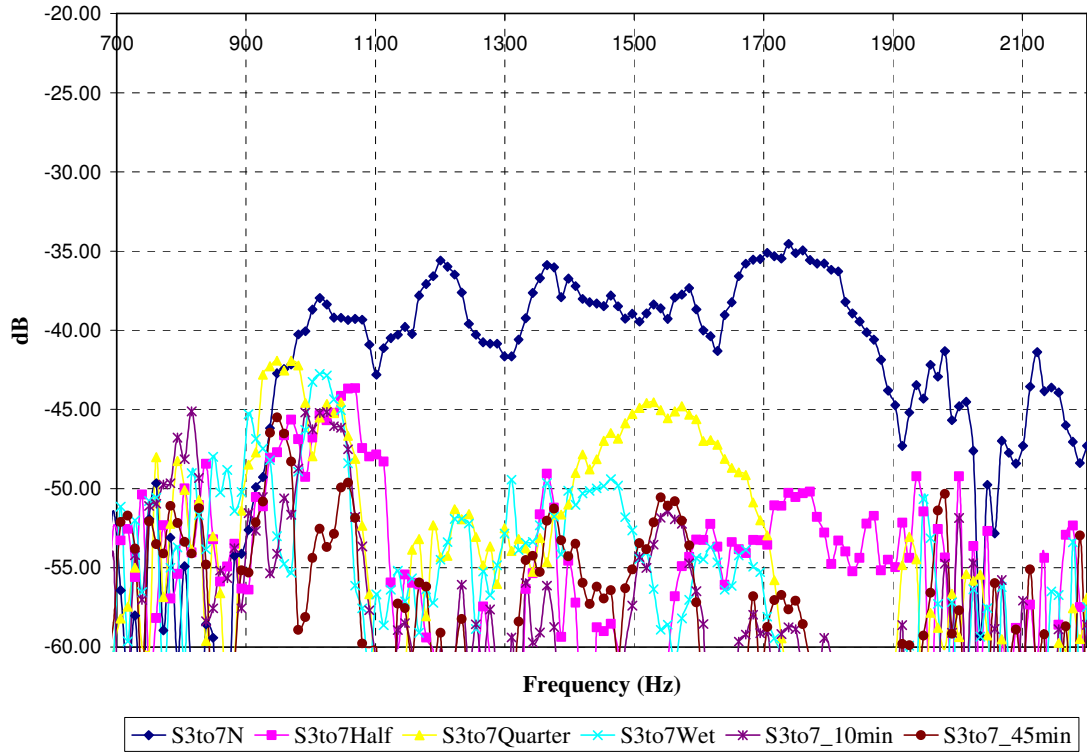


**Figure 7.16** Transmission measurement receiver (Port 7)-transmitter (Port 3) during saturation

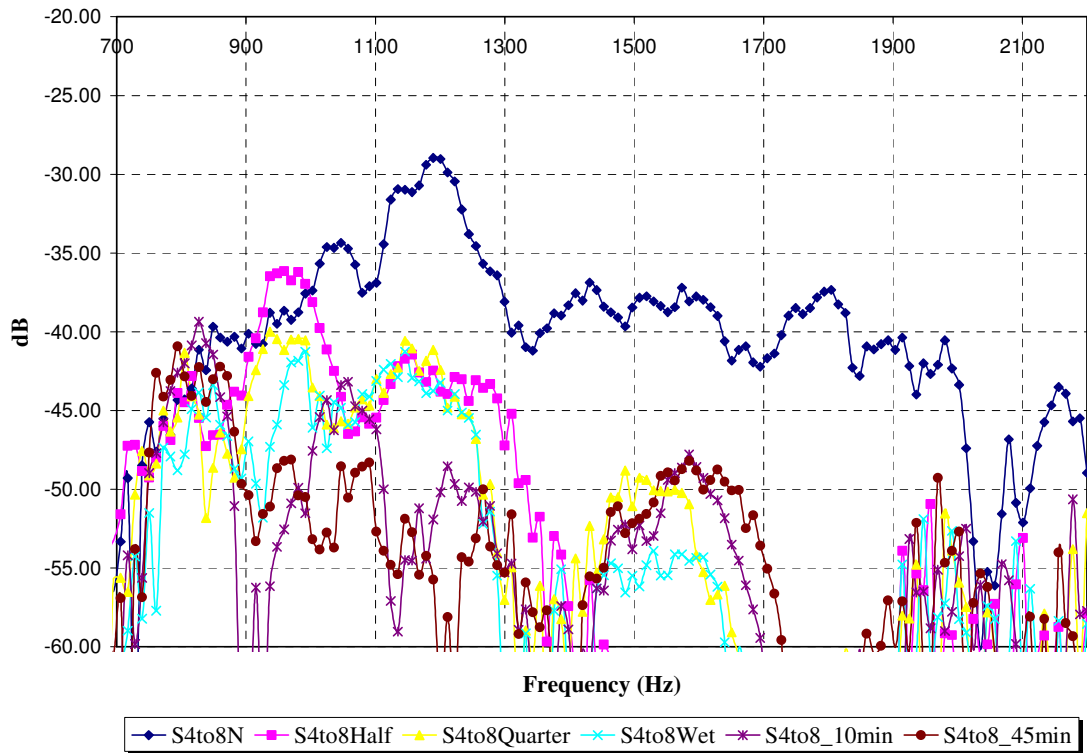


**Figure 7.17** Transmission measurement receiver (Port 8)-transmitter (Port 4) during saturation

### *7.2.2.1 Transmission response under water saturation*

Comparison of transmission measurements for conditions prior to saturation from antenna 1 (close to soil-surface) to other antennas across the soilBed (Figure 7.11 to Figure 7.14) indicate greater attenuation losses at greater raypath distances. The shortest distance (i.e., raypath 1 to 5) also coincides with the driest soil condition and therefore lowest attenuation losses during the saturation experiments.

Generally, greater attenuation losses are observed when water saturated conditions exists near the measurement antennas (Figure 7.11 to Figure 7.14). Because saturation degree is from the bottom of the soilBed, the absolute effect depends on the location of the antenna. For antennas located near the soil surface (Figure 7.11), this does not occur until the soilBed is fully saturated. For antennas 10-cm below the surface (20-cm above the soilBed bottom) it does not occur until the soilBed is approximately 75% saturated. The effect of water presence is, however, perceived by the antennas for saturation levels below this level, indicating wave scattering effects. Transmission measurements for deeper saturated ports (Figure 7.13 and Figure 7.14) indicate greater attenuation losses at greater degrees of soilBed saturation, reaching values near noise level at saturation. The lower transmission response (greater losses) is attributed to greater conduction losses in the presence of water and greater reflection losses caused by the water-air interface.

Comparison of antenna transmission response along horizontal raypaths at 5 cm (Figure 7.11), 10 cm (Figure 7.15), 15 cm (Figure 7.16), and 20 cm (Figure 7.17) depth prior to,

during, and after saturation reflect depth-dependent variations caused by antenna, bulk soil, and saturation differences.

Transmission measurements prior to saturation behave similarly in all antennas. The raypath closest to the surface (Figure 7.11) show the lowest attenuation losses with transmission measurements between -25dB and -40dB for frequencies between 1000 and 2000 MHz. Greatest variations are observed for antennas at 10 cm below soil surface, ranging mostly between -32dB and -45dB for the same frequency. Differences along the horizontal raypaths for conditions prior to injection are attributed to medium heterogeneities and potential boundary effects.

Similar to the transmission behavior for cross raypaths measurements, attenuation losses along horizontal raypaths are greater for all antennas at saturation. Antenna response at saturation for depths below 10 cm (Figure 7.15 to Figure 7.17) show greater losses than the antenna close to the surface (Figure 7.11), and subjected lower saturation depth. Deeper antennas measurements fall below noise level for frequencies ranging between 1650 and 1900 MHz.

### *7.2.2 2 Reflection response under water saturation*

The reflection response of antennas at 5 cm (Figure 7.18), 10 cm (Figure 7.19), 15 cm (Figure 7.20), and 20 cm (Figure 7.21) below the soil surface show similar return-losses behavior to those observed for initially-dry experiments (Figure 7.8 to Figure 7.10). Under water saturation there is, however, differences between measurements taken prior

to water saturation and after saturation has commenced. An apparent shift in the reflection response is observed in which peak responses (maxims and minims) are shifted to slightly higher frequencies after water saturation. The behavior is depth dependent, with greater return losses observed for the antennas farther from the top and bottom boundaries (antennas at Port 2 and 3, Figure 7.19 and Figure 7.20, respectively).

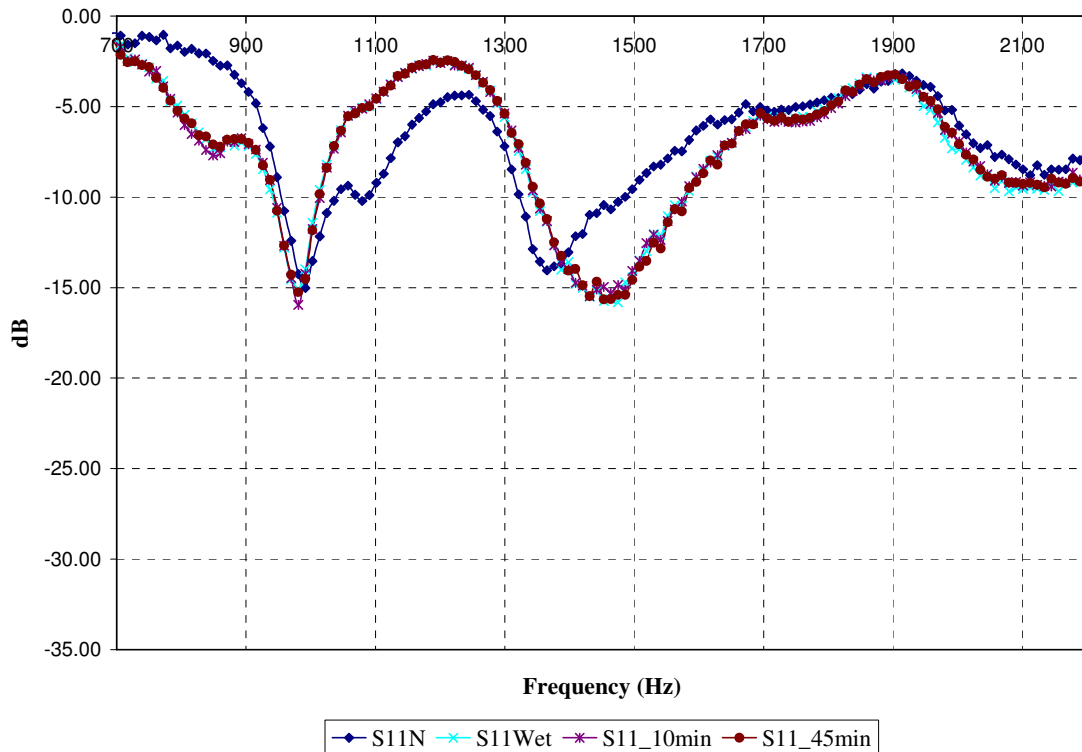


**Figure 7.18 Influence of depth in reflection response at Port 1 (at 5 cm from top) - saturated condition**

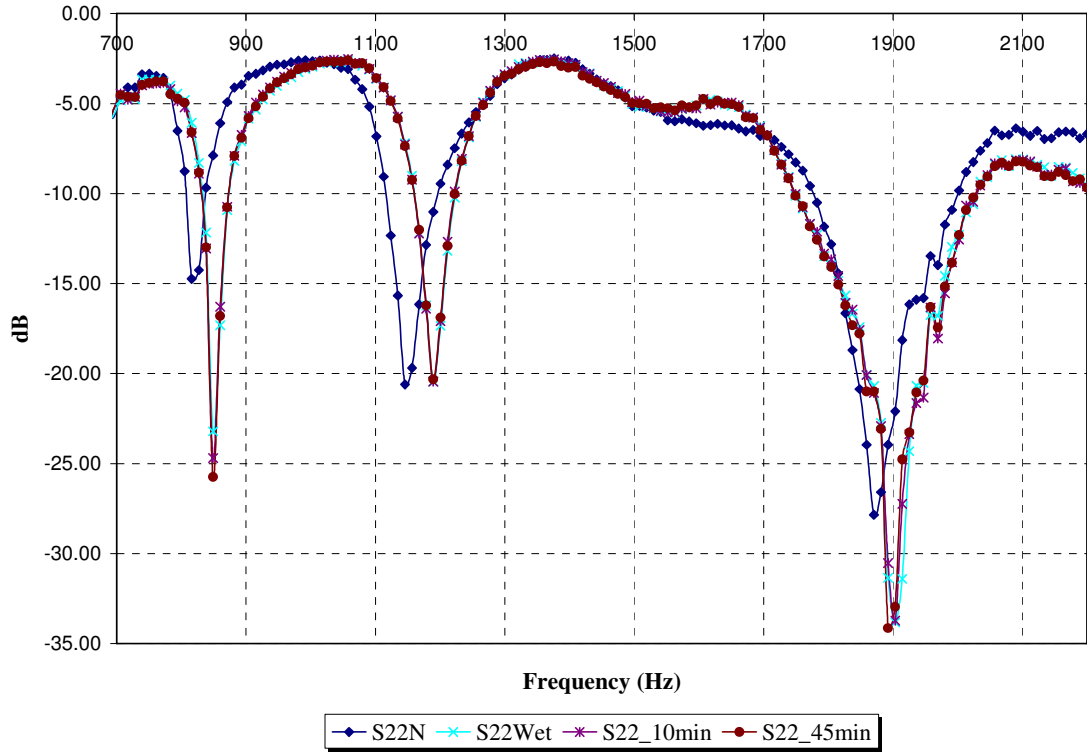


**Figure 7.19 Influence of depth in reflection response at Port 2 (at 10 cm from top) - saturated condition**

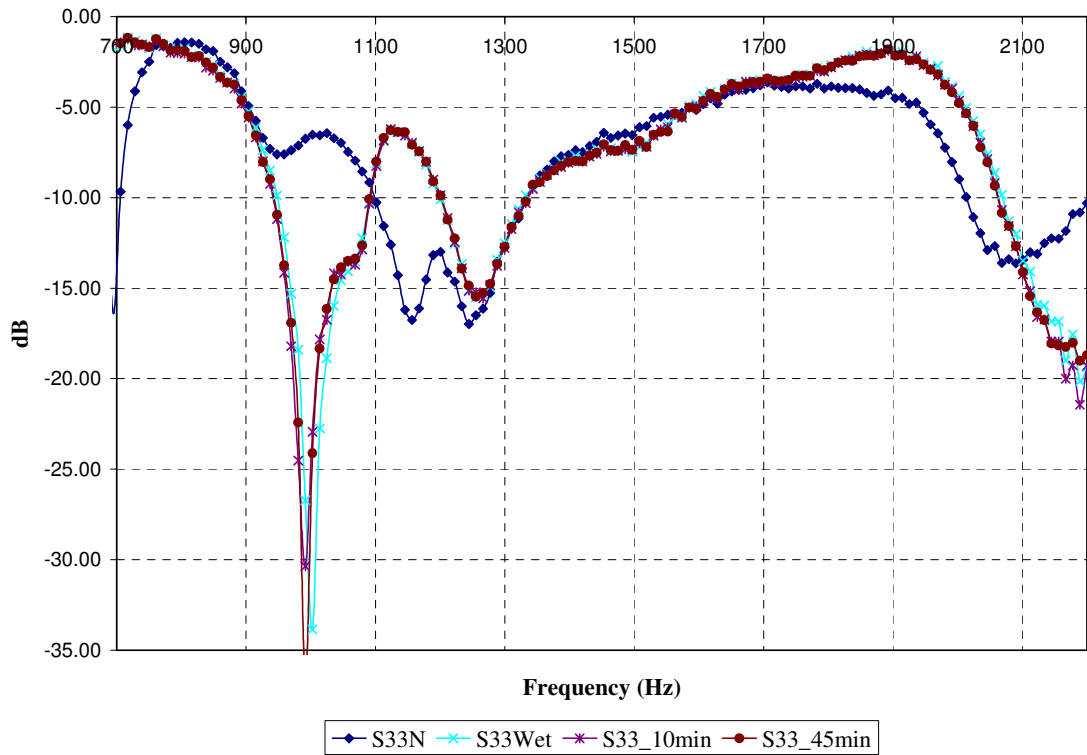


**Figure 7.20 Influence of depth in reflection response at Port 3 (at 15 cm from top) - saturated condition**

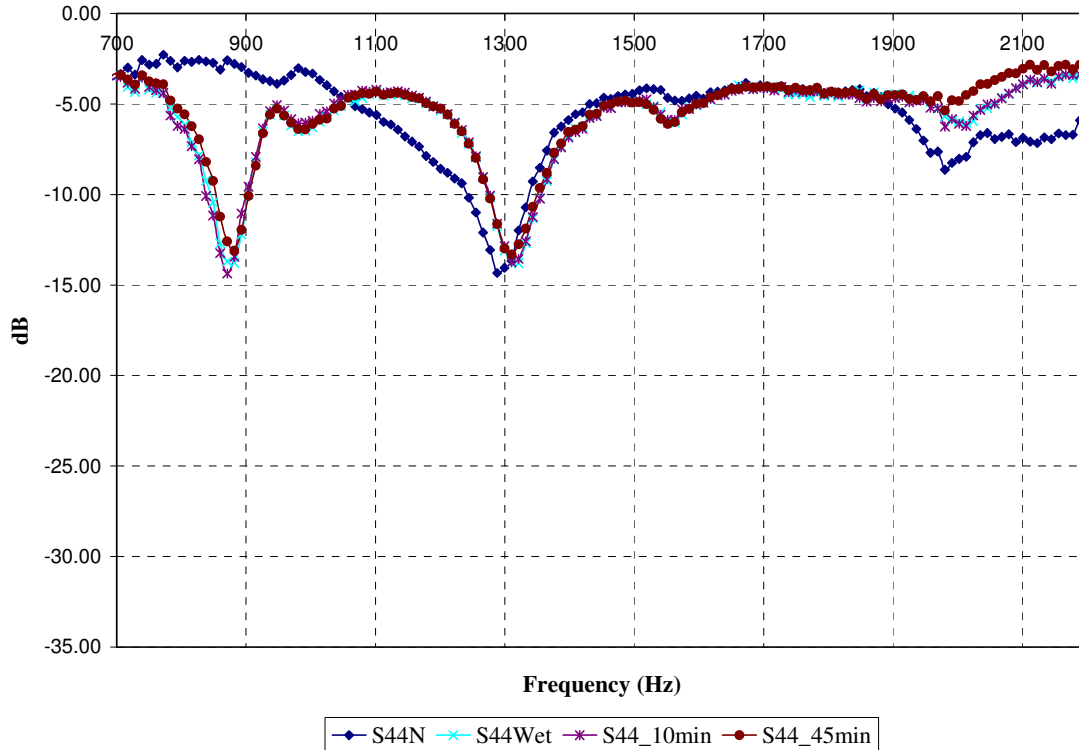


**Figure 7.21 Influence of depth in reflection response at Port 4 (at 20 cm from top)-saturated condition**

Greater return losses are observed for frequencies between 800 and 1000 MHz and 1200 to 1500 MHz for the antennas closest to the top and bottom boundaries (Port 1 and 4, Figure 7.18 and Figure 7.21, respectively). From the antennas farther away from the boundaries high return losses are observed for frequencies between 800 and 1000 MHz, 1100 and 1300 MHz, and 1800 and 2100 MHz. These results suggest some effect from the boundary condition of the soil and/or soil heterogeneities.

The relative reflection response of the antennas (relative to conditions prior to water saturation) shows frequency dependence. For frequencies below about 1000MHz, these return losses tend to be higher for water-saturated than dry soil. For greater frequencies, relative return losses depend in the location of the antennas, but generally show greater

return losses for dry soils between 1000 and 1300 MHz. For the antennas near the surface (Figure 7.18) greater return losses are observed, again, for frequencies between 1350 – 1700 MHz) for saturated conditions and above about 2000 MHz. Antennas near the bottom (Figure 7.21) show little difference prior to and after saturation from 1300 to about 1900 MHz. Above this frequency range the dry soil shows greater returns losses. The overall reflection results suggest that the frequency-dependent radiation characteristics of the antennas are influenced by the saturation condition of the soil.

### *7.2.2.3 Electromagnetic measurements in the presence of TCE in water-saturation experiments*

Transmission measurements during TCE injection under water saturated conditions show slight variations from measurements taken prior to injection (Figure 7.11 to Figure 7.17), but are too close to the VNA noise level to make conclusive remarks. Low transmission measurements are attributed to the attenuation losses caused by water prior to the TCE injection. Slight differences in measurements before and after TCE injection are more noticeable from shorter raypath (Figure 7.11 and Figure 7.12) in the frequency range between about 1400 to 1600 MHz due to lower attenuation path. At these frequencies range the presence of TCE shows a slight increase in attenuation losses, but they are depth (or location) dependent. Slight variations are also observed for horizontal raypaths at 15 and 20 cm depths (Figure 7.16 and Figure 7.17) in the 900 to 1100 MHz. The slight attenuation losses may be attributed to energy losses caused by reflection at TCE-soil-water interfaces. Because of the heterogeneities distribution of the TCE and the closeness of measurements to noise level it is, however, difficult to identify tendencies in

the transmission measurements. Reflection measurements (Figure 7.18 to Figure 7.22) show no major differences before and after TCE injections except at the deeper depths (Figure 7.20 and Figure 7.21) for frequencies above 2000 MHz.

### **7.3 VARIATIONS IN DIELECTRIC PERMITTIVITY**

All experiments were conducted to identify the CWR efficiency to detect DNAPLs and/or object inside the soil matrix using S-parameters, which are used to estimated variations in dielectric properties. These properties were estimated in a sandy soil under dry and saturated conditions using a code developed in Matlab (Appendix 1).

Transmission and reflection measurements (Section 7.2) indicate that the EM response is affected when a fluid is introduced into the system. This effect is caused by changes in dielectric properties of the bulk soil in the presence of fluid, object, or soil heterogeneities (Figure 7.22 to Figure 7.36). Assuming lossless medium, these changes are mostly associated with variations in the relative permittivity of the perturbed medium. Based on the premises described in Chapter 3 (section 3.6), and assuming perfectly coupled and identical radiation characteristics of antennas, relative permittivity along raypaths were determined from transmission and reflection measurements. Permittivity values were estimated for measurements taken under the imposed experimental conditions using the Permittivity Code developed in Matlab (Appendix 1). Because these properties are frequency dependent, the permittivities were estimated for a frequency range around 1100 MHz ( $\pm 100$  MHz). This frequency range was selected because the electromagnetic

measurements were above the noise level (Figure 7.22 and Figure.7.23). The other electromagnetic responses for the other experimental data are included in Appendix 6.

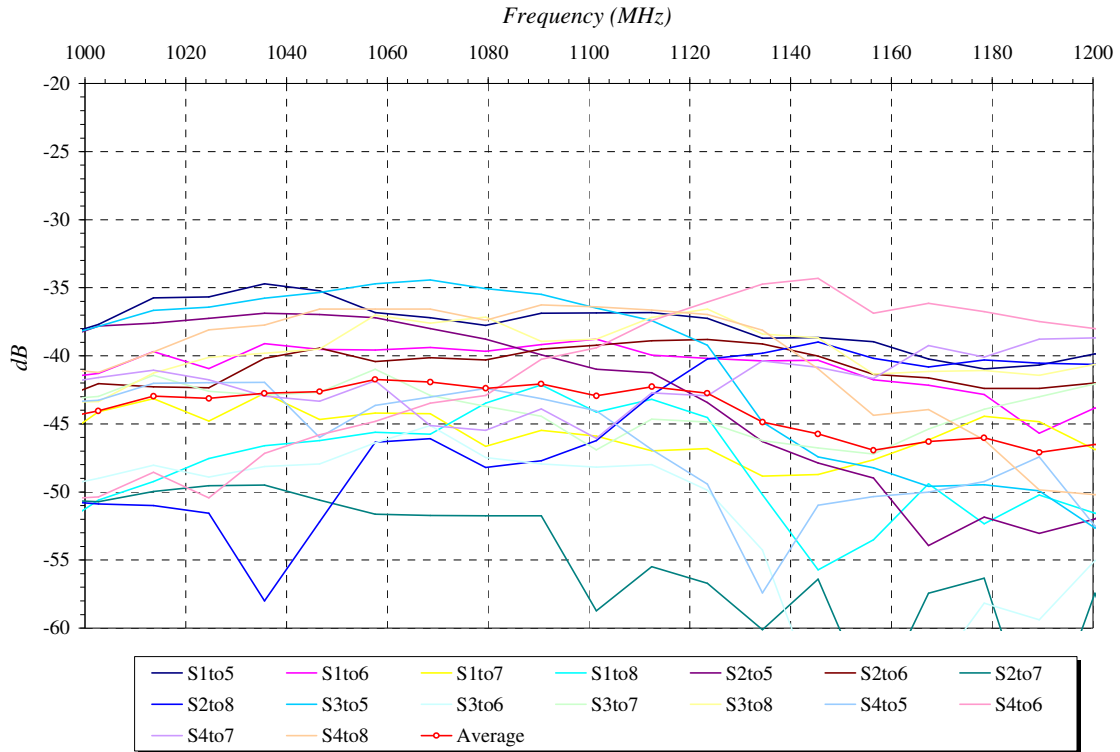


**Figure 7.22 Transmission electromagnetic response in initially-dry experiments**

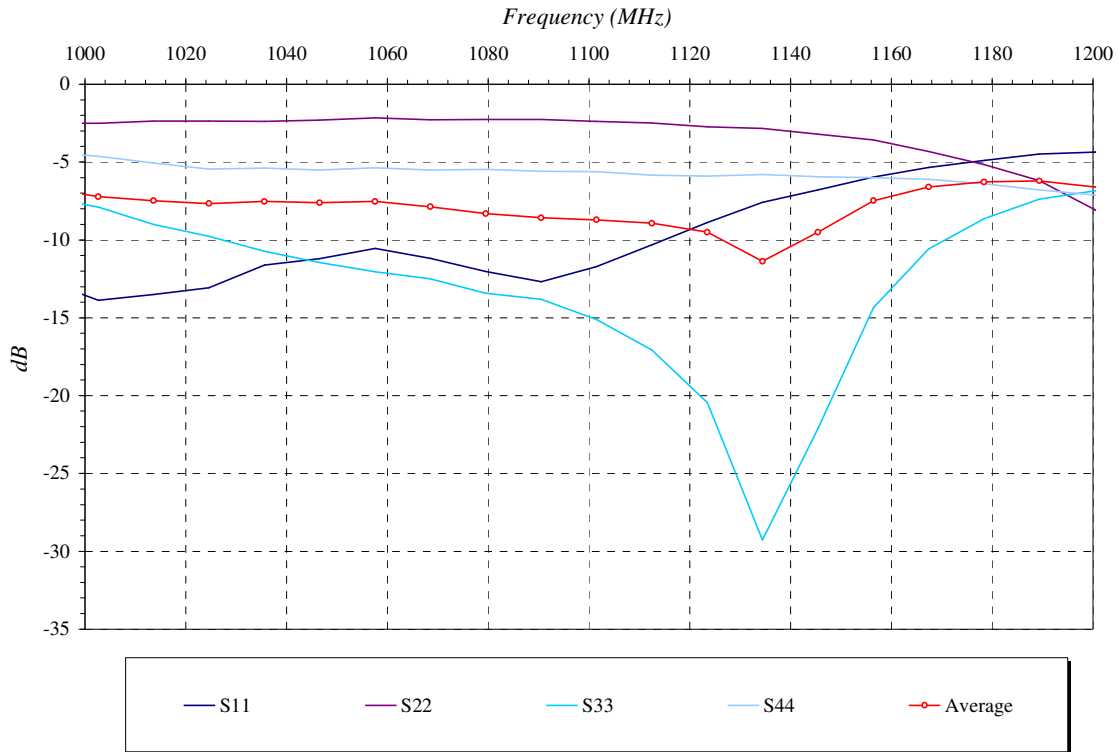


**Figure.7.23 Reflection electromagnetic response in initially-dry experiments**

### 7.3.1 Variations of dielectric properties in initially dry soil experiments

Permittivity estimates prior to and after 5, 10, and 30 minutes TCE injection are shown in Figure 7.24 to Figure 7.27. Physically impossible relative permittivity below 1 are observed at various frequencies. The unrealistic estimates are attributed to the effect of: (1) different radiation characteristics of antennas; (2) measurement proximity to soilBed boundaries; (3) lossless medium assumption; and (4) straight raypath assumptions. It is recommended that these effects be addressed in future studies to enhance the estimates of electromagnetic properties. For comparative purposes and change detection assessment all acceptable values ( $>1$ ) are believed to be applicable.

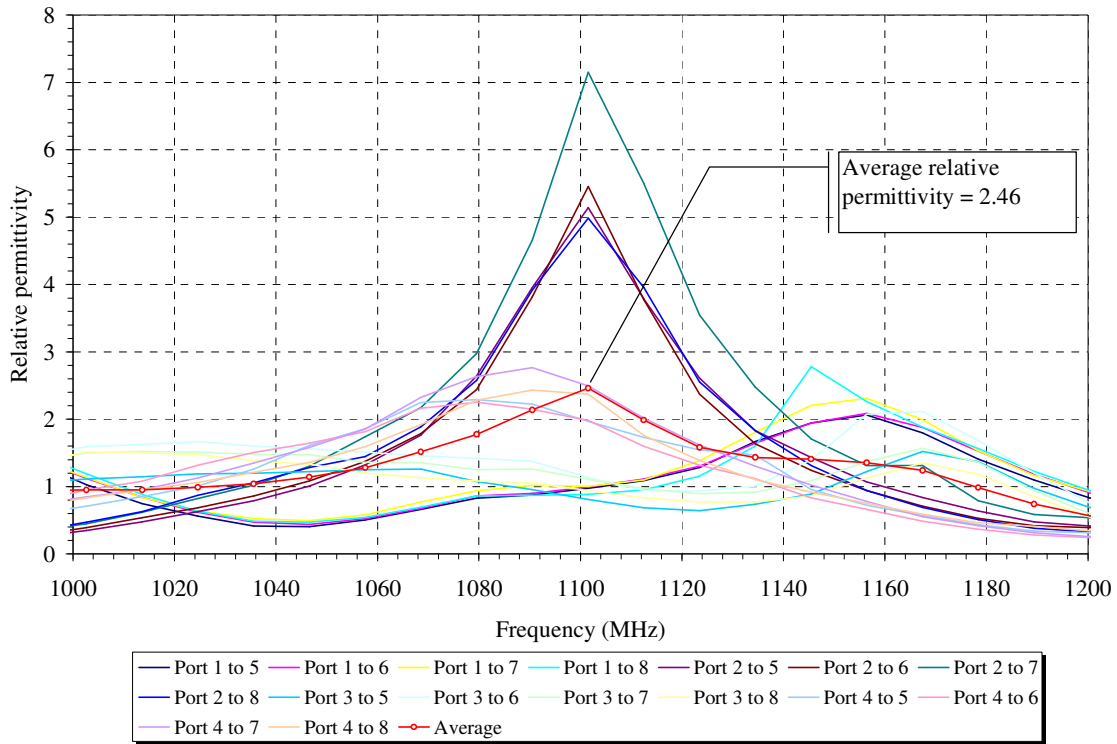


**Figure 7.24** Relative permittivity values for dry soil in initially-dry experiments

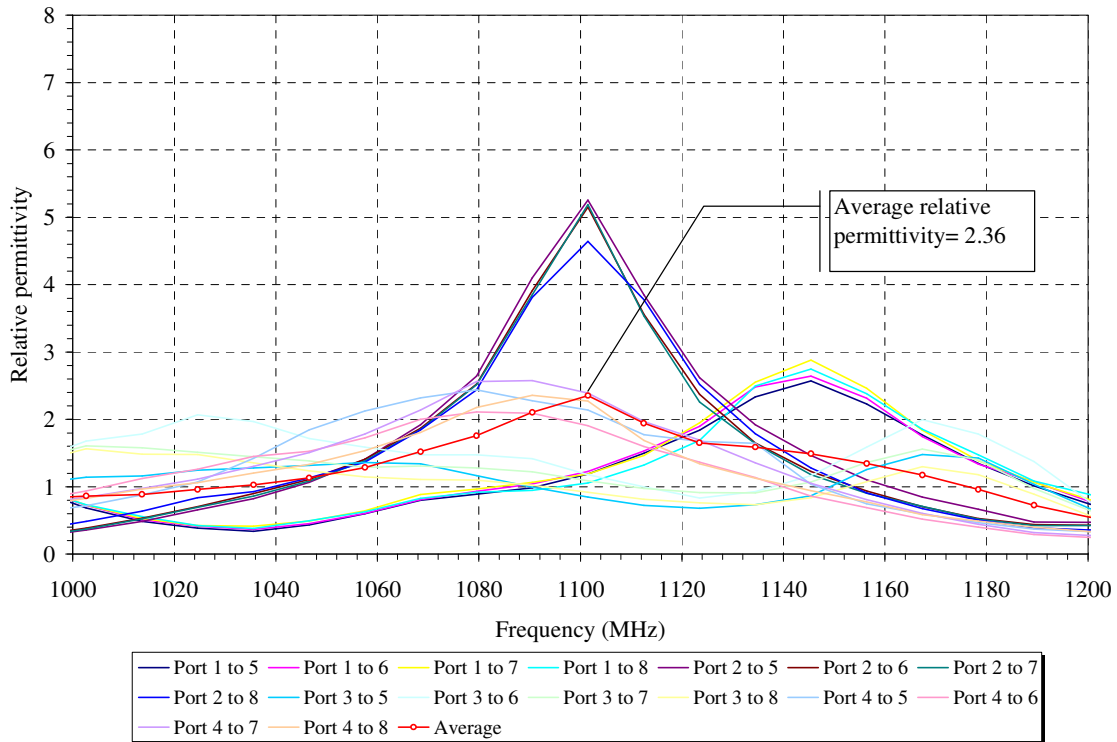


**Figure 7.25** Relative permittivity values after 5 min TCE injection in initially-dry experiments

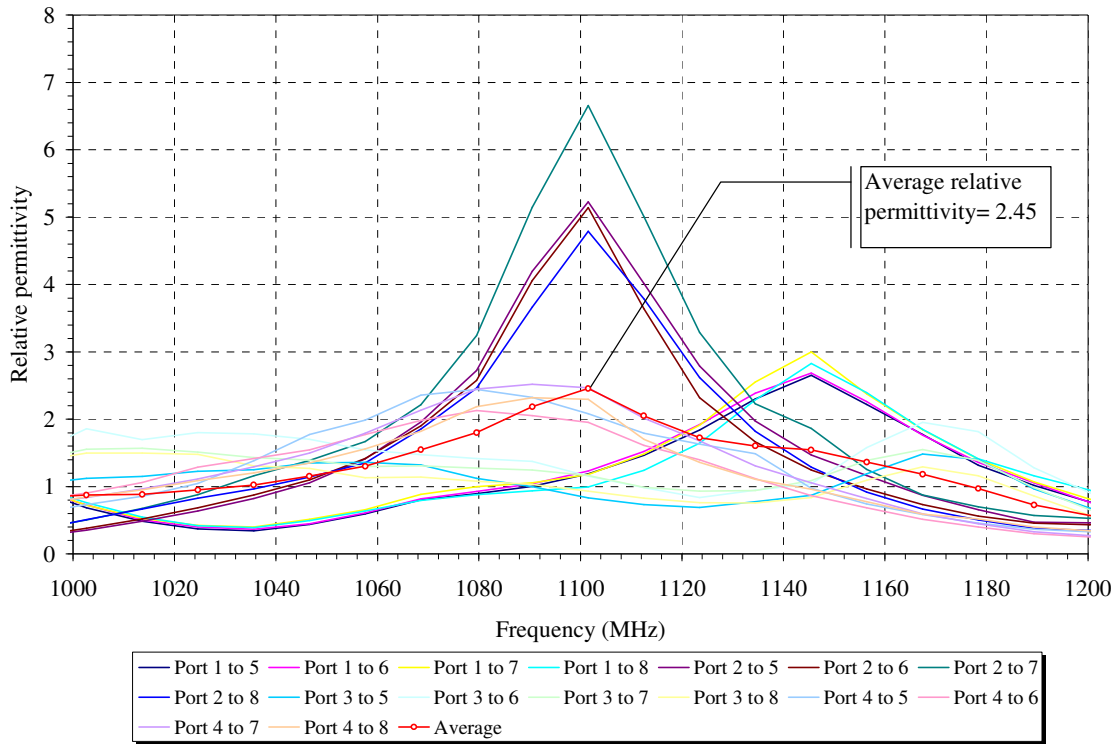


**Figure 7.26** Relative permittivity value after 10 min TCE injection in initially-dry experiments

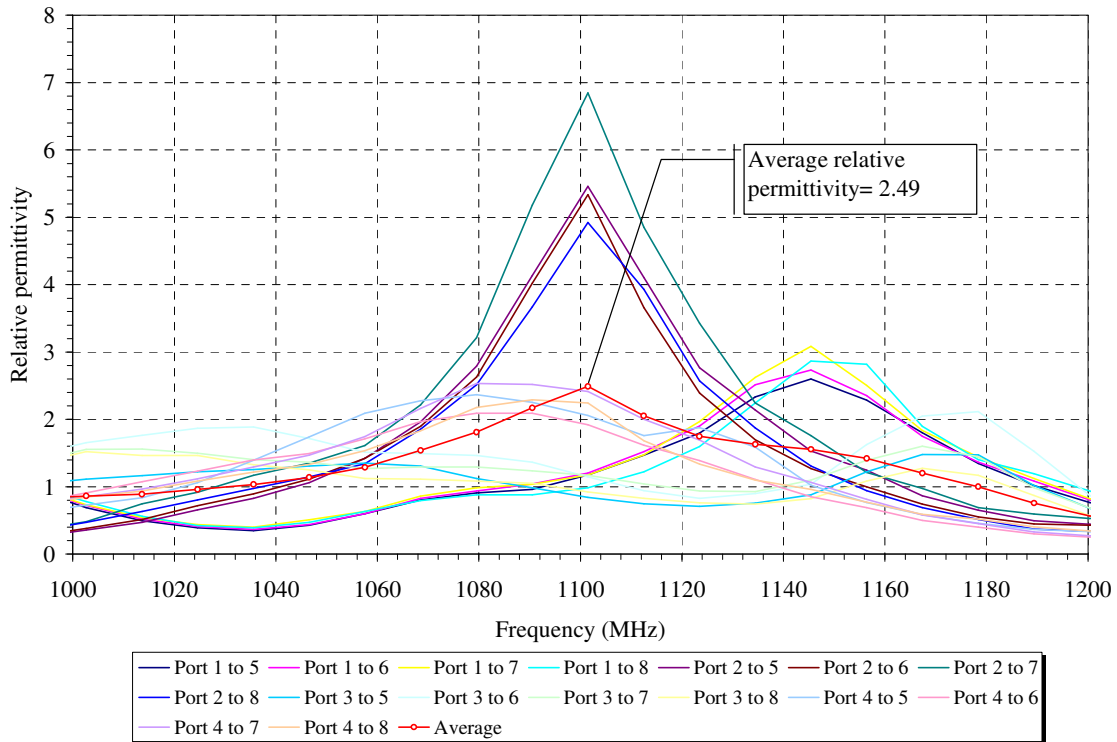


**Figure 7.27** Relative permittivity values after 30 min TCE injection in initially-dry experiments

For the initial dry conditions prior to TCE injection (Figure 7.24) most permittivity estimates fall within acceptable values for frequencies between 1040 and 1160 MHz. Permittivity estimates within the evaluated frequency range tend to initially increase with frequency, reaching a maximum and then decreasing with further increase in frequency. The maximum values and frequency at maximum values seem to be related to position of sending antenna. Maximum estimated values were observed for measurements sent from Port 2 (located 10 cm from the soil surface) at about 1100 MHz and range between 5 and 7. Lowest maximum estimates (between 1.3 and 2) were observed at about 1170 MHz for measurements sent from Port 3 (located 15 cm from the surface). Differences in magnitude and frequency at maximum value may be attributed to the effect of soil bottom and top boundaries, the presence of heterogeneities (such as that created by the injection to be located at 15 below the surface), and different radiation characteristics of the sending and receiving antennas. Maximum average permittivity of 2.46 ( $\pm 0.38$ ) is estimated for the dry sand at about 1000 MHz. This value is within the range of reported permittivity values for dry sand (see Table 2.3).

Some variations in permittivity estimates are observed as TCE is injected into the soilBed (Figure 7.25 to Figure 7.27). Preliminary statistical analysis (Appendix 7), indeed, suggest potential significant variations between measurements taken prior to and after injection of TCE and water. Average permittivity estimates decrease slightly after commencement of TCE injection (Table 7.1) and then increase. Although values are expected to increase because of the displacement of the fluid (air) with a lower  $\epsilon_r$  value by another fluid (TCE) with higher  $\epsilon_r$  values, lower permittivity values are presented

when TCE enters the system, and may be caused by greater heterogeneities in the dielectric properties of the system. It is observed that the variations in average values are mostly influenced by variations in relative permittivity estimates in Port 2.

Water infiltration after TCE injection tends to increase relative permittivity estimates within the range of frequencies evaluated (Table 7.1, Figure.7.28 to Figure 7.30). The presence in water is expected to increase permittivity values of the bulk soil because of the greater permittivity values of water. The increase may be offset to a certain degrees by heterogeneities in fluid distribution.

**Table 7.1 Average maximum relative permittivity values estimated**

Case	$\epsilon_r$
Dry condition	2.46 ± (0.38)
After 5 min TCE injection	2.35 ± (0.63)
After 10 min TCE injection	2.45 ± (0.82)
After 30 min TCE injection	2.49 ± (1.21)
After 50 min TCE injection	2.96 ± (1.09)
After 80 min TCE injection	2.75 ± (1.15)
After 130 min TCE injection	3.16 ± (1.84)

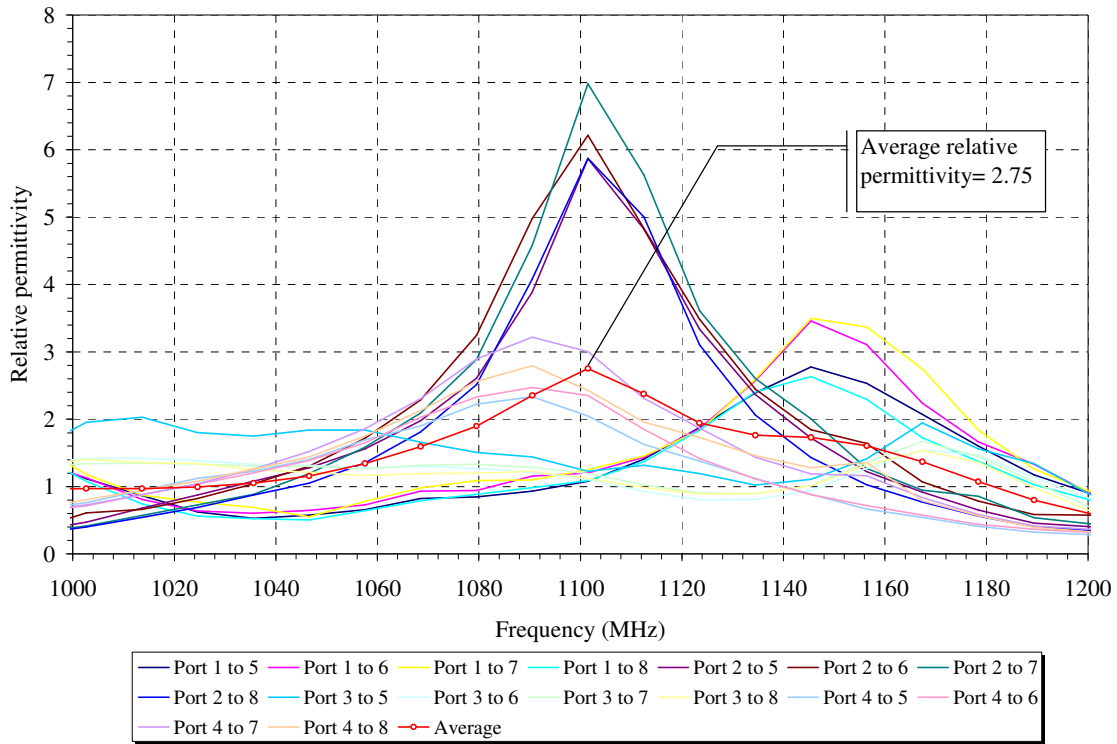


**Figure.7.28** Relative permittivity value after 50 min TCE injection in initially-dry experiments

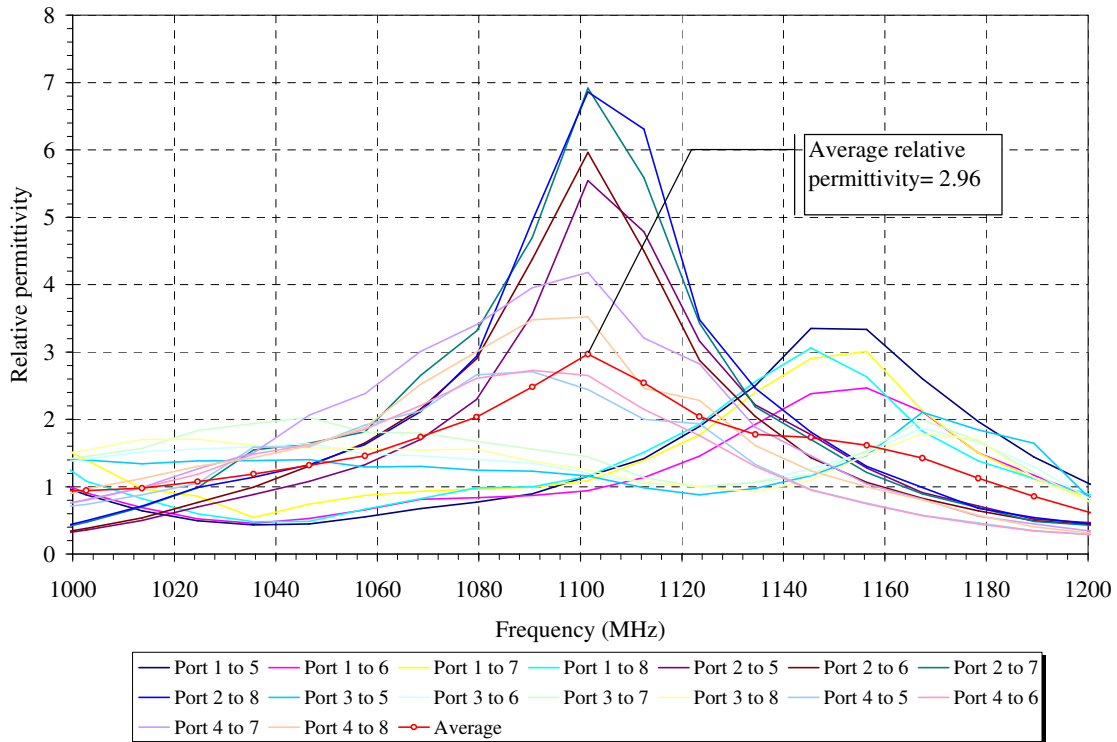


**Figure 7.29** Relative permittivity value after 80 min TCE injection in initially-dry experiments

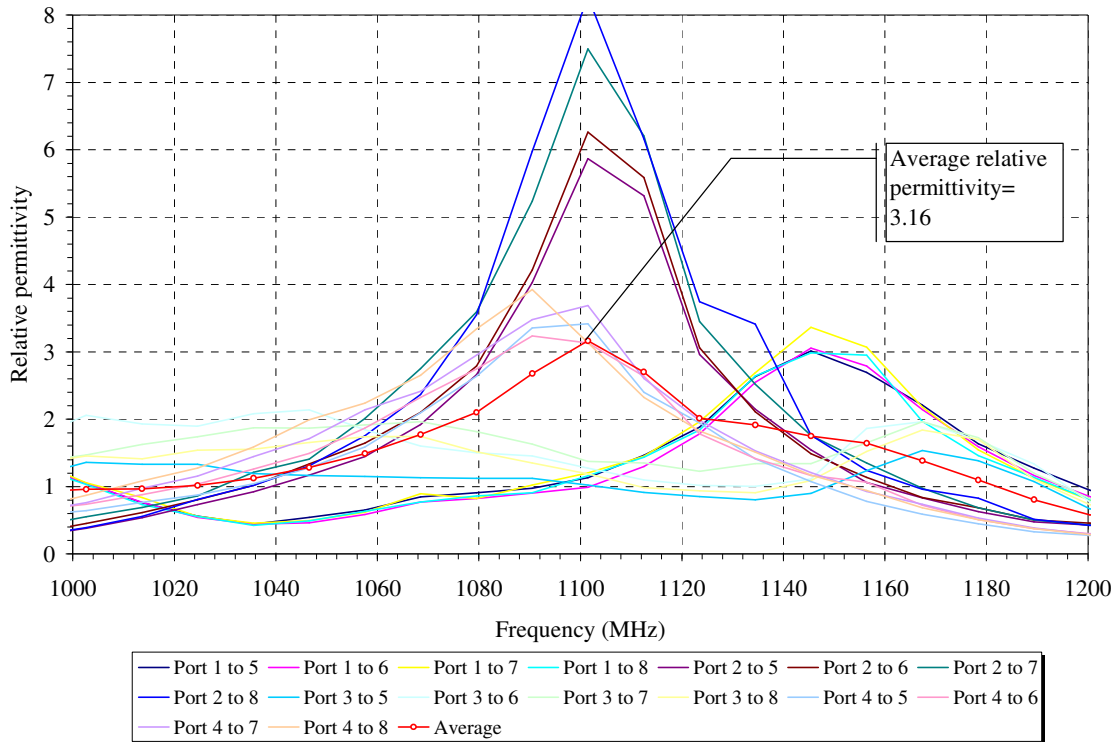


**Figure 7.30** Relative permittivity value after 130 min TCE injection in initially-dry experiments

These experiments show that the combination of four-component dielectric mixture (air, bulk soil, bound water, and free water) in a soil medium affects the electrodynamic behavior of the soil matrix. Moreover, factors as frequency, bulk soil density, and particle shapes influence in the soil dielectric constant estimation. These results demonstrate that the presence of organic contaminant in the pore can affect the dielectric constant parameters. Changes in the moisture content showed an increase in dielectric constant as has been exposed by Harmsen and Parsiani, 2003. The results, however, demonstrate that mixing models may not appropriately describe variations in bulk permittivity values, and that other factor such as fluid distribution heterogeneities may also be taken into account.

### 7.3.2 Variations of dielectric permittivity in saturation experiments

The dielectric properties were evaluated during the saturation of the soilBed (half tank saturation, three quarter tank saturation, completely saturated), and after TCE injection (10 and 45 minutes after the injection) in the saturated tank (Figure 7.31 to Figure 7.36).

Similar to the initially-dry experiments, relative permittivity estimates in the saturation experiments in the frequency range evaluated (1000 MHz to 1200 MHz) increased with frequency to a maximum value and then decreased with further increase in frequencies (Figure 7.31 to Figure 7.36). Maximum values and frequency at maximum value varied with location of sending antenna and saturation conditions. Acceptable estimated relative permittivity of dry soil prior to saturation ranged from 1 to about 4 (Figure 7.31) with a maximum average of 1.4 (see Table 7.2). Similar to the initially dry-experiments (Figure 7.24) maximum values were estimated for the port at 10 cm from the surface (Port 2). The values were, however, lower (2.4 to 4.0) than those estimated in the same port for initially-dry experiments (5.0 to 7.10). Lower estimated values for dry conditions in saturation experiments are attributed to differences in soil packing and antennas radiation properties. Lowest maximums are observed in measurements associated with Port 1 (not Port 3 as for initially-dry experiments). This location is near (5cm) the soil atmospheric interface and is aligned with the TCE injection tube (which is 5 cm below the soil surface for saturated experiments). These results support the conjecture that the presence of the TCE injection system results in lower permittivity estimates, since lowest estimated values for dry soil in the two experimental setups coincided with the location (depth) of the injection tube.

**Table 7.2 Average maximum relative permittivity values**

Case	$\epsilon_r$
Dry Conditions	1.40 ± (0.51)
Half tank with wet soil	1.50 ± (0.71)
Quarter tank with wet soil	1.68 ± (0.55)
Total Tank with wet soil	3.17 ± (1.09)
10min TCE injection in wet soil	3.30 ± (1.25)
45min TCE injection in wet soil	3.31 ± (1.15)

Permittivity estimates when the soilBed is fifty percent saturated shows a shift on the frequencies at maximum values, and a general slight increase in frequency-shifted maximum values (Table 7.2, Figure 7.32). At higher saturation the shift on the frequencies at maximum values for all antenna location trends toward 1100 MHz and maximum average tends to increase. Although the presence of water increased the relative permittivity values (Figure 7.31 to Figure 7.36), the values measured are below the values reported in the literature. An increase in permittivity is expected as water, having greater permittivity than air, displaces air. The slight variation is possibly due to differences in antennas characteristics, effect of soilBed and air-water boundaries, and scattering from heterogeneities form by capillary rise and air entrapment during saturation.

Results indicate that the position of the water table does affect the dielectric properties of the medium. For instance, the maximum estimated permittivity for Port 4 (20 cm below the soil surface) varies as the tank is saturated, even though this port always saturated. Similarly, the estimated permittivity for Port 1 (5 cm from the surface) shows continued

increase in values as the tank is saturated, even though it is considered unsaturated when the tank is half or quarter saturated.

TCE injection into the soilBed resulted in slightly higher permittivity values of the medium (Table 7.2, Figure 7.35 and Figure 7.36). Because of the lower than water permittivity of TCE, bulk estimated permittivity values are expected to decrease as TCE displaces water. The effect of upward water displacement in the soilBed as TCE is injected may, however, offset the expected decrease. This is because as TCE displaced water upward, the location of the air-water interfaces increases. In general, preliminary statistical analysis (Appendix 7) suggests potential significant differences between relative permittivity estimates for different degrees of water and TCE saturations.

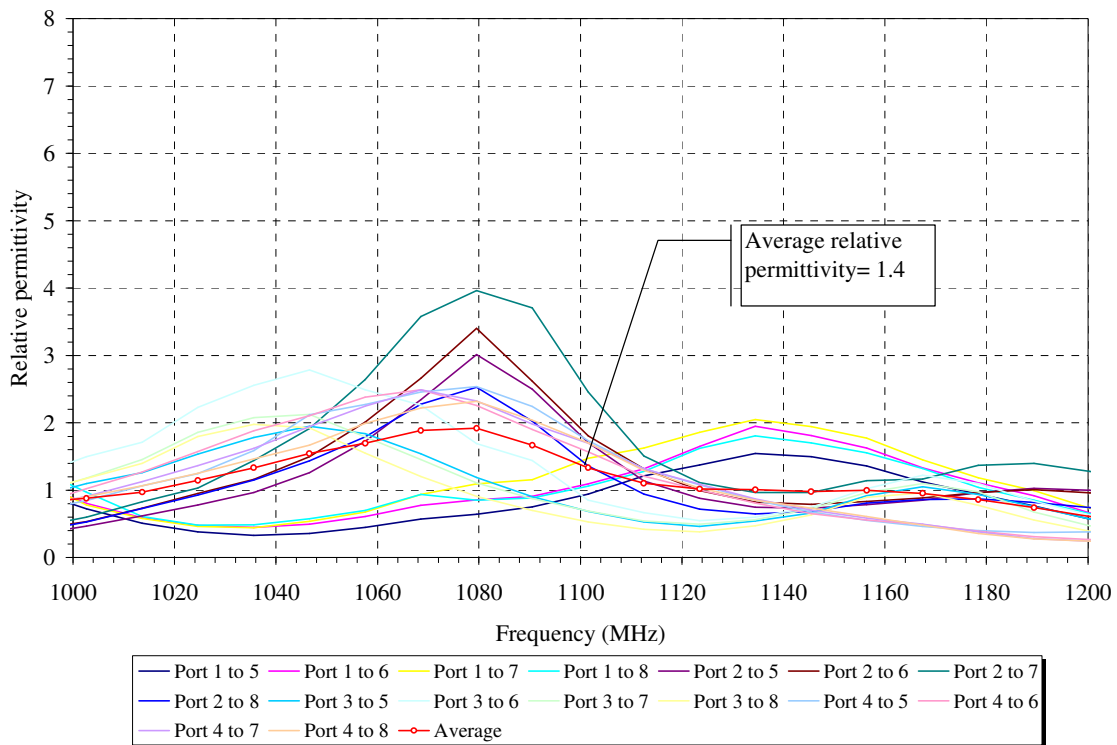


**Figure 7.31 Relative permittivity values in dry soil prior to saturation experiments**

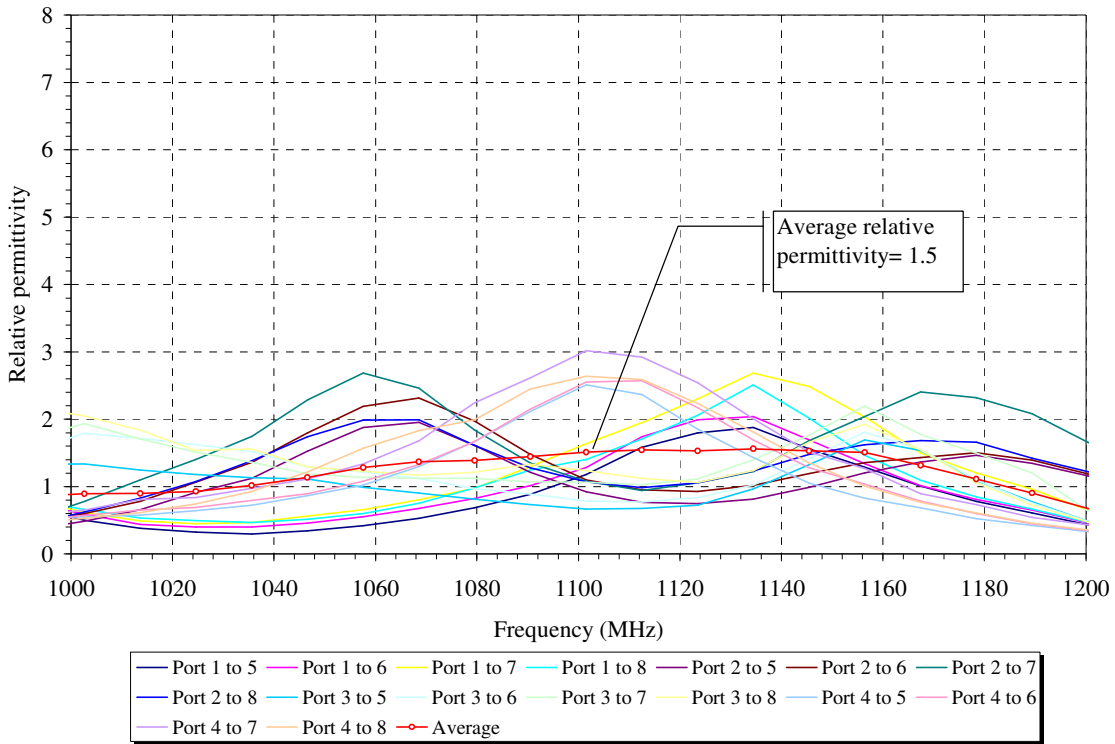


**Figure 7.32** Relative permittivity values when the tank is fifty percent saturated

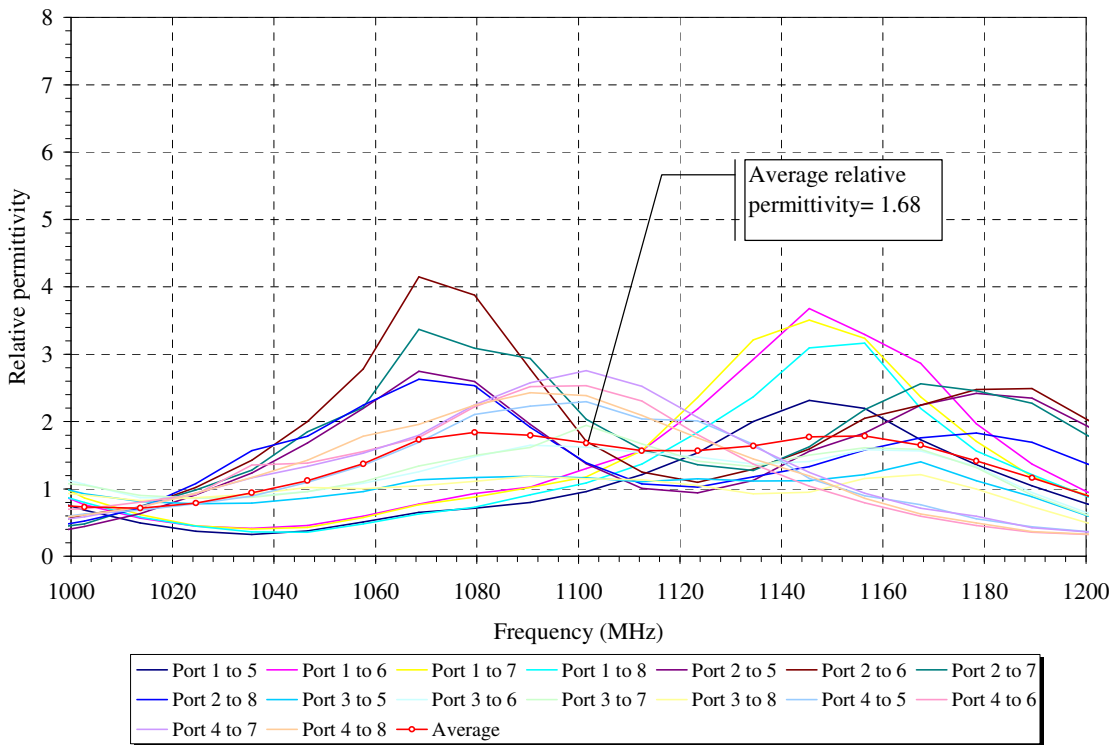


**Figure 7.33** Relative permittivity values when the tank is seventy five percent saturated

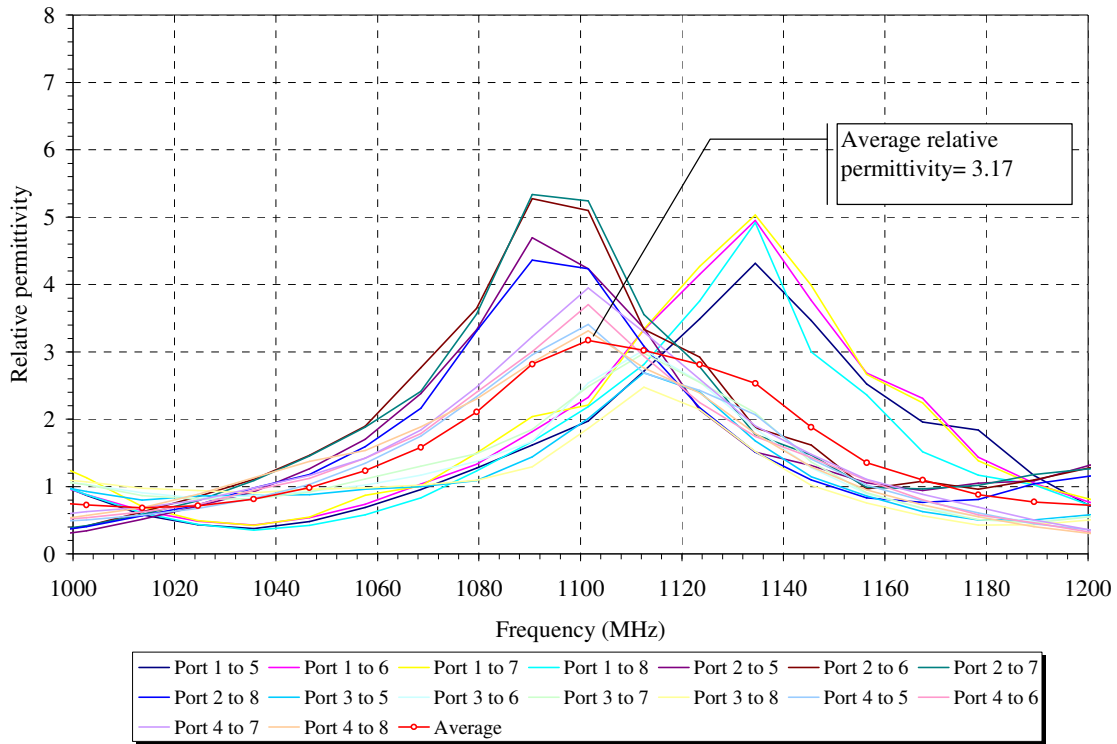


**Figure 7.34 Relative permittivity values when tank is one hundred percent saturated**

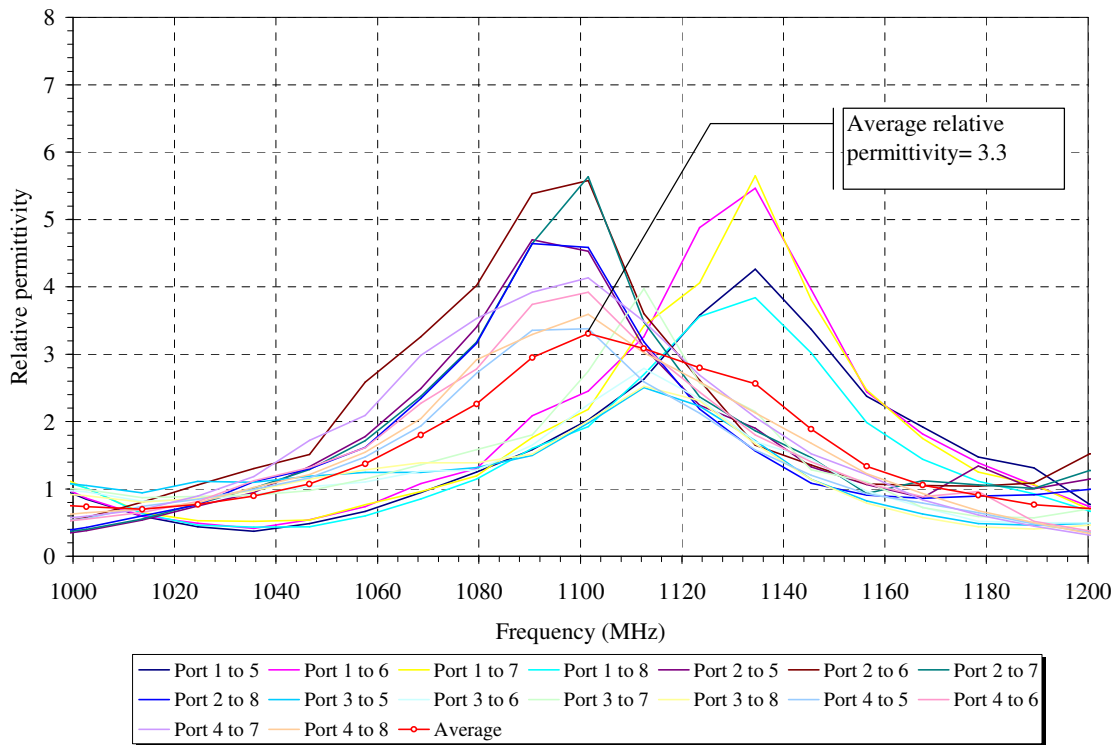


**Figure 7.35 Relative permittivity values at 10 min after TCE injection in saturated soil**

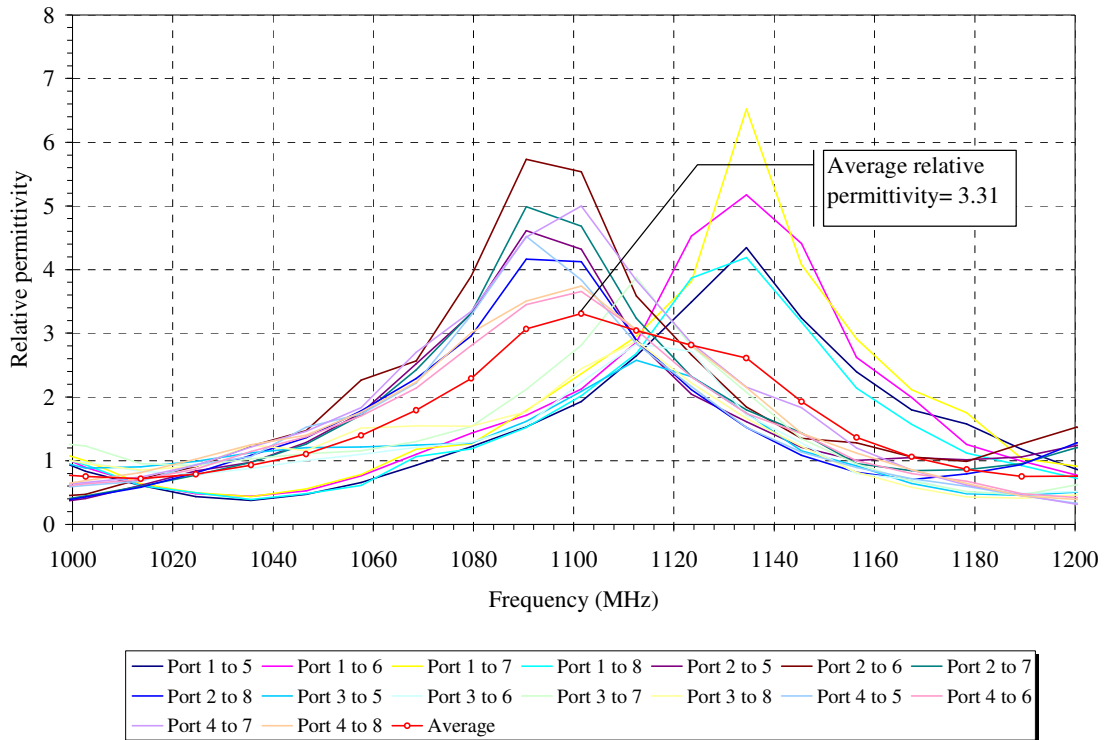


**Figure 7.36** Relative permittivity value at 45 min after TCE injection in saturated soil

#### 7.4 TOMOGRAMS DURING TCE INJECTION IN DRY CONDITIONS AND SATURATED CONDITIONS

Electromagnetic measurements were used to estimate dielectric permittivity properties of the soil in dry and saturated condition during TCE injection. The permittivity estimates along raypaths were then used to develop tomographic images of the medium using SART.

#### 7.4.1 Tomograms for initially-dry experiments

These tomograms are prepared using a relative permittivity estimated with S-parameters in the frequency range of 1 GHz to 1.2GHz. Tomograms show changes between initial condition and different stage of the experiment (Figure 7.37 to Figure 7.41). Permittivity results (Figure 7.37b) show a relatively uniformed distribution in dry conditions, except near Port 6. An anomaly near Port 6 showing relative permittivities over 30 may be caused by the EM data collected within the antenna at Port 10 cm below soil surface. This anomaly is shown in all stages during the initially-dry experiments. Slight variations are observed in the tomograms after TCE injections (Figure 7.38 to Figure 7.40). These variations are, however, mask by the low tomography resolutions obtained with 4 sets of antennas. Average permittivities for the tomographic grid (Table 7.3) suggest increase values as TCE is injected in the system.

The addition of infiltrating water over the surface of the soil also results in variations of tomographic images (Figure 7.41). Average permittivities for the tomographic grid increase after 100 minutes of water infiltration.

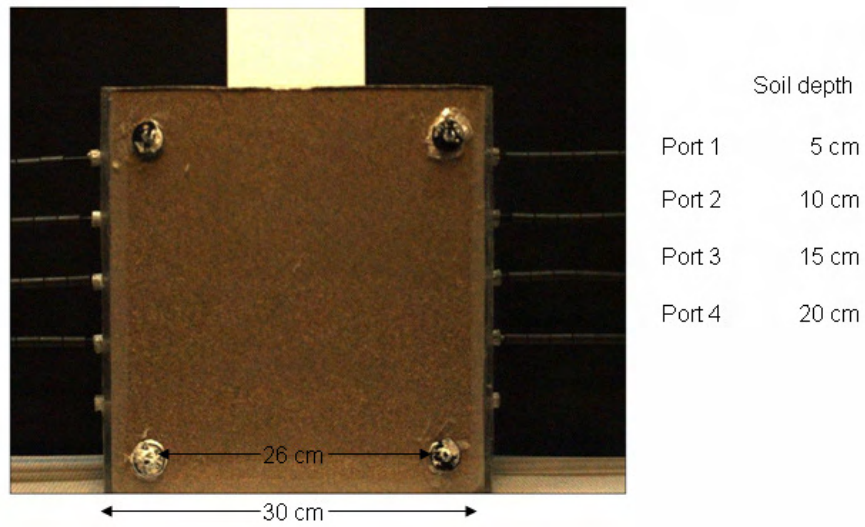
Tomographic images of wave slowness (Figure 7.42 to Figure 7.46) show greater variations upon the injection of TCE than those of relative permittivities. Average wave slowness for the tomographic grid varied from a value around 0.00600  $\mu\text{s}/\text{m}$  to 0.00628  $\mu\text{s}/\text{m}$  during TCE injection (Table 7.3). This increase is attributed to variations in relative permittivities since they are directly related (see Equation 6.7). Slightly greater

permittivities are generally expected when a fluid of higher permittivity displaces another fluid of lower permittivity (such as air). The variations in permittivity, however, will depend on the formation of fluid heterogeneities.

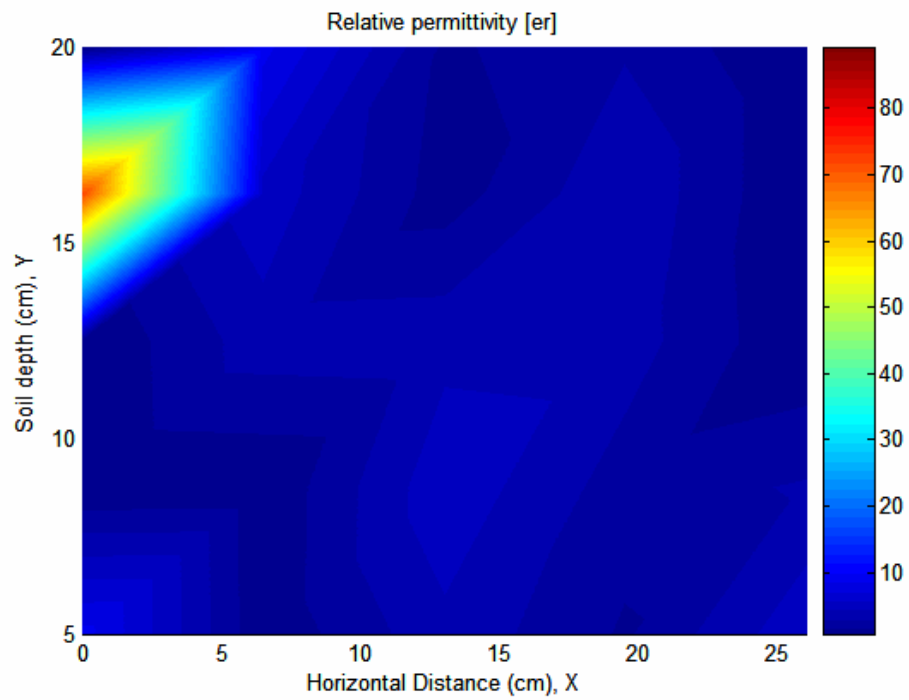
Tomographic images of wave slowness show variations after 100 minutes of water infiltration (Figure 7.46) corresponding to variations in relative permittivities. Average slowness for the tomographic grid varies from 0.00600  $\mu\text{s/m}$  prior to water infiltration to 0.00628  $\mu\text{s/m}$ , suggesting increases in permittivity value.

**Table 7.3 Average permittivity and slowness for TCE in initially dry experiments**

Case	$\epsilon_r$	Slowness $\mu\text{s/m}$
Dry Conditions	$2.88 \pm 1.22$	$0.00600 \pm 0.00210$
5 min after TCE injection	$3.37 \pm 0.68$	$0.00612 \pm 0.00190$
10 min after TCE injection	$3.28 \pm 1.23$	$0.00604 \pm 0.00120$
30 min after TCE injection	$3.54 \pm 1.66$	$0.00628 \pm 0.00026$
130 min after TCE injection (100 min of infiltration)	$3.68 \pm 0.12$	$0.00640 \pm 0.00002$

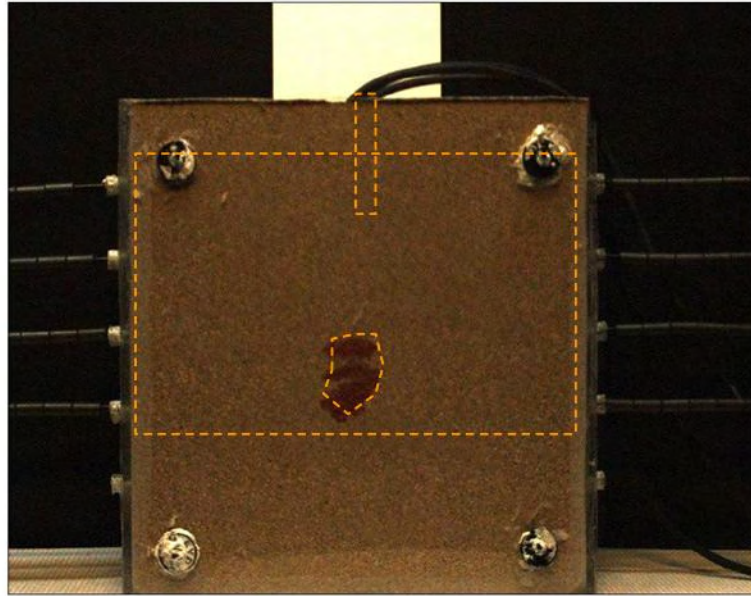


a) Digital image

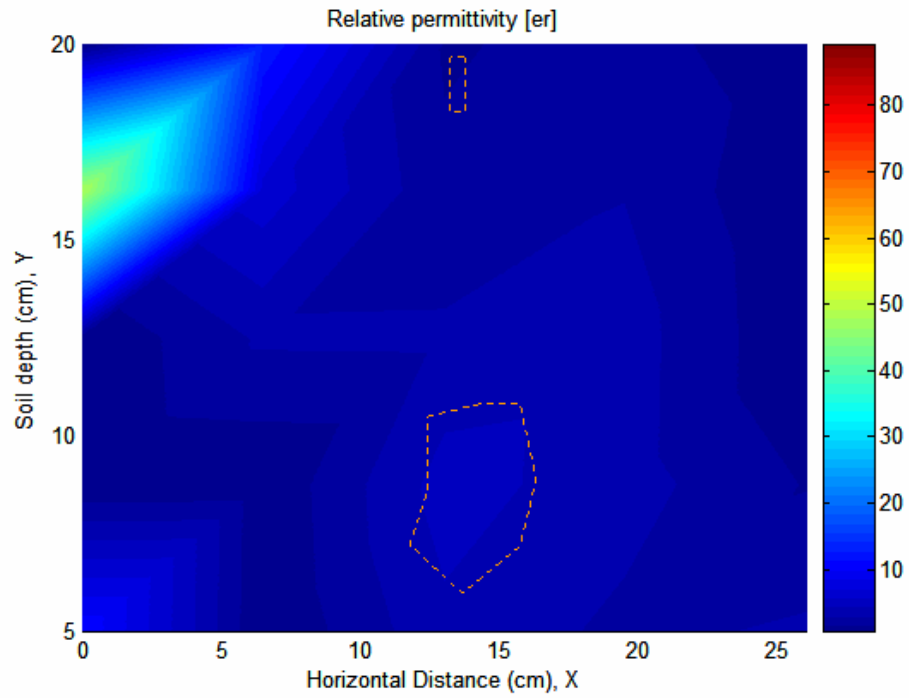


a) Tomogram

**Figure 7.37 Results of: a) digital image, and b) tomogram of dry soil prior to injection of TCE in initially-dry experiments**

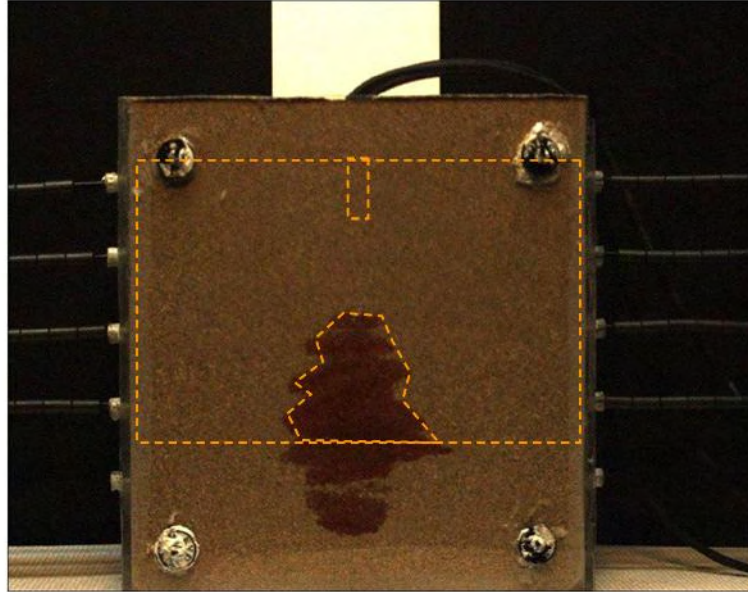


a) Digital image

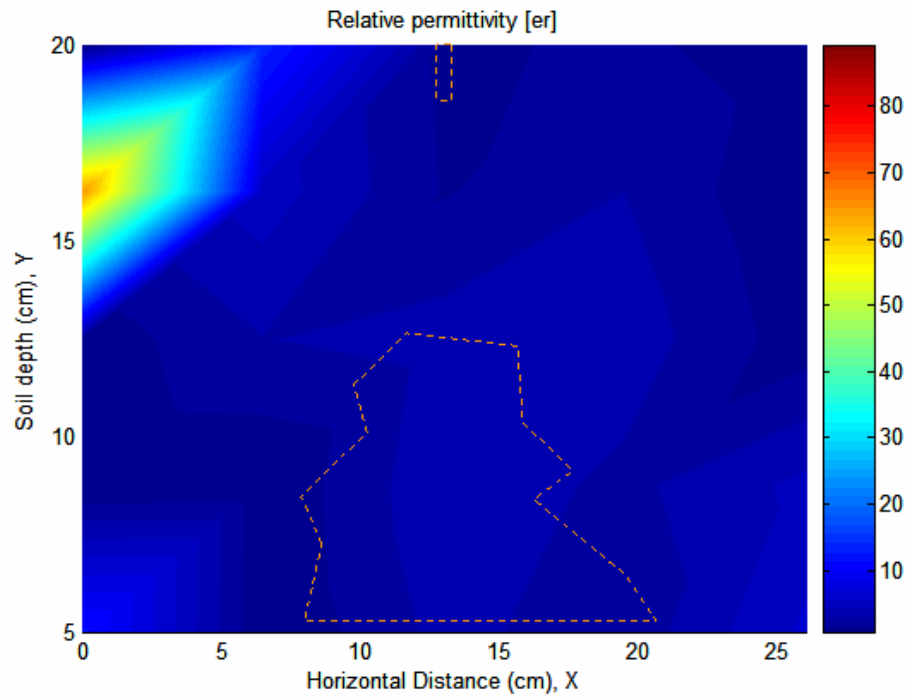


b) Tomogram

**Figure 7.38 Results of: a) digital image, and b) tomogram at 5 min TCE in initially-dry experiments**

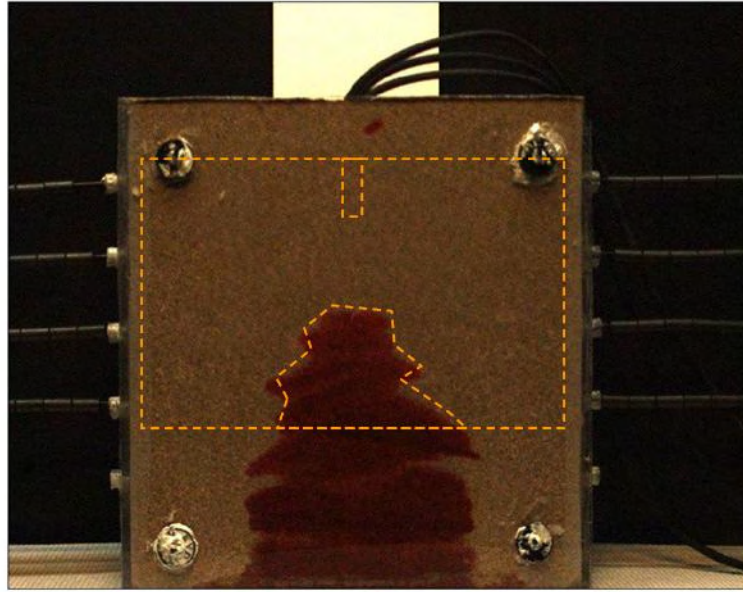


a) Digital image

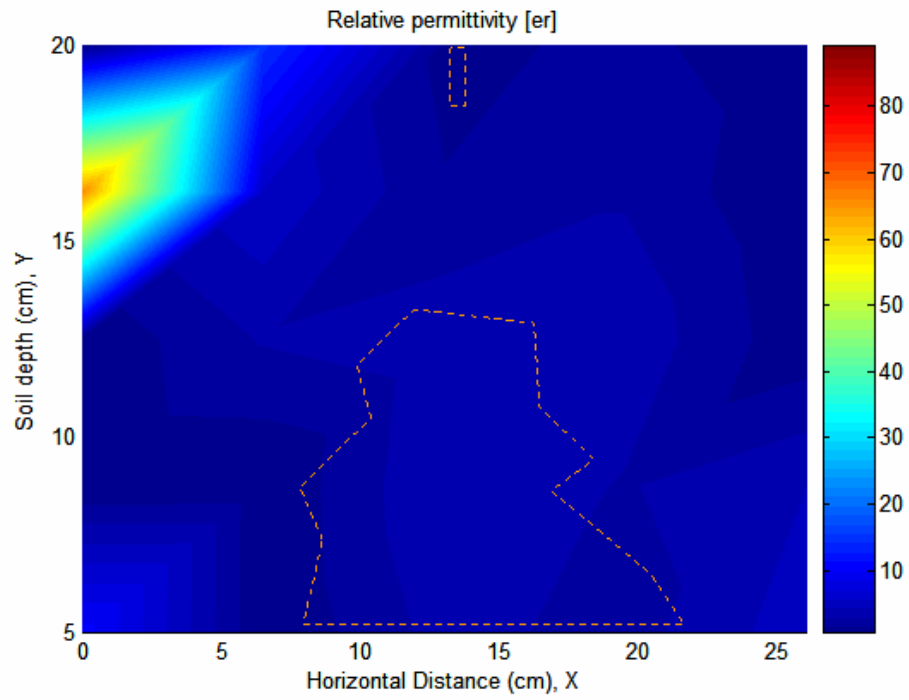


b) Tomogram

**Figure 7.39 Results of: a) digital image, and b) tomogram at 10 min TCE in initially-dry experiments**

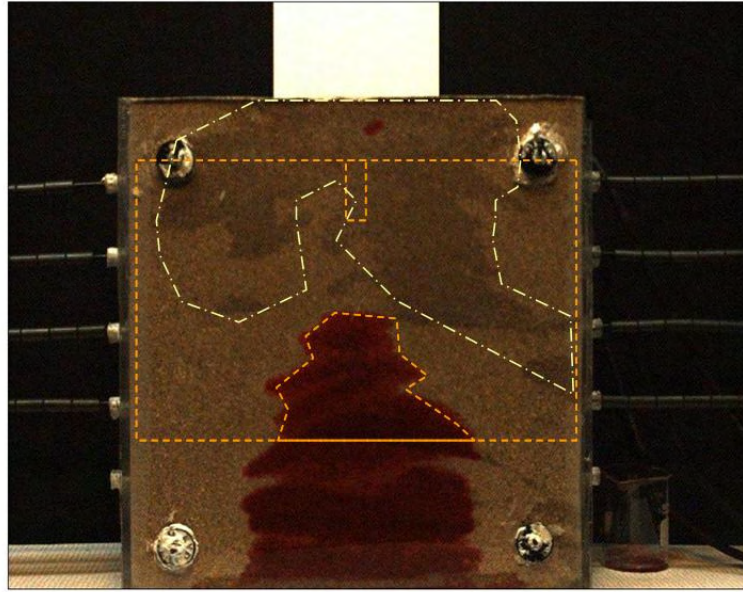


a) Digital image

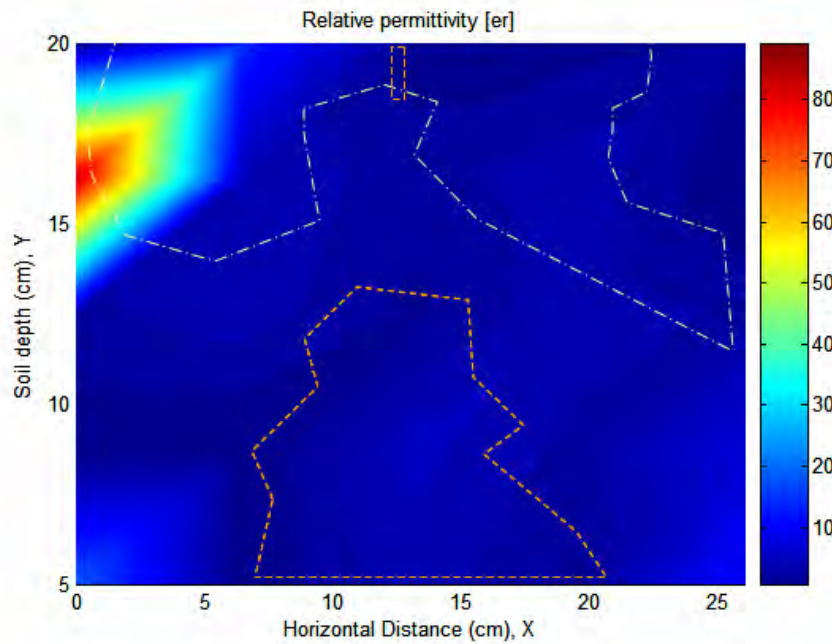


b) Tomogram

**Figure 7.40 Results of: a) digital image, and b) tomogram at 30 min TCE in initially-dry experiments**



a) Digital image



b) Tomogram

**Figure 7.41 Results of: a) digital image, and b) tomogram at 130 min TCE in initially-dry experiments**

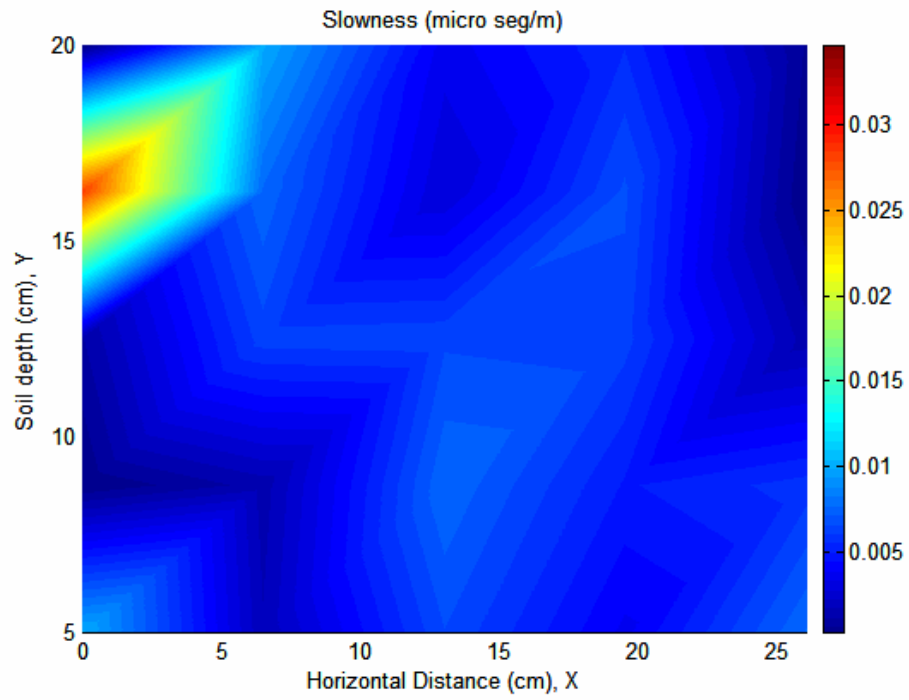


**Figure 7.42 Slowness distribution in initially-dry experiments**

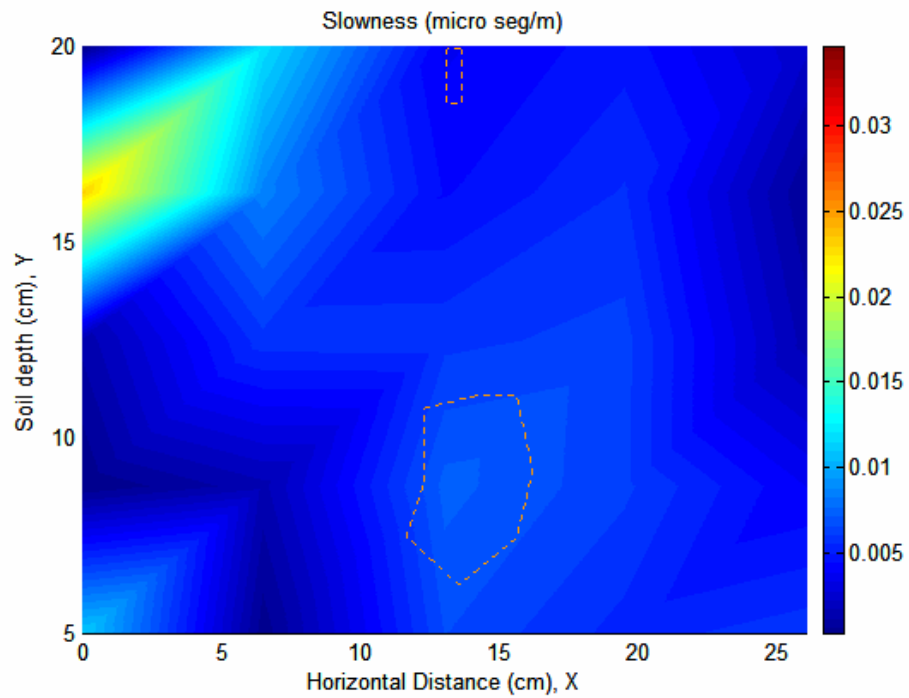


**Figure 7.43 Slowness distribution at 5 min of TCE in initially-dry experiments**

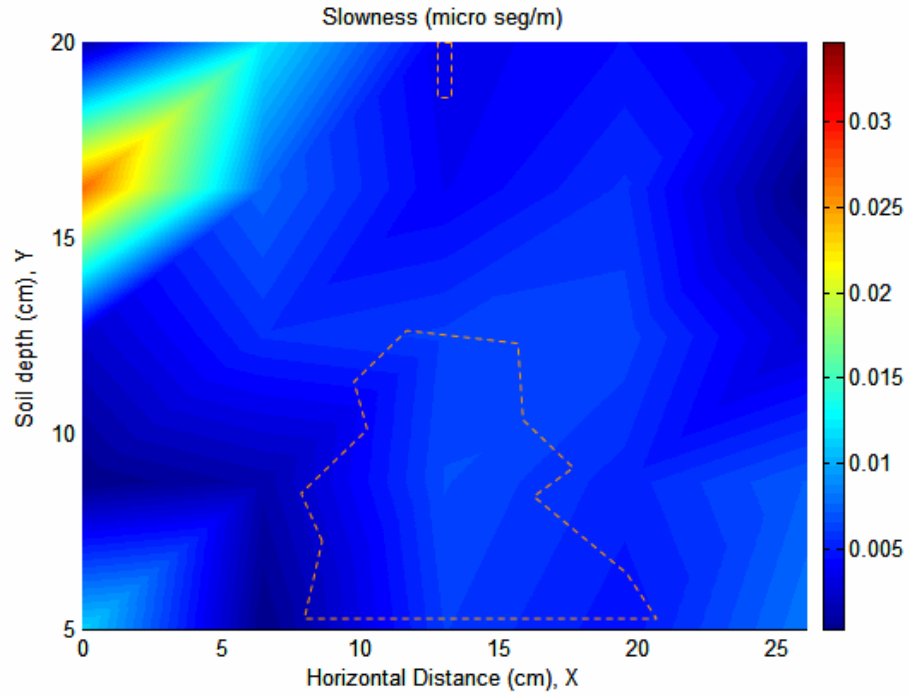


**Figure 7.44 Slowness distribution at 10 min of TCE in initially-dry experiments**

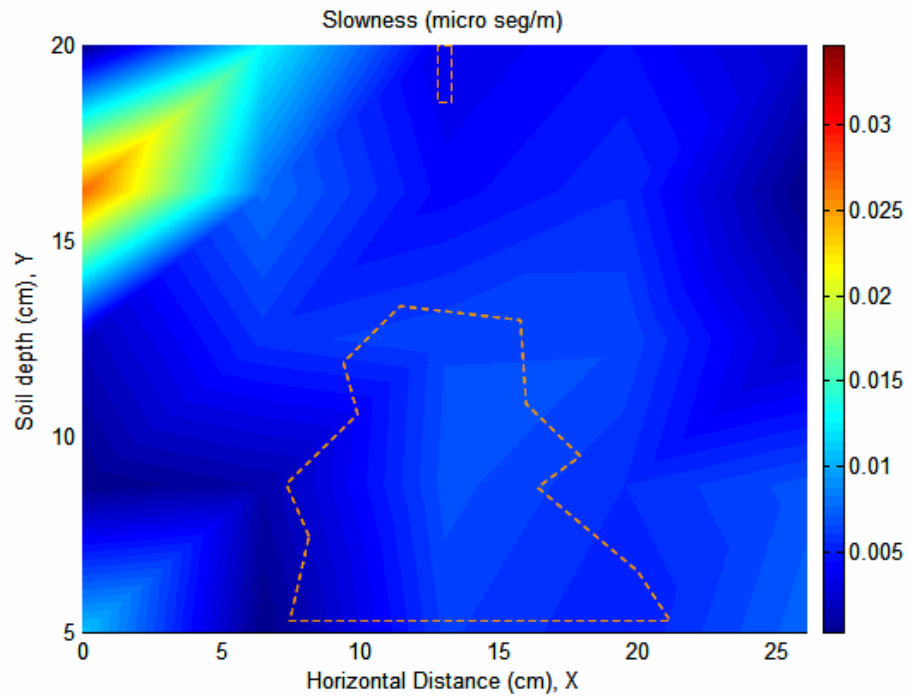


**Figure 7.45 Slowness distribution at 30 min of TCE in initially-dry experiments**

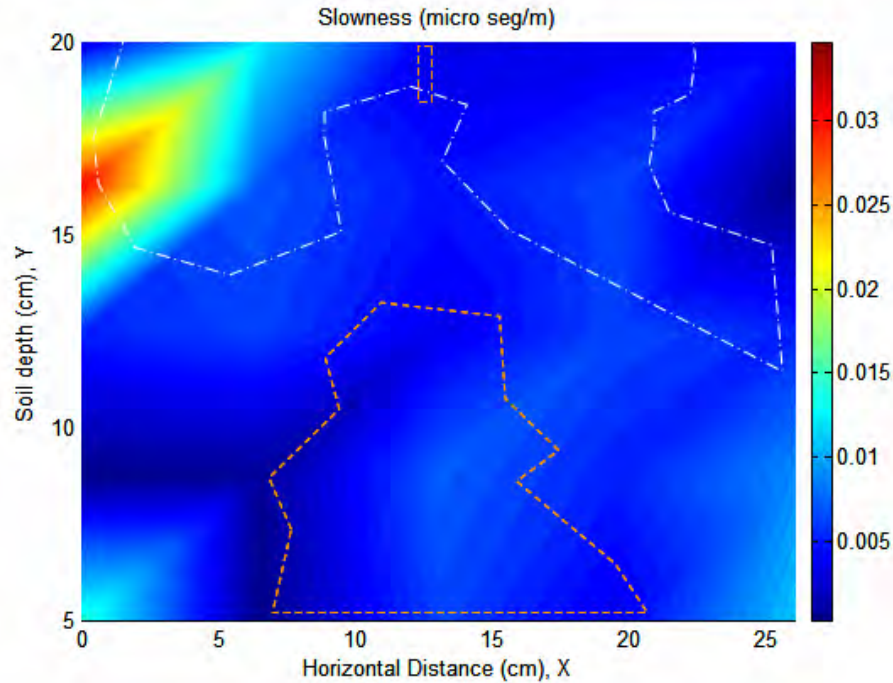


**Figure 7.46 Slowness distribution at 130 min of TCE in initially-dry experiments**

#### 7.4.2 Tomograms for soil under water-saturation experiments

These tomograms are prepared using a relative permittivity estimated using S-parameters in the frequency range of 1 GHz to 1.2GHz. Tomograms show changes between initial condition and different stage of the saturation experiment (Figure 7.47 to Figure 7.50). The tomographic permittivity distribution for dry soil prior to saturation (Figure 7.47) shows lower values than for the dry soil set up used for the initially-dry experiments (Figure 7.24). The differences are probably caused by the high permittivity anomaly developed around Port 6 in the previously-dry experiments. Although a permittivity anomaly is also observed near one of the ports (Port 3 at 15 cm below soil surface) in the setup used for saturation experiments, it is of lower magnitude. Apart from this anomaly, relative permittivity values in the tomographic image of the dry soil prior to saturation

(Figure 7.47) range from 1 to near 5. Relative permittivity for the tomographic grid averages 2.79 (Table 7.4) which is slightly lower than found for the dry soil in initially-dry experiments (Table 7.3).

**Table 7.4 Average relative permittivity and slowness for TCE-saturated conditions**

Case	$\epsilon_r$	Slowness $\mu\text{s/m}$
Dry Conditions	$2.79 \pm 0.57$	$0.0056 \pm 0.00057$
Half tank with wet soil	$2.95 \pm 0.32$	$0.0057 \pm 0.00033$
Quarter tank with wet soil	$3.27 \pm 0.46$	$0.0060 \pm 0.00052$
Total Tank with wet soil	$4.20 \pm 0.41$	$0.0068 \pm 0.00041$
10min TCE injection in wet soil	$2.48 \pm 0.91$	$0.0053 \pm 0.00016$
45min TCE injection in wet soil	$2.66 \pm 0.89$	$0.0054 \pm 0.00022$

As the soilBed saturates the tomographic distribution of relative permittivities tend to increase slightly (Figure 7.47 to Figure 7.50). Relative permittivity values near the anomaly developed around Port 3 significantly increased in the presence of water. In general, increased soilBed saturation resulted in higher relative permittivity averages (Table 7.4). The higher permittivities and wave slowness properties (Table 7.4) are attributed to greater water contents in the soilBed and to greater scattering and reflection energy losses caused by fluid heterogeneities and the air-water interface.

Even though the relative permittivity increases during the saturation process, the values obtained are low compared to reported values in the literature. Relative permittivity in saturated soils has been reported close to 20 (Farid et al., 2004), while in this experiment the average relative permittivity for the tomographic grid was 4.20 in saturated

conditions. Differences may be attributed to differences in antenna radiation characteristics, effects of soilBed and air-water interface boundaries, and scattering and wave bending across heterogeneities formed by capillary rise and air entrapment during saturation.

Slight decrease in relative permittivity is observed when TCE is injected into the saturated soil (Figure 7.51 and Figure 7.52, Table 7.4). The decrease is attributed to the displacement of a higher relative permittivity fluid (water) with the lower permittivity TCE-NAPL.

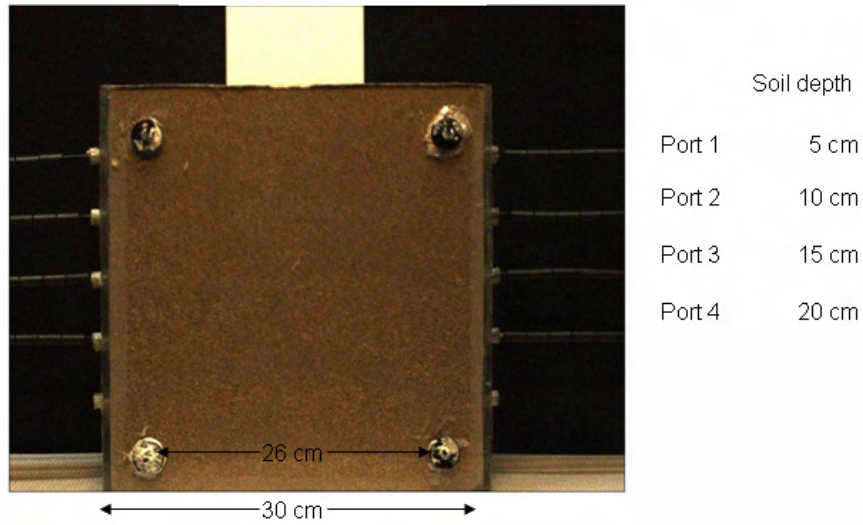
#### 7.4.3 Tomographic limitations

The method developed to generate tomographic images using permittivity estimates along raypaths produce acceptable tomograms provided that there is sufficient density of antennas array, and proper grid spacing. This is not, however, the case with the experimental system used to capture electromagnetic variations. The experimental system was composed of 4 antennas pairs, mainly because of limitation on the coaxial cables available for the experiments. The lower-than-required density of antennas resulted in variation between tomographic images of different conditions that were associated with the experimental conditions or their variations. Consequently, the tomograms are limited for the characterization and detection of fluid distribution under transient conditions. In addition to lack of measurement density, other factors may contribute to these limitations. These include:

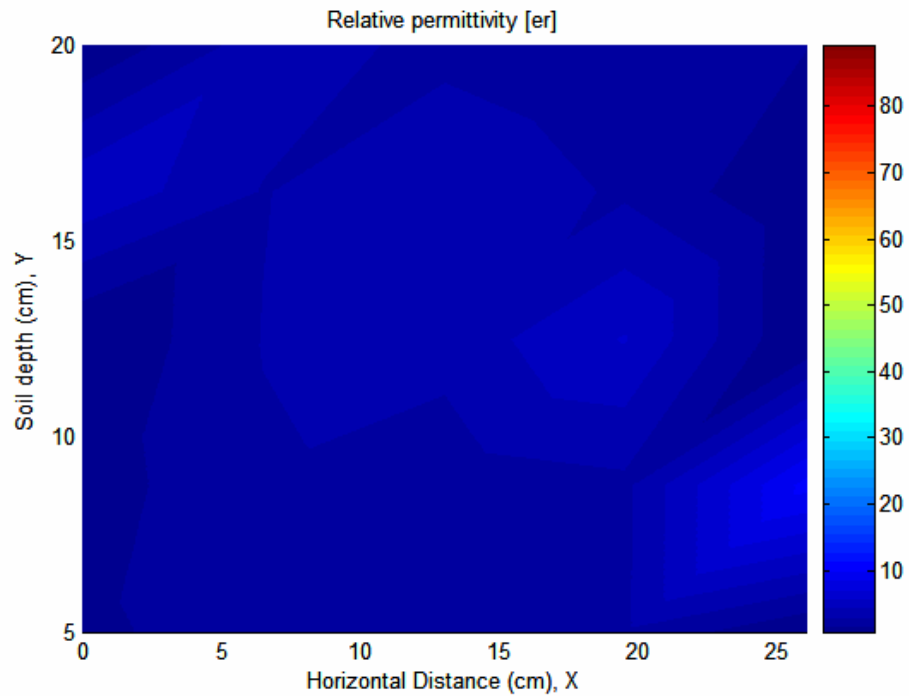
- The variability in radiation characteristics of antennas.
- The assumption of lossless medium. Transmission and reflection measurements suggest potential influence caused by conduction losses.
- The assumption of straight raypaths. It is possible that the amount and size of heterogeneities formed by fluid flow and interfaces causes the raypath to bend.
- The assumption of no influence from soilBed boundaries. Transmission and reflection measurements and relative permittivity estimates suggest some effect of soilBed boundaries.
- The frequency rang used for the analysis. Electromagnetic measurements and relative permittivity estimates suggest that the presence and changes in fluid composition of different electromagnetic properties induce shifts in the frequency-dependent response of the antennas as a function of fluid distribution.

It is believed that these limitations may be minimized and tomographic images improved with the following recommendations:

- Increase electromagnetic measurement density
- Normalizing the radiation characteristics of antennas through channel transfer functions similar to those developed by Farid, 2004.
- Integrating conduction losses into equations used to estimate electromagnetic properties.
- Performing the analysis at various frequency ranges.
- Relocating antennas further away from boundary conditions.



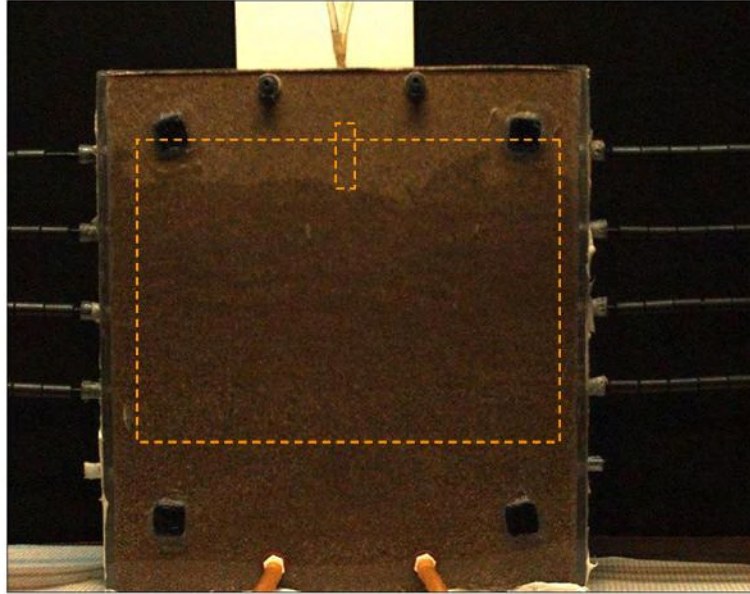
a) Digital image



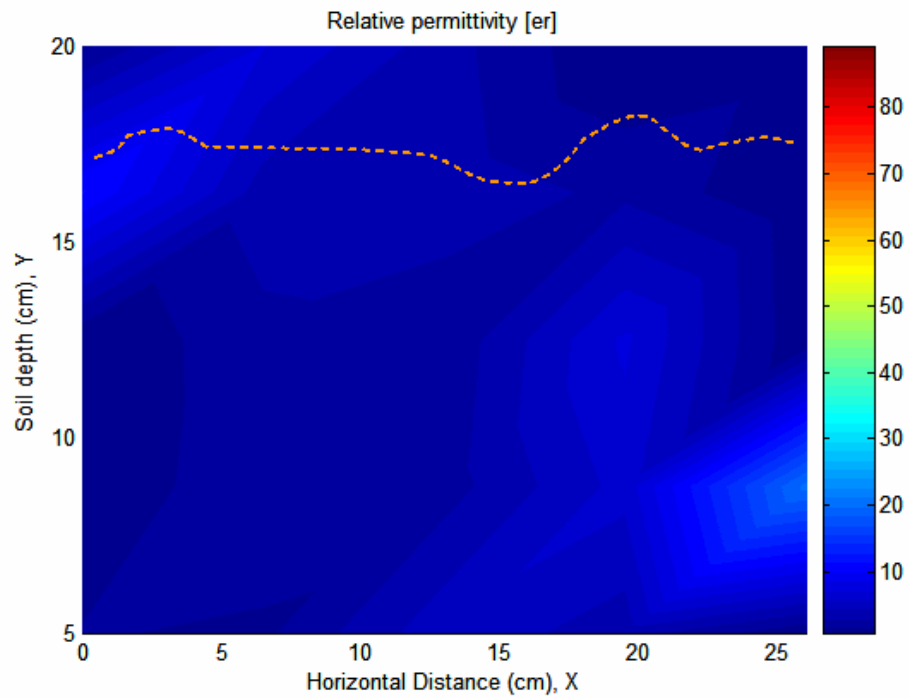
b) Tomogram

**Figure 7.47 Results of a) digital image, and b) tomograms for dry soil prior to saturation experiments**



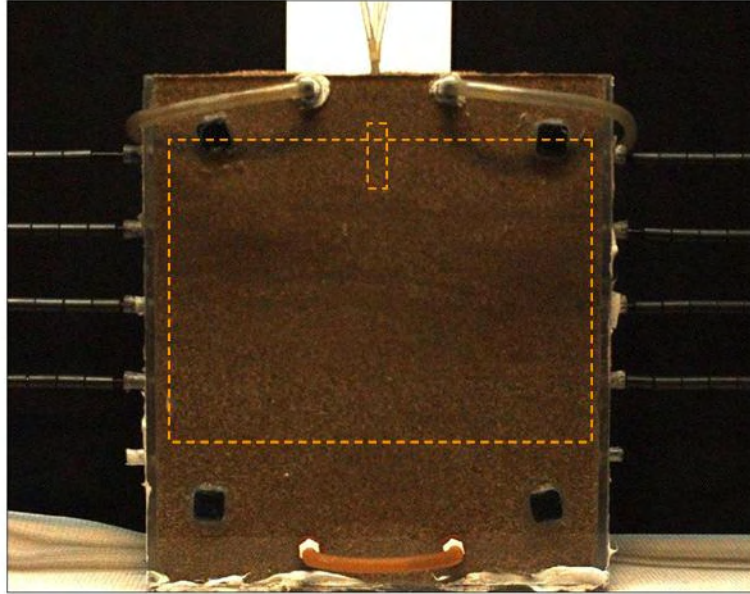


a) Digital image

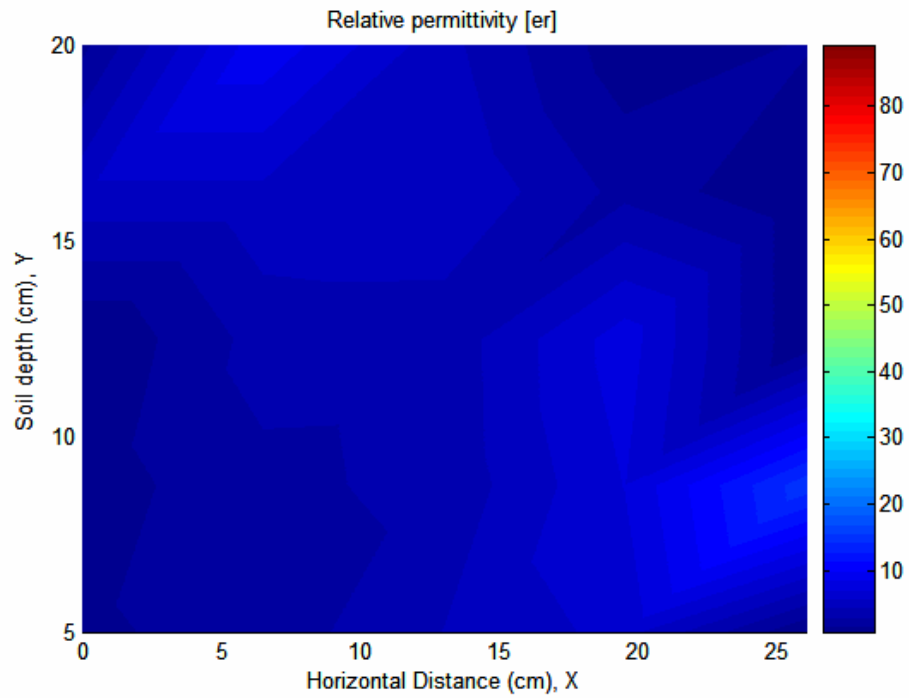


b) Tomogram

**Figure 7.49 Results of a) digital image, and b) tomograms for seventy five percent soilBed saturation**

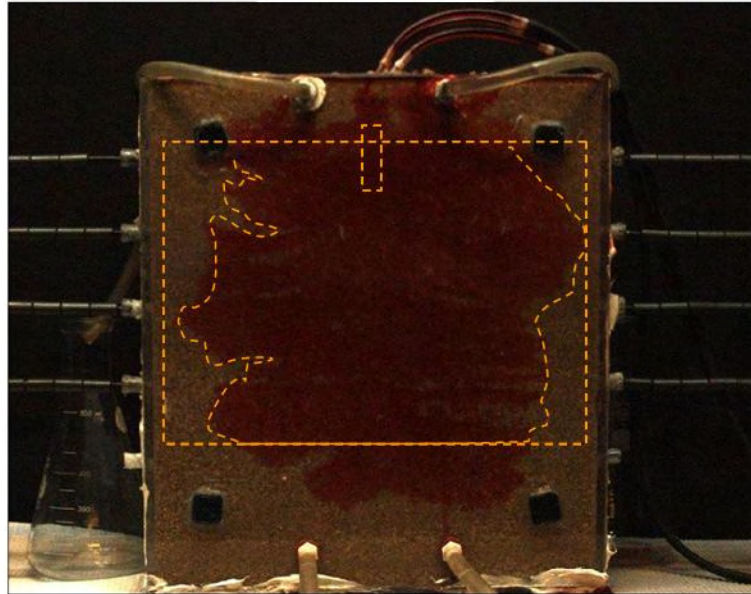


a) Digital image

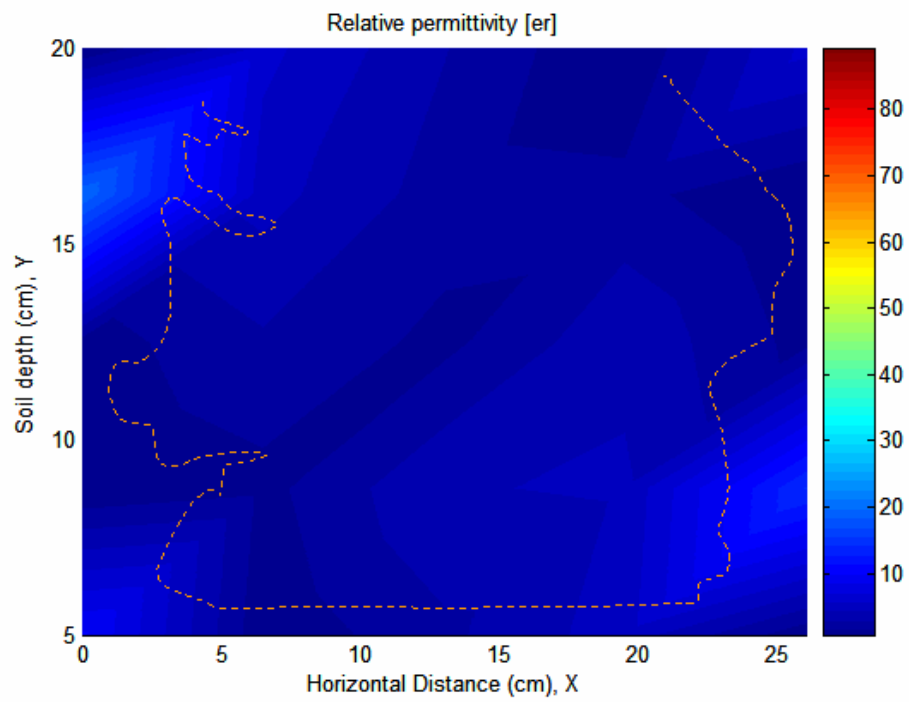


b) Tomogram

**Figure 7.50 Results of a) digital image, and b) tomograms for one hundred percent soilBed saturation**

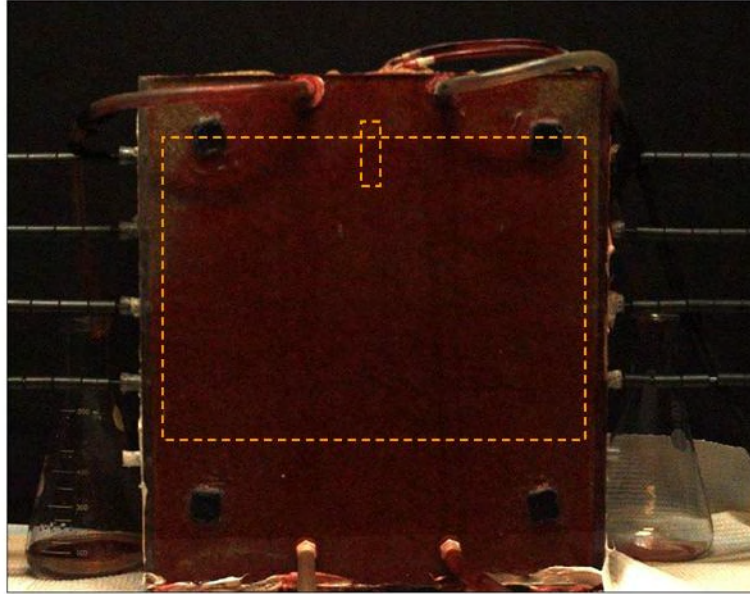


a) Digital image

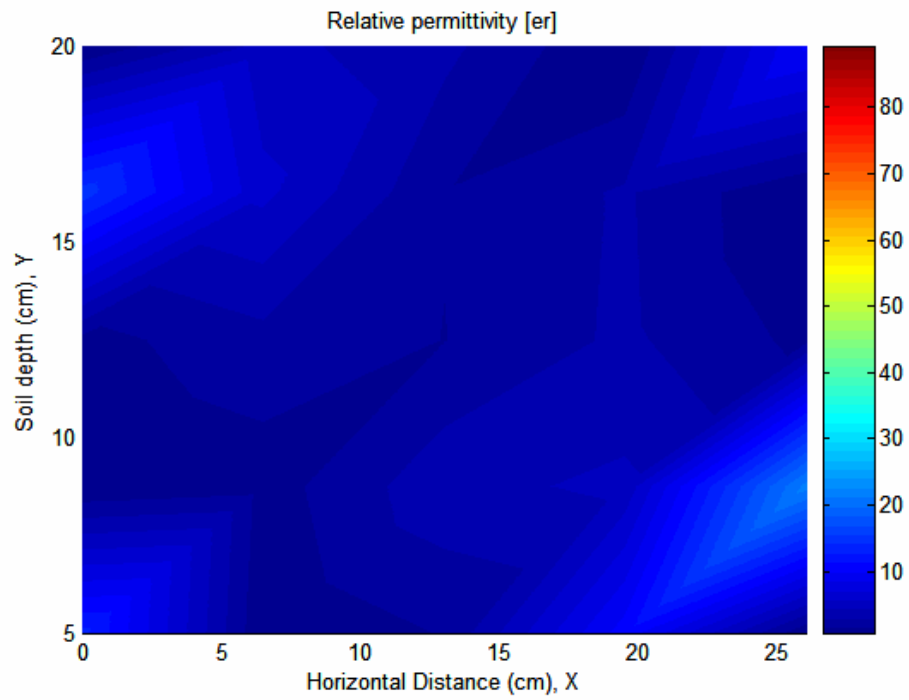


b) Tomogram

**Figure 7.51 Results of a) digital image, and b) tomograms at 10 min of TCE injection- saturated soil**



a) Digital image



b) Tomogram

**Figure 7.52 Results of a) digital image, and b) tomograms at 45 min of TCE injection- saturated soil**

## **7.5 DIGITAL VISUALIZATION AND IMAGE ANALYSIS DURING TCE INJECTION IN INITIALLY-DRY AND SATURATED CONDITIONS**

Digital images were taken prior to and during TCE and water injection in initially-dry and saturated experiments. The images served as a ground truth of the experimental conditions imposed and were compared to tomographic images developed from electromagnetic measurements. Images taken for dry-soils prior to TCE injection in initially dry experiments (Figure 7.37a) and prior to saturation in water-saturation experiments (Figure 7.47a) show homogeneous color distribution.

Images taken during TCE injection in initially-dry experiments (Figure 7.37 to Figure 7.39) show how TCE tends to move downward in unsaturated soils. The images also show contrasting colors within and non-uniform shape of TCE plume, indicating non-homogeneous movement of the TCE.

Infiltrating water in initially-dry soil containing dyed TCE reflected in digital images as a darker color in the background (Figure 7.41a). The image shows that the water does not infiltrate homogeneously in the soilBed, resulting in a heterogeneous water content distribution. Comparison of images during water infiltration (Figure 7.41a) with those taken during bottom-fed water-saturation (Figure 7.48a and Figure 7.49a) show darker colors in water-saturated zones than in unsaturated zones on water infiltration regions and near the water table. The images demonstrate the heterogeneous nature of fluid

distribution in and near unsaturated zones, and show a non-uniform distribution of the air-water interface in the soilBed.

A digital image of the soilBed completely saturated (Figure 7.50a) shows contrasting darkness/brightness throughout the system, suggesting incomplete saturation, air-entrapment, and/or the development of medium heterogeneities. Instead, it is believed that differences arise from different light contrast, and light reflection caused by decloping of the previously established medium/wall contact.

Digital images taken during TCE injection under water saturated conditions (Figure 7.51a, and Figure 7.52a) suggest faster movement of TCE in saturated than unsaturated (Figure 7.40a, and Figure 7.41a) environments. This also suggests greater horizontal displacement in saturated systems. Similar to the TCE injection in unsaturated soil, the movement of TCE in saturated conditions is non-homogeneous and result in heterogeneous TCE distribution.

#### 7.5.1 Image processing and analysis

Digital images were taken during the experiment and stored as a truecolor image or RGB image. The color of each pixel in these images is determined by the combination of the red, green, and blue intensities stored in each color plane at the pixel's location. RGBs images are represented with three matrices of sizes matching the image format. Each matrix corresponds to one of the colors (red, green or blue). Each pixel color is described

by a range of color intensity or brightness, characterized by integer numbers between 0 and 255. The value 0 corresponds to black and 255 to white. Each digital image is represented as a matrix where every element has a value corresponding to how bright/dark the pixel at the corresponding position is.

Image processing algorithms (Appendix 2 and 3) were used to acquire and analyze visual images taken during the experiment in dry and saturated conditions. The code compares pixel intensities between the initial condition before the injection of the dyed-DNAPL and the condition at given times after the onset of the DNAPL injection, estimates the percent change in pixel intensities, develops a processed image, and generates a histogram of percent change in pixel intensity prior to and during TCE and water injection. The percent change is the difference between the initial and final conditions at a given time. The processed image is developed according to a percent-change scale, where specific pixel values are assigned to areas within predetermined percent changes: a pixel value of zero (0) is assigned to areas with less than 10% change; 85 to areas with percent changes between 10 and 20%; 120 to areas with percent changes between 20 and 50%; and 255 to areas with percent changes greater than 50%. Histograms of percent change between images taken prior to and during TCE and water injection reflect the distribution (number) of pixel. Data points (bar height) having a given percent change (horizontal axis).

Image processing and analysis was applied to a fraction of the soilBed area, representing a snapshot of the fluid dynamics in a particular area. The processed image area

represented an area of 15 cm\* 20 cm of the soilBed (ID 2, Table 3.2) centered at 5 cm below the soil surface and 7.5 cm from the horizontal origin (left side) in initially-dry experiments. The processed image area represented an area of 26 cm\* 20 cm of the soilBed (ID 2, Table 3.2) centered at 5 cm below the soil surface and 2 cm from the horizontal origin (left side) in saturated experiments. This area was selected for comparison basis among all experimental conditions. Initial evaluation of the images suggests that imaging areas with large background values were influenced biasly by the background conditions. Consequently, an area was selected that could be applied to all experimental conditions with minimal background bias. It is suggested that a weighting factor must be incorporated into the code to eliminate background bias during image processing analysis.

Noticeable variations in pixel intensity were identified during the TCE injection in initially-dry experiments (Figure 7.53a), water saturation (Figure 7.54a), and TCE injection in saturated soil (Figure 7.55a). The average pixel intensity value decreased after the TCE injection and after water was added into the initially-dry systems (Figure 7.59). This decrease is caused by loss in brightness in the pixels affected by the presence of the darker dyed chemical or water.

Histograms at early TCE injection in initially-dry conditions (5, 10 minutes) (Figure 7.53b) show a peak that corresponds to the influence caused by soil background in the image where a high number of pixels have changed less than twenty percent. Notorious changes in histograms at later times indicate greater percentage of affected soil compared

with the initial condition. Generally, as TCE enters the system, intensity pixel distribution of pixels data having greater percent changes increase (i.e., there is a greater number of data having greater percentage changes) and becomes bimodal. The infiltration of water is significantly shown in the process image (Figure 7.53b), but does not reflect strong percent changes. Consequently, the histogram distribution do not show much difference as water infiltrates the system.

Digital images taken prior to and during water saturation (Figure 7.47b and Figure 7.55b) shown that as the soilBed saturates from initially-dry conditions, there is a significant decrease in pixel intensity, and large percent changes. As the soilBed continues to saturate, the percent change seem to decrease, and the percent change distribution shifts toward a lower change distribution.

Digital images taken prior to and during TCE injection under saturated conditions (Figure 7.58b) show significant decreasing in pixel intensity as TCE moves through the system. The histogram shows that more than fifty percent of values changed after 10 minutes of TCE injection. As more TCE displaces water, a greater number of pixels are shown to have greater changes.

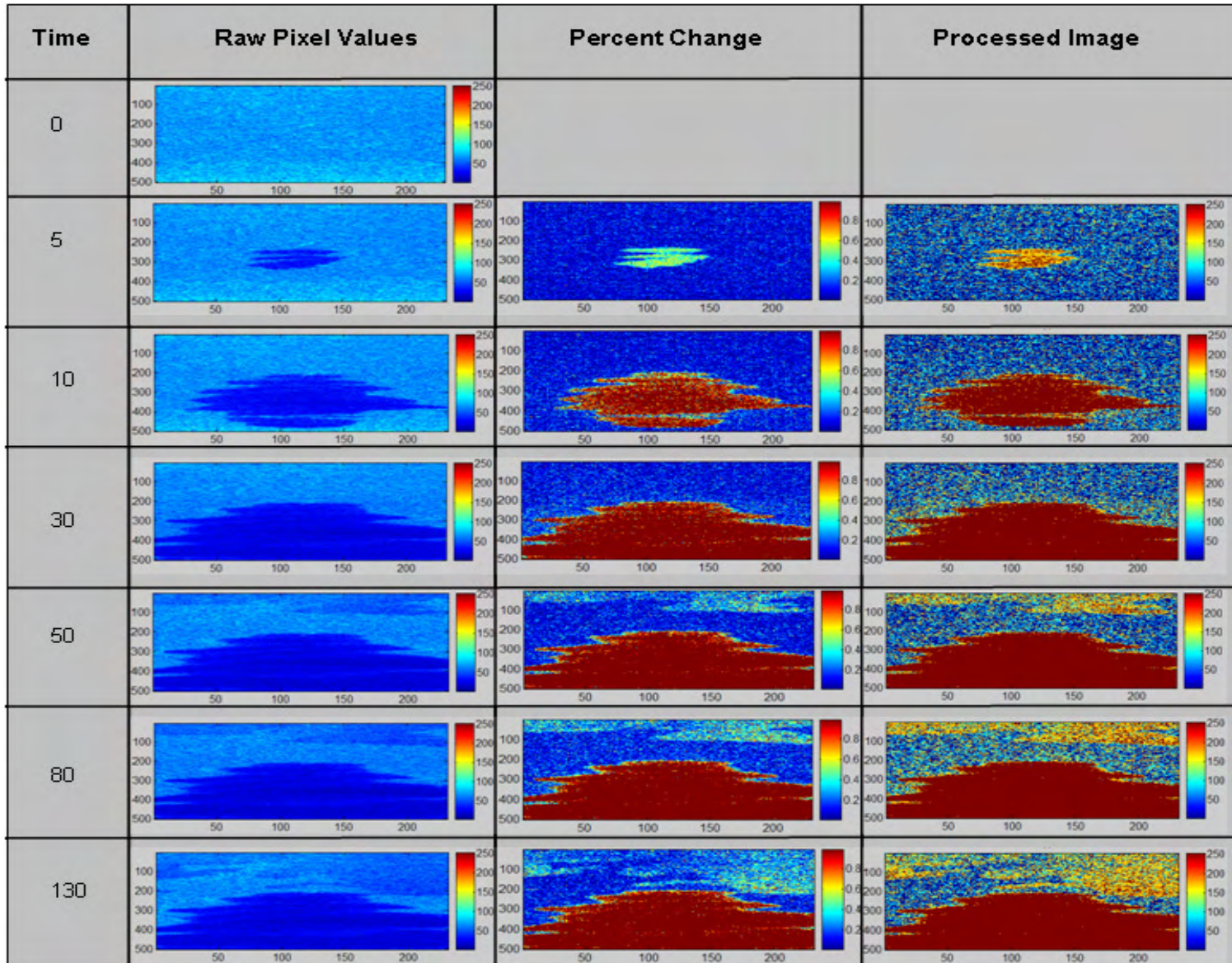


Figure 7.53 a) Image analysis during initially -dry experiments

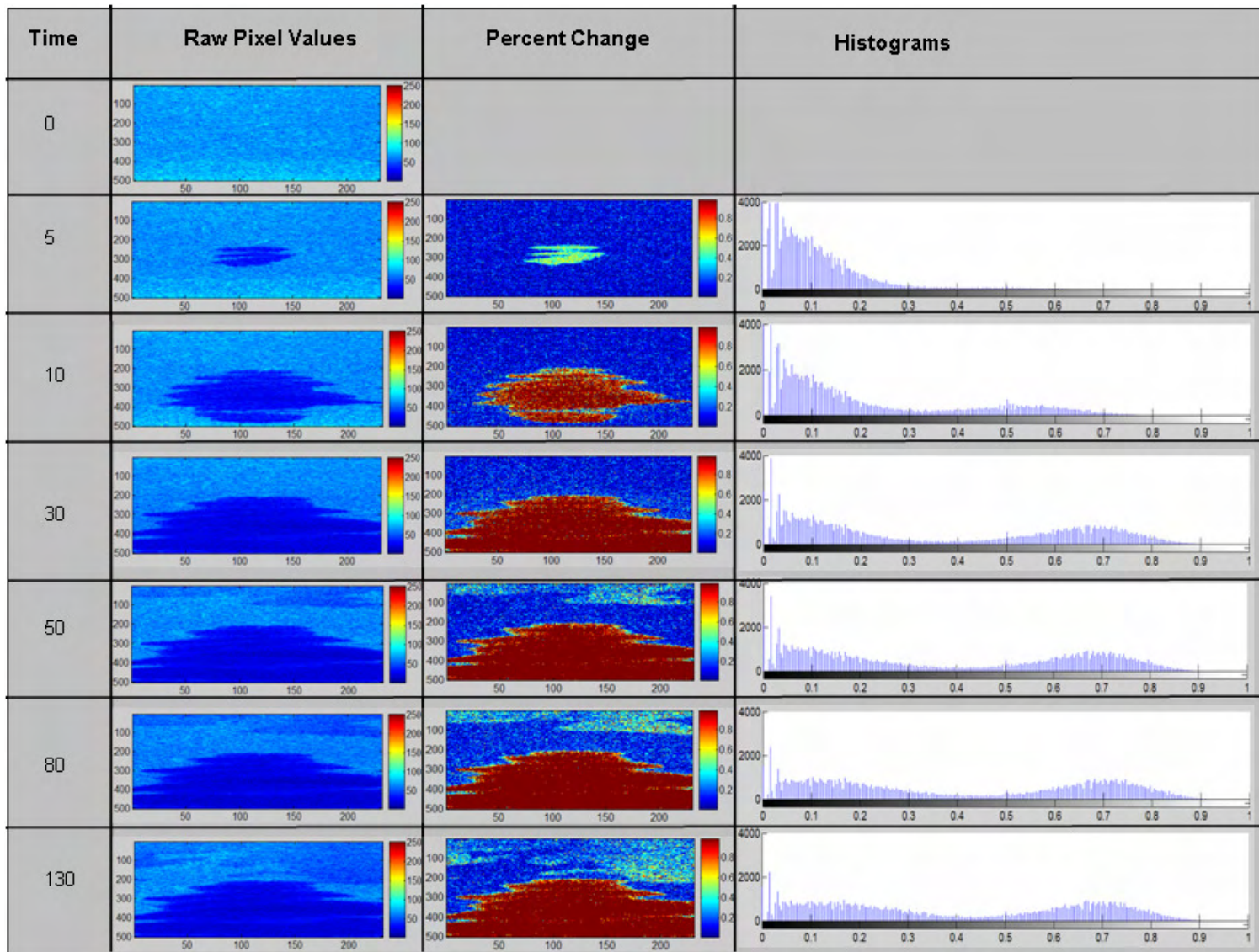
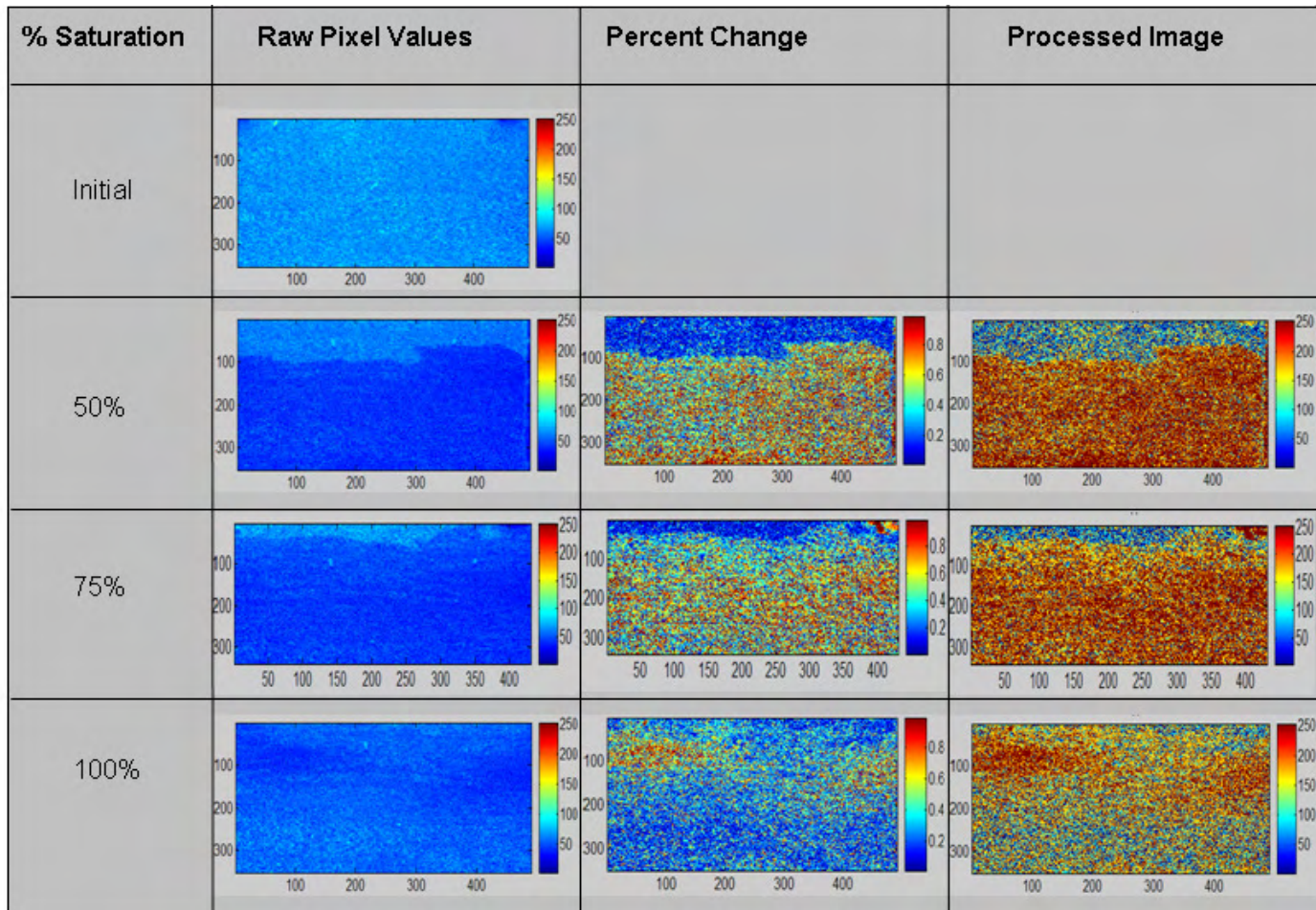


Figure 7.54 b) Histograms during initially -dry experiments



**Figure 7.55 a) Image analysis during saturation process**

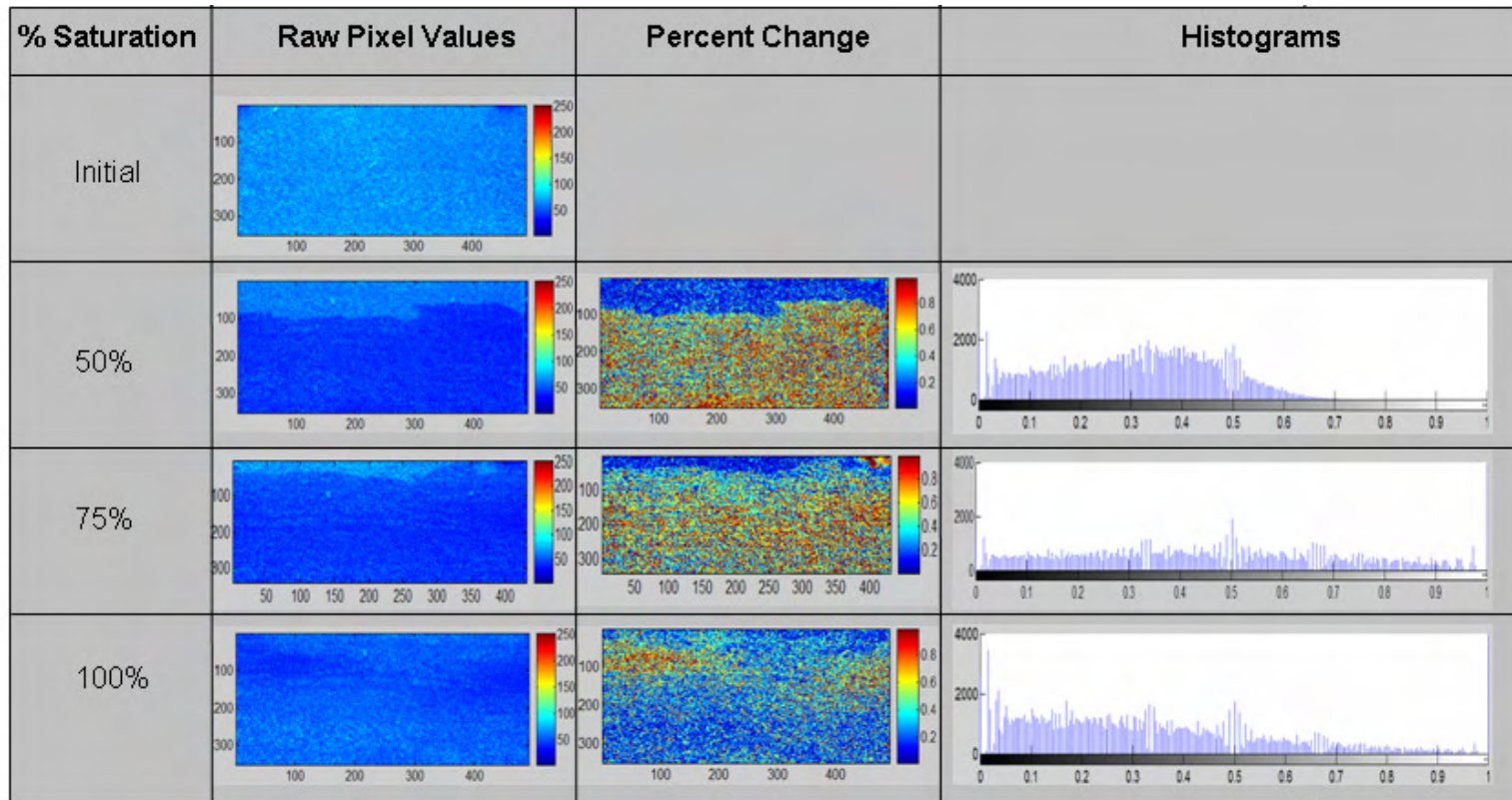


Figure 7.56 b) Histograms during saturation process

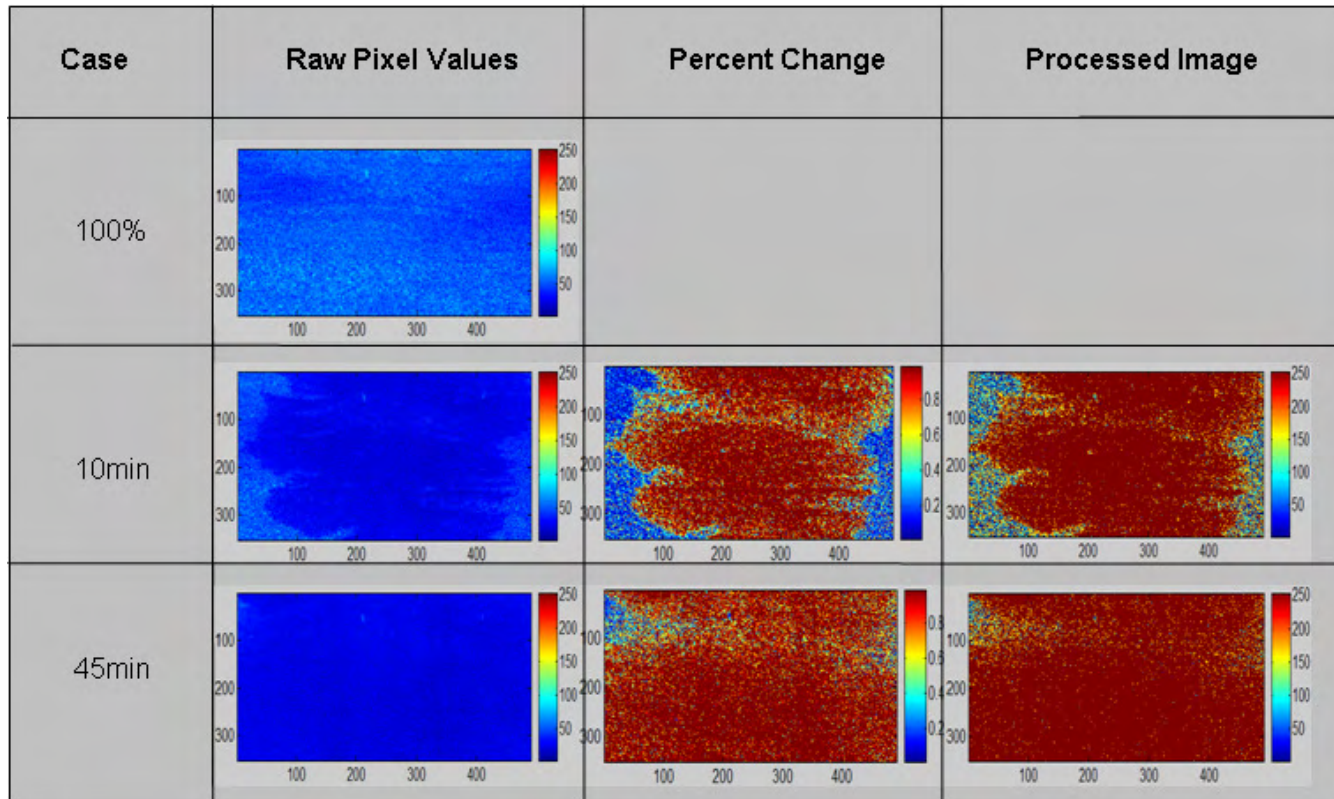


Figure 7.57 a) Image analysis during TCE injection in saturated soil

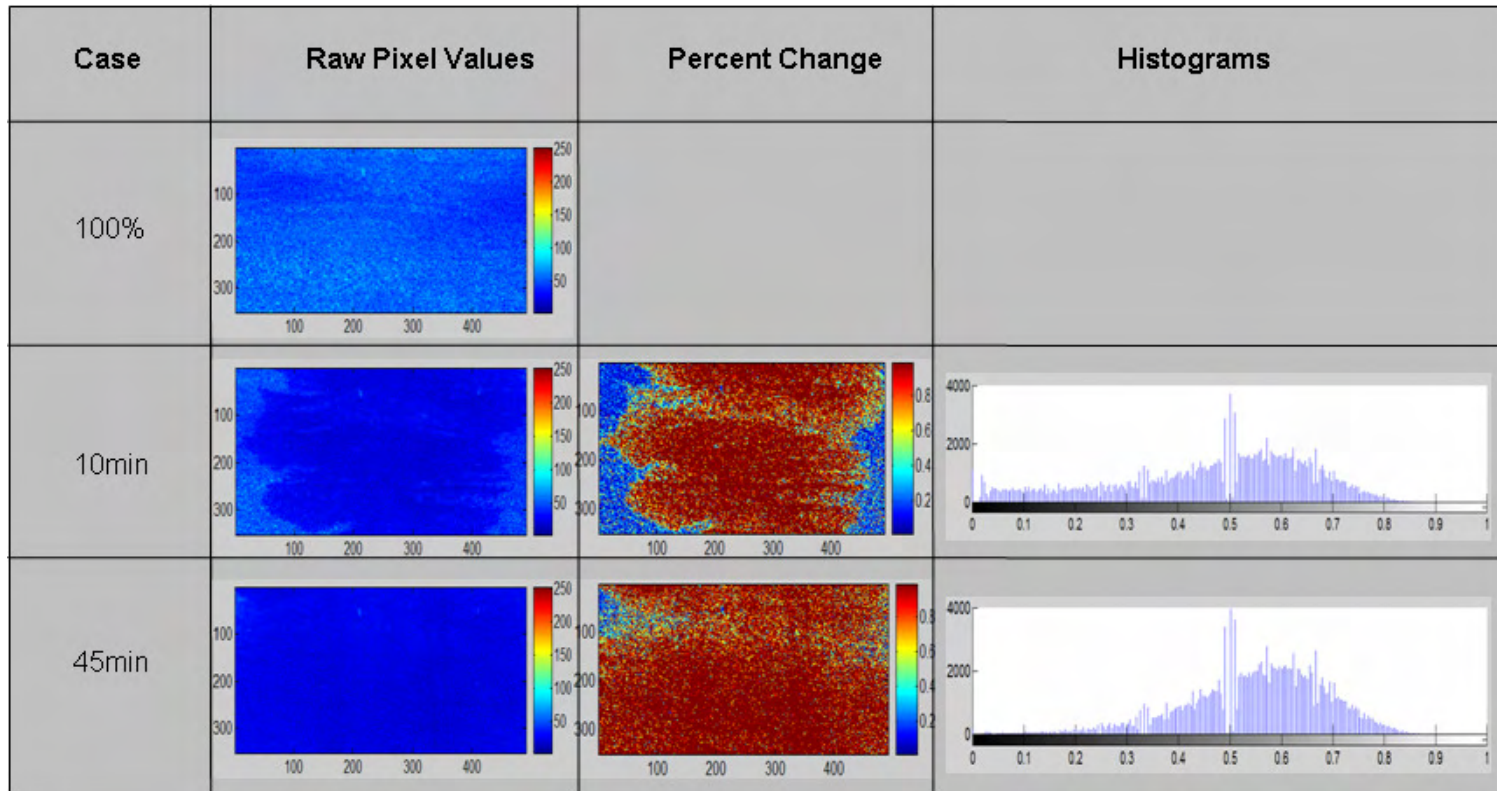
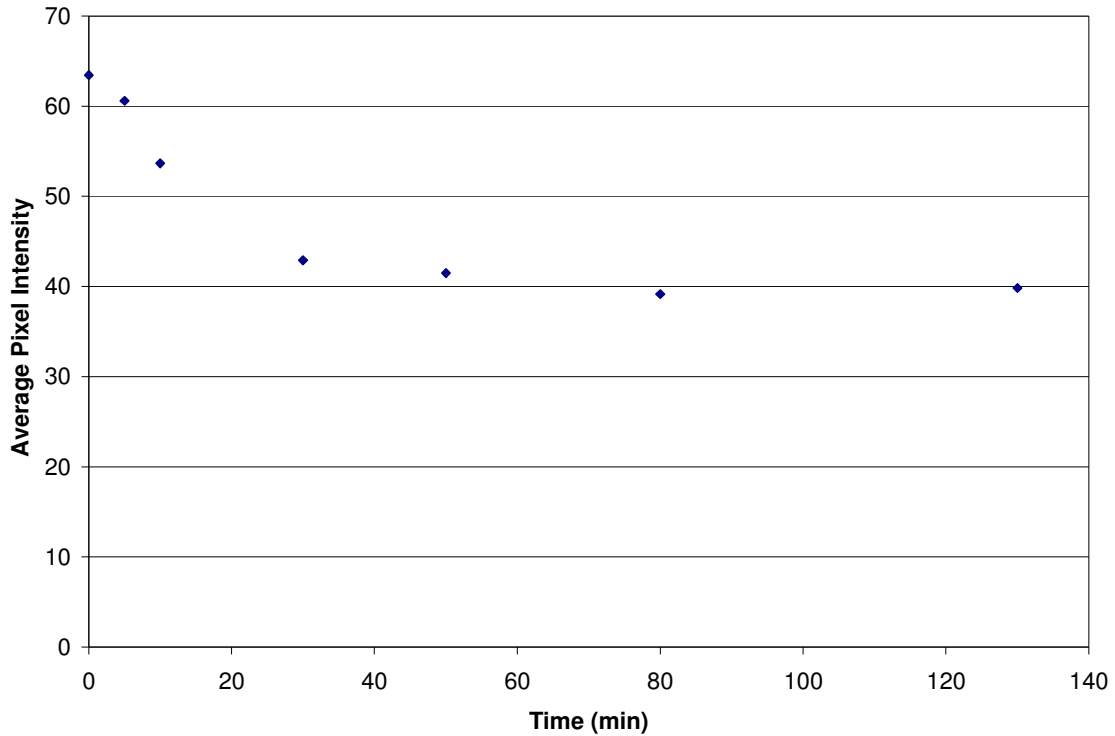


Figure 7.58 b) Histograms during TCE injection in saturated soil



**Figure 7.59 Variations in pixel intensity in dry soil**

Overall, the results indicate that the image processing and analysis techniques developed in this research are effective in detecting changes by fluid flow and distribution. Differences in color intensity in the presence of water, suggest that this technique may be applicable to monitor water flow and saturation changes on pixel intensity during dyed-TCE injection also indicate its application to monitor transport and mass of TCE in the system. Results from initial calibration (Section 5.4.4) indicate that, indeed, this technique can be used to determine TCE volume (and mass) in the image area, for small areas (3 cm \* 3 cm). For larger areas, the technique should be modified to minimize background bias.

## **8. SUMMARY, CONCLUSIONS, AND RECOMMENDATIONS**

Contamination of soils and groundwater by dense non-aqueous phase liquids (DNAPLs) result in detrimental effect of the environment and pose serious threats to public health. In subsurface environments DNAPLs are difficult to locate, characterize, and remediate. It is, therefore, necessary, to develop technologies that will enhance our ability to characterize contaminated sites, locate underground contaminants, evaluate fate and transport processes, and remediate these contaminated sites.

Cross Well Radar (CWR) is a semi-invasive technology, which relies on the response of the media to the propagation of induced electromagnetic waves. It involves placing antennas into distant boreholes and emitting radar waves from the transmitting antennas in one borehole, through the soil, to the receiving antennas in other locations. This research addresses the development and evaluation of CWR for detection and monitoring of DNAPL in subsurface environments under variable flow and saturation conditions.

Cross Well Radar technology was tested and evaluated using 2D soilBed setups, which minimize the generation of DNAPL contaminated soil and permit the establishment of a controlled flow system. Several 2D soilBeds were developed and tested. They incorporated perfectly reflecting plates perpendicular to the transmitting signal. Metal mesh panels, which can create a 2D permanent electromagnetic field of perfect reflection,

while maintaining a 2D flow in the system, were used for this purpose. Experimental results show that the 2Ds setups are applicable for CWR measurements, provided that electromagnetic and flow design considerations are met. These considerations include soilBed geometry and boundaries, separation of metal plates, antennas configuration, and placement of flow boundary conditions. The geometry and scale of the soilBeds must be designed so that boundary conditions do not influence wave propagation, fluid flow, and respective measurements in the system. The design must also contemplate particular limitations of the sampling and instrumentation technology available. The separation of the metal plates is inversely proportional to the frequency and electromagnetic permittivity of the medium. Antennas configuration must consider type, size, orientation, and arrangement of antennas.

Initial transmission and reflection testing for selection of antennas suggested that dipole antennas performed better than monopole antennas in 2D systems. The required length (<2.2cm) and orientation toward perfectly reflective boundaries limited the testing and evaluation to loop antennas. Transmission and reflection measurements indicate that the loop antennas used are reliable, but the antennas response varies with method of construction.

Loop antennas consist of a conducting wire looped in multiturns around a core material. Hence their design must consider material used, loop diameter, and number of loops. Several loop antennas were tested for a final selection of the antenna design. Based in

transmission and reflection measurements loop antennas having 24 turns helicoidal ferrite core material were used for this work.

The separation distance and arrangement of antennas also play an important role in the measurement reliability in the system. Initial assessment showed acceptable antenna response to a linear arrangement. The separation distance was, however, limited by the dielectric properties of the media, and the radiation characteristics of the antenna and instrumentation. Generally, greater separation distances resulted in greater insertion losses (attenuation) as the wave propagates. Consequently, measurements are closer to noise level of the instrument at greater distances. Dielectric properties which enhance insertion losses, further influence measurement limitations. Results from this research indicate that insertion losses are greater for wet and saturated soil than dry soil. These variations must be taken into account when designing the separation distance between transmitting and receiving antennas.

The final design of the 2D soilBed consisted of a plexiglass tank (83 cm \* 83 cm \* 7 cm) having two parallel metal mesh plates along the length of the tank with a separation distance of 2.2 cm. Antennas were inserted thorough horizontal boreholes located at the lateral panels of the tank. Their horizontal separation distance was approximately 58 cm. Although transmission and reflection measurements were possible and reliable for dry conditions, measurement levels were close to noise levels. For conditions with greater attenuation losses (e.g., wet, contaminated, heterogeneous) measurements would not be reliable. A smaller soilBed prototype (30 cm \* 30 cm \* 7 cm) was therefore used for

electromagnetic measurements in the presence of water and non-aqueous trichloroethylene (TCE).

Experimental transmission and reflection results in various soilBeds indicate that CWR measurements may be applied to detect changes in wave propagation characteristics caused by the presence of underground target elements (UTE), such as metal and plastic objects, and DNAPL contamination. CWR technology may also be applied to detect EM changes caused by medium and fluid heterogeneities. Accurate characterization and location of UTEs and heterogeneities must utilize inversion and imaging tools to interpret and translate indirect electromagnetic measurements into applicable subsurface characteristics.

CWR technologies were applied during TCE and water injection in 2D soilBeds to assess its applicability for DNAPL detection and monitoring in subsurface environments under variable flow conditions. Transmission measurements reflect detectable changes in electromagnetic properties of the soil as TCE and water enter the silBeds. These changes are frequency-dependent and vary with saturation conditions and antenna separation, distance, and depth.

For initially dry soil transmission response prior and during TCE injection differ significantly for frequencies above 1700 MHz at most depths, but the magnitude of the difference depend on a depth and time after injection. Generally, at these higher frequencies, the presence of TCE shows lower attenuation losses suggesting

electromagnetic insulation characteristics of TCE at these frequencies. No major difference in transmission measurements are observed at lower frequencies, except for the antennas located closest to the soil surface.

Water infiltration and saturation generally tends to lower the transmission response in the antennas for frequencies above 900 MHz. Generally, lower transmission responses are observed when water-saturation conditions exist near antennas. Lower transmission response in the presence of water is attributed to greater attenuation losses caused by water absorption, conduction, and scattering effects and reflection at heterogeneous air-water interface.

Transmission measurements during TCE injection under water saturated conditions show slight variations from measurements taken prior to injection (Figure 7.11 to Figure 7.17), but are too close to the VNA noise level to make conclusive remarks. Low transmission measurements are attributed to the attenuation losses caused by water prior to the TCE injection.

Differences in transmission response at various depths are attributed to differences in fluid distribution heterogeneities, potential boundary effects, and differences in the radiation properties of the antennas. Although tests were conducted to determine the effect of boundary conditions, they were conducted in soilBed of different dimensions. The smaller tanks used for the TCE and saturation experiments were not tested. Similar pattern response for transmission and reflection measurements near the bottom and top

boundaries suggest some EM influence by the boundaries. This potential effect is further supported by the soilBed EM model (Section 5.4.3) developed by Certuche and Rodriguez (2007). The effect of these boundaries shall be evaluated and incorporated into design parameters for 2D soilBeds.

In addition to the effect of soilBed boundaries, differences in antenna's transmission and reflection measurements for pre-injection conditions suggest different radiation characteristics of the antennas. Initial studies revealed differences in antenna response depending on the construction of the antennas. Slight variations in antennas construction thus may explain response differences. Any variations in the antenna coupling characteristics would also results in response differences. These differences should be appropriately quantified through reflection measurements and normalized using a channel transfer functiosn similar to those developed by Farid (2004).

Transmission and reflection measurements (Section 7.2) indicate that the EM response is affected when a fluid is introduced into the system. This effect is caused by changes in dielectric properties of the bulk soil in the presence of fluid, object, or soil heterogeneities (Figure 7.24 to Figure 7.36). Assuming lossless medium these changes are mostly associated with variations in the relative permittivity of the perturbed medium. An inverse tool may, thus, be applicable to determine relative permittivity from transmission and reflection measurements.

An inverse algorithm (Permittivity Code, Appendix 1) was developed to estimate relative permittivity values from the transmission and reflection signals received and emitted by the antennas. The algorithm inherently assumed lossless medium and perfectly coupled and identical radiation characteristics of the antennas. The algorithm can be applied to any frequency range, but a range around 1000 to 1200 MHz was selected for this analysis. Estimated values within the evaluated frequency are frequency dependent, showing a rise to a peak maximum value followed by decreasing permittivities. The peak value and frequency at peak value are relative to the location of the antennas. Estimated permittivity values below 1 are considered erroneous values, which may arise from the effects of differences in antenna radiations, boundary proximity, lossless medium assumption, and raypath bending across heterogeneities.

Peak relative permittivity estimates for dry soils range from about 1.4 to 7 depending on Port location. Maximum average relative permittivity estimates fall within reported values ( $2.46 \pm 0.38$ ) for a dry-soil system, but slightly lower ( $1.4 \pm 0.51$ ) for another. These differences are attributed to difference in soil packing and antenna's radiation properties.

Some variations in permittivity estimates are observed as TCE is injected into initially-dry soil. Preliminary statistical analysis, indeed, suggest potential significant variations between measurements taken prior to and after injection of TCE and water. Initially, relative permittivity estimates decrease as TCE enters the system, but increase at greater injection times (i.e. greater TCE volumes). Lower initial values are attributed to the

formation of fluid heterogeneities of different dielectric properties in the system. Later increase is associated with the inclusion of a fluid with greater permittivity.

Water infiltration after TCE injection tends to increase relative permittivity estimates. The presence of water is expected to increase permittivity values of the bulk soil because of the greater permittivity values of water. Changes in permittivity estimates may also occur from fluid distribution heterogeneities.

Generally, as the soilBed is saturated the permittivity estimates tend to increase, and the frequencies at maximum values are shifted. Although the presence of water increased the relative permittivity values (Figure 7.31 to Figure 7.36), the values measured are below the values reported in the literature. An increase in permittivity is expected as water, having greater permittivity than air, displaces air. The slight variation is possibly due to differences in antennas characteristics, effect of soilBed and air-water boundaries, and scattering from heterogeneities form by capillary rise and air entrapment during saturation. Futhermore, results indicate that the position of the water table affect the dielectric permittivity estimates. This indicates that permittivity values are influenced by the air-water interface, as previously suggested by a soilBed EM model developed by Certuche and Rodriguez (2007).

TCE injection into the saturated soilBed resulted in slightly higher permittivity values of the medium (Table 7.2, Figure 7.35 and Figure 7.36). Because of the lower than water permittivity of TCE, bulk estimated permittivity values are expected to decrease as TCE

displaces water. The effect of upward water displacement in the soilBed as TCE is injected may, however, offset the expected decrease. This is because as TCE displaced water upward, the location of the air-water interface increases.

The general results obtained demonstrate that the inclusion of DNAPL organic contaminants and water in soil affects the dielectric permittivity of the medium. Preliminary statistical analysis suggest potential significant differences in relative permittivity estimates for different degrees of water and TCE saturation. The results, however, also demonstrate that mixing models may not appropriately describe variations in bulk permittivity, under variable flow conditions and those factors such as fluid distribution and heterogeneities may also have to be taken into account.

Results also suggest that the medium may not be completely lossless as assumed for the inversion algorithm. Other potential errors in assumptions, such as perfectly coupled and similar radiation characteristics of antennas, and no effect of soilBed boundaries, may influence the permittivity estimates reliability. These assumptions should be revised and tested to entrance reliability of the estimates.

Better assessment of permittivity estimates may also be accomplished by considering other range of frequencies in the analysis. Transmission and reflection measurements indicate frequency dependent behavior of the wave propagation properties. Evaluating the dielectric properties at different frequency ranges may provide more information on the wave propagation characteristics in the medium. Based on the transmission and

reflection results, there may be some frequencies at which the mass of water and TCE maybe related to the EM response of the antennas. Furthermore, results suggest that the inclusion of fluids of different permeabilities in the medium results in a shift of the frequency at which peak values occur. This shift appears to be related to the volume and type of fluid and may be related to EM phase shift, but further assessment must be conducted to evaluate these observations.

A Tomography code was developed to generate tomographic images using the permittivity estimates of all raypaths between transmitting and receiving antennas. The code uses simultaneous algebraic reconstruction techniques (SART) to develop the tomographic images. The code assumes straight raypaths, and may loose resolution if raypath are bent due to spatially varying velocity profiles. These tomograms may be used to image and visualize the presence of disturbances in the medium. The developed Tomography code generates acceptable tomograms of UTEs in soils, provided that there is sufficient density of antennas arrays, and proper grid spacing. The codes, thus, provides an excellent tool for optimal CWR system design and can be applied to determine the number of antennas required for good resolution of a specific geometry in lossless medium. Simulations of squared UTE using the code indicate that an array of 5 antennas on each side is required for proper resolution of tomograms in a 2D SoilBed having dimensions of 30 cm x 30 cm. The accuracy of using only 4 antennas in each side of the setup reduces resolution of the detection technique. It is deduced that better tomographic results bay be achieved for a greater number of borehole transmission and

reflection measurements. This code should therefore be used to optimize the number and distribution of antennas required for the development of a soilBed design.

Tomograms generated with relative permittivity estimates using S-parameters measurements in the 1 to 1.2 GHz frequency range show variations between initial conditions and those at different fluid flow and distribution conditions during the experiments. Tomographic images of dry soils show relatively uniform distribution of relative permittivity except for certain anomalies near one of the antennas. This anomaly is generated during the tomographic iteration process. The anomaly may result from low resolution of the measurements, and the imposed conditions of zero difference between measured and calculated values in all antennas. Furthermore, this error may arise from mathematical compensation of radiation differences between the antennas. Further work should be conducted to assess and correct the generation of the anomalies.

Generated images suggest slight variations of the tomogram after injection of TCE and water in the system. These variations, however, be masked by the low tomographic resolution obtained with 4 sets of antennas. As soilBeds saturates the tomographic distribution of relative permittivity tends to increase slightly. The higher relative permittivity and wave-slowness properties may be attributed to greater water content in the soilBed, and to greater scattering and reflection energy losses caused by fluid heterogeneities and the air-water interface. Even tough the relative permittivity increases during the saturation process, the values obtained are low compared to reported values in the literature. Relative permittivity in saturated soils has been reported close to 20 (Farid

et al., 2004), while in this experiment the average relative permittivity for the tomographic grid was 4.20 in saturated conditions. Differences may be attributed to differences in antenna radiation characteristics, effects of soilBed and air-water interface boundaries, and scattering and wave bending across heterogeneities formed by capillary rise and air entrapment during saturation.

In general, the tomographic results show changes caused by variable flow and fluid saturation and distribution conditions. The experimental resolution, and potential measurement error limit the asseverance of conclusive remarks in the systems. In addition to increasing the density of measurements, it is recommended that targeted experiment be conducted in the future to better characterize electromagnetic soil properties under time domain and various frequency ranges.

Image acquisition and processing algorithms were developed to analyze visual images of dyed contaminants, discriminate between regions of different amounts of DNAPLs, and assess potential relationships between electromagnetic variations and the spatially-distributed DNAPL in the soil. Digital images taken during experiments suggest non-homogeneous movement of TCE and water, resulting in fluid heterogeneities. These heterogeneities are thought to influence EM measurements in the soilBed.

Overall, the results indicate that the image processing and analysis techniques developed in this research are effective in detecting changes by fluid flow and distribution. Differences in color intensity in the presence of water, suggest that this technique may be

applicable to monitor water flow and saturation changes on pixel intensity during dyed-TCE injection also indicate its application to monitor transport and mass of TCE in the system. Results from initial calibration (Section 5.4.4) indicate that, indeed, this technique can be used to determine TCE volume (and mass) in the image area, for small areas (3 cm \* 3 cm). For larger areas, the technique should be modified to minimize background bias.

Direct comparison of CWR measurements and digital processed images were not possible at this stage of the research because of the low tomographic resolution obtained and the limited and variable area required for the digital image analysis. Further work has, however, been recommended to improve these limitations, and it is believed that once resolved direct comparison will be attainable.

The research presented has developed a methodology to detect electromagnetic changes caused by variable spatial and temporal distribution of fluids with different electromagnetic properties. It further developed a method to estimated electromagnetic properties of bulk soil having variable fluid distribution from measured S-parameters. A tomographic method, which applies the estimated electromagnetic properties to generate tomographic images of the properties, was also developed and applied. These developments pose significant contributions, which bring underground detection technologies closer to real applications. The methods, however, can be improved through the following recommendations:

- Increase electromagnetic measurement density
- Normalizing the radiation characteristics of antennas through channel transfer functions similar to those developed by Farid, 2004.
- Integrating conduction losses into equations used to estimate electromagnetic properties.
- Performing the analysis at various frequency ranges.
- Relocating antennas further away from boundary conditions.

In conclusion, the results from this research demonstrate that:

Sufficient contrast exists between EM properties of uncontaminated and DNAPL-contaminated soil to apply CWR for contaminant detection. It is further postulated that this contrast detection depends on water content. The contrast is dependent on water content, frequency range of analysis, fluid movement, distribution, and heterogeneities, and the presence of physical, and fluid interfacial areas.

Dielectric properties along raypath between transmitting and receiving CWR antennas can be determined in a 2D electromagnetic soilBed bound by perfectly reflecting parallel surfaces. Accurate estimates of the dielectric properties must take into account differences in radiation characteristics between antennas, and should be far away from soilBed boundaries. The assumptions related to lossless medium, straight raypaths, and equal radiation properties of antennas must be revised for more accurate estimates.

Spatially-distributed measurements of effective dielectric properties along raypaths in a 2D electromagnetic soilBed can be used to form tomographic images of distributed contamination under variable saturation conditions. The resolution of the tomographic images, however, depends on the density of the measurement, and on factors affecting electromagnetic measurements and estimates of dielectric properties.

Image processing and analysis of dyed-DNAPLs serve to determine amount of DNAPLs mass in a visual region. At the moment, this technology is applicable for areas with small background bias. It is suggested that a weighting factor be incorporated into the code to eliminate background bias during image processing and analysis.

## 9. REFERENCES

Agilent Technologies, *Basics of Measuring the Dielectric Properties of Materials*, Application Note 1217-1, 32p, 2005.

Agilent Technologies, *Materials Measurement: Measuring the Dielectric Constant of Solids with the HP 8510 Network Analyzer*, Product Note 8510-3, 12p, 1985.

Agilent Technologies, *Test & Measurement: S-Parameter Techniques*, Application Note 95-1, 79p 1995.

Agilent Technologies, *Understanding the Fundamental Principles of Vector Network Analysis*, Application Note 1287-1, 14p, 1997.

Agilent Technologies, *Time Domain Analysis Using a Network Analyzer*, Application Note 5989-5723EN, 48p, 2007.

Antonik N.A., I.S. Kruglow, L.P., Ligthart, V.V. Zagoskin, A.S.Shostak, V.N. Iljushenko, *Measurement of the Complex Dielectric Permittivity of Stratified Media with Dipole Antenna Sensors*, in European Radar Conference, Amsterdam, pp. 173-176, 2004.

ASTDR, *Toxicological Profiles*. Agency for Toxic Substances and Disease Registry, U.S. Public Health Service (CD-ROM), 1997.

ASTDR, *Toxicological Profile 1 for Chlorine*, Agency for Toxic Substances and Disease Registry, U.S. Public Health Service, pp.318,2007.

Balanis C., *Antenna Theory: A Review*, Proceedings of the IEEE, vol. 80, no. 1, pp. 7-23, 1992.

Balanis C., *Antenna Theory: Analysis and Design*, Third Edition, published by Wiley-Interscience, John Wiley & Sons, Inc., New Jersey, 2005.

Baker-Jarvis J., E.J.Vanzura, and W. A. Kissick, *Improved Technique for Determining Complex Permittivity with the Transmission/Reflection Method*, IEEE Transactions on Microwave Theory and Techniques, vol 38, no. 8, pp. 1096-1103, 1990.

Bedient P. B., H.S. Rifai, and C.J. Newell, *Ground Water Contamination Transport and Remediation*, Second Edition, Prentice Hall, NJ, 1997

Benson A., K. L. Payne, and M. A. Stubben, *Mapping Groundwater Contamination using dc Resistivity and VLF Geophysical Methods- A Case Study*, Geophysics, vol. 62, no. 1, pp. 80-86, 1997.

Binley A., P. Winship, R. Middleton, M. Pokar, and J. West, *High-resolution Characterization of Vadose Zone Dynamics Using Cross-borehole Radar*, *Water Resources Research*, vol. 37, no. 11, pp. 2639-2652, 2001.

Binley A., G. Cassiani, R. Middleton, and P. Winship, *Vadose Zone Flow Model Parameterisation Using Cross-borehole Radar and Resistivity Imaging*, *Journal of Hydrology*, vol. 267, pp. 147-159, 2002.

Borns D.J.G. Newman, L. Stolarczyk, and W. Mondt, *Cross Borehole Electromagnetic Imaging of Chemical and Mixed Waste Landfills*, *Proceedings of the Symposium on the Application of Geophysics to Engineering and Environmental Problems*, vol. 1, San Diego, pp. 91- 105, 1993.

Brewster M.L. and A. P. Annan, *Ground-penetrating Radar Monitoring of a Controlled DNAPL Release: 200MHz Radar*, *Geophysics*, vol. 59, no. 8, pp. 1211-1221, 1994

Brewster M.L., A.P. Annan, J.P. Greenhouse, B.H. Kueper, G.R. Olhoeft, J.D. Redman and K.A. Sander, *Observed migration of a controlled DNAPL release by geophysical methods*, *Ground Water* , vol. 33, no. 6, pp. 977–987, 1995.

Brown R.A., R. Hines, M.C. Leahy, and J. Cho, *Abiotic and Biotic Pathways in Chlorinated Solvent Natural Attenuation*, *Battelle's Fifth International Conference on Remediation of Chlorinated and Recalcitrant Organics*, Monterrey, May, 2006.

Brusseau M.L., N.T. Nelson, M. Oostrom, M. White, and T.W. Wietsma, *Partitioning Tracers for In-Situ Measurement of Nonaqueous Phase Liquids in the Subsurface*, Department of Energy, United States of America, Project Number 54908, Grant Number: DE-FG-96ER14722. Available: <http://www.osti.gov/bridge/servlets/purl/790174-P9o0iz/native/790174.PDF>, 2000. Accessed on February 2006.

Brusseau M.L., N.T. Nelson, and M.S. Constanza-Robinson, *Partitioning Tracers Tests for Characterizing Immiscible-fluid Saturations and Interfacial Areas in the Vadose Zone*, *Vadose Zone Journal*, vol. 2, pp. 138-147, 2003.

Bunkowski A., O. Burmeister, D. Friedrich, K. Danzmann, and R. Schanabel, *High Reflectivity Grating Waveguide Coatings for 1064 nm*, *Classical and Quantum Gravity*, vol. 23, pp. 7297-7303, 2006.

Buselli G. and K. Lu, *Groundwater Contamination Monitoring with Multichannel Electrical and Electromagnetic Methods*, *Journal of Applied Geophysics*, vol. 48, no. 1, pp. 11-23, 2001.

Buyukozturk O., Tzu-Yang Yu., and J.O.Ortega, *A Methodology for Determining Complex Permittivity of Construction Materials Based on Transmission-only Coherent, Wide-bandwidth Free-space Measurements*, *Cement & Concrete Composites*, vol. 28, pp. 349-359, 2006.

Carcione J.M., G.Seriani, and D. Gei, *Acoustic and Electromagnetic Properties of Soils Saturated with Salt Water and NAPL*, Journal of Applied Geophysics, vol. 52, no. 4, pp. 177-191, 2003.

Cassiani G., C. Strobbia, and L. Gallotti, *Vertical Radar Profiles for the Characterization of Deep Vadose Zones*, Vadose Zone Journal, vol. 3, pp. 1093-1105, 2004.

Castiglione P., P. J. Shouse, and J. M. Wraith, *Multiplexer-Induced Interference on TDR Measurements of Electrical Conductivity*, Soil Science Society of America Journal, vol. 70, pp. 1453-1458, 2006.

Censor Y., *Finite Series-Expansion Reconstruction Methods*, Proceedings of the IEEE, vol. 71, no. 3, pp. 409-419, 1983.

Certuche L. and R. Rodriguez, *An Electromagnetic Model of a 2D soilBed*, written communication (See appendix 6), 2007.

Chambers J.E., M.H. Loke, R.D. Ogilvy, and P. I. Meldrum, *Noninvasive Monitoring of DNAPL Migration through a Saturated Porous Medium using Electrical Impedance Tomography*, Journal of Contaminant Hydrology, vol. 64, pp. 1-22, 2004.

Chen B., Z. Hu and W. Li, *Using Ground Penetrating Radar to Determine Water Content of Rehabilitated Coalmine Soils Treated by Different Methods*, in Tenth International Conference on Ground Penetrating Radar, Netherland, June, pp. 513-516, 2004.

Chen L., and R. C. Knox, *Using Vertical Circulation Wells for Partitioning Tracers Tests and Remediation of DNAPLs*, Ground Water Monitoring and Remediation, vol. 17, pp. 161-170, 1997.

Clement W.P. and M. D. Knoll, *Tomographic Inversion of Crosshole Radar Data: Confidence in Results*, in Proceedings of the Symposium on the Application of Geophysics to Environmental and Engineering Problems, Arlington, VA, pp. 553-562, 2000.

Clement W. P., W. Barrash, and M. D. Knoll, *Reflectivity Modeling of a Ground-Penetrating-Radar Profile of a Saturated Fluvial Formation*, Geophysics, vol. 71, no. 3, pp. 59-66, 2006.

Corwin D.L, and S. M. Lesch, *Application of soil Electrical Conductivity to Precision Agriculture: Theory, Principles, and Guidelines*, Agronomy Journal, vol. 95, no. 3, pp. 455-471, 2003.

Cohen R. and J. Mercer, *DNAPL Site Evaluation*, C.K. Smoley/CRC Press, Boca Raton, Florida, 1993. Also available as EPA Publication EPA 600-R-93-022, 1993.

Crescimanno G., and P. Garofalo, *Management of Irrigation with Saline Water in Cracking Clay Soils*, Soil Science Society of America Journal, vol. 70, pp. 1774-1787, 2006.

Curtis W.L., and R. J. Coe, *A Microwave Technique for the Measurement of the Dielectric Properties of the Soil*, IEEE Transactions on Microwave Theory and Techniques, Aero Space Division The Boeing Company, vol. 11, no. 3, pp 211- 212, 1963.

Day-Lewis, F. D., Lane, J. W., Harris, J. M., and Gorelick, S. M, *Time-lapse Imaging of Saline Tracer Transport in Fractured Rock using Difference Radar Attenuation Tomography*, Water Resources Research, vol. 39, 1290, 2003.

Divine C. E., W. E. Sanford, J. E. McCray, *Helium and Neon Groundwater Tracers to Measure Residual DNAPL: Laboratory Investigation*, Vadose Zone Journal, vol. 2, pp. 382-388, 2003.

Dines K., and R.J. Lytle, *Computerized Geophysical Tomography*, Proceedings of the IEEE, vol. 67, no. 7, pp. 1065-1073, 1979.

Dong-Ho H. and Yuand-Liand Li, *Complex Dielectric Constant Measurement techniques for High-Speed Signaling*, *Electrical Performance of Electronic Packaging*, IEEE, pp. 137-140, 2001.

Durnford D.S., D.B. Mc. Whorter, C.D. Miller, A. Swanson, F. Marinelli and H. L. Trantham, *DNAPL and LNAPL distributions in soils; experimental and modeling studies*, Colorado State University, October. Available: <http://handle.dtic.mil/100.2/ADA342524>, 1997. Accessed on April, 2006.

Eigenberg R. A., J. A. Nienaber, B. L. Woodbury, and R. B. Ferguson, *Soil Conductivity as a Measure of Soil and Crop Status- A Four-year Summary*, Soil Science Society of America Journal, vol. 70, pp. 1600-1611, 2006.

Ellifsen K.J., *Crosswell Radar: A Feasibility Test at the M-Area Settling Basin, Savannah River Site, South Caroline*, U.S. Geological Survey, Open-File Report 97-144, 1997.

Environment Agency, *Guidance on the Assessment and Monitoring of Natural Attenuation of Contaminants in Groundwater*, R&D Publication 95, Environment Agency, Bristol, 2000.

Environmental Protection Agency (EPA), *Estimating the Potential for Occurrence of DNAPL at Superfund Sites*, Environmental Protection Agency Office of Solid Waste and Emergency Response, Publication 9355.4-07, Washington D.C., pp.10, 1992.

Environmental Protection Agency (EPA), *Geophysical Techniques to Locate DNAPLs: Profiles of Federally Funded Projects*, Environmental Protection Agency Report number 542-R-98-020. Available: <http://www.frtr.gov/pdf/dnapls.pdf>, pp.31, 1998. Accessed February, 2008.

Environmental Protection Agency (EPA), *Demonstration of Biodegradation of DNAPL through Biostimulation and Bioaugmentation at Launch Complex 34 in Cape Canaveral Air Force Station*, Florida Innovative Technology Evaluation Report, EPA/540/R-07/007 September, pp.103, 2004

Environmental Security Technology Certification Program (ESTCP), *Bioaugmentation for Remediation of Chlorinated Solvents: Technology Development, Status, and Research Needs*, Department of Defense United States of America. Available: <http://docs.serdp-estcp.org/viewfile.cfm?Doc=BioaugmentationWhitePaper.pdf>, 2005. Accessed on March 2007.

Eppstein M. and D. Dougherty, *Efficient Three-dimensional Data Inversion: Soil Characterization and Moisture Monitoring from Cross-Well Ground-Penetrating Radar at a Vermont Test Site*, Water Resources Research, vol. 34, no. 8, pp. 1889-1900, 1998.

Farid, M., Alshwabkeh, A. N., and Rappaport, C. M., *DNAPL Detection using Cross-Well Radar*, Environmental Geotechnics, Proceeding, 4th ICEG, pp. 465-470, 2002.

Farid, M., A.N. Alshawabkeh, and C.M. Rappaport, *Modeling Borehole Dipole Antenna Patterns for Cross-well Radar DNAPL Imaging*, Electronic Proceedings of the 12th Pan-American Conference on Soil Mechanics and Foundation Engineering, Cambridge, MA., pp. 261-268, 2003(a).

Farid, M., Alshawabkeh, A. N., and Rappaport, C. M., *Laboratory Experimental Setup for Cross-well Radar*, Proceedings of SAGEEP Conference, San Antonio, TX, 2003(b).

Farid, M., *DNAPL Detection Using Cross Well Radar*, PhD. Dissertation, Northeastern University, Boston, 2004.

Feng B., *Extracting Material Constitutive Parameters from Scattering Parameters*, PhD. Dissertation, Naval Postgraduate School, Monterrey, California, 2006.

Feng H., W. C. Karl, and D. A. Castanon, *A Curve Evolution Approach to Object-Based Tomographic Reconstruction*, IEEE Transactions on Image Processing, vol. 12, no. 1, pp 44-57, 2003.

Fetter C.W., *Contaminant Hydrogeology*, Macmillan Publishing Company, 1993.

Finci A.G. and D. F. Stanfill, *Feasibility of Non-intrusive and Remote Identification of Chemical Contaminant Using Ground Penetrating Radar (GPR)*, Air Force Research Laboratory, AFRL-MN-EG-TR-1999-7015, pp.288, 1998.

Fischbein N., *Waiting for Clean-up: Unaddressed Risks at Potential Superfund Sites*, March 2005, <http://www.tceblogger.com/post/1111865024.shtml>, accessed in September 20th, 2006.

Fountain, J.C., *Technologies for Dense Nonaqueous Phase Liquid Source Zone Remediation*, Technology Evaluation Report, Ground-Water Remediation Technologies Analysis Center, TE-98-02, 1998.

Fox G. and R. Metla, *Soil Property Analysis using Principal Components Analysis, Soil Line, and Regression Models*, Soil Science Society of America Journal, 69, pp. 1782-1788, 2005.

Francisca F. and V. A. Rinaldi, *Complex Dielectric Permittivity of Soil-Organic Mixtures (20MHz-1.3GHz)*, Journal of Environmental Engineering, April, vol. 129, no. 4, pp. 347-357, 2003.

Franchetti G., A. Iodice, D. Riccio and G. Ruello, *SAR Raw Signal Simulation for Urban Structures*, IEEE Transactions on Geoscience and Remote Sensing, vol. 41, no. 9, pp. 1986-1995, 2003.

Friedman S., *Soil Properties Influencing Apparent Electrical Conductivity: a Review*, Computers and Electronics in Agriculture, vol. 46, pp. 45-70, 2005.

Fullagar, P. K., Livelybrooks, D. W., Zhang, P., and Calvert, A. J., *Radio Tomography and Borehole Radar Delineation of the McConnell Nickel Sulfide Deposit, Sudbury, Ontario, Canada*, Geophysics, vol. 65, pp. 1920–1930, 2000.

Furman A., T. P. A. Ferré, and, A.W. Warrick, *A Sensitivity Analysis of Electrical Resistivity Tomography Array Types Using Analytical Element Modeling*, Vadose Zone Journal, vol. 2, pp. 416-423, 2003.

Furman A., A.W. Warrick, and T. P. A. Ferré, *Electrical Potential Distributions in a Heterogeneous Subsurface in Response to Applied Current: Solution for Circular Inclusions*, Vadose Zone Journal, vol. 1, pp. 273-280, 2002.

Garambois S., P. Sénéchal, and H. Perroud, *On the Use of Combined Geophysical Methods to Assess Water Content and Water Conductivity of Near-surface formations*, Journal of Hydrology, vol. 259, no. 1, pp. 32-48, 2002.

Gardner C.M.K., T.J. Dean, and J.D. Cooper, *Soil Water Content Measurement with a High-Frequency Capacitance Sensor*, Journal of Agricultural Engineering Research, vol. 71, pp. 395-403, 1998.

Gasulla M., J. Jordana, and R. Pallás-Areny, *2D and 3D Subsurface Resistivity Imaging Using a Constrained Least-Squares Algorithm*, First World Congress on Industrial Process Tomography, Buxton, Greater Manchester, April 14-17, 1999.

Gimmi T. and N. Ursino, *Mapping Material Distribution in a Heterogeneous Sand Tank by Image Analysis*, Soil Science Society of America Journal, vol. 68, pp. 1508-1514, 2004.

Gu H., C. Cai, and Y. Wang, *Investigation of Fractures Using Seismic Computerized Crosshole Tomography*, Journal of Environmental and Engineering Geophysics, vol. 11, no. 2, pp. 143-150, 2006.

Guilbeault M.A., B.L.Parker, and J.A.Cherry, *Mass and Flux Distributions from DNAPL zones in Sandy Aquifers*, Ground Water, vol.43, no. 1, pp. 70-86, 2005.

Hagrey Said Attia al, *Geophysical Imaging of Root-zone, Trunk, and Moisture Heterogeneity*, Journal of Experimental Botany Advance Access, vol. 58, no. 4, pp. 839-854, 2007.

Hallikainen M. T., M.C. Dobson, and L. Wu, *Microwave Dielectric Behavior of Wet Soil- Part I: Empirical Models and Experimental Observations*, IEEE Transactions on Geoscience and Remote Sensing, vol. 23, no. 1, pp. 25-34, 1985.

Hanafy S. and S.A. al Hagrey, *Ground-Penetrating Radar Tomography for Soil-moisture Heterogeneity*, Geophysics, vol. 71, no. 1, pp. 9-18, 2006.

Harlow R. C., E. J. Burke, T. Ferré, J. C. Bennett, and W. James Shuttleworth, *Measuring Spectral Dielectric Properties Using Gated Time Domain Transmission Measurements*, Vadose Zone Journal, vol. 2, pp. 424-432, 2003.

Harmsen E. W. and H. Parsiani, *Inverse Procedure for Estimating Vertically Distributed Soil Hydraulic Parameters Using GPR*, NOAA-CREST/NASA-EPSCoR Joint Symposium for Climate Studies University of Puerto Rico- Mayaguez, 2003.

Harmsen E. W., H. Parsiani and M. Torres, *Evaluation of Several Dielectric Mixing Models for Estimating Soil Moisture Content in Sand, Loam, and Clay Soils*, Technical Presentation at the 2003 ASAE Annual International Meeting sponsored by ASAE, Las Vegas, 2003.

Hendrick J.M.H., B.Borchers, D.L.Corwin, S.M.Lesch, A.C.Hilgendorf, and J. Schlue, *Inversion of Soil Conductivity Profiles from Electromagnetic Induction Measurements: Theory and Experimental Verification*, Soil Science Society of America Journal, vol. 66, pp.673-685, 2002.

Hilhorst M.A., *A Pore Water Conductivity Sensor*, Soil Science Society of America Journal, vol. 64, pp. 1922-1925, 2000.

Hilhorst M.A., C. Dirksen, F.W.H. Kampers, and R.A. Feddes, *New Dielectric Mixture Equation for Porous Materials Based on Depolarization Factors*, Soil Science Society of America Journal, vol. 64, pp.1581-1587, 2000.

Hipp J.E., *Soil Electromagnetic Parameters as Functions of Frequency, Soil Density, and Soil Moisture*, Proceedings of the IEEE, vol. 62, no. 1, pp. 98-103, 1974.

Hoekstra P. and A. Delaney, *Dielectric Properties of Soils at UHF and Microwave Frequencies*, Journal of Geophysical Research, vol. 79, pp.1699-1708, 1974.

Hubbard S.S. and Y. Rubin, *Hydrogeological Parameter Estimation Using Geophysical Data: a Review of Selected Techniques*, Journal of Contaminant Hydrology, vol 45, pp.3-34, 2000.

Huisman J.A., S. S. Hubbard, J. D. Redman, and A. P. Annan, *Measuring Soil Water Content with Ground Penetrating Radar: A Review*, Vadose Zone Journal, vol. 2, pp. 476-491, 2003.

Husserl J., *Design of a Two-dimensional Model and Investigation of DNAPL Recovery by Water and Co-solvent Flooding*, PhD. Dissertation, Tulane University, 2003.

ITRC Interstate Technology and Regulatory Council, *Dense Non-Aqueous Phase Liquids (DNAPLs): Review of Emerging Characterization and Remediation Technologies*  
Available: <http://www.itrcweb.org/Documents/DNAPLs-1.pdf> , 2000, accessed on September 2006.

ITRC Interstate Technology and Regulatory Council, *DNAPL Source Reduction: Facing the Challenge*. Available: <http://www.itrcweb.org/Documents/DNAPLs-2.pdf> , 2002, accessed on October 2006.

Jackson, M. J., and D. R. Tweeton, *MIGRATOM - Geophysical Tomography Using Wavefront Migration and Fuzzy Constraints*, Bureau of Mines Report of Investigations 9497, 35 p., 1994.

Jackson R.E and V. Dwarakanath, *Chlorinated Degreasing Solvents: Physical-Chemical Properties Affecting Aquifer Contamination and Remediation*, Ground Water Monitoring and Remediation, Fall, vol. 19, no. 4, pp. 102-110, 1999.

Jalbert M. and J. H. Dane, *Correcting Laboratory Retention Curves for Hydrostatic Fluid Distributions*, Soil Science Society of America Journal, vol. 65, pp. 648-654, 2001.

Jang H., M. Kyung Park, and H.J. Kim, *Numerical Modeling of Electromagnetic Waveguide Effects on Crosshole Radar Measurements*, Exploration Geophysics, vol. 38, pp. 69-76, 2007.

Jin, M., M. Delshad, V. Dwarakanath, D.C. McKinney, G.A. Pope, K. Sepehrnoori, C. Tilburg, R.E. Jackson, *Partitioning Tracer Test for Detection, Estimation and Performance Assessment of Subsurface Non-Aqueous Phase Liquids*, Water Resources Research, vol. 30, no. 5, pp. 1201, 1995.

Johnson R.H., *Characterization of Subsurface DNAPL Movement with Ground Penetrating Radar and Inverse Multiphase Flow Simulations*, PhD Dissertation, The Colorado School of Mines, Colorado, 2005.

Johnson R. H., and E. P. Poeter, *Interpreting DNAPL Saturations in a Laboratory-Scale Injection Using One- and Two-Dimensional Modeling of GPR Data*, Ground Water Monitoring and Remediation, vol. 25, no. 1, pp. 159-169, 2005.

Jung W. K., N. R. Kitchen, K. A. Sudduth, R. J. Kremer, and P. P. Motavalli, *Relationship of Apparent Soil Electrical Conductivity to Claypan Soil Properties*, Soil Science Society of America Journal, vol. 69, pp. 883-892, 2005.

Jury W., Z. Wang, and A. Tuli, *A Conceptual Model of Unstable Flow in Unsaturated Soil during Redistribution*, Vadose Zone Journal, vol. 2, pp. 61-67, 2003.

Kak A.C. and M. Slaney, *Principles of Computerized Tomographic Imaging*, IEEE Press Books, Electronic Copy. Available: <http://www.slaney.org/pct/>, 1988. Accessed on June 2007.

Kasteel R., M. Burkhardt, S. Giesa, and H. Vereecken, *Characterization of Field Tracer Transport Using High-Resolution Images*, *Vadose Zone Journal*, vol. 4, no. 11, pp. 101-111, 2005.

Kemna A., A. Binley, and L. Slater, *Crosshole IP Imaging for Engineering and Environmental Applications*, *Geophysics*, vol. 69, no. 1, pp. 97-107, 2004.

Kelleners T. J., D. A. Robinson, P.J. Shouse, J.E. Ayars, and T.H. Skaggs, *Frequency Dependence of the Complex Permittivity and Its Impact on Dielectric Sensor Calibration in Soils*, *Soil Science Society of America Journal*, vol.76, pp 67-76, 2005.

Kim J., S.Cho, M. Yi, and M. Sato, *Application of Anisotropy Borehole Radar Tomography in Korea*, Tenth International Conference on Ground Penetrating Radar, Netherlands, 21-14 June, 2004.

Kim H., S. Lee, J. Moon, and P. S. Rao, *Gas Transport of Volatile Organic Compounds in Unsaturated Soils: Quantitative Analysis of Retardation Processes*, *Soil Science Society of America Journal*, 69, pp. 990-995, 2005.

Kruk J, *Properties of Surface Waveguides Derived from Inversion of Fundamental and Higher Mode Dispersive GPR Data*, IEEE Transactions on Geoscience and Remote Sensing, vol. 44, no. 10, pp. 2908-2915, 2006.

Kueper B.H., G.P. Wealthall, J.W.N. Smith, S.A. Leharne, and D.N. Lerner, *An Illustrated Handbook of DNAPL Transport and Fate in the Subsurface*, Environment Agency, Bristol U.K., 67 pp. , 2003.

Lacko P.R., W. W. Clark, K. Sherbondy, J. M. Ralston and E. Dieguez, *Studies of Ground Penetrating Radar*, Second International Workshop and Advanced GPR, The Netherlands, 14-16 May, 2003.

Ladas K. T. and A. J. Devaney, *Iterative Methods in Geophysical Diffraction Tomography*, Inverse Problems, vol. 8, no. 1, pp. 119-132, 1992.

Lambot S., M. Antoine, I. van den Bosch, M. Vanclooster, and E. C. Slob, *Effect of Soil Roughness on the Inversion of Off-ground Monostatic GPR signal for Noninvasive Quantification of Soil Properties*, Water Resources Research, vol. 42, no. 3, p. W3403, 2006.

Lambot S., M. Antoine, I. van den Bosch, E. C. Slob, and M. Vanclooster, *Electromagnetic Inversion of GPR Signals and Subsequent Hydrodynamic Inversion to*

*Estimate Effective Vadose Zone Hydraulic Properties*, Vadose Zone Journal, vol. 3, pp. 1072-1081, 2004 (a).

Lambot S., E.C. Slob, I. van den Bosch, B. Stockbroeckx, B. Scheers, and M. Vanclooster, *Estimating Soil Electric Properties from Monostatic Ground Penetrating Radar signal Inversion in the Frequency Domain*, Water Resources Research, vol. 40, W04–W205, 2004 (b).

Lambot S., E.C. Slob, I. van den Bosch, B. Stockbroeckx, B. Scheers, and M. Vanclooster, *Modeling of Ground Penetrating Radar for Accurate Characterization of Subsurface Electric Properties*, IEEE Transactions on Geoscience and Remote Sensing, vol. 42, no. 11, pp. 2555-2568, 2004 (c).

Lambot S., E.C. Slob, I. van den Bosch, B. Stockbroeckx, B. Scheers, and M. Vanclooster, *GPR Design and Modeling for Identifying the Shallow Subsurface Dielectric Properties*, Second International Workshop on Advanced GPR, 14-16 May, Delft, pp. 130-135, 2003.

Lane J.W., F.D. Day-Lewis, R.J.Versteeg, and C. C. Casey, *Object-Based Inversion of Crosswell Radar Tomography Data to Monitor Vegetable Oil Injection Experiments*, Proceedings at the Symposium on the Application of Geophysics to Environmental and Engineering Problems SAGEEP, Texas. Available: [http://water.usgs.gov/ogw/bgas/publications/SAGEEP03\\_Lane/index.html](http://water.usgs.gov/ogw/bgas/publications/SAGEEP03_Lane/index.html), 2003, accessed on June 2007.

Lane J., F.D. Day-Lewis, J.M. Harris, F.P. Haeni, and S.M. Gorelick, *Attenuation-difference Radar Tomography Results of a Multiple Plane Experiment at the U.S. Geological Survey fractured Rock Research Site*, USGS Ground Water Information, Branch of Geophysics, Mirror Lake, New Hampshire, 1999a. Available online: <http://water.usgs.gov/ogw/bgas/publications/attenuation/>, accessed on February, 2008.

Lane Jr. J.W., F. D. Day-Lewis, and C. Casey, *Geophysical Monitoring of a Field-Scale Biostimulation Pilot Project*, Ground Water, vol. 44, no. 3, pp. 430-443, 2006.

Lane J.W., D. L. Wright, and E.P. Haeni, *Borehole Radar Tomography Using Saline Tracer Injections to Image Fluid Flow in Fractured Rock*, in Morganwalp, D.W. and Buxton, H.T., eds., U.S. Geological Toxic Substances Hydrology Program -- Proceedings of the Technical Meeting, Charleston, South Carolina, USGS Water-Resources Investigations Report 99-4018C, vol. 3, pp. 747-756, 1999 (b). Available: <http://water.usgs.gov/ogw/bgas/imaging/>, accessed on March, 2007.

Lee Jong-Sub, *High Resolution Geophysical Techniques for Small-Scale Soil Model Testing*, PhD Dissertation, Georgia Institute of Technology, December, 2003.

Lehmann P., P. Wyss, A. Flisch, E. Lehmann, P. Vontobel, M. Krafczyk, A. Kaestner, F. Beckmann, A. Gygi and H. Fluhler, *Tomographical Imaging and Mathematical*

*Description of Porous Media Used for the Prediction of Fluid Distribution*, Vadose Zone Journal, vol. 5, pp. 80-97, 2006.

Lenk F. and R. Doerner, *A New Multiport Measurement-Method Using a Two-Port Network Analyzer*, in Microwave Symposium Digest IEEE, pp. 1663-1666, 2005.

Lin Ch., *Frequency Domain vs Travel Time Analysis of TDR Waveforms for Soil Moisture Measurements*, Soil Science Society of America Journal, vol. 67, pp.720-729, 2003.

Liu Z., R. G. Arnold, E.A. Betterson, and E. Smotkin, *Reductive Dehalogenation of Gas-Phase Chlorinated Solvents Using a Modified Fuel Cell*, vol. 35, no. 21, pp. 4320-4326, 2001.

Liu S. and T. Yeh, *An Integrative Approach for Monitoring Water Movement in the Vadose Zone*, Vadose Zone Journal, vol. 3, pp. 681-692, 2004.

Logsdon S. D., *Soil Dielectric Spectra from Vector Network Analyzer Data*, Soil Science Society of America Journal, vol. 69, pp. 983-989, 2005.

Mackay D., W.Y. Shiu, and K.C. Ma, *Illustrated Handbook of Physical-chemical Properties and Environmental Fate of Organic Chemicals*, Volatile Organic Chemicals, vol. 3, Lewis Publisher, Boca Raton, Florida, 1993.

Masbruch K. and T.P.A. Ferré, *A Time Domain Transmission Method for Determining the Dependence of the Dielectric Permittivity on Volumetric Water Content: An Application to Municipal Landfills*, Vadose Zone Journal, vol. 2, pp. 186-192, 2003.

Matzler Christian, *Microwave Permittivity of Dry Sand*, IEEE Transactions on Geoscience and Remote Sensing, vol. 36, no. 1, pp. 317-319, 1998.

McMechan G.A., J. M. Harris, and L. M. Anderson, *Cross-hole Tomography for Strongly Variable Media with Applications to Scale Model Data*, Bulletin of Seismological Society of America, vol. 77, no. 6, pp. 1945-1960, 1987.

Meinardus, Hans W., Richard E. Jackson, Minquan Jin, John T. Londergan, *Characterization of a DNAPL Zone with Partitioning Interwell Tracer Tests, Non-Aqueous Phase Liquids—Remediation of Chlorinated and Recalcitrant Compounds*, 1998.

Merck Research Laboratories Division of Merck and CO., Inc., *Merck Index*, Thirteenth Edition, 2001.

Middleton N.T and M.T. Harman, *A Preprocessor for Geotomographic Imaging of Irregular Geometric Scans*, IEEE Transactions on Industry Applications, vol. 28, no. 5, pp. 1148-1153, 1992.

Miller T.W., J.M. Hendrickx, and B. Borchers, *Radar Detection of Buried Landmines in Field Soils*, Vadose Zone Journal, vol. 3, pp. 1116-1127, 2004.

Mironov V.L., *Spectral Dielectric Properties of Moist Soils in the Microwave Band*, in Geoscience and Remote Sensing Symposium IEEE, pp. 3474-3477, 2004.

Moran, M. L., and Greenfield, R. J., *Radar Signature of a 2.5-D Tunnel*, Geophysics, vol. 58, pp. 1573–1587, 1993.

Moran M., J. S. Zagorski, and P.J. Squillage, *Chlorinated Solvents in Groundwater of the United States*, Environmental Science and Technology, vol. 41, no. 1, pp. 74-81, 2007.

Mueller K. and R. Yagel, *On the Use of Graphics Hardware to Accelerate Algebraic Reconstruction Methods*, in Proceedings of SPIE Medical Imaging Conference 1999, Physics of Medical Imaging, number 3659-62, San Diego, 1999.

Nadler A., E. Raveh, U. Yermiyahu, and S. Green, *Stress Induced Water Content Variations in Mango Stem by Time Domain Reflectometry*, Soil Science Society of America Journal, vol. 70, pp. 510-520, 2006.

National Research Council, *Seeing into the Earth: Noninvasive characterization of the shallow subsurface for environmental and engineering applications*, National Academy Press, Washington D.C., 2000(a).

National Research Council, *Research needs in subsurface environments*, National Academy Press, Washington D.C., 2000(b).

Oostrom M., J. H. Dane, and T. W. Wietsma, *A Review of Multidimensional, Multifluid Intermediate-Scale Experiments: Nonaqueous Phase Liquid Dissolution and Enhanced Remediation*, *Vadose Zone Journal*, vol. 5; pp. 570-598, 2006.

Oostrom M., M.D. White, R. J. Lenhard, P.J. Van Geel, and T.W. Wietsma, *A Comparison of Models Describing Residual NAPL Formation in the Vadose Zone*, *Vadose Zone Journal*, vol. 4, pp. 163-174, 2005.

Oostrom M., T. W. Wietsma, and N. S. Foster, *The Subsurface Flow and Transport Experimental Laboratory: A New Department of Energy User's Facility for Intermediate-Scale Experimentation*, *Hydrology days*, pp. 182-189, 2004.

Pankow J.F. and J.A. Cherry, *Dense Chlorinated Solvents and Other DNAPLs in Groundwater*, Waterloo Press, pp. 522, 1996.

Pantazidou M. and N. Sitar, *Emplacement of Nonaqueous Liquids in the Vadose Zone*, Water Resources Research, vol, 29, no. 3, pp. 705-722, 1993.

Parker B.L., J. A. Cherry, S. W. Chapman, and M. A. Guilbeault, *Review and Analysis of Chlorinated Solvent Dense Nonaqueous Phase Liquid Distributions in Five Sandy Aquifers*, Vadose Zone Journal, vol. 2, pp. 116-137, 2003.

Pelton W.H., S.H. Ward, P.G. Hallof, W.R. Sill, and P. H. Nelson, *Mineral Discrimination and Removal of Inductive Coupling with Multifrequency IP*, Geophysics, vol. 43, no. 3, pp. 588-609, 1978.

Peplinski N.R., F. T. Ulaby, and M. C. Dobson, *Dielectric Properties of Soils in the 0.3-1.3GHz Range*, IEEE Transactions on Geoscience and Remote Sensing, vol. 33, no. 3, pp.803-807, 1995.

Persson M., *Accurate Dye Tracer Concentration Estimations Using Image Analysis*, Soil Science Society of America Journal, 69, pp. 967-975, 2005(a).

Persson M., *Estimating Surface Soil Moisture from Soil Color Using Image Analysis*, Vadose Zone Journal, vol. 4, pp. 1119-1122, 2005(b).

Persson M. and J.M.Wraith, *Shaft-mounted Time Domain Reflectometry Probe for Water Content and Electrical Conductivity Measurements*, Vadose Zone Journal, vol. 1, pp. 316-319, 2002.

Persson M., S. Haridy, J. Olsson, and J. Wendt, *Solute Transport Dynamics by High-Resolution Dye Tracer Experiments-Image Analysis and Time Moments.*, *Vadose Zone Journal*, vol. 4, pp. 856-865, 2005 (c ).

Persson M. and C.B.Uvo, *Estimating Soil Solution Electrical Conductivity from Time Domain Reflectometry Measurements using Neural Networks*, *Journal of Hydrology*, vol. 273, no. 1, pp. 249-256, 2003.

Peterson J.E., B.N.P. Paulsson, and T.V. McEvelly, *Applications of Algebraic Reconstruction Techniques to Crosshole Seismic Data*, *Geophysics*, vol. 50, no. 10, pp. 1566-1580, 1985.

Peterson J.K, and D. C. Nobes, *Environmental Geophysics at Scott Base: Ground Penetrating Radar and Electromagnetic Induction as Tools for Mapping Contaminated Ground at Antarctic Research Bases* ,*Cold Regions Science and Technology*, vol. 37, no. 2, pp. 187-195, 2003.

Ramirez A., Daily W., and LaBrecque D., *Complex Electrical Resistance Tomography of a Subsurface PCE Plume*, *Symposium on the Application of Geophysics to Engineering and Environmental Problems (SAGEEP)*, Keystone, CO, April 28-May 1, pp. 753-762, 1996.

Rappaport, C. M., Wu, S., Kilmer, M. E., Miller, E. L., *Distinguishing Shape Details of Buried Non-Metallic Minelike Objects with GPR*, Proceedings SPIE AeroSense Symposium, Detection Technologies for Mines and Minelike Targets IV, Abinash C. Dubey, James F. Harvey, J. Thomas Broach, and Regina E. Dugan editors, Vol. 3710, Orlando Fl., pp.1419—1428, 1999.

Regalado C.M., *A Physical Interpretation of Logarithmic TDR Calibration Equations of Volcanic Soils and Their Solid Fraction Permittivity based on Lichtenecker's Mixing Formulae*, Geoderma, vol. 123, no. 1, pp. 41-50, 2004.

Reynolds J., *An Introduction to Applied and Environmental Geophysics*, printed and bound in Great Britain by Antony Rowe LTd. Chippenham, Wiltshire, 1997.

Robinson D.A., C.M.K. Gardner, and J. D. Cooper, *Measurement of Relative Permittivity in Sandy Soils Using TDR, Capacitance and Theta Probes: Comparison Including the Effects of Bulk Soil Electrical Conductivity*, Journal of Hydrology, vol. 223, no. 3, pp.198-211,1999.

Robinson D.A., T.J.Kelleners, J. D. Cooper, C.M.K. Gardner, P.Wilson, I.Lebtron, and S. Logsdon, *Evaluation of a Capacitance Probe Frequency Response Model Accounting for Bulk Electrical Conductivity: Comparison with TDR and Network Analyzer Measurements*, Vadose Zone Journal, vol. 4, pp. 992-1003, 2005.

Rodriguez S., I. Padilla, and I. Santiago, Development of a Multiscale Packing Methodology for Evaluating Fate and Transport Processes of Explosive-related Chemicals in Soil Physical Models, Proceeding of SPIE, vol. 6217, 2006.

Rossabi J., B. D.Riha, C.A. Eddy-Dilek, B. Loooney, and W. Keith Hyde, *Recent Advances in Characterization of Vadose Zone Dense Non-Aqueous Phase Liquids*, Environmental and Engineering Geoscience, vol. 9, pp. 25-36, 2003.

Rucker D. and T.P.A. Ferré, *Near-surface Water Content Estimation with Borehole Ground Penetrating Radar Using Critically Refracted Waves*, Vadose Zone Journal, vol. 2, pp. 247-252, 2003.

Sadiku M., Elements of Electromagnetic, Third Edition, published by Oxford University Press, Inc., 2001.

Sarabandi K., and F. T. Ulaby, *Technique for Measuring the Dielectric Constant of Thin Materials*, IEEE Transactions on Instrumentation and Measurement, vol. 37, no. 4, pp. 631-636, 1988.

Schillig P., M. McGlashan, J.F. Devlin, G. Tsoflias, and J. Roberts, *Using Groundwater Point Velocity Probes and Ground Penetrating Radar to Investigate Microbially Mediated Changes in Flow Properties of a Contaminated Aquifer*, Eos. Trans. AGU, vol. 88, no. 23, Jt. Assem. Suppl., Abstract NS51A-02, 2007.

Schwarzenbach R. P., P.M. Gschwend, D.M. Imboden, *Environmental Organic Chemistry*, Wiley-Interscience, Second Edition, 2003.

Serrano-Guzman Maria F., Padilla I., and R. Rodriguez, *Two-Dimensional Detection of Underground Contamination and Buried Objects Using Cross-Well Radar*, Proceeding of SPIE Radar sensor technology. Conference Vol. 6210 , Orlando, pp. R1-R11, 2006.

Serrano-Guzmán , Maria F., Ingrid Padilla, and Rafael Rodriguez, *Bimodal detection of underground contamination in two dimensional systems*, Proceedings. of SPIE on Optics and Photonics in Global Homeland Security III, edited by Theodore T. Saito, Daniel Lehrfeld, Michael J. DeWeert, Vol. 6540 65401O-1-13, 2007.

Seyfried M.S. and M.D. Murdock, *Measurement of Soil Water Content with a 50-MHz Soil Dielectric Sensor*, Soil Science Society of America Journal, vol. 68, pp. 394-403, 2004.

Sharma P., *Environmental and Engineering Geophysics*, first edition published by the Press Syndicate of the University of Cambridge, 1997.

Smith G.S., *Radiation Efficiency of Electrically Small Multiturn Loop Antennas*, IEEE Transactions on Antennas and Propagation, vol. 20, no. 5, pp. 656-657, 1972.

Sneddon K.W., G. R. Olhoeft, and M. H. Powers, *Determining and Mapping DNAPL Saturation Values from Noninvasive GPR Measurements*, in Proceeding of SAGEEP Arlington, 21-25 February, 2000.

Sneddon K.W., M. H. Powers, R. H. Johnson, and E. P. Poeter, *Modeling GPR Data to Interpret Porosity and DNAPL Saturations for Calibration of a 3-D Multiphase Flow Simulation*, United States Geological Survey, Open File Report 2002-2451, Denver, 2002.

Srivastava S. K. and G. P. Mishra, *Study of the Characteristics of the Soil of Chhattisgarh at X-band frequency*, Sadhana, vol. 29, no. 4, India, pp. 343-347, 2004.

Stadler D., M. Stahli, P. Aeby, and H. Fluhler, *Dye Tracing and Image Analysis for Quantifying Water Infiltration into Frozen Soils*, Soil Science Society of America Journal, vol. 64, pp. 505-516, 2000.

Starr G.C., P. Barak, B. Lowery, and M. Avila-Segura, *Soil Particle Concentrations and Size Analysis Using a Dielectric Method*, Soil Science Society of America Journal, vol. 64, pp. 858-866. , 2000a.

Starr G.C., B. Lowery, and E.T. Cooley, *Soil Water Content Determination using a Network Analyzer and Coaxial Probe*, Soil Science Society of America Journal, vol. 64, pp. 867-878, 2000b.

Starr G.C., B. Lowery, E.T. Cooley, and G.L. Hart, *Soil Water Content Determination using Network Analyzer Reflectometry Methods*, Soil Science Society of America Journal, vol. 63, pp. 285-289, 1999.

Stewart M. and L. North, *A Borehole Geophysical Method for Detection and Quantification of Dense Non Aqueous Liquids (DNAPL) in Saturated Soils*, Journal of Applied Geophysics, vol. 60, no. 2, pp. 87-99, 2006.

Tikhonov V.V., *Model of Complex Dielectric Constant of Wet and Frozen Soil in the 1-40GHz Frequency Range*, in IEEE Geoscience and Remote Sensing Symposium: Surface and Atmospheric Remote Sensing Technologies, Data Analysis and Interpretation, pp. 1576-1578, 1994.

Tikhonov V.V., *Dielectric Model of Bound Water in Wet Soils for Microwave Remote Sensing*, in IEEE Geoscience and Remote Sensing: A Scientific Vision for Sustainable Development, pp. 1108-1110, 1997.

Titov K., A. Kemna, A. Tarasov, and H. Vereecken, *Induced Polarization of Unsaturated Sands Determined through Time Domain Measurements*, Vadose Zone Journal, vol. 3, pp. 1160-1168, 2004.

Todd D. K. and L. W. Mays, *Groundwater Hydrology*, Third Edition , John Wiley and Sons, Inc., 2005.

Trantham H.H. and D.S. Durnford, *DNAPL Source Zone Characterization using a Stochastic Aggregation Model, Proceedings of the 1998 Conference on Hazardous Waste Research: Bridging Gaps in Technology and Culture*, 18-21 May, Snowbird, UT, 1998.

Vall-Iossera M., M. Cardona, S. Blanch, A. Camps, A. Monerris, I. Corbella, F. Torres, and N. Duffo, *L-Band Dielectric Properties of Different Soil Types Collected during the MOUSE 2004 Field Experiment*, Geoscience and Remote Sensing Symposium, Proceedings, IEEE International, pp. 1109-1112, 2005.

Vanderborght J., P. Gahwiller, H. Wydler, U. Schultze, and H. Fluhler, *Imaging Fluorescent Dye Concentrations on Soil Surfaces: Uncertainty of Concentration Estimates*, Soil Science Society of America Journal, vol. 66, pp. 760-773, 2002.

Van Dam R. L, B. Borchers, and J. M. Hendrickx, Methods for prediction of soil dielectric properties: a review, Proceedings of the SPIE Detection and Remediation Technologies for Mines and Minelike Targets, Volume 5794, pp. 188-197 SPIE, 2005(a).

Van Dam R. L, B. Borchers, and J. M. Hendrickx, *Strength of Landmine Signatures Under Different Soil Conditions: Implications for Sensor Fusion*, International Journal of Systems Science, vol. 36, no. 9, pp. 573-588, 2005(b).

Vertiy A., S. Gavrilov, I. Voynosvskiy, S. Aksoy, and A.O. Salman, *Diffraction Tomography Method Development in Wide Frequency Range*, Proceedings VIII-th

International Conference on Mathematical Methods in Electromagnetic Theory, Ukraine, vol. 1, pp. 61-67, 2000.

Wadley L.S., R. W. Gillham, and L. Gui, *Remediation of DNAPL Source Zones with Granular Iron: Laboratory and Field Tests*, Ground Water, vol. 43, no. 1, pp. 9-18, 2005.

Wakayama C. and J. Loyer, *Correlation between VNA and TDR/TDT Extracted S-Parameters up to 20GHz*, Intel Corporation White Paper, 2007.

Watson K., D. Fitterman, R.W. Saltus, A. McCafferty, G. Swayze, S.Church, K. Smith, M. Goldhaber, S. Robson, and P. McMahon, *Application of Geophysical Techniques to Minerals-Related Environmental Problems*, United States Geological Survey, Open File Report 01-458. Available: <http://pubs.usgs.gov/of/2001/ofr-01-0458/ofr-01-0458.pdf> , 2001.

Whitely G.A., D.C. McKinney, G.A. Pope, B.A. Rouse, and N.E. Deeds, *Contaminated Vadose Characterization Using Partitioning Gas Tracers*, ASCE Journal of Environmental Engineering, vol. 125, no. 6, pp. 575-582, 1999.

Woodhead I. M., G.D. Buchan, J. H. Christie, and K. Irie, *A General Dielectric Model for Time Domain Reflectometry*, Biosystems Engineering, vol. 86, no. 2, pp. 207-216, 2003.

Wosik J., J.H.Miller, D.S. McKay, D.Warmflash, M.Kamel, L. Xue, S. Hirsh, and N. Withers, *High-Frequency Dielectric Spectroscopy for Martian Soil Samples*, ISSO Annual Report, University of Houston, pp. 114-118, 2004.

Wraith J. M., D. A. Robinson, S. B. Jones, and D.S. Long, *Spatially Characterizing Apparent Electrical Conductivity and Water Content of Surface Soils with Time Domain Reflectometry*, *Computers and Electronics in Agriculture*, vol. 46, pp. 239-261, 2005.

Yang J., *Three-Dimensional Complex Resistivity Analysis for Clay Characterization in Hydrogeologic Study*, PhD Dissertation, University of California, Berkeley, 2002.

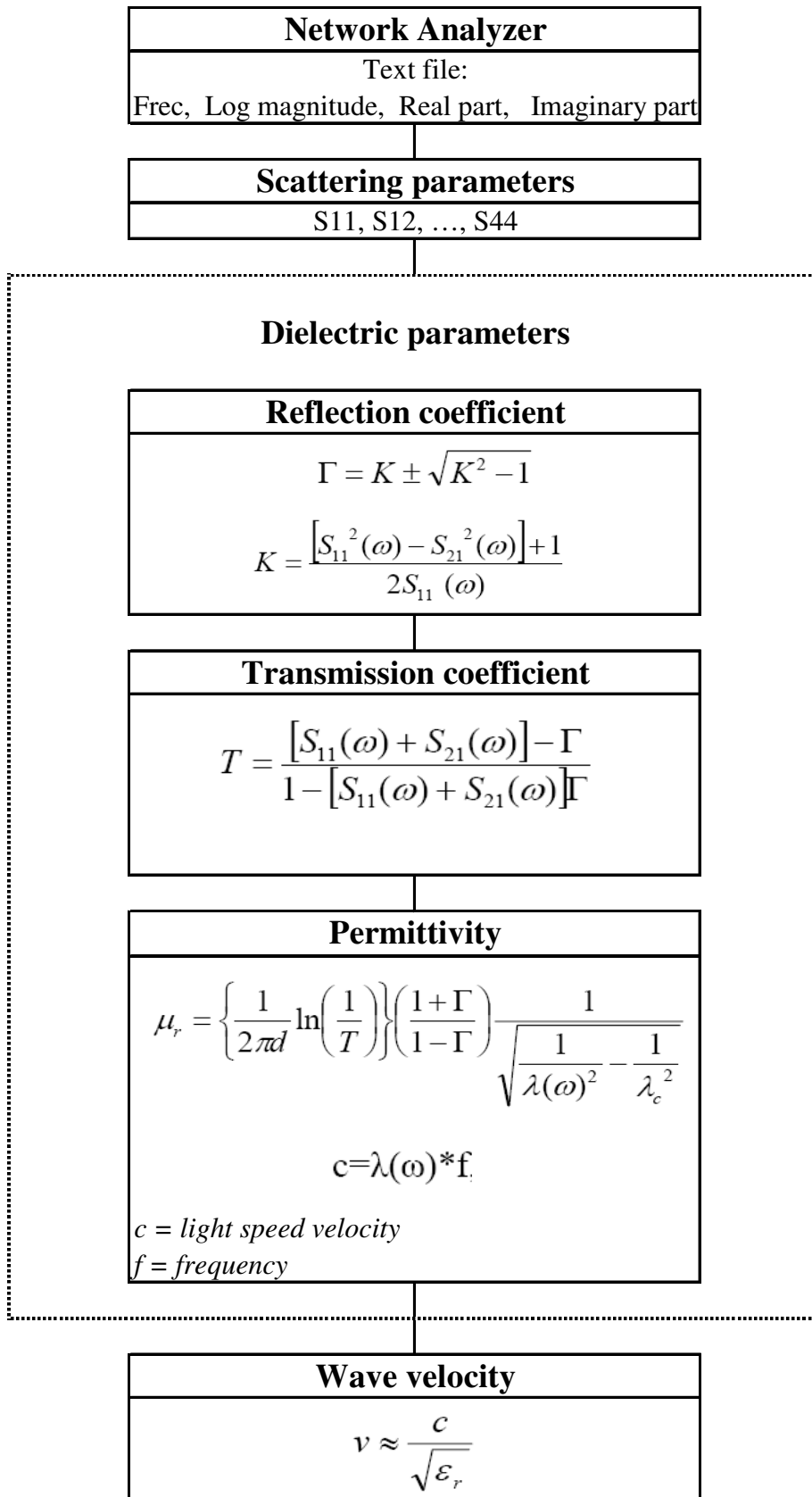
Zagoskin V.V., A.P. Batsula, V.N. Ijushenko, L.P. Ligthard, A.S. Shostak and B. I. Avdochenko, *Influence of the Dielectric Properties of Inhomogeneous Soil on the Dipole Antennas Normalized Impedance*, 15th International Conference on Microwaves, Radar and Wireless Communications, Mikon, vol. 3, pp. 948-952, 2004.

Zhang N., G.Fan, K.H.Lee, G.J. Kluitenberg, and T.M.Loughin, *Simultaneous Measurement of Soil Water Content and Salinity using a Frequency-Response Method*, *Soil Science Society of America Journal*, vol. 68, 1515-1525, 2004.

Zhu X. and G.A.McMechan, *2-D Tomographic Imaging of Velocities in the Wichita Uplift-Anadarko Basin Region of Southwestern Oklahoma*, *Bulletin of the Seismological Society of America*, vol. 79, no. 3, pp. 873-887, 1989.

Zwick T., A. Chandrasekhar, C. W. Baks, U. R. Pfeiffer, S. Brebels, B. P. Gaucher, *Determination of the Complex Permittivity of Packaging Materials at Millimeter-wave Frequencies*, IEEE Transactions on Microwave Theory and Techniques, vol. 54, no. 3, pp.1001-1010, 2006.

Appendix 1 Dielectric Properties Flow Chart and Code



Code

```

clear all; close all; clc

c=3e10;%cm/s

eps_0 = 8.85e-12;
mu_0 = 4*pi*1e-7;          % free space permeability (H/m)

f_max=2200e6; %Hz
f_min=0.3e6;
d=26;%cm
% fo=1e10
%fc=6.557e9;%Hz
fc=0.3e6;%Hz
lc=round(c/fc*1000)/1000;

%-----Loading File Name
[FileName,PathName] = uigetfile('*.xls','Select Data File');
if isequal(FileName,0),
    disp('User selected Cancel')
else
    disp(['User selected', fullfile(PathName, FileName)])

    File=strcat(PathName,FileName);
    % NameHT = Name of Transmission data sheet with object
    % NameHR = Name of Reflection data sheet with object
    NameHT='Sitoj';
    NameHR='Sjj';
    % NameHT = Name of Transmission data sheet with object
    % NameHR = Name of Reflection data sheet with object
    NameHTN=[NameHT 'N']
    NameHRN=[NameHR 'N']
    Rowend='202';
%-----Calculations for data without object
% TRANSMISSION DATA
[FT,RT,IT,CT]=LoadXLSData(File,NameHTN,Rowend)

%REFLECTION DATA
[FR,RR,IR,CR]=LoadXLSData(File,NameHRN,Rowend)
% er, Ur calculation
[erN,UrN]=EandUCalc(c,d,lc,FR,CT,CR)

%-----Calculations for data with object

```

```

% TRANSMISSION DATA
[FT,RT,IT,CT]=LoadXLSData(File,NameHT,Rowend)

% REFLECTION DATA
[FR,RR,IR,CR]=LoadXLSData(File,NameHR,Rowend)
% er, Ur calculation
[er,Ur]=EandUCalc(c,d,lc,FR,CT,CR)

end

% % % FIGURES
%
figure(1)
set(1,'name', 'Ur-Real')
plot(FT, abs(Ur(:,2)),FT, abs(UrN(:,2)))
xlabel('Frequency (GHz)')
ylabel('Real part of Permeability')
legend('Background', 'Buried Object')
title('Relative Permeability - Real Part')

figure(2)
set(2,'name', 'Ur-Imag')
plot(FT, abs(Ur(:,3)),FT, abs(UrN(:,3)))
xlabel('Frequency (GHz)')
ylabel('Imaginary part of Permeability')
legend('Background', 'Buried Object')
title('Relative Permeability - Imaginary Part')

figure(3)
set(3,'name', 'er-Real')
plot(FT, abs(er(:,2)),FT, abs(erN(:,2)))
xlabel('Frequency (GHz)')
ylabel('Real part of Permittivity')
legend('Background', 'Buried Object')
title('Relative Permittivity - Real Part')

figure(4)
set(4,'name', 'er-Imag')
plot(FT, abs(er(:,3)),FT, abs(erN(:,3)))
xlabel('Frequency (GHz)')
ylabel('Imaginary part of Permittivity')
legend('Background', 'Buried Object')
title('Relative Permittivity - Imaginary Part')

```

Appendix 2 Tomography Flow Chart and Tomography Code

### Input Data

- Transmitter and receivers coordinates
- Wave velocity data
- Number of mesh points
  - ◆ Horizontal direction
  - ◆ Vertical direction
- Wave velocity range (optional)
- Relaxation parameter ( $\lambda$ )
- Number of iterations

### Distance matrix

$$d_j = \sqrt{(\Delta x_j^2 + \Delta y_j^2)}$$

$d_i$  = travel distance on cell  $i$

$\Delta x_i$  = x coordinate difference on cell  $i$

$\Delta y_i$  = y coordinate difference on cell  $i$

### Travel time

$$T_k = \frac{\vec{D}_k}{\vec{V}_k}$$

$$T_k = \vec{D}_k \vec{S}_k$$

$\vec{D}_k$  = the distance vector for the ray path  $k$

$\vec{S}_k$  = the slowness vector =  $1/v$ .

$T_k$  = travel time for the object on path  $k$

### Slowness matrix (SART)

$$\vec{S}^j = \vec{S}^{(j-1)} + \frac{\vec{S}^{(j-1)} \cdot \vec{D}_k - T_k}{\vec{D}_k \cdot \vec{D}_k^T} \vec{D}_k$$

## Code

```

%%%%%%%%MENU
function varargout = Menu(varargin)
% MENU M-file for Menu.fig
%   MENU, by itself, creates a new MENU or raises the existing
%   singleton*.
%
%   H = MENU returns the handle to a new MENU or the handle to
%   the existing singleton*.
%
%   MENU('CALLBACK',hObject,eventData,handles,...) calls the local
%   function named CALLBACK in MENU.M with the given input arguments.
%
%   MENU('Property','Value',...) creates a new MENU or raises the
%   existing singleton*. Starting from the left, property value pairs are
%   applied to the GUI before Menu_OpeningFunction gets called. An
%   unrecognized property name or invalid value makes property application
%   stop. All inputs are passed to Menu_OpeningFcn via varargin.
%
%   *See GUI Options on GUIDE's Tools menu. Choose "GUI allows only one
%   instance to run (singleton)".
%
% See also: GUIDE, GUIDATA, GUIHANDLES

% Copyright 2002-2003 The MathWorks, Inc.

% Edit the above text to modify the response to help Menu

% Last Modified by GUIDE v2.5 17-Jun-2007 00:17:32

% Begin initialization code - DO NOT EDIT

gui_Singleton = 1;
gui_State = struct('gui_Name',    mfilename, ...
                  'gui_Singleton', gui_Singleton, ...
                  'gui_OpeningFcn', @Menu_OpeningFcn, ...
                  'gui_OutputFcn', @Menu_OutputFcn, ...
                  'gui_LayoutFcn', [] , ...
                  'gui_Callback', []);
if nargin && ischar(varargin{1})
    gui_State.gui_Callback = str2func(varargin{1});
end

```

```

if nargout
    [varargout{1:nargout}] = gui_mainfcn(gui_State, varargin{:});
else
    gui_mainfcn(gui_State, varargin{:});
end
% End initialization code - DO NOT EDIT

% --- Executes just before Menu is made visible.
function Menu_OpeningFcn(hObject, eventdata, handles, varargin)
% This function has no output args, see OutputFcn.
% hObject    handle to figure
% eventdata  reserved - to be defined in a future version of MATLAB
% handles    structure with handles and user data (see GUIDATA)
% varargin   command line arguments to Menu (see VARARGIN)

% Choose default command line output for Menu
handles.output = hObject;

% Update handles structure
guidata(hObject, handles);

% UIWAIT makes Menu wait for user response (see UIRESUME)
% uiwait(handles.figure1);

% --- Outputs from this function are returned to the command line.
function varargout = Menu_OutputFcn(hObject, eventdata, handles)
% varargout  cell array for returning output args (see VARARGOUT);
% hObject    handle to figure
% eventdata  reserved - to be defined in a future version of MATLAB
% handles    structure with handles and user data (see GUIDATA)

% Get default command line output from handles structure
varargout{1} = handles.output;

function S_Callback(hObject, eventdata, handles)
% hObject    handle to S (see GCBO)
% eventdata  reserved - to be defined in a future version of MATLAB
% handles    structure with handles and user data (see GUIDATA)

% Hints: get(hObject,'String') returns contents of S as text
%        str2double(get(hObject,'String')) returns contents of S as a double
%Smooth=get(hObject,'Value')
% hndlS=findobj(allchild(0),'Tag','Smin','-or','Tag','Smax')

```

```

% % hndl_editSmax=findobj(allchild(0),'Tag','Smax')
% %
% % hndls = [hndl_editSmin,hndl_editSmax];
% if Smooth==1
%   set(hndlS,'Enable','on','Visible','on');
% else
%   set(hndlS,'Enable','off','Visible','on');
% end

% % --- Executes on button press in S.
% function radiobutton1_Callback(hObject, eventdata, handles)
% % hObject   handle to S (see GCBO)
% % eventdata reserved - to be defined in a future version of MATLAB
% % handles   structure with handles and user data (see GUIDATA)
%
% % Hint: get(hObject,'Value') returns toggle state of S

function Smin_Callback(hObject, eventdata, handles)
% hObject   handle to Smin (see GCBO)
% eventdata reserved - to be defined in a future version of MATLAB
% handles   structure with handles and user data (see GUIDATA)

% Hints: get(hObject,'String') returns contents of Smin as text
%   str2double(get(hObject,'String')) returns contents of Smin as a double
% Smin=str2double(get(hObject,'String'))

% --- Executes during object creation, after setting all properties.
function Smin_CreateFcn(hObject, eventdata, handles)
% hObject   handle to Smin (see GCBO)
% eventdata reserved - to be defined in a future version of MATLAB
% handles   empty - handles not created until after all CreateFcns called

% Hint: edit controls usually have a white background on Windows.
%   See ISPC and COMPUTER.
if ispc
    set(hObject,'BackgroundColor','white');
else
    set(hObject,'BackgroundColor',get(0,'defaultUicontrolBackgroundColor'));
end

function Smax_Callback(hObject, eventdata, handles)
% hObject   handle to Smax (see GCBO)
% eventdata reserved - to be defined in a future version of MATLAB
% handles   structure with handles and user data (see GUIDATA)

% Hints: get(hObject,'String') returns contents of Smax as text

```

```
% str2double(get(hObject,'String')) returns contents of Smax as a double
%Smax=str2double(get(hObject,'String'))
```

```
% --- Executes during object creation, after setting all properties.
function Smax_CreateFcn(hObject, eventdata, handles)
% hObject handle to Smax (see GCBO)
% eventdata reserved - to be defined in a future version of MATLAB
% handles empty - handles not created until after all CreateFcns called
```

```
% Hint: edit controls usually have a white background on Windows.
% See ISPC and COMPUTER.
if ispc
    set(hObject,'BackgroundColor','white');
else
    set(hObject,'BackgroundColor',get(0,'defaultUicontrolBackgroundColor'));
end
```

```
function edit3_Callback(hObject, eventdata, handles)
% hObject handle to edit3 (see GCBO)
% eventdata reserved - to be defined in a future version of MATLAB
% handles structure with handles and user data (see GUIDATA)
```

```
% Hints: get(hObject,'String') returns contents of edit3 as text
% str2double(get(hObject,'String')) returns contents of edit3 as a double
Nx=str2double(get(hObject,'String'))
```

```
% --- Executes during object creation, after setting all properties.
function edit3_CreateFcn(hObject, eventdata, handles)
% hObject handle to edit3 (see GCBO)
% eventdata reserved - to be defined in a future version of MATLAB
% handles empty - handles not created until after all CreateFcns called
```

```
% Hint: edit controls usually have a white background on Windows.
% See ISPC and COMPUTER.
if ispc
    set(hObject,'BackgroundColor','white');
else
    set(hObject,'BackgroundColor',get(0,'defaultUicontrolBackgroundColor'));
end
```

```
function Nx_Callback(hObject, eventdata, handles)
% hObject handle to Nx (see GCBO)
% eventdata reserved - to be defined in a future version of MATLAB
% handles structure with handles and user data (see GUIDATA)
```

```

% Hints: get(hObject,'String') returns contents of Nx as text
%      str2double(get(hObject,'String')) returns contents of Nx as a double
%Nx=str2double(get(hObject,'String'))

function Ny_Callback(hObject, eventdata, handles)
% hObject  handle to Ny (see GCBO)
% eventdata reserved - to be defined in a future version of MATLAB
% handles  structure with handles and user data (see GUIDATA)

% Hints: get(hObject,'String') returns contents of Ny as text
%      str2double(get(hObject,'String')) returns contents of Ny as a double
%Ny=str2double(get(hObject,'String'))

% --- Executes during object creation, after setting all properties.
function Ny_CreateFcn(hObject, eventdata, handles)
% hObject  handle to Ny (see GCBO)
% eventdata reserved - to be defined in a future version of MATLAB
% handles  empty - handles not created until after all CreateFcns called

% Hint: edit controls usually have a white background on Windows.
%      See ISPC and COMPUTER.
if ispc
    set(hObject,'BackgroundColor','white');
else
    set(hObject,'BackgroundColor',get(0,'defaultUicontrolBackgroundColor'));
end

function edit5_Callback(hObject, eventdata, handles)
% hObject  handle to edit5 (see GCBO)
% eventdata reserved - to be defined in a future version of MATLAB
% handles  structure with handles and user data (see GUIDATA)

% Hints: get(hObject,'String') returns contents of edit5 as text
%      str2double(get(hObject,'String')) returns contents of edit5 as a double
Alfa=str2double(get(hObject,'String'))

% --- Executes during object creation, after setting all properties.
function edit5_CreateFcn(hObject, eventdata, handles)
% hObject  handle to edit5 (see GCBO)
% eventdata reserved - to be defined in a future version of MATLAB
% handles  empty - handles not created until after all CreateFcns called

% Hint: edit controls usually have a white background on Windows.
%      See ISPC and COMPUTER.
if ispc
    set(hObject,'BackgroundColor','white');

```

```

else
    set(hObject,'BackgroundColor',get(0,'defaultUicontrolBackgroundColor'));
end

% --- Executes on selection change in Method.
function Method_Callback(hObject, eventdata, handles)
% hObject    handle to Method (see GCBO)
% eventdata  reserved - to be defined in a future version of MATLAB
% handles    structure with handles and user data (see GUIDATA)

% Hints: contents = get(hObject,'String') returns Method contents as cell array
%        contents{get(hObject,'Value')} returns selected item from Method
%Method=get(hObject,'Value')

% --- Executes during object creation, after setting all properties.
function Method_CreateFcn(hObject, eventdata, handles)
% hObject    handle to Method (see GCBO)
% eventdata  reserved - to be defined in a future version of MATLAB
% handles    empty - handles not created until after all CreateFcns called

% Hint: popupmenu controls usually have a white background on Windows.
%       See ISPC and COMPUTER.
if ispc
    set(hObject,'BackgroundColor','white');
else
    set(hObject,'BackgroundColor',get(0,'defaultUicontrolBackgroundColor'));
end

% --- Executes on button press in Run.
function Run_Callback(hObject, eventdata, handles)
% hObject    handle to Run (see GCBO)
% eventdata  reserved - to be defined in a future version of MATLAB
% handles    structure with handles and user data (see GUIDATA)
clc
hdl_radiobutton=findobj(allchild(0),'Style','radiobutton');
hdl_buttons=findobj(allchild(0),'Style','push');
hdl_popups=findobj(allchild(0),'Style','popup');
hdl_edits=findobj(allchild(0),'Style','edit');
hndls = [hdl_radiobutton;hdl_buttons;hdl_popups;hdl_edits];
hdl_quit=findobj(allchild(0),'Tag','Exit');
set(hndls,'Enable','off','Visible','on');
set(hndl_quit,'Enable','on');

Varnum=findobj(allchild(0),'Style','edit');

```

```

for i =1:6
    Vars(i)=str2num(get(Varnum(i),'String'));
end

Varnum=findobj(allchild(0),'Style','radiobutton','-or','Tag','Method');
for i =1:3
    Vars(i+6)=get(Varnum(i),'Value');
end
Tomography(Vars);
set(hndls,'Enable','on');

% --- Executes on button press in Exit.
function Exit_Callback(hObject, eventdata, handles)
% hObject    handle to Exit (see GCBO)
% eventdata  reserved - to be defined in a future version of MATLAB
% handles    structure with handles and user data (see GUIDATA)

hndl_radiobutton=findobj(allchild(0),'Style','radiobutton');
hndl_buttons=findobj(allchild(0),'Style','push');
hndl_popups=findobj(allchild(0),'Style','popup');
hndl_edits=findobj(allchild(0),'Style','edit');

hndls = [hndl_radiobutton;hndl_buttons;hndl_popups;hndl_edits];

set(hndls,'Enable','on');
CloseAll
button = questdlg('Ready to quit?', ...
    'Exit Dialog','Yes','No','No');
switch button
case 'Yes',
    disp('Exiting MATLAB');
    %Save variables to matlab.mat
    %save
    set(0,'ShowHiddenHandles','on');
    delete(get(0,'Children'));
case 'No',
    quit cancel;
end

function edit7_Callback(hObject, eventdata, handles)
% hObject    handle to edit7 (see GCBO)
% eventdata  reserved - to be defined in a future version of MATLAB
% handles    structure with handles and user data (see GUIDATA)

```

```

% Hints: get(hObject,'String') returns contents of edit7 as text
%       str2double(get(hObject,'String')) returns contents of edit7 as a double

% --- Executes during object creation, after setting all properties.
function edit7_CreateFcn(hObject, eventdata, handles)
% hObject    handle to edit7 (see GCBO)
% eventdata  reserved - to be defined in a future version of MATLAB
% handles    empty - handles not created until after all CreateFcns called

% Hint: edit controls usually have a white background on Windows.
%       See ISPC and COMPUTER.
if ispc
    set(hObject,'BackgroundColor','white');
else
    set(hObject,'BackgroundColor',get(0,'defaultUicontrolBackgroundColor'));
end

function text1_DeleteFcn(hObject, eventdata, handles)
% --- Executes during object deletion, before destroying properties.
function text3_DeleteFcn(hObject, eventdata, handles)
% hObject    handle to text3 (see GCBO)
% eventdata  reserved - to be defined in a future version of MATLAB
% handles    structure with handles and user data (see GUIDATA)

function text4_DeleteFcn(hObject, eventdata, handles)

%%%%%%%%%MESH
function PlotMeshProbes(Xt, Yt, Xr, Yr, MeshPix, MeshC)
%-----Plot Mesh and probes
figure(3)
set(3,'name','Ray Path Length')
hold all
plot(Xt, Yt, 'bo', 'LineWidth', .02, ...
     'MarkerEdgeColor', 'k', ...
     'MarkerFaceColor', 'r', ...
     'MarkerSize', 8)
plot(Xr, Yr, 'bo', 'LineWidth', .02, ...
     'MarkerEdgeColor', 'k', ...
     'MarkerFaceColor', 'r', ...
     'MarkerSize', 8)
plot(MeshPix(:,1), MeshPix(:,2), 'ro', 'LineWidth', .02, ...
     'MarkerEdgeColor', 'r', ...
     'MarkerFaceColor', 'r', ...

```

```

    'MarkerSize',2)
plot(MeshC(:,1),MeshC(:,2),'r+','LineWidth',.02,...
    'MarkerEdgeColor','g',...
    'MarkerFaceColor','r',...
    'MarkerSize',80)
xlabel('Horizontal Distance, X')
ylabel('Depth, Y')
title('Ray path length')

%-----Eng plot Mesh and probes

%%%%%%%%%TARGET
function PlotTarget(Xcoor,Ycoor,Target,Xt,Yt,Xr,Yr,MeshPix,MeshC)
hold off
figure(4)
set(4,'name','Target Location')
hold
surf(Xcoor,Ycoor,Target)

plot(Xt,Yt,'ro','LineWidth',.02,...
    'MarkerEdgeColor','k',...
    'MarkerFaceColor','r',...
    'MarkerSize',8)
plot(Xr,Yr,'ro','LineWidth',.02,...
    'MarkerEdgeColor','k',...
    'MarkerFaceColor','r',...
    'MarkerSize',8)
plot(MeshPix(:,1),MeshPix(:,2),'ro','LineWidth',.02,...
    'MarkerEdgeColor','r',...
    'MarkerFaceColor','g',...
    'MarkerSize',2)
% plot(MeshC(:,1),MeshC(:,2),'r+','LineWidth',.02,...
%     'MarkerEdgeColor','b',...
%     'MarkerFaceColor','r',...
%     'MarkerSize',25)
xlabel('Horizontal Distance, X')
ylabel('Depth, Y')
title('Target Location')

% file=strcat(tmp_folder,'Braw.mat');
% save(file,'Utotal','Uinc');
% save('Target','Target');

%%%%%%%%%TOMOGRAPHY
function varargout = Tomograph(varargin)
% TOMOGRAPH M-file for Tomograph.fig

```

```

% TOMOGRAPH, by itself, creates a new TOMOGRAPH or raises the existing
% singleton*.
%
% H = TOMOGRAPH returns the handle to a new TOMOGRAPH or the handle to
% the existing singleton*.
%
% TOMOGRAPH('CALLBACK',hObject,eventData,handles,...) calls the local
% function named CALLBACK in TOMOGRAPH.M with the given input arguments.
%
% TOMOGRAPH('Property','Value',...) creates a new TOMOGRAPH or raises the
% existing singleton*. Starting from the left, property value pairs are
% applied to the GUI before Tomograph_OpeningFunction gets called. An
% unrecognized property name or invalid value makes property application
% stop. All inputs are passed to Tomograph_OpeningFcn via varargin.
%
% *See GUI Options on GUIDE's Tools menu. Choose "GUI allows only one
% instance to run (singleton)".
%
% See also: GUIDE, GUIDATA, GUIHANDLES

% Copyright 2002-2003 The MathWorks, Inc.

% Edit the above text to modify the response to help Tomograph

% Last Modified by GUIDE v2.5 07-Jun-2007 22:46:23

% Begin initialization code - DO NOT EDIT
gui_Singleton = 1;
gui_State = struct('gui_Name',    mfilename, ...
                  'gui_Singleton', gui_Singleton, ...
                  'gui_OpeningFcn', @Tomograph_OpeningFcn, ...
                  'gui_OutputFcn', @Tomograph_OutputFcn, ...
                  'gui_LayoutFcn', [] , ...
                  'gui_Callback', []);
if nargin && ischar(varargin{1})
    gui_State.gui_Callback = str2func(varargin{1});
end

if nargout
    [varargout{1:nargout}] = gui_mainfcn(gui_State, varargin{:});
else
    gui_mainfcn(gui_State, varargin{:});
end
% End initialization code - DO NOT EDIT

```

```

% --- Executes just before Tomograph is made visible.
function Tomograph_OpeningFcn(hObject, eventdata, handles, varargin)
% This function has no output args, see OutputFcn.
% hObject    handle to figure
% eventdata  reserved - to be defined in a future version of MATLAB
% handles    structure with handles and user data (see GUIDATA)
% varargin   command line arguments to Tomograph (see VARARGIN)

% Choose default command line output for Tomograph
handles.output = hObject;

% Update handles structure
guidata(hObject, handles);

% UIWAIT makes Tomograph wait for user response (see UIRESUME)
% uiwait(handles.figure1);

% --- Outputs from this function are returned to the command line.
function varargout = Tomograph_OutputFcn(hObject, eventdata, handles)
% varargout  cell array for returning output args (see VARARGOUT);
% hObject    handle to figure
% eventdata  reserved - to be defined in a future version of MATLAB
% handles    structure with handles and user data (see GUIDATA)

% Get default command line output from handles structure
varargout{ 1 } = handles.output;

% -----
function Load_Callback(hObject, eventdata, handles)
% hObject    handle to Load (see GCBO)
% eventdata  reserved - to be defined in a future version of MATLAB
% handles    structure with handles and user data (see GUIDATA)

% -----
function LoadR_Callback(hObject, eventdata, handles)
% hObject    handle to LoadR (see GCBO)
% eventdata  reserved - to be defined in a future version of MATLAB
% handles    structure with handles and user data (see GUIDATA)

% -----
function Save_Callback(hObject, eventdata, handles)
% hObject    handle to Save (see GCBO)

```

```
% eventdata reserved - to be defined in a future version of MATLAB
% handles structure with handles and user data (see GUIDATA)
```

```
% -----
function Preferences_Callback(hObject, eventdata, handles)
% hObject handle to Preferences (see GCBO)
% eventdata reserved - to be defined in a future version of MATLAB
% handles structure with handles and user data (see GUIDATA)
```

```
% -----
function File_Callback(hObject, eventdata, handles)
% hObject handle to File (see GCBO)
% eventdata reserved - to be defined in a future version of MATLAB
% handles structure with handles and user data (see GUIDATA)
```

```
% -----
function ART_Callback(hObject, eventdata, handles)
% hObject handle to ART (see GCBO)
% eventdata reserved - to be defined in a future version of MATLAB
% handles structure with handles and user data (see GUIDATA)
```

```
% -----
function SIRT_Callback(hObject, eventdata, handles)
% hObject handle to SIRT (see GCBO)
% eventdata reserved - to be defined in a future version of MATLAB
% handles structure with handles and user data (see GUIDATA)
```

```
% -----
function Tomography_Callback(hObject, eventdata, handles)
% hObject handle to Tomography (see GCBO)
% eventdata reserved - to be defined in a future version of MATLAB
% handles structure with handles and user data (see GUIDATA)
```

```
% -----
function Probes_Callback(hObject, eventdata, handles)
% hObject handle to Probes (see GCBO)
% eventdata reserved - to be defined in a future version of MATLAB
% handles structure with handles and user data (see GUIDATA)
```

```

% -----
function RaySec_Callback(hObject, eventdata, handles)
% hObject handle to RaySec (see GCBO)
% eventdata reserved - to be defined in a future version of MATLAB
% handles structure with handles and user data (see GUIDATA)

% -----
function Target_Callback(hObject, eventdata, handles)
% hObject handle to Target (see GCBO)
% eventdata reserved - to be defined in a future version of MATLAB
% handles structure with handles and user data (see GUIDATA)

% -----
function Run_Callback(hObject, eventdata, handles)
% hObject handle to Run (see GCBO)
% eventdata reserved - to be defined in a future version of MATLAB
% handles structure with handles and user data (see GUIDATA)

% -----
function View_Callback(hObject, eventdata, handles)
% hObject handle to View (see GCBO)
% eventdata reserved - to be defined in a future version of MATLAB
% handles structure with handles and user data (see GUIDATA)
% % % % % SART

function [S,RecE]=SART(D,TT,S,Nx,Ny,Iter,Alfa,Smin,Smax,Smooth,Method);
% -----Forward Projection Process
% Inverts matrix S using reconstruction algorithm SART
% SART: Simultaneous Algebraic Reconstruction Technique
%  $S \cdot D = T$ 
% D = Weighting factor KxM Matrix
% - (K = Number of ray paths, M = Number of cells)
% S = Slowness, Kx1 vector
% T = Ray-sum measured (K,1) vector

[K,M]=size(D);
SCorr=0;
for i=1:Iter,
    %For each ray path, j
    for j=1:K,
        Corr=(D(j,:).*(TT(j)-(D(j,:)*S')))/sum(D(j,:));
        %Corr=(D(j,:).*(TT(j)-(sign(D(j,:)*S'))))/sum(abs(D(j,:)));
        SCorr=SCorr+Corr;
    end
end

```

```
end;  
S = S+Alfa*SCorr/K;  
S = S.*(1+sign(S))/2.*abs(sign(S));  
if Method==4  
    [S]=SmoothP(S,M,Nx,Ny,Smooth);  
end  
Tc = S*D';  
DT=(TT-Tc);  
e2(i)=DT*DT'/K;  
Var(i)=var(TT);  
RecE(i)=e2(i)/Var(i);  
end;  
if Method==3  
    [S]=SmoothP(S,M,Nx,Ny,Smooth);  
end
```

Appendix 3 Image Acquisition Code

```
%This program calculates timelapse photography to take digital pictures
%The initial version was developed by Matilda Urie and was improved
%by Msc Carlos Rivera
```

```
clear all
disp('This program is designed to run a session of time-lapse photography.')
disp('The acquisition is divided into two phases.')
disp('The first phase will commence at a certain rate that will slow exponentially.')
disp('The second phase is assigned a constant rate of picture acquisition.')
disp('If at any point during this program you wish to abort, press Ctrl c.')
disp('-')
totalDuration = input('Enter the total number of *days* desired to run time-lapse
photography\n however, if you wish to select a time span less than one day enter 0. ');
if totalDuration<1
    totalDuration= input('You have selected a time span less than one day, please enter the
total number of hours. ');
    totalDuration = (totalDuration/24)
end
phase1 = input('Enter the amount of time desired, in hours, for the first phase of image
acquisition ');
phase1Frames = input('Enter the number of frames desired to acquire during phase one
');
frameRatePhase2 = input('Enter the number of frames per hour desired to acquire during
phase two ');
disp('-')
disp('The total number of frames refers to the sum of the number of frames acquired in
phase one')
disp('plus the number of frames acquired in phase two.')
disp('-')
totalNumFrames = (phase1Frames + (((totalDuration*24) - phase1)*frameRatePhase2))
format short
exponent = log((phase1*60))/(phase1Frames);
fprintf('The exponent (n) is %.4f\n',exponent)
disp('This number refers to the rate of image acquisition in phase one.')
disp('The rate of acquisition in phase one is a function of the frames desired and the
time.')
disp('f(x)->minutes transpired    x->number of frame    f(x)= e^(n*x)')
disp('For example if phase one is 60 min and we want to take 20 pictures -> 60 =
e^(n*20)')
disp('the exponent (n) = ln(60)/20 = .205')
format bank
frames1 = [1:1:phase1Frames];
minutes1 = [exp(frames1.*exponent)];
frames2 = [phase1Frames+1:1:totalNumFrames];
```

```

minutes2 =
[ ((phase1*60)+(frameRatePhase2*60)): (frameRatePhase2*60): (totalDuration*24*60)];
tableFM(:,1)=[frames1';frames2'];
tableFM(:,2)=[minutes1';minutes2'];
disp('  Frame Number  Time Transpired(min)')
disp(tableFM)
xlswrite('Frames over Time',tableFM);
figure
plot(frames1,minutes1,'k*','LineWidth',.8)
xlabel('Specific Frame to Acquire')
ylabel('Time Elapsed')
title('\bf\fontsize{13}Detailed View of Frames Captured During Phase One')
text(1,(max(minutes1)-5),'The time elapsed between frames in phase one is
increasing.','EdgeColor','r','LineWidth',2)
figure
hold on
plot(frames1,minutes1,'color','b','lineWidth',3)
plot(frames2,minutes2,'color','c','lineWidth',3)
xlabel('Specific Frame to Acquire')
ylabel('Time Elapsed')
title('\bf\fontsize{14}Total Frames Captured During Time-Lapse Test')
legend('Phase One','Phase Two',2)
hold off

vid=videoinput('matrox',1,'M_RS170');
triggerconfig(vid, 'Manual');
set(vid, 'FramesPerTrigger',1);
%set(vid,'FrameGrabInterval',30)
%set(vid,'LoggingMode','disk&memory');%Avia file necessary
set(vid,'LoggingMode','memory')
triggerconfig(vid,'Manual')
%set(vid,'LoggingMode','disk') %Avi file necessary
%logfile = avifile('my_datalog.avi','Colormap',gray(256));% gray scale

%set(vid,'TriggerFrameDelay',5);
set(vid,'TriggerRepeat',max(totalNumFrames))
start(vid);
for 1:1:max(totalNumFrames))
trigger(vid)
end
Running= isrunning(vid)
logging= islogging(vid)

wait(vid,max(totalNumFrames))
numOfFrames =get(vid,'FramesAcquired')
frmsAvail = get(vid,'FramesAvailable')

```

```
%flushdata(vid,'triggers');% deletes the frames associated with the oldest trigger  
%flushdata(vid); %deletes all frames  
%delete(vid)  
%clear vid  
  
%frame =getsnapshot(vid)%single frame acquisition  
%imshow(frame)
```

Appendix 4 Image Processing

### Input data:

Initial *I* and Final *F* Image: Digital pictures stored in a Work Directory. The command *imread* import the file. To extract the portion of one of this image (I1 or F1), the command *imcrop* is used. In this case, an area of 25 cm \* 15cm has been cropped using 230\*500 pixels from a whole of 900\*1200 pixels.

### Image Processing:

- To further illustrate the concept of the three separate color planes used in an RGB image, the code sample below separate the RGB image in red, green, and blue, and then creates the histogram for each of its separate color planes (red, green, and blue).

```
F1B = F1(:,:,3); imshow(F1B); imhist(F1B); colorbar ; title('Blue in Saturation Condition');
```

- The percentage of change is estimated with the ratio of difference between final image minus initial image, over Initial Image.

### Output Data:

Comparison between initial and final condition is summarized in a plot that includes the initial condition, final condition, percentage of change, and image processed.

Code:

```
clc; close all; clear all;  
O=imread('C:\work\ \2DTCE1ph1.jpg','jpg');  
figure(1),colormap(jet),imshow(O)
```

```
O1=imcrop(O,[470 250 230 500]);  
figure(2),colormap(jet),imshow(O1)
```

```
figure (3)  
O1R = O1(:,:,1);  
subplot(2,1,1);  
imshow(O1R);  
subplot(2,1,2);  
imhist(O1R);  
colorbar  
title('Red TCE 5 min');
```

```
figure (4);  
O1G = O1(:,:,2);  
subplot(2,1,1);  
imshow(O1G);  
subplot(2,1,2);  
imhist(O1G);  
colorbar  
title('Green TCE 5 min');
```

```
figure (5);  
O1B = O1(:,:,3);  
subplot(2,1,1);  
imshow(O1B);  
subplot(2,1,2);  
imhist(O1B);  
colorbar  
title('Blue TCE 5 min');
```

```
I=imread('C:\work\ \2DTCE1ph1.jpg','jpg'\2DTCE1ph1.jpg','jpg');  
I1=imcrop(I,[470 250 230 500]);  
figure(7),colormap(jet),imshow(I1)
```

```
figure (8)  
I1R = I1(:,:,1);  
subplot(2,1,1);  
imshow(I1R);
```

```
subplot(2,1,2);  
imhist(I1R);  
colorbar  
title('Red TCE 5 min');
```

```
figure (9);  
I1G = I1(:, :, 2);  
subplot(2,1,1);  
imshow(I1G);  
subplot(2,1,2);  
imhist(I1G);  
colorbar  
title('Green TCE 5 min');
```

```
figure (10);  
I1B = I1(:, :, 3);  
subplot(2,1,1);  
imshow(I1B);  
subplot(2,1,2);  
imhist(I1B);  
colorbar  
title('Blue TCE 5 min');
```

```
F=imread('C:\work\ \2DTCE1ph1.jpg','jpg'\Fotos\2DTCE9ph1.jpg','jpg');  
F1=imcrop(F,[470 250 230 500]);  
figure (11),colormap(jet),imshow(F1)
```

```
figure (12)  
F1R = F1(:, :, 1);  
subplot(2,1,1);  
imshow(F1R);  
subplot(2,1,2);  
imhist(F1R);  
colorbar  
title('Red TCE 5 min');
```

```
figure (13);  
F1G = F1(:, :, 2);  
subplot(2,1,1);  
imshow(F1G);  
subplot(2,1,2);  
imhist(F1G);  
colorbar  
title('Green TCE 5 min');
```

```
figure (14);
```

```

F1B = F1(:, :, 3);
subplot(2,1,1);
imshow(F1B);
subplot(2,1,2);
imhist(F1B);
colorbar
title('Blue TCE 5 min');

I=rgb2gray(I);
F=rgb2gray(F);

I3=double(I(250:750,470:700));
F3=double(F(250:750,470:700));

C=(abs(F3-I3)./I3);

R=uint8(0*(C<0.1)+85*(C>=0.1&C<0.2)+170*(C>=0.2&C<0.5)+255*(C>=0.5));

figure (15)
subplot(3,2,1);imagesc(I3,[0 255]);title('Initial condition');colormap gray; colorbar;
subplot(3,2,2);imagesc(F3,[0 255]);title('Final condition at 5 minutes');colormap gray;
colorbar;
subplot(3,2,3);imagesc(C,[0 1]);title('% of change');colormap gray; colorbar
subplot(3,2,4);imagesc(R);title('Colorimetric Approach');colormap jet; colorbar
subplot(3,1,3);imhist(C);

N2=abs(double(I1)-double(F1));%imagen final menos imagen inicial

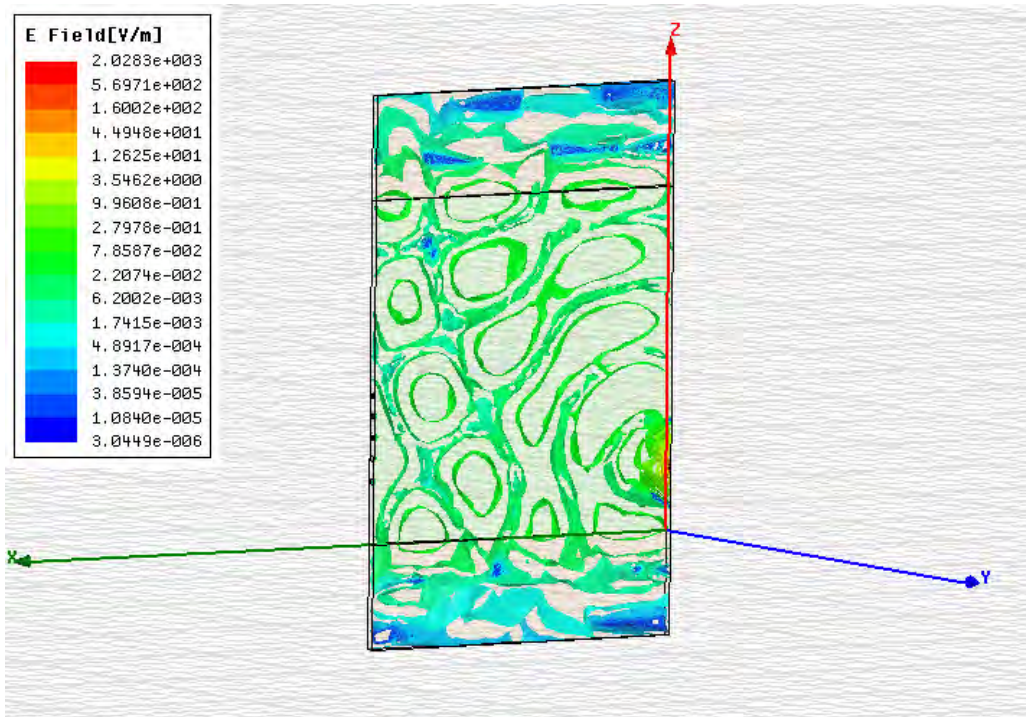
Average2=mean2(N2)
AverIniti=mean2(double(I1))
Averfinal=mean2(double(F1))
AverageDif=mean2(abs(double(I1)-double(F1)))
AverRF1=mean2(F1R)
AverBF1=mean2(F1B)
AverGF1=mean2(F1G)
AverRI1=mean2(I1R)
AverBI1=mean2(I1B)
AverGI1=mean2(I1G)

```

Appendix 5 An electromagnetic model of the Soil-Bed setup

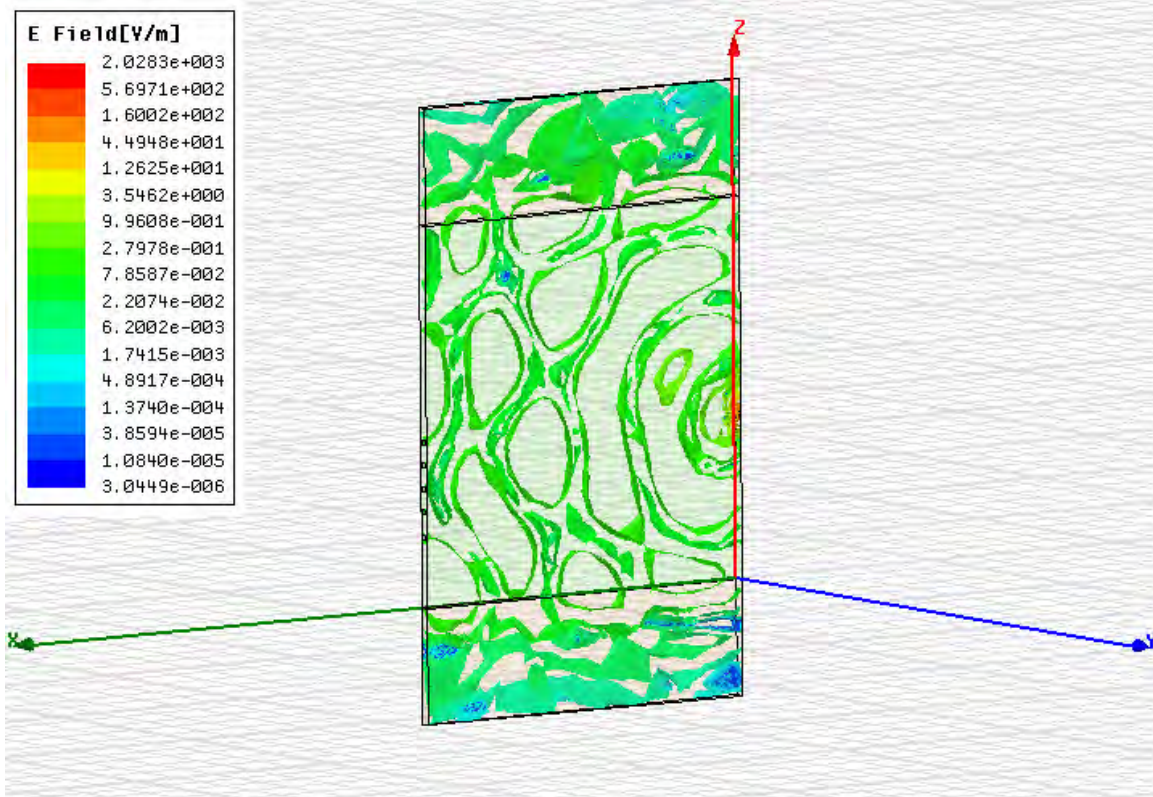
An electromagnetic model of the Soil-Bed setup was developed using Ansoft's HFSS finite-element based electromagnetic simulator. The soil region was modeled by a box of lossy dielectric of dimensions 82 cm x 2 cm x 25 cm. The soil box walls parallel to the xz-plane were set as perfect conductor to simulate the conducting mesh in the experimental setup. Above and below the soil box, boxes of air of dimensions 82 cm x 2 cm x 82 cm were placed to provide a proper termination of the computational space. All external walls of the air boxes were set as radiating boundaries. Six wave-ports were placed on the walls parallel to the yz-plane, one transmitting on the right wall, and five receiving on the left wall. The position of the transmitting port was varied to look at the wave patterns in the soil, and the scattering parameters between wave-ports. The transmitting port is Port 1, receiving ports are numbered from bottom to top; the bottom port is Port 2, and the top port is Port 6. The model geometry is shown in Figures 1, 3, 5, 7, 9 and 11. All simulations were performed at 600 MHz.

In the first test case, the soil in the soil box was assumed to be dry sand, with relative electrical permittivity of 2.55, and conductivity of 0.003 S/m. The loss tangent at 600 MHz is 0.035, which indicates a good dielectric. Figure 1 shows the wave propagation in the tank. The transmit port is located at 14.5 cm above the bottom of the soil box. Note that the energy levels outside the tank are at least 5 orders of magnitude smaller than the levels inside the soil box. This confirms that the perfectly conducting walls provide a parallel-plate waveguide structure. Note that the wave propagates radially from the transmitting port and that a partial standing-wave pattern forms because of the air-soil interface. Scattering parameters for all receiving ports with respect to Port 1 are lower than -100 dB, ranging between -110 and -110 dB.



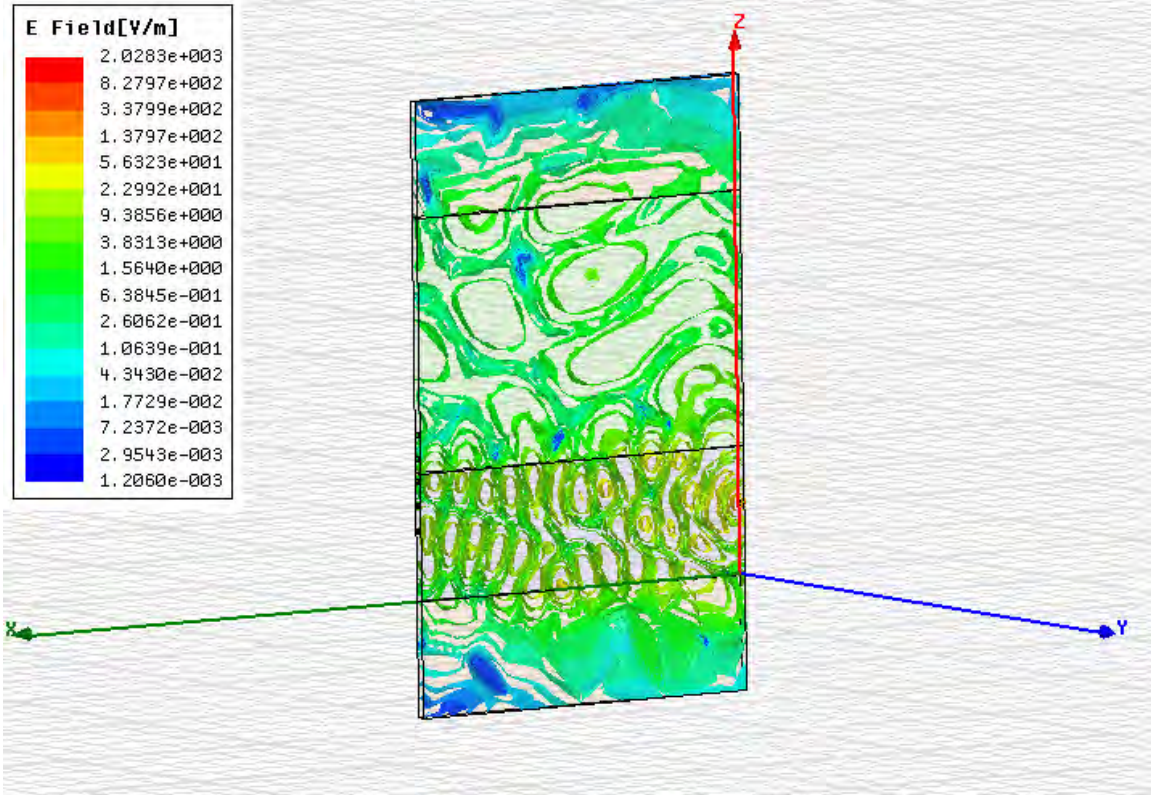
A 5 Figure 1. Soil-Bed electromagnetic model for dry sand. The transmitting port is located 14.5 cm above the bottom of the soil box and the receiving ports are 5 cm apart.

A5 Figure 3 shows the wave propagation for the port located at 35 cm above the soil box bottom. The propagation is still radial from the transmitting port, but since the port is closer to the center of the wall, the field distribution is more symmetric. For this case, the scattering parameters with respect to Port 1 are higher than in the previous one (transmitting port at 14.5 cc), ranging between -150 and -100 dB.

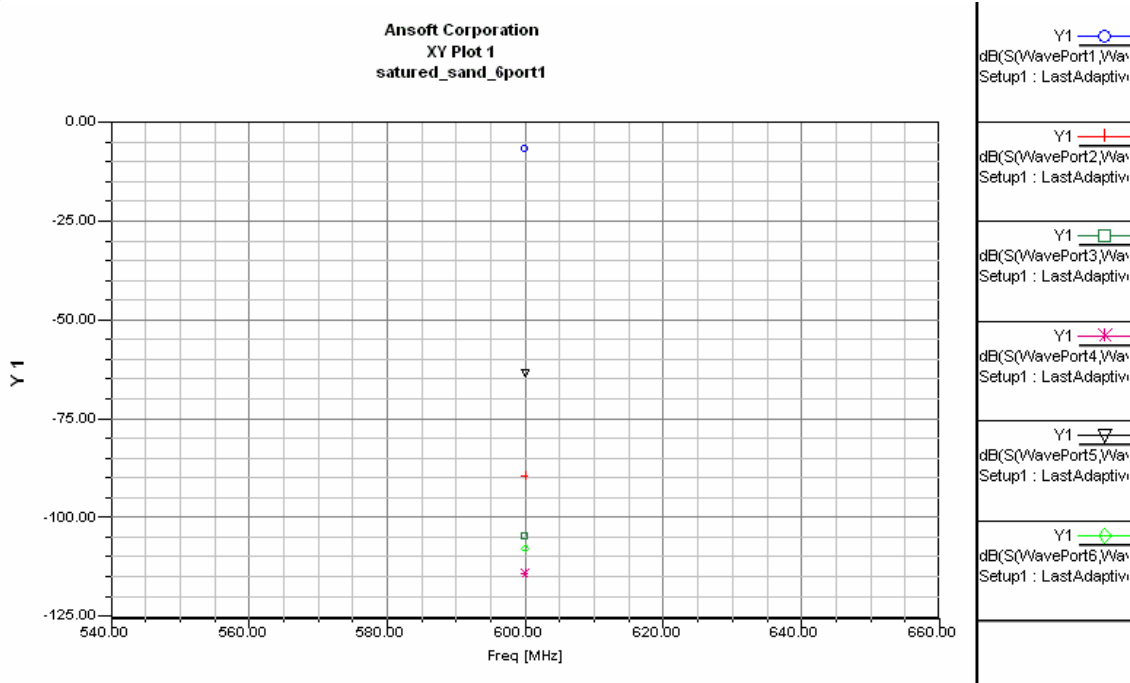


A5 Figure 3. Soil-Bed electromagnetic model for dry sand. The transmitting port is located 35 cm above the bottom of the soil box and the receiving ports are 5 cm apart.

The second case examines the wave propagation when the bottom third of the soil region is saturated sand. For this model the soil box was split in two boxes, the bottom box simulates saturated sand with a relative electrical permittivity of 20 and an electrical conductivity of 0.03 S/m. The loss tangent at 600 MHz is 0.045, slightly larger than for dry sand, but still a good dielectric. The saturated sand box has a height of 27.3 cm. The transmitting port was located at a height of 14.5 cm (Figure 5) and 35 cm (Figure 7) above the bottom of the soil. The port was below and above the saturated-sand/dry-sand interface respectively. Note in Figure 5 the propagation in the x-direction, the shorter wavelength and the concentration of the energy in the saturated sand region. The scattering parameters are higher than the scattering parameters for dry sand only because of the standing wave patterns created by the addition of the dry/saturated sand interface. Figure 6 shows the scattering parameters for this simulation.

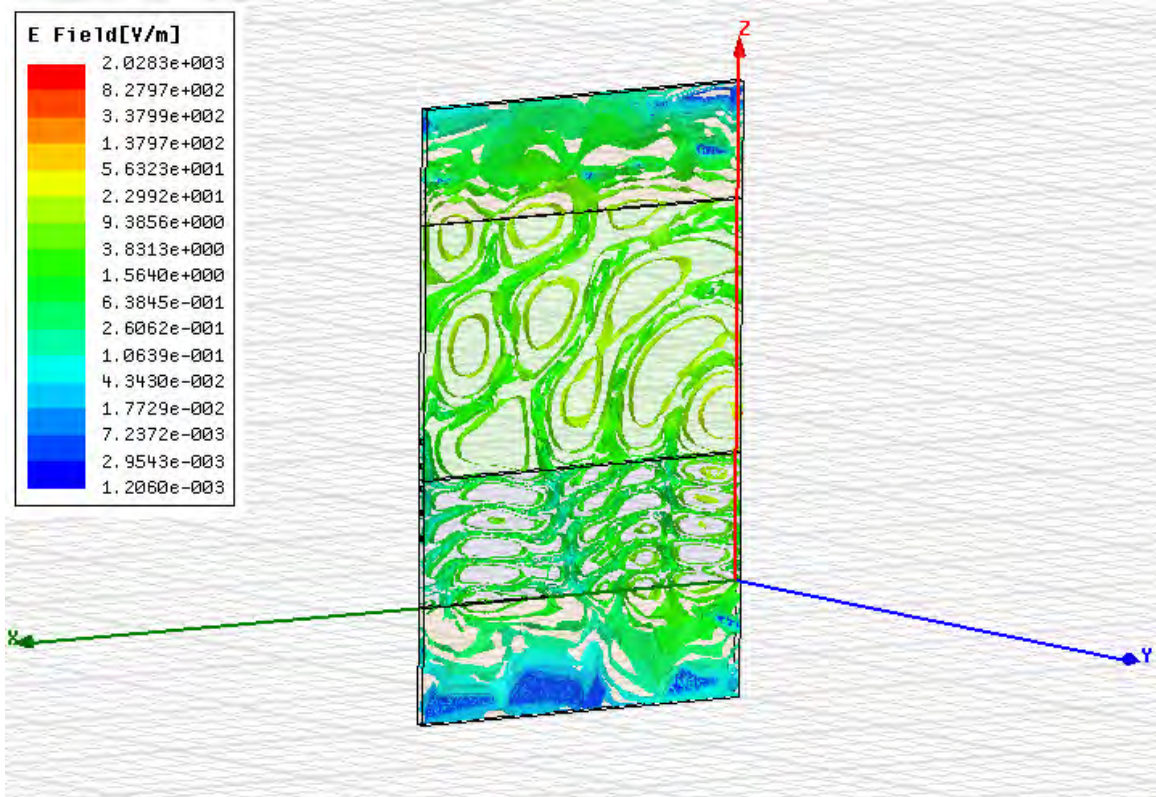


A5 Figure 5. Soil-Bed electromagnetic model for saturated sand on the bottom third and dry sand on the top two thirds. The transmitting port is located 14.5 cm above the bottom of the soil box (below the dry/saturated sand interface) and the receiving ports are 5 cm apart.

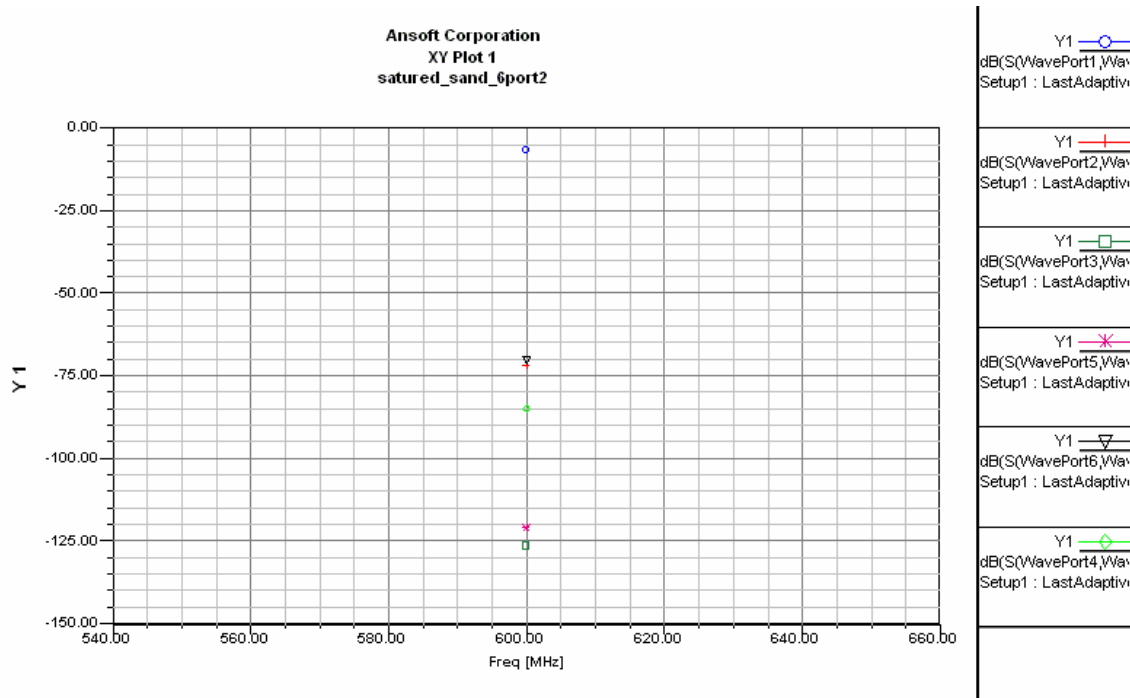


A5 Figure 6. Scattering parameters for the 2/3 dry sand and 1/3 saturated sand Soil-Bed with transmitting port 14.5 cm above the soil box bottom.

A5 Figure 7 shows that when the transmitting port is placed at 35 cm above the bottom of the soil box, it is on the dry sand region. Note that the wave in the saturated soil region propagates almost downwards (in the  $-z$ -direction). Figure 8 shows that the scattering parameters are slightly slower than for the port placed at 14.5 cm.

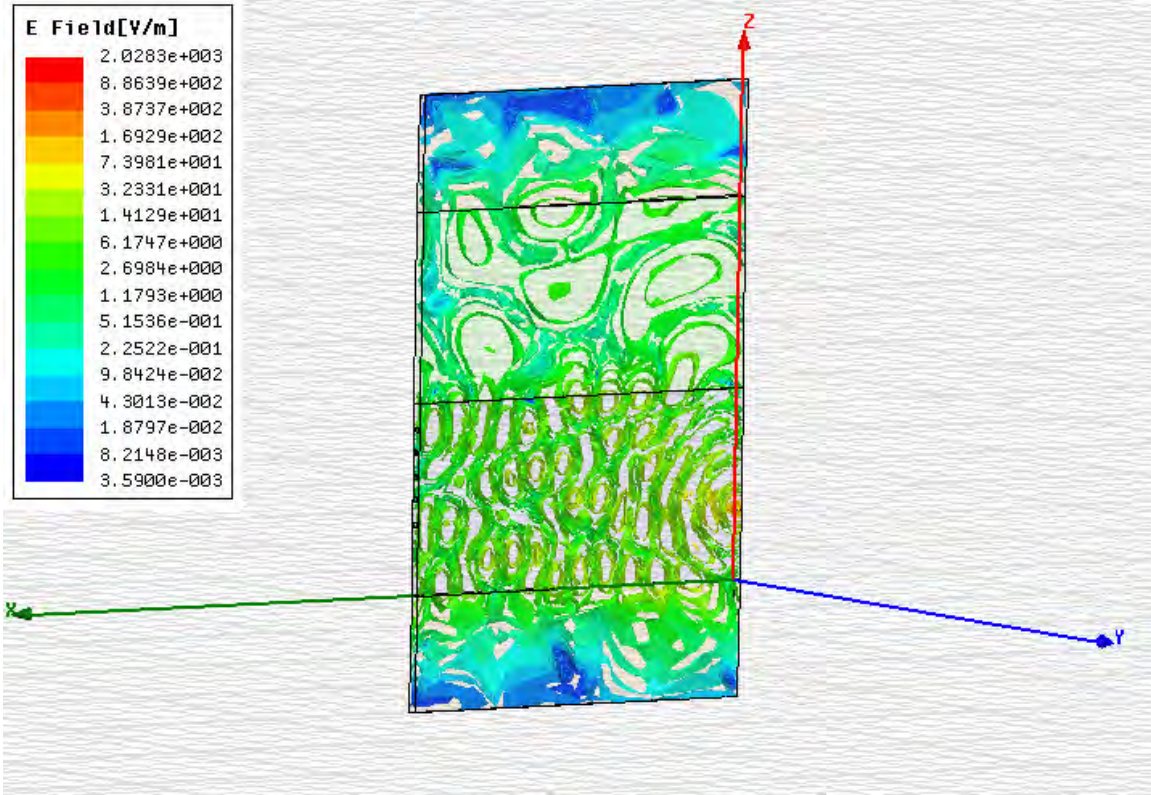


A5 Figure 7. Soil-Bed electromagnetic model for saturated sand on the bottom third and dry sand on the top two thirds. The transmitting port is located 35 cm above the bottom of the soil box (above the dry/saturated sand interface) and the receiving ports are 5 cm apart.

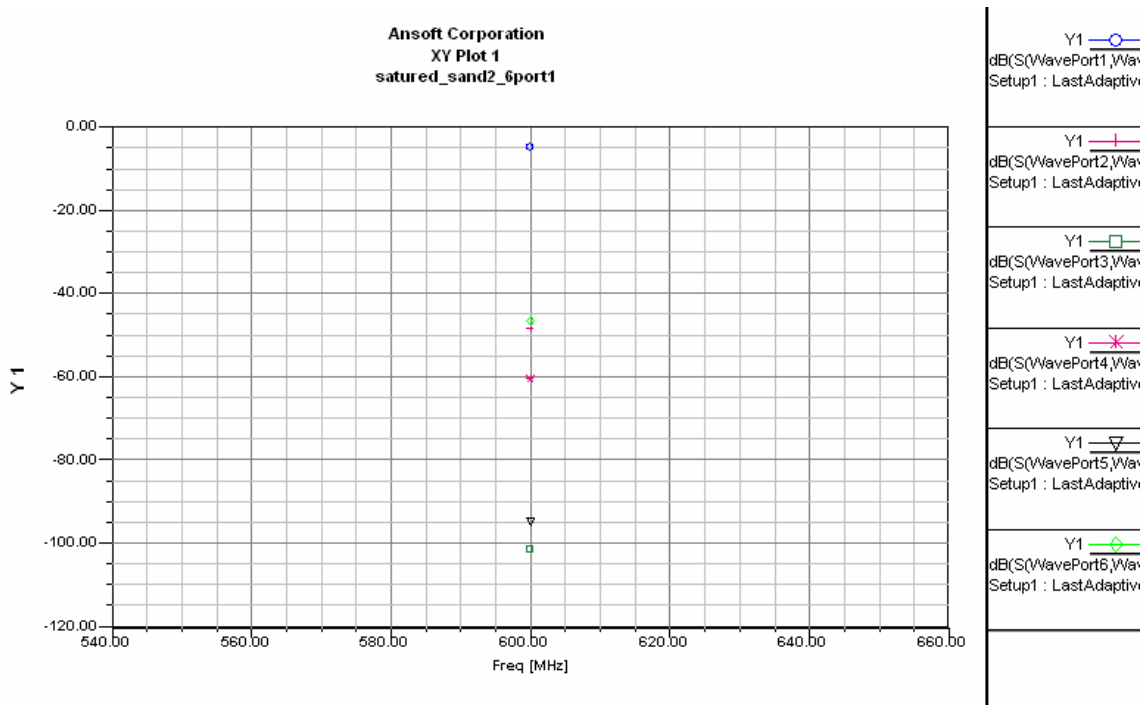


A5 Figure 8. Scattering parameters for the 2/3 dry sand and 1/3 saturated sand Soil-Bed with transmitting port 35 cm above the soil box bottom.

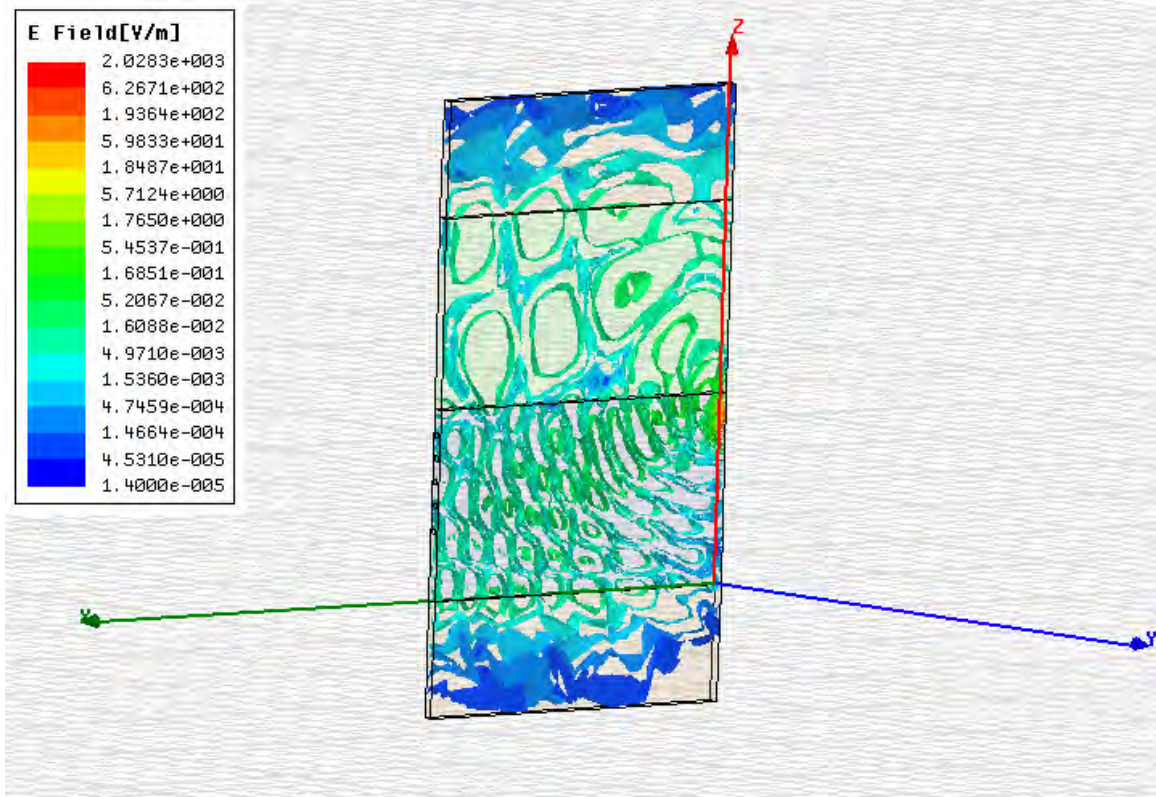
The last case shows the soil region split into two equal boxes of saturated sand (bottom) and dry sand (top). The transmitting port was located at a height of 14.5 cm (Figure 9) and 35 cm (A5 Figure 8) above the bottom of the soil. The port was below the dry/saturated sand interface for both situations. Note in Figure 9 that the propagation of the wave is almost horizontal for the port at 14.5 cm, and in Figure 11 the wave travels at an angle of about 30 degrees from the horizontal for the port at 35 cm. This explains the much lower scattering parameters of Figure 12 for the port at 35 cm, as compared with Figure 10 for the ports at 14.5 cm



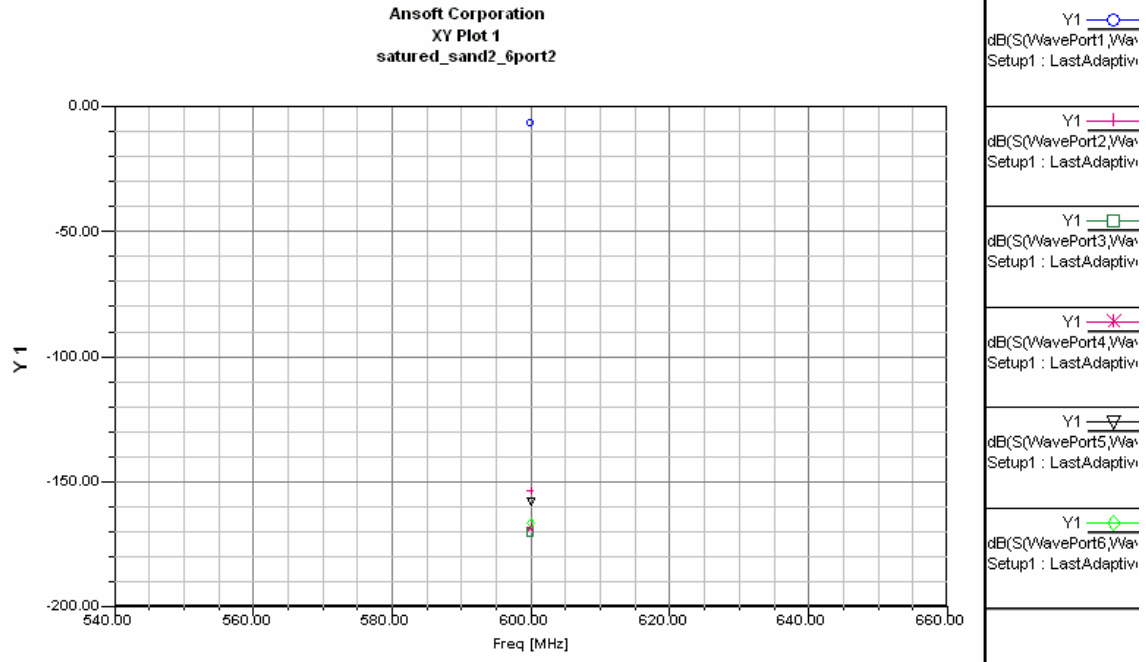
A5 Figure 9. Soil-Bed electromagnetic model for saturated sand on the bottom half and dry sand on the top half. The transmitting port is located 14.5 cm above the bottom of the soil box (above the dry/saturated sand interface) and the receiving ports are 5 cm apart.



A5 Figure 10. Scattering parameters for the 1/2 dry sand and 1/2 saturated sand Soil-Bed with transmitting port 14.5 cm above the soil box bottom.



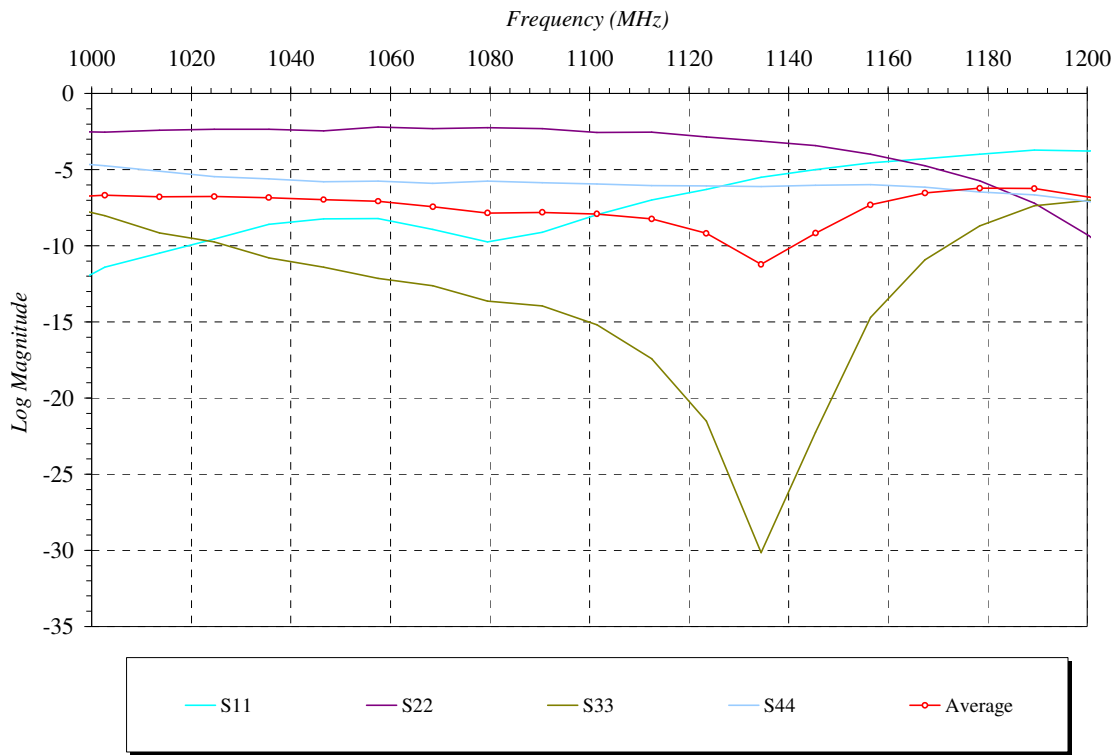
A5 Figure 11. Soil-Bed electromagnetic model for saturated sand on the bottom half and dry sand on the top half. The transmitting port is located 35 cm above the bottom of the soil box (above the dry/saturated sand interface) and the receiving ports are 5 cm apart.



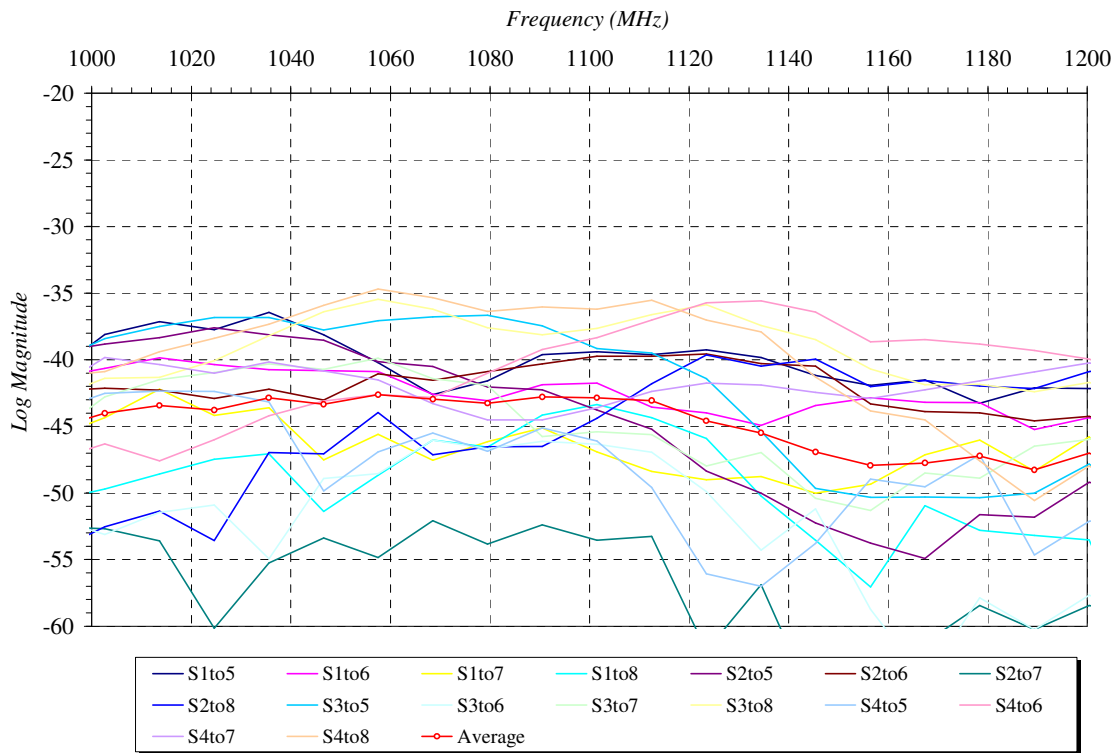
A5 Figure 12. Scattering parameters for the 1/2 dry sand and 1/2 saturated sand Soil-Bed with transmitting port 35 cm above the soil box bottom.

Appendix 6 Transmission and reflection data all antennas to estimate permittivity

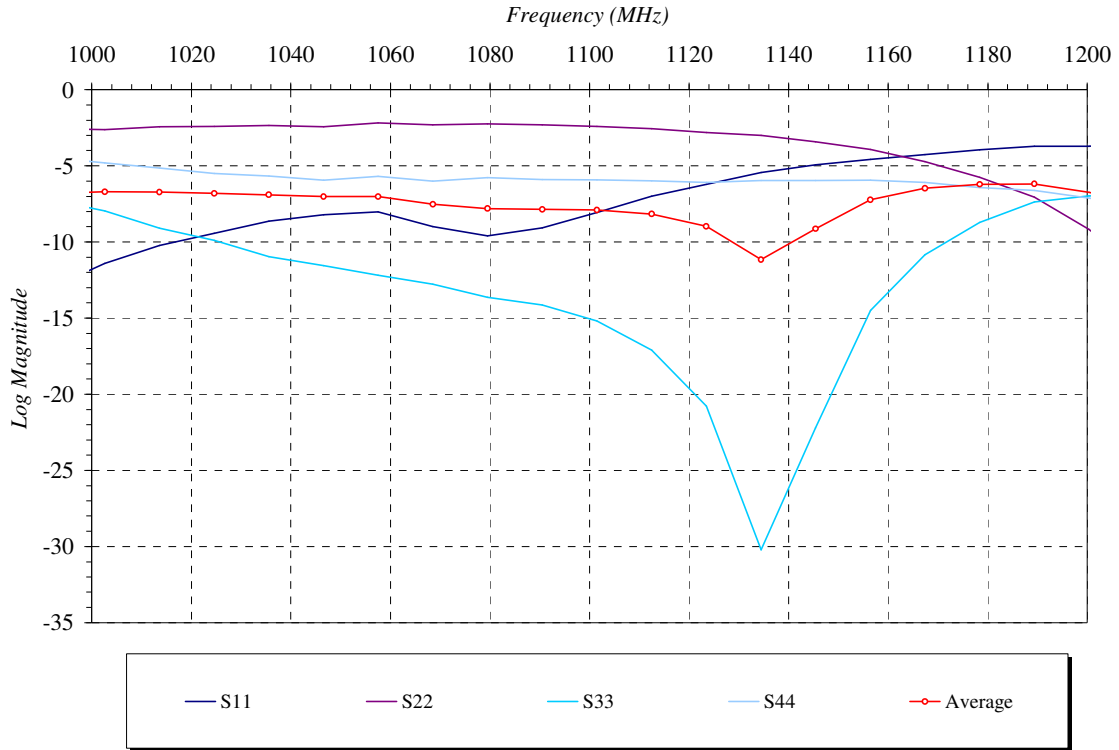
A6 Figure 60 Transmission Data- at 5 min TCE injection –Dry Conditions



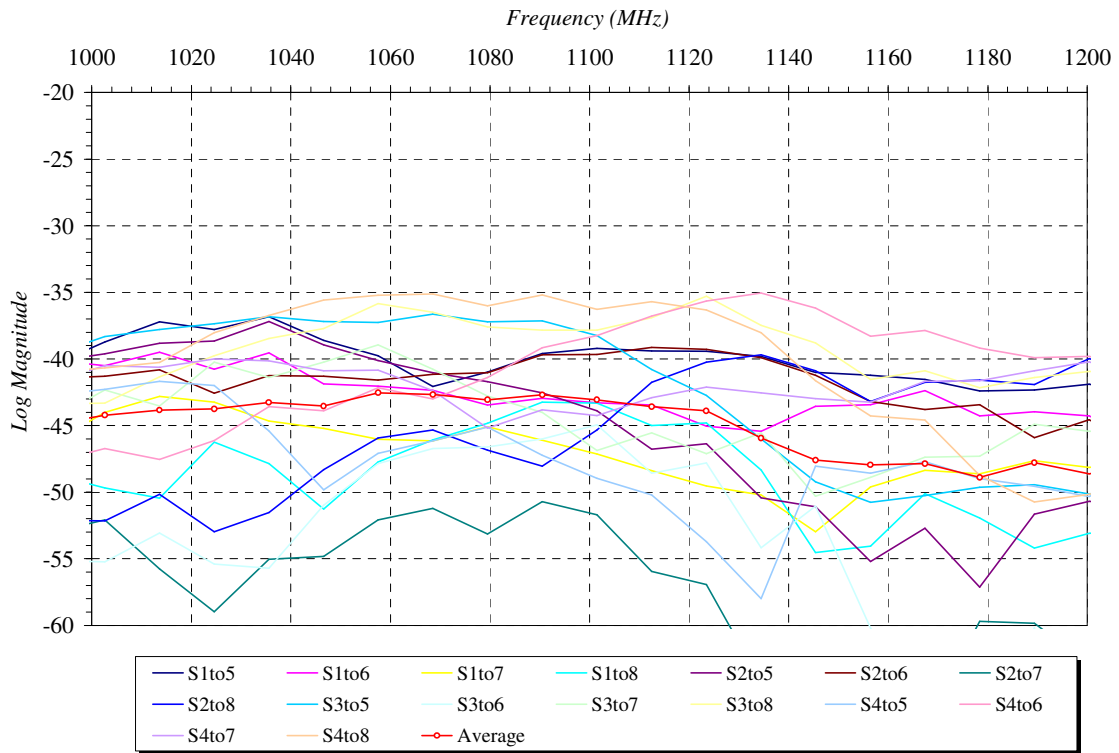
A6 Figure 2 Reflection Data – at 5 mn TCE injection- Dry Conditions



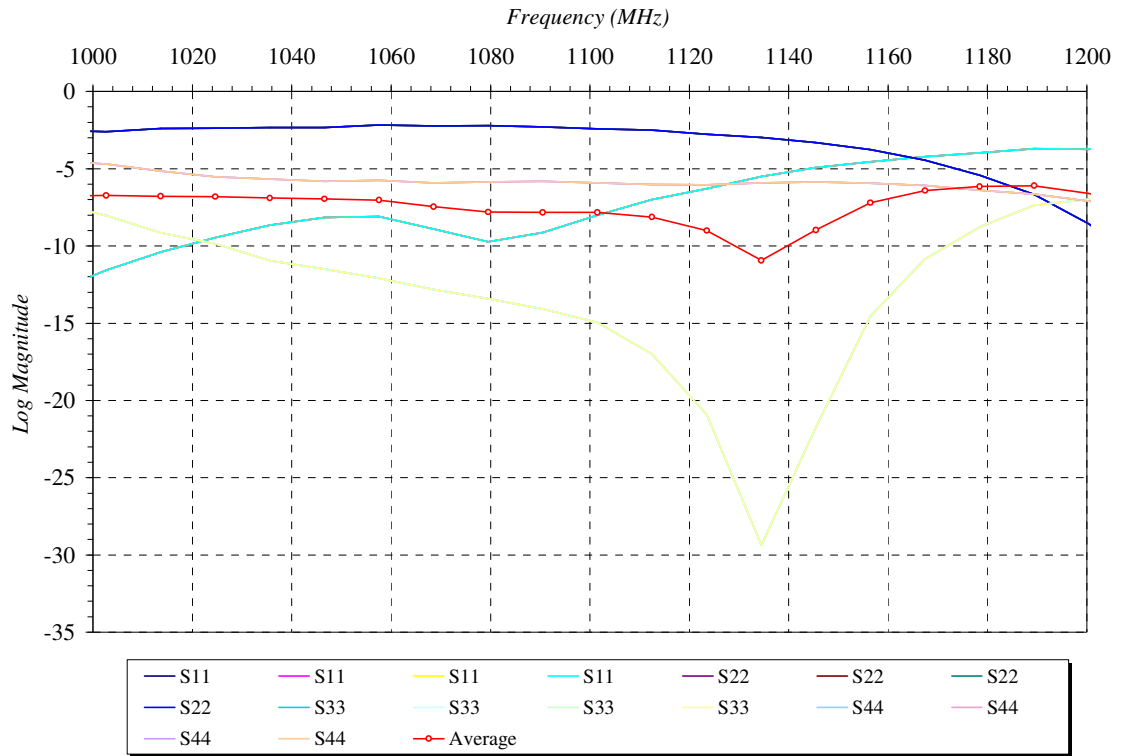
A6 Figure 3 Transmission Data 10 min after TCE injection- Dry Conditions



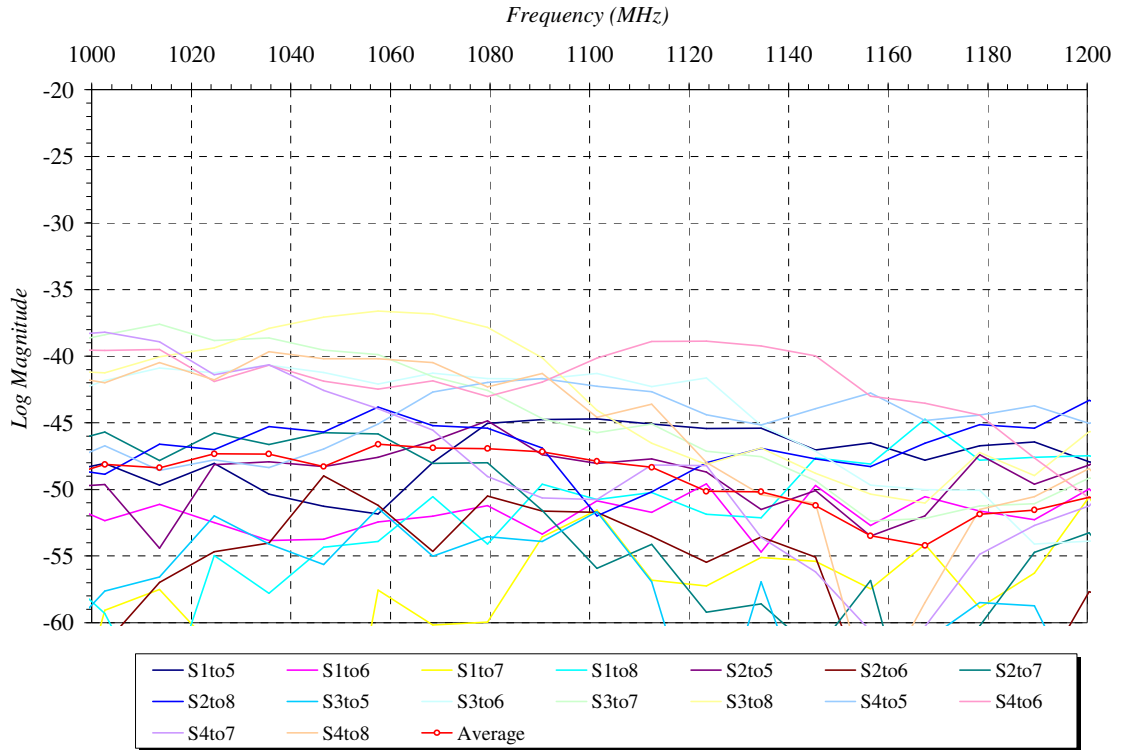
**A6 Figure 4 Reflection Data 10 min after TCE injection- Dry Conditions**



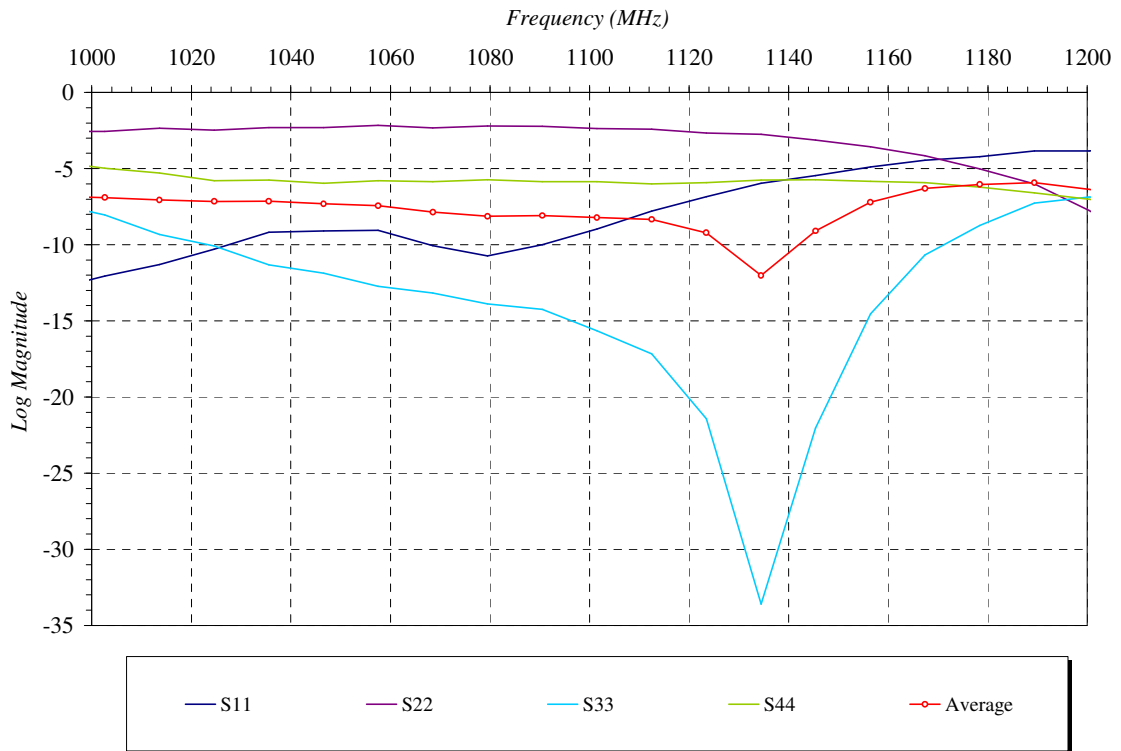
**A6 Figure 5 Transmission Data 30 min after TCE injection- Dry Conditions**



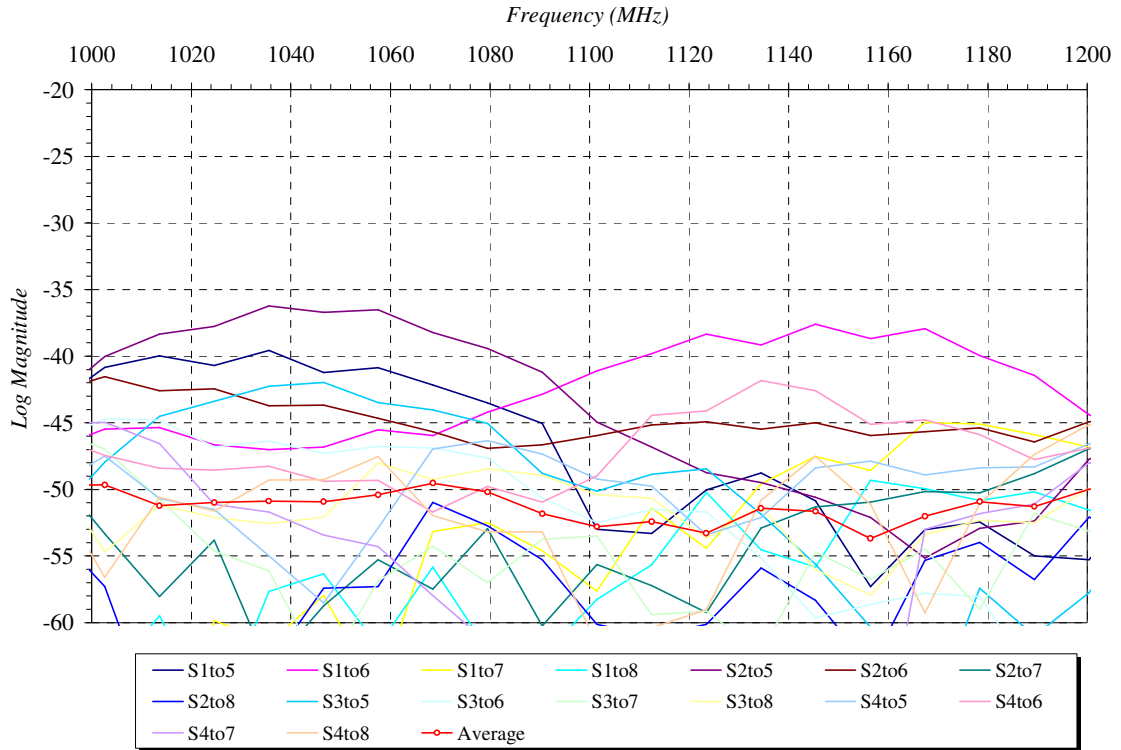
**A6 Figure 6 Reflection Data 30 min after TCE injection- Dry Conditions**



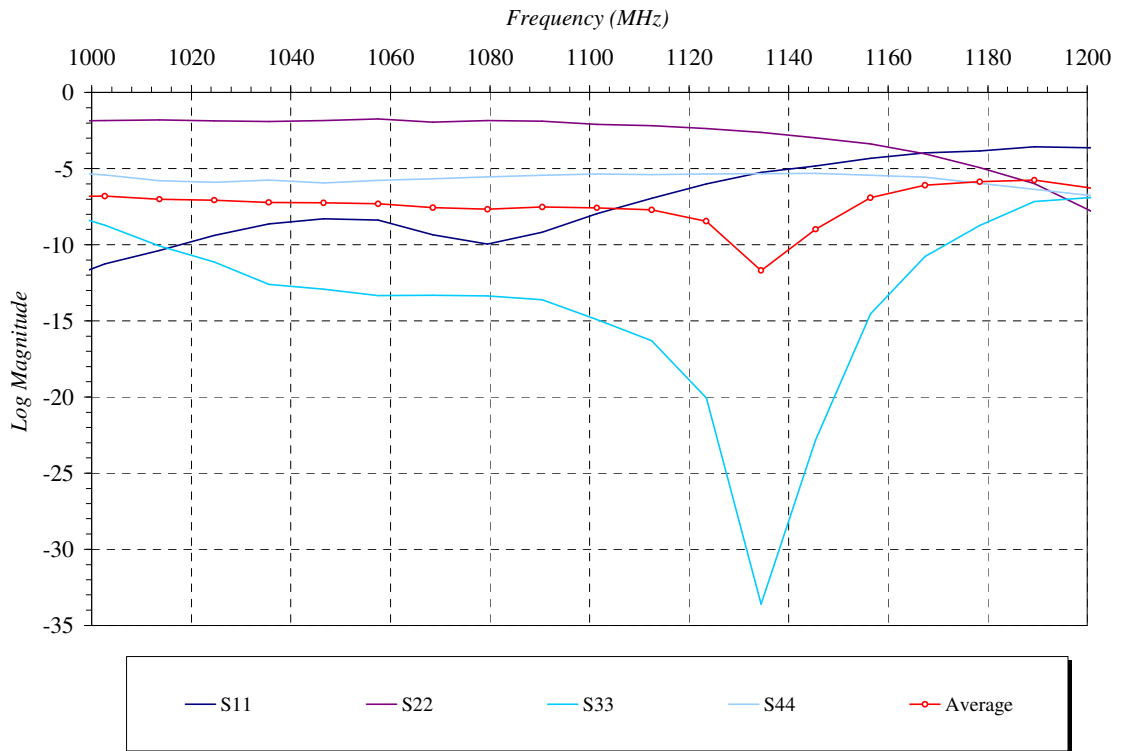
**A6 Figure 7 Transmission Data 50 min after TCE injection – Dry Condition**



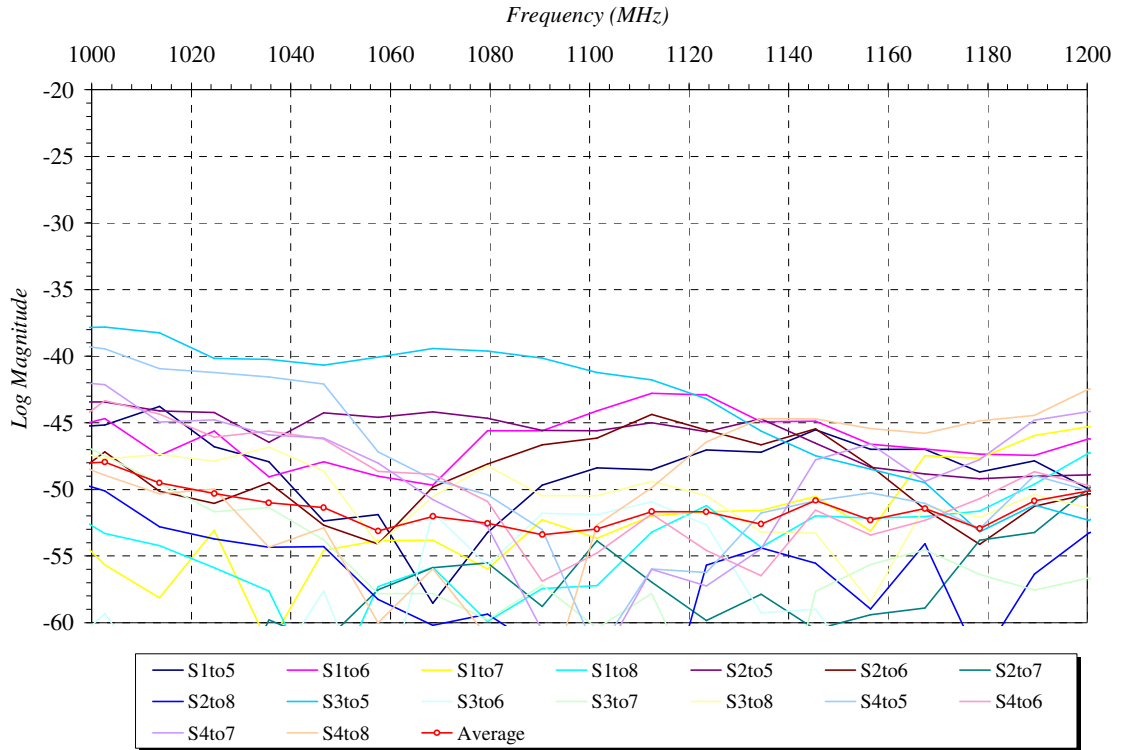
**A6 Figure 8 Reflection data 50 min after TCE injection- Dry condition**



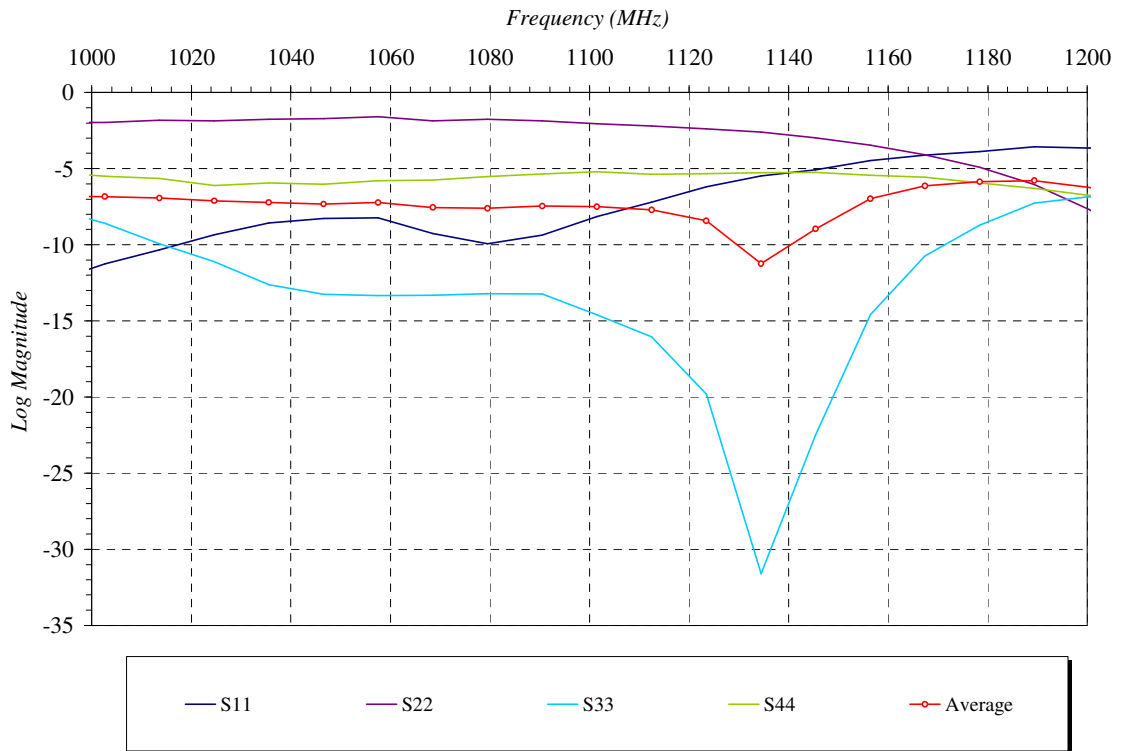
**A6 Figure Transmission data 80 min after TCE injection – Dry condition**



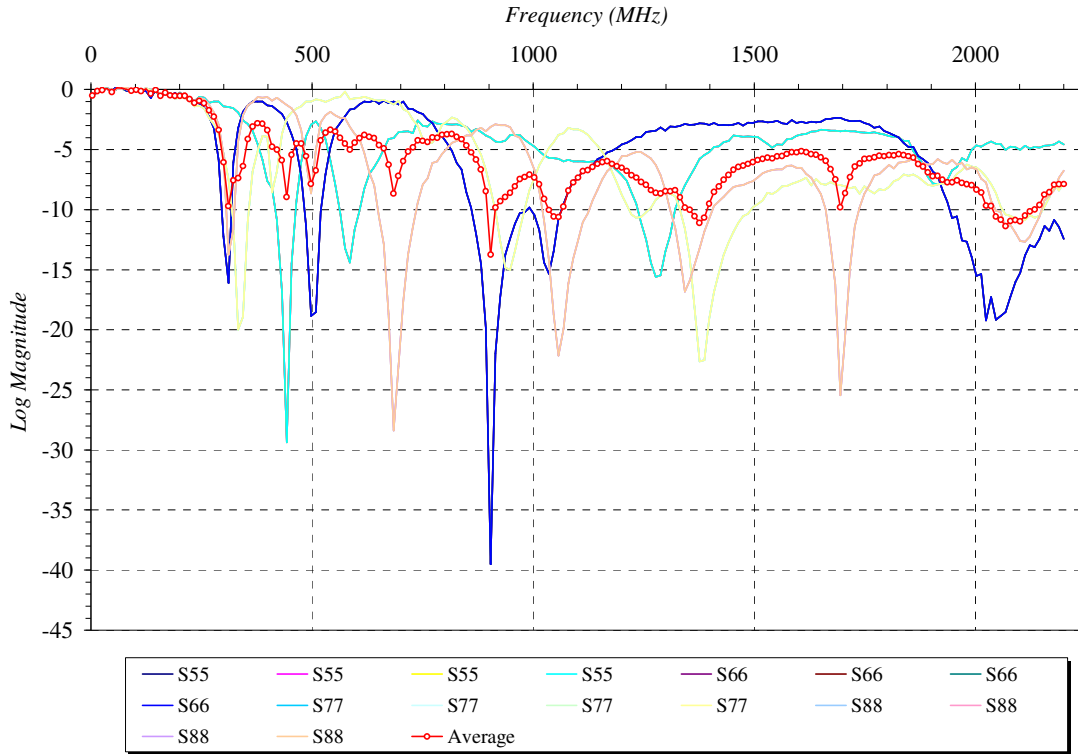
**A6 Figure 10 Reflection data 80 min after TCE injection – dry condition**



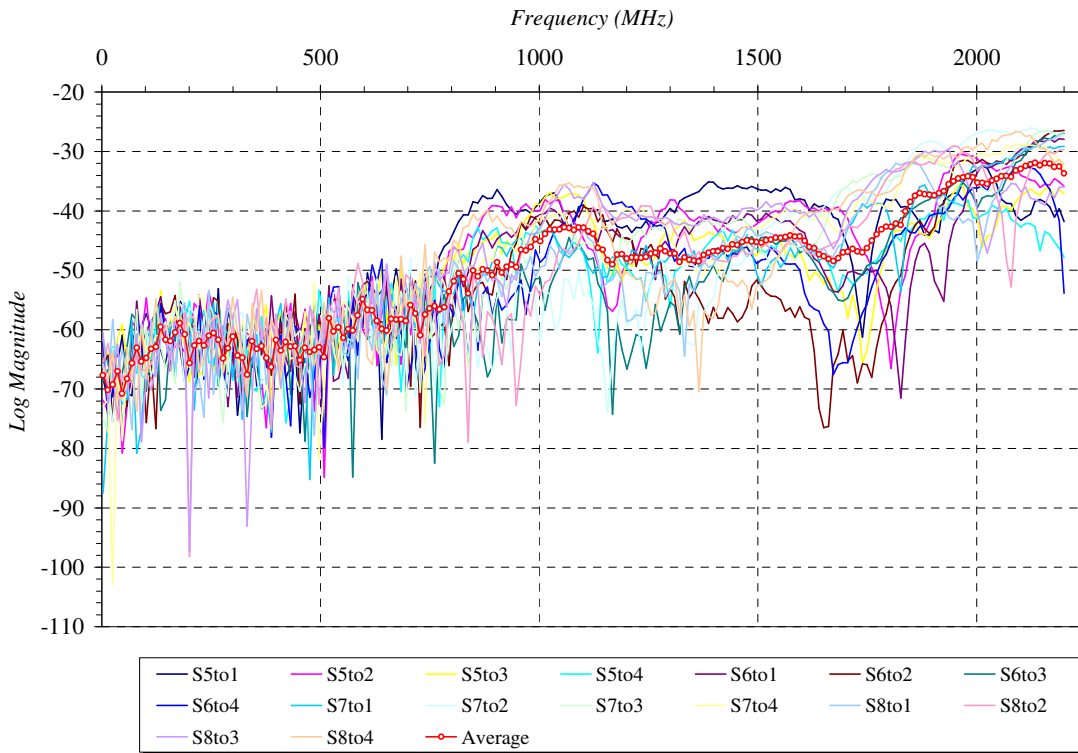
**A6 Figure 11 Transmission Data 130 min after TCE Injection- Dry Condition**



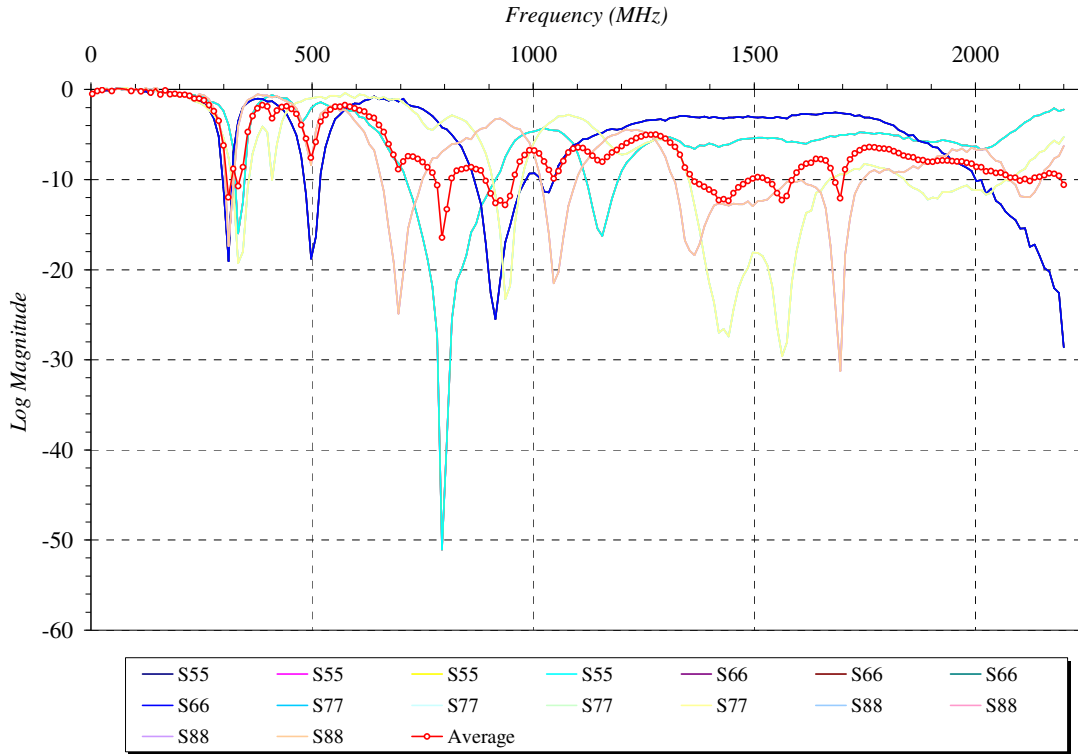
**A6 Figure 12 Reflection Data 130 min after TCE injection- Dry Condition**



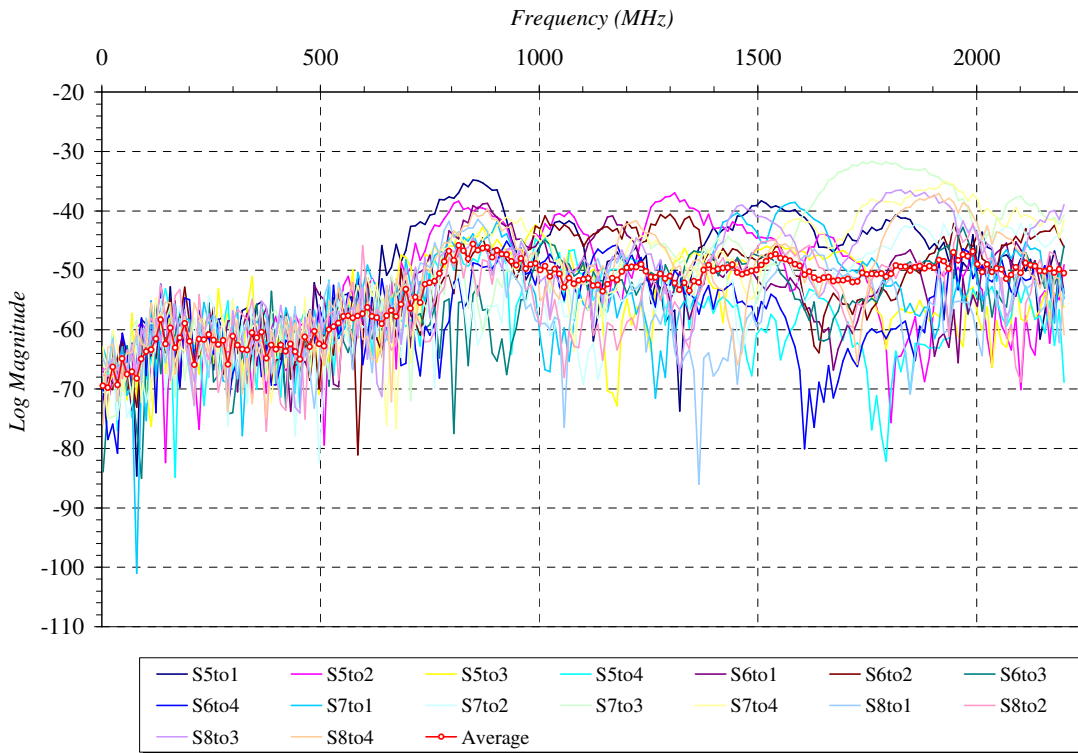
A6 Figure 13 Reflection data 10 min after TCE injection- dry conditions



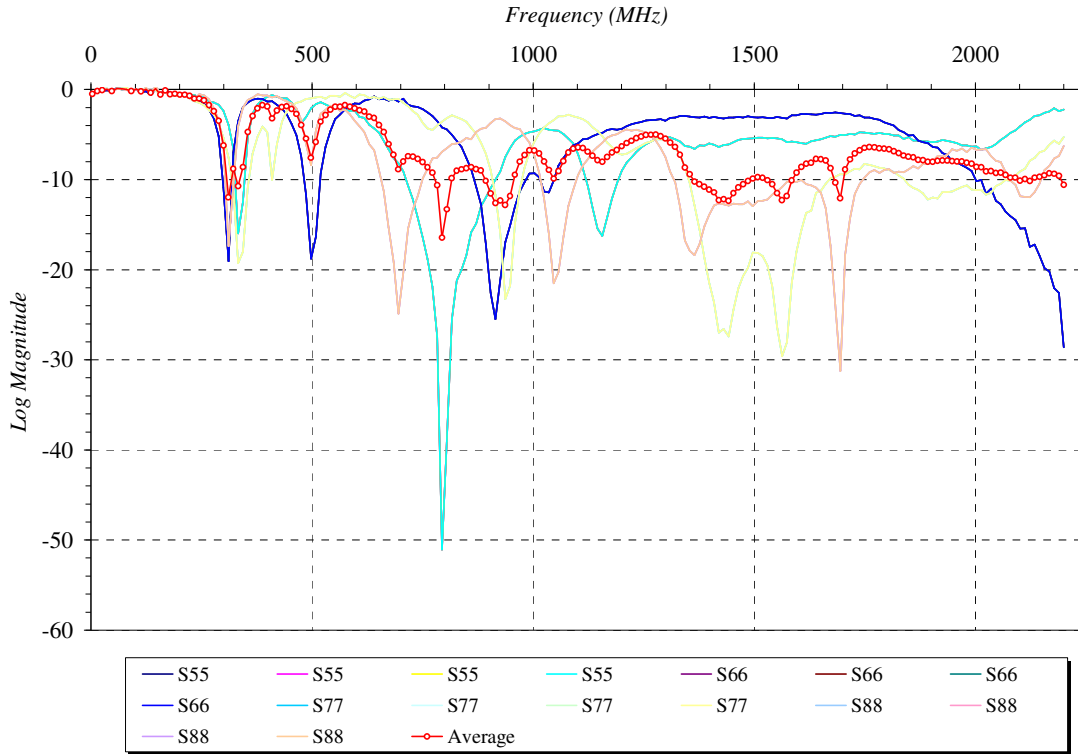
A6 Figure 14 Transmission data 10 min after TCE injection-dry conditions



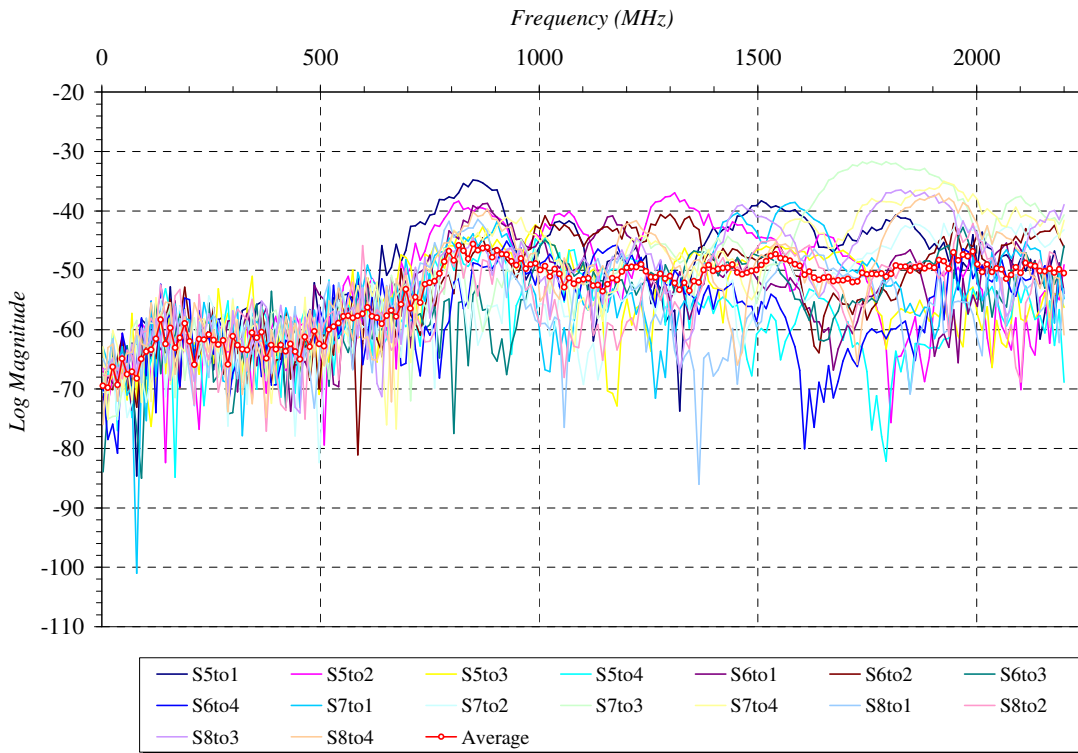
A6 Figure 15 Reflection data 30 min after TCE injection-dry conditions



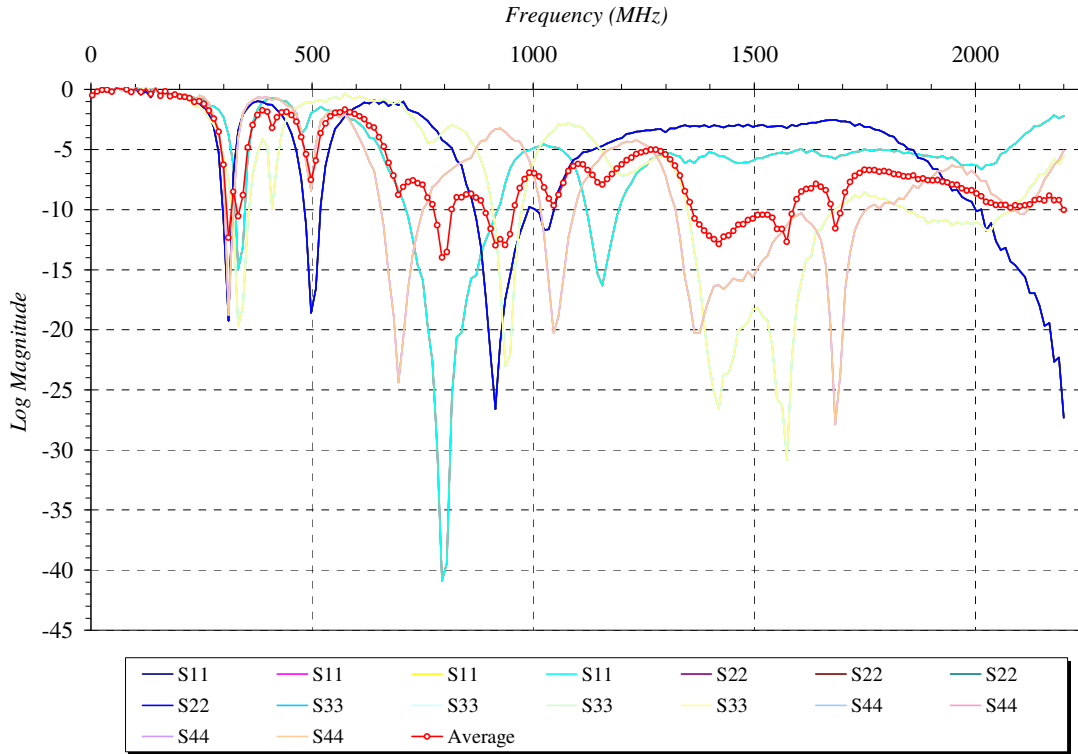
A6 Figure 16 Transmission data 30 min after TCE injection-dry conditions



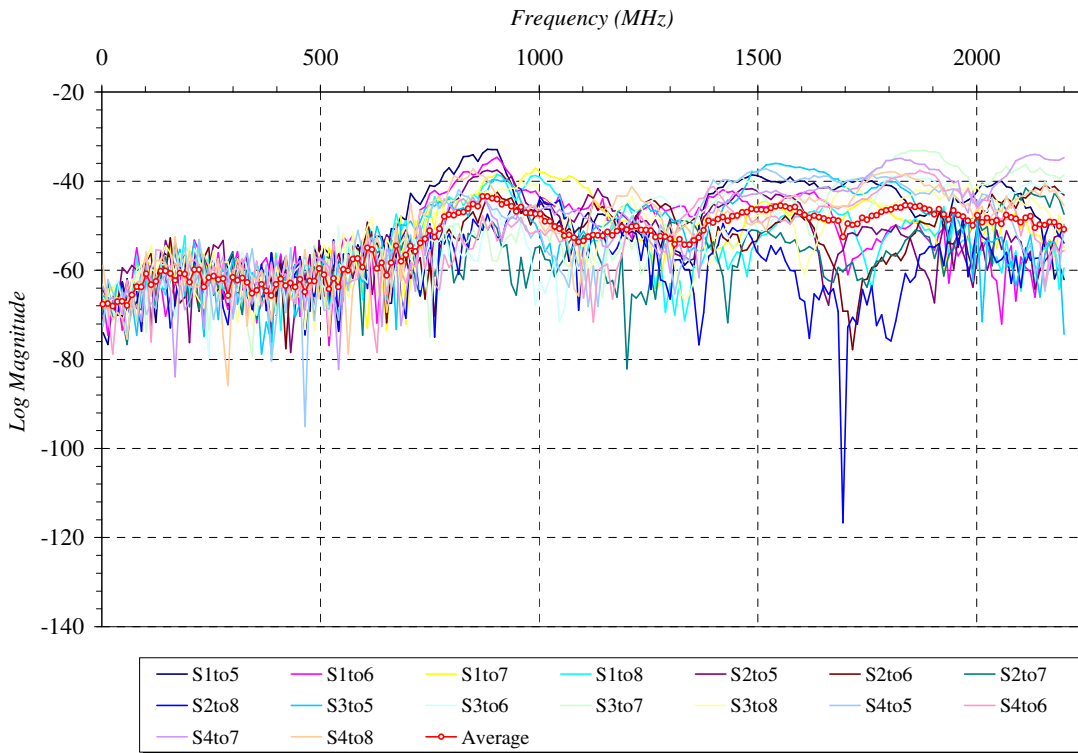
A6 Figure 17 Reflection data 50 min after TCE injection-dry conditions



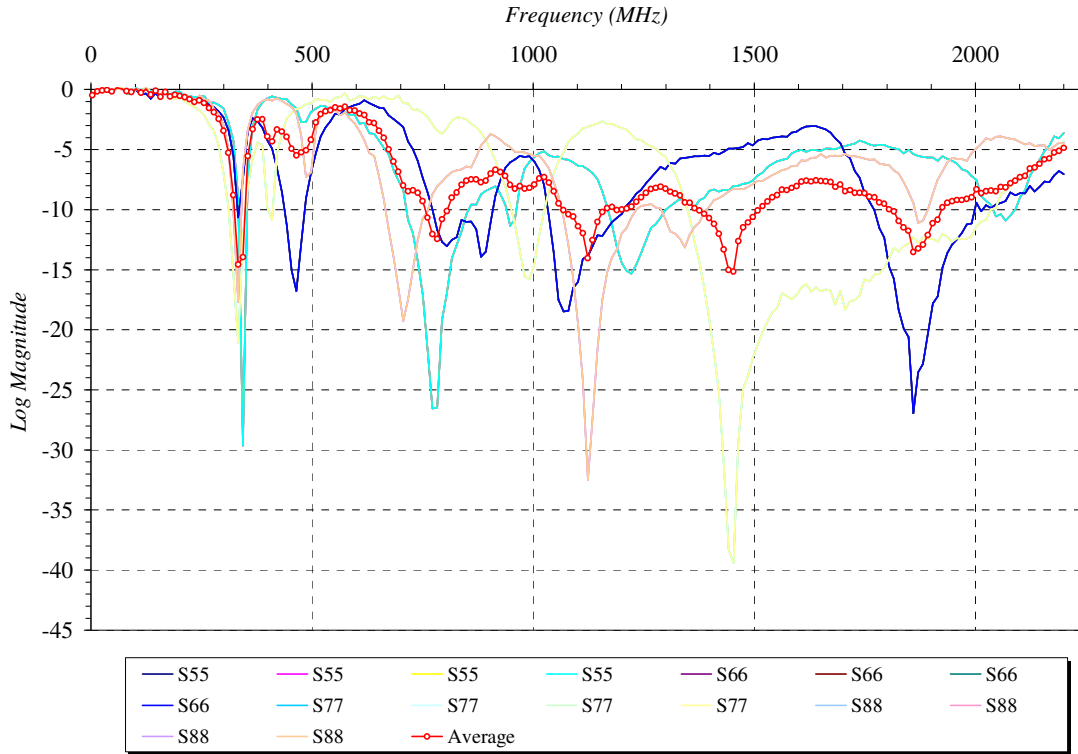
A6 Figure 18 Transmission data 50 min after TCE injection- dry conditions



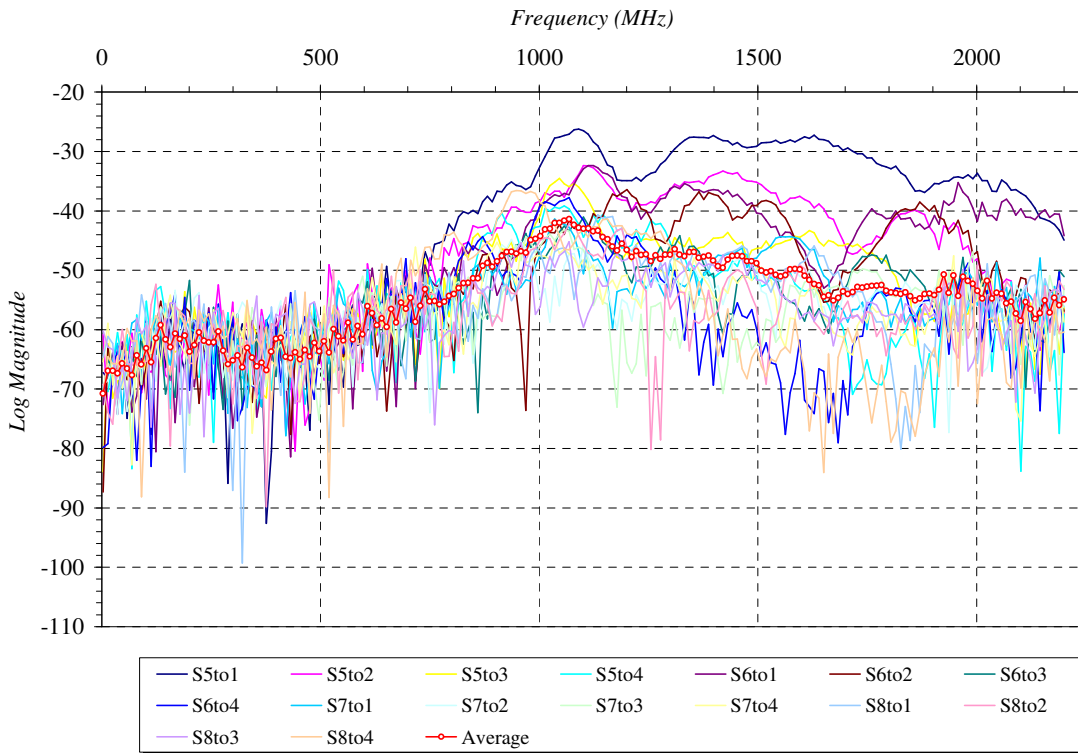
A6 Figure 19 Reflection data 130 min after TCE injection – dry conditions



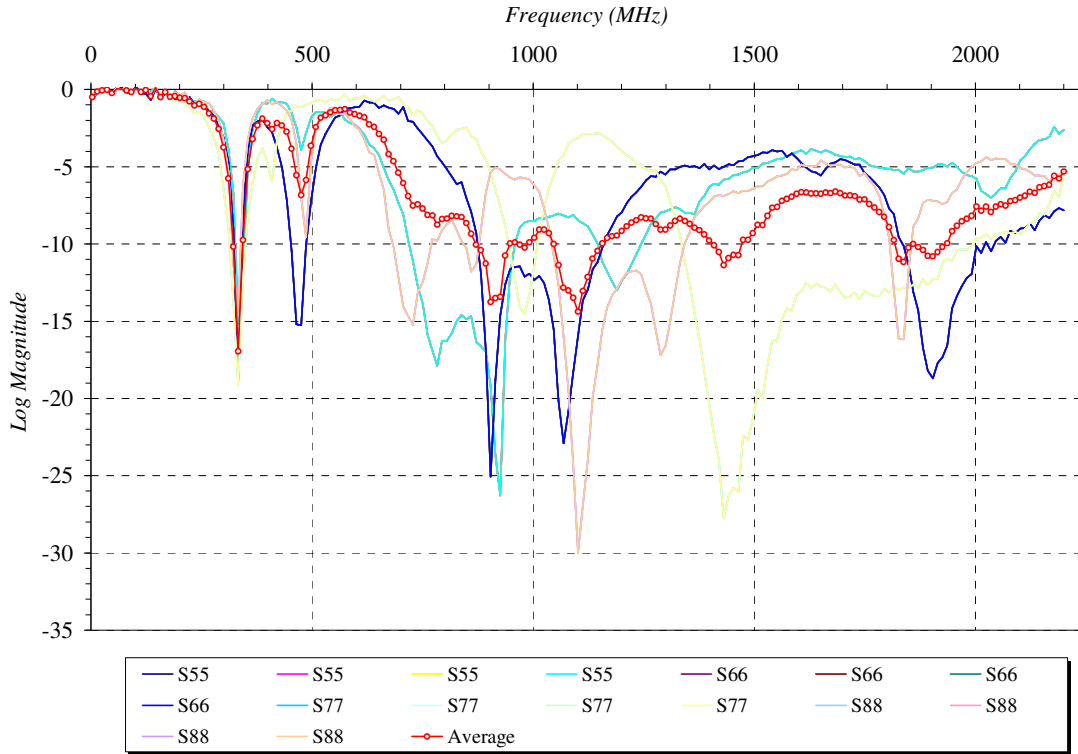
A6 Figure 20 Transmission data 130 min after TCE injection-dry conditions



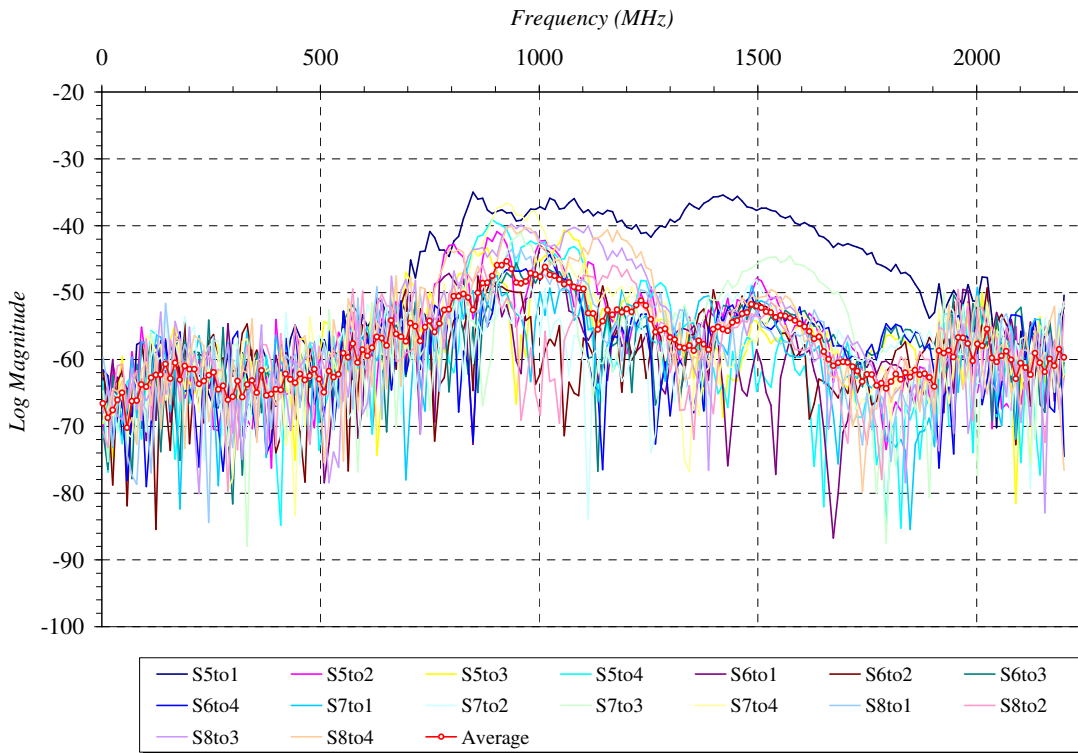
A6 Figure 21 Reflection data when soil is 50% saturated



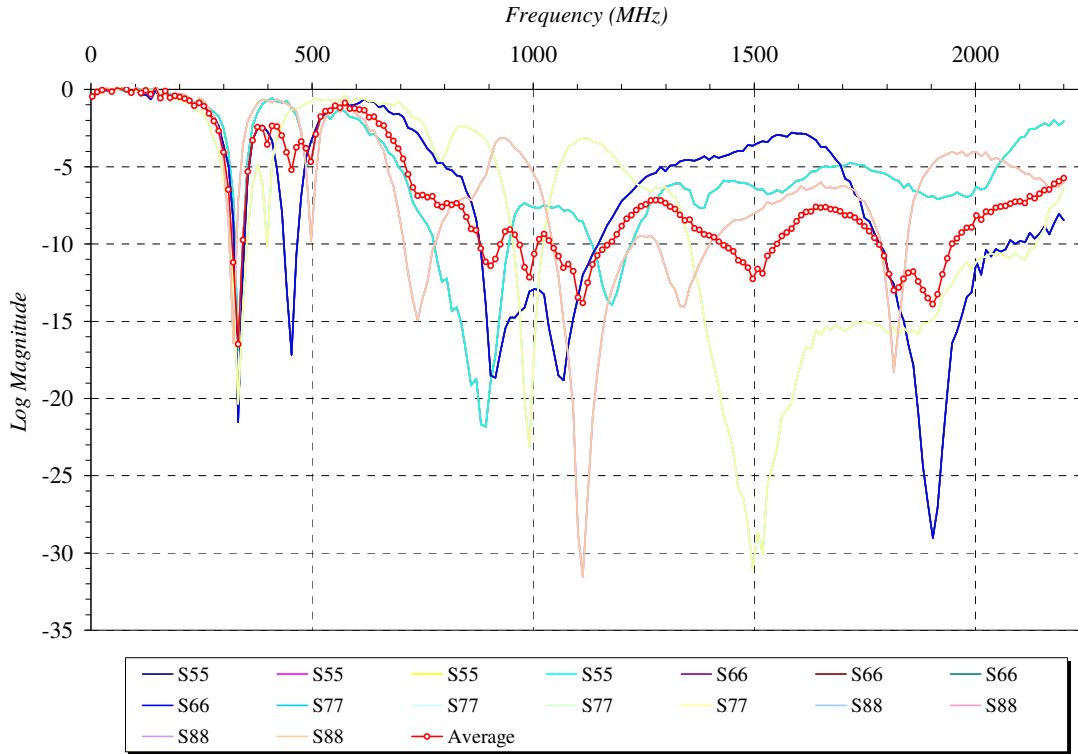
A6 Figure 22 Transmission data when soil is 50% saturated



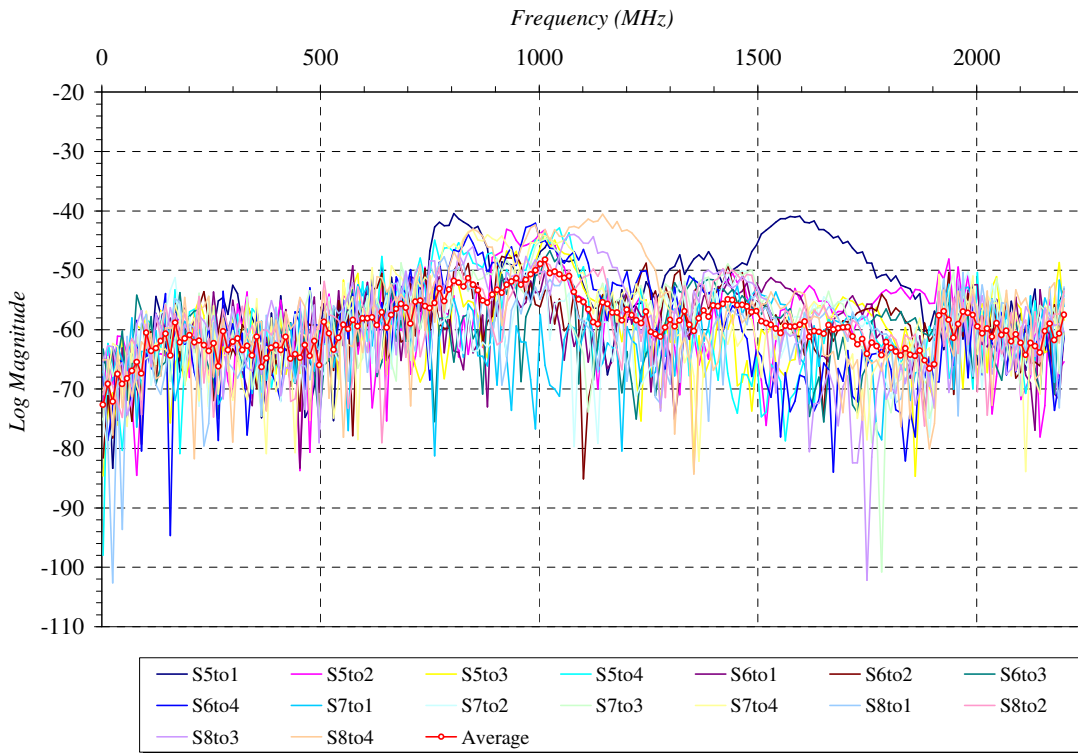
A6 Figure 23 Reflection data when soil is 75% saturated



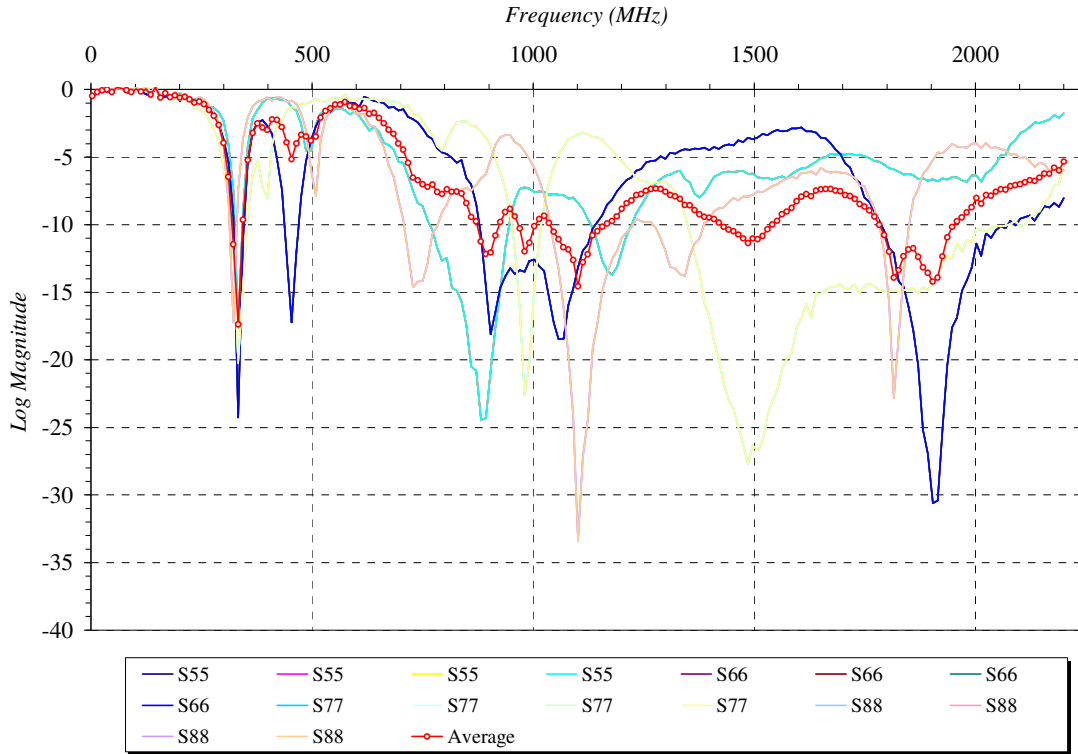
A6 Figure 24 Transmission data when soil is 75% saturated



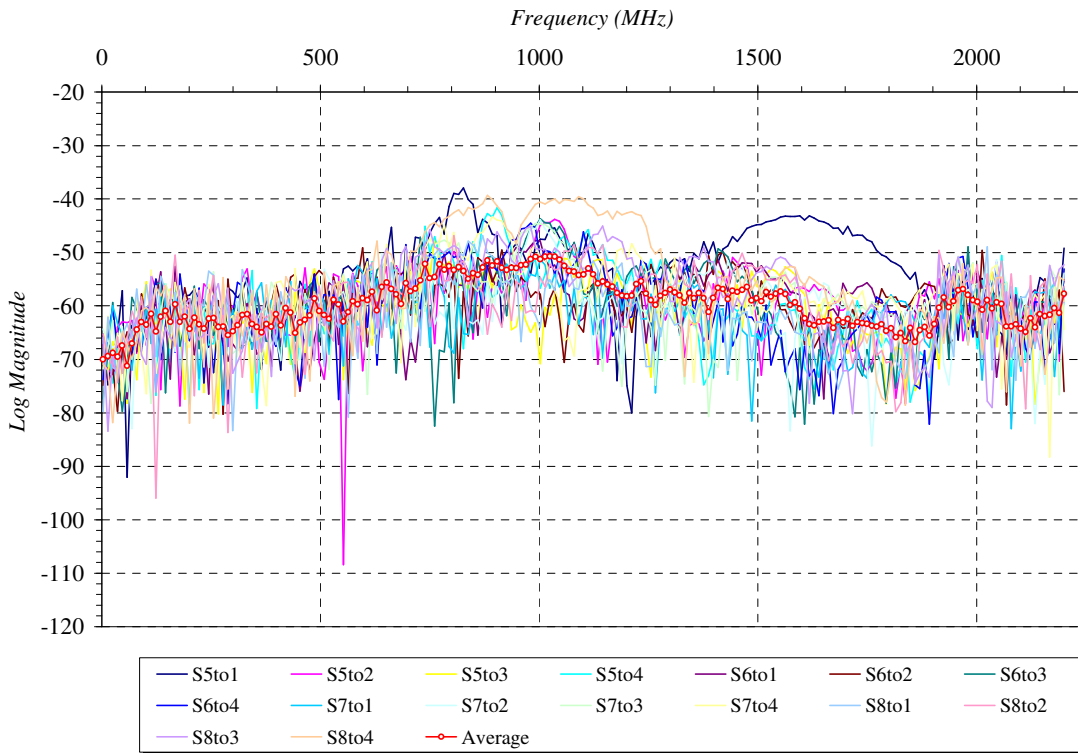
A6 Figure 25 Reflection data in soil 100% saturated



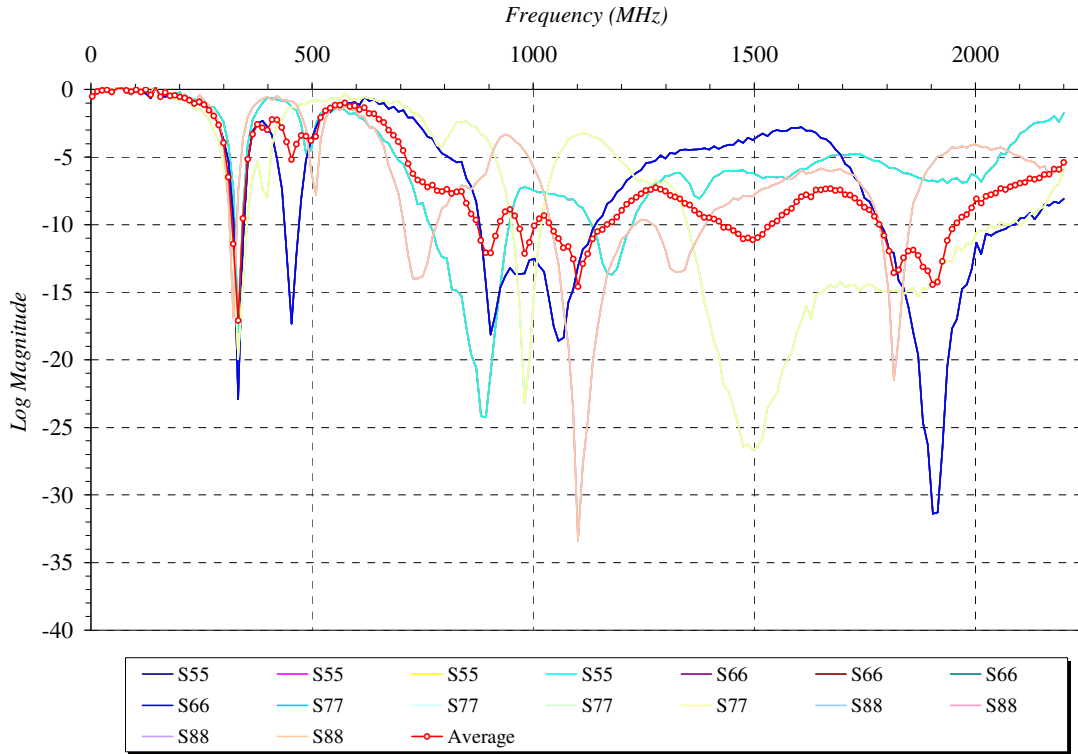
A6 Figure 26 Transmission data in soil 100% saturated



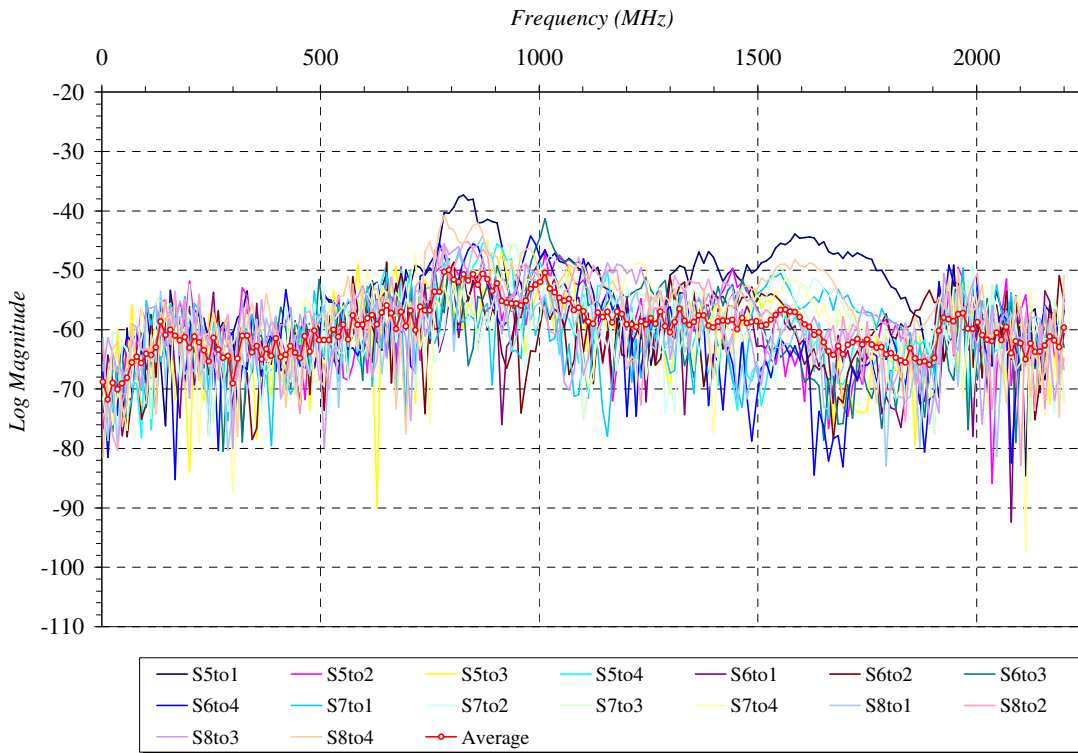
A6 Figure 27 Reflection data in saturated soil after 10 min TCE injection



A6 Figure 28 Transmission data in saturated soil after 10 min TCE injection



A6 Figure 29 Reflection data in saturated soil after 45 min TCE injection



A6 Figure 30 Transmission data in saturated soil after 45 min TCE injection

*Appendix 7 Preliminary Statistical Analysis*

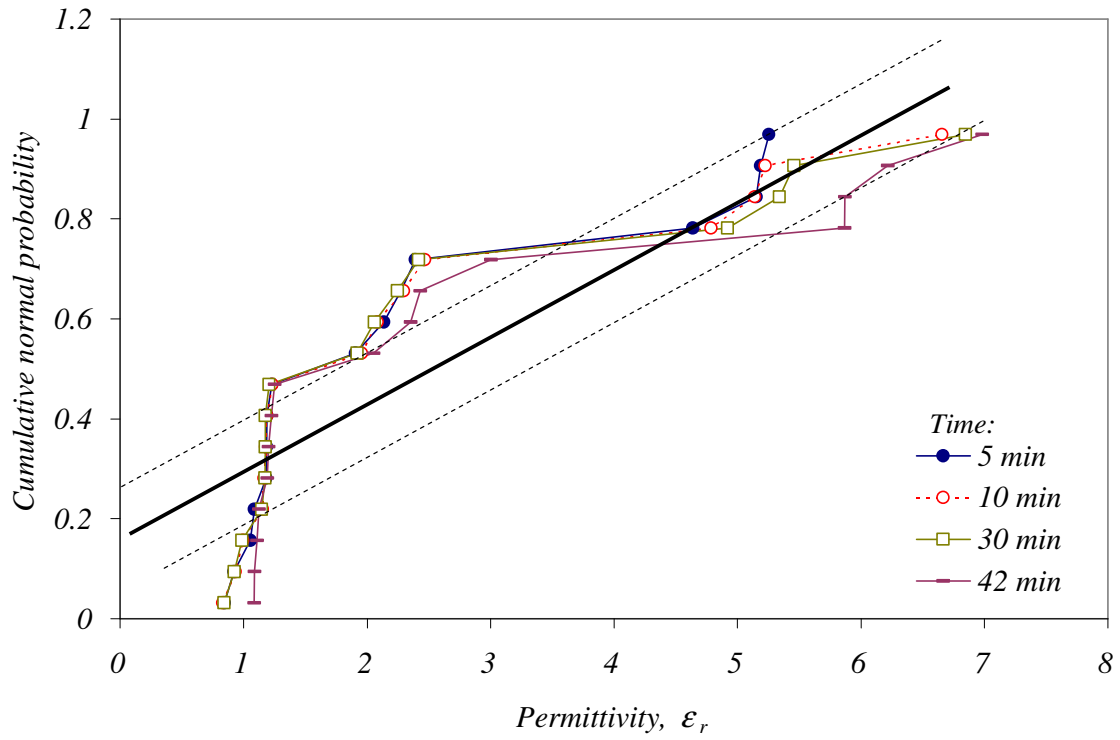
## PRELIMINARY STATISTICAL ANALYSIS

Basic preliminary statistical analysis was performed on soilBed average permittivity estimates for EM measurements taken prior to, and during injection of TCE and water in soil. The analysis was conducted using StatMost for Windows. Average and variance were estimated for all relative permittivity values for the soilBed of statistical populations representing: “dry” conditions prior to injection; 5, 10, and 30 minutes after TCE injection in initially dry experiments; 20, 50 and 100 minutes after water infiltration (50, 80, 130 minutes after TCE injection in initially dry soil); “dry” conditions prior to saturation; 50%, 75%, 100% saturation; and 10 and 45 minutes after injection in saturated soils. Statistical comparison between population groups was performed using the two sample t-tests.

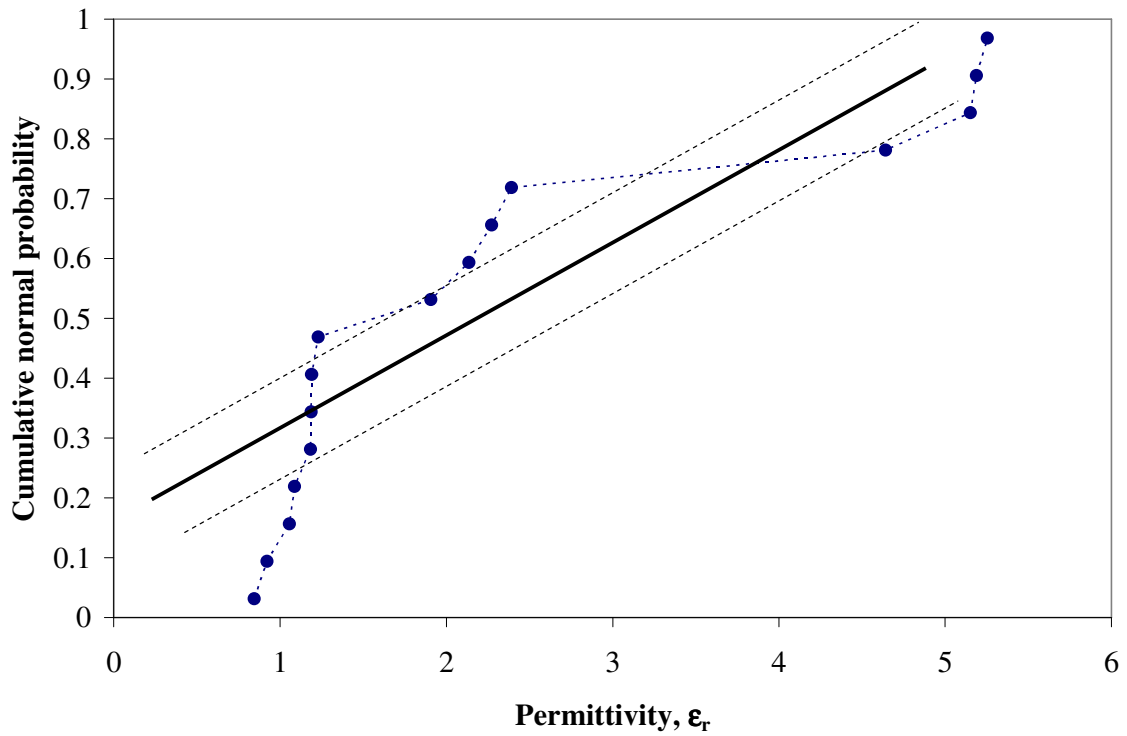
According to Montgomery (2000), the two sample t test assumes that the two populations from which the samples were selected are independent and can be described by a normal distribution, and that the observations are independent random variables. Although the normality assumption is required to develop the test procedure formally, “moderate departures from normality will not seriously affect the results”.

The normality assumption is easy to check using normal probability plot. In order to construct a normal probability plot, the observations are first ranked from smallest to largest, in order to calculate their cumulative frequencies  $(j - 0.5)/n$ , where  $j$  is the rank order and  $n$  is the sample size. A normal distribution is expected when the data in the probability plot fall in a linear trend within the 95% confidence intervals.

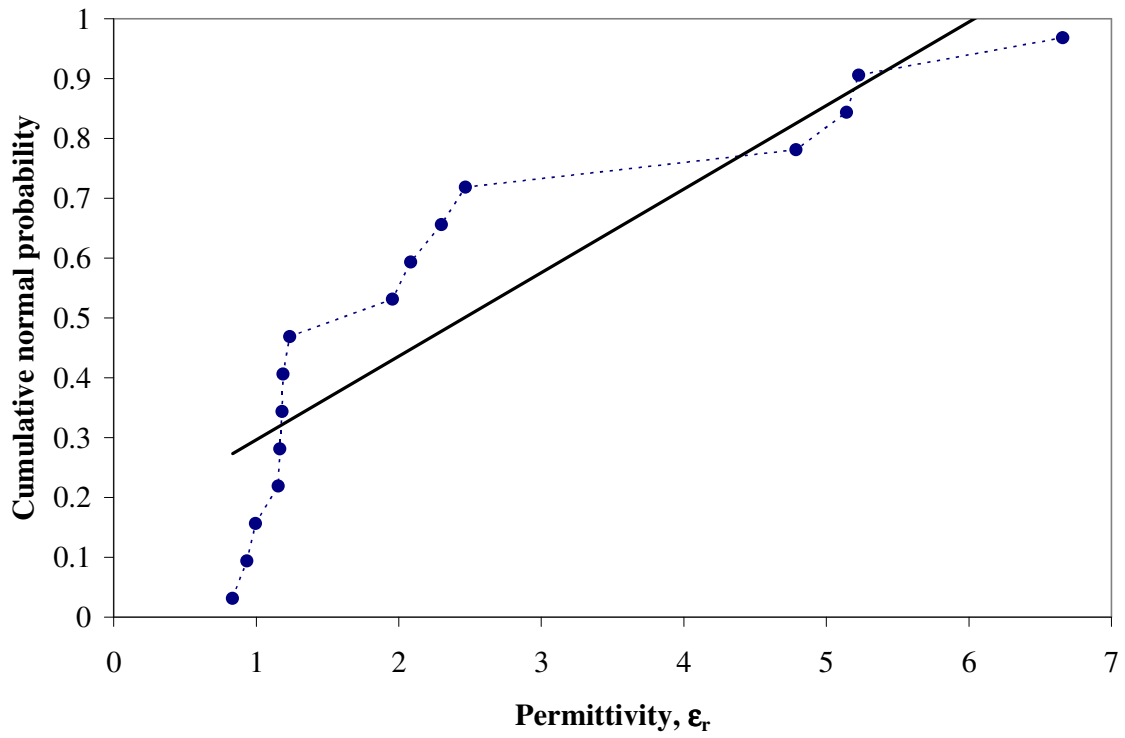
Preliminary normality tests (Figure A7.1 to Figure A7.11 ) indicate that data for all-non saturated populations do not follow a normal distribution whereas most saturated cases do. Preliminary assessment of permittivity estimates for all antennas suggest that non-normal distribution maybe strongly influenced by differences in antennas estimates (Figure A7.1) Although the two-sample t-test may not be applicable for non saturated experiments preliminary two-sample t-test analysis of data was conducted for comparative purposes (See report dry conditions and wet conditions). A more in-depth statistical analysis should be performed to include proper assessment of non-normal distributions.



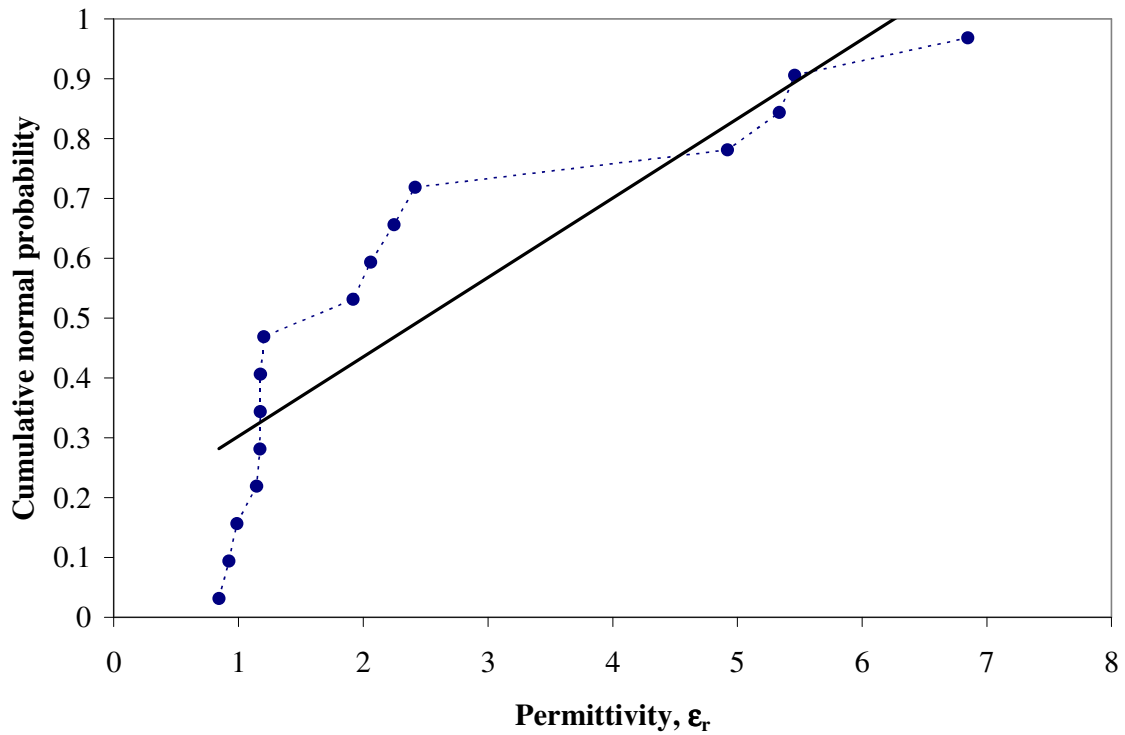
A7 Figure 1 Normal probability plot of permittivity in dry soil contaminated with TCE.



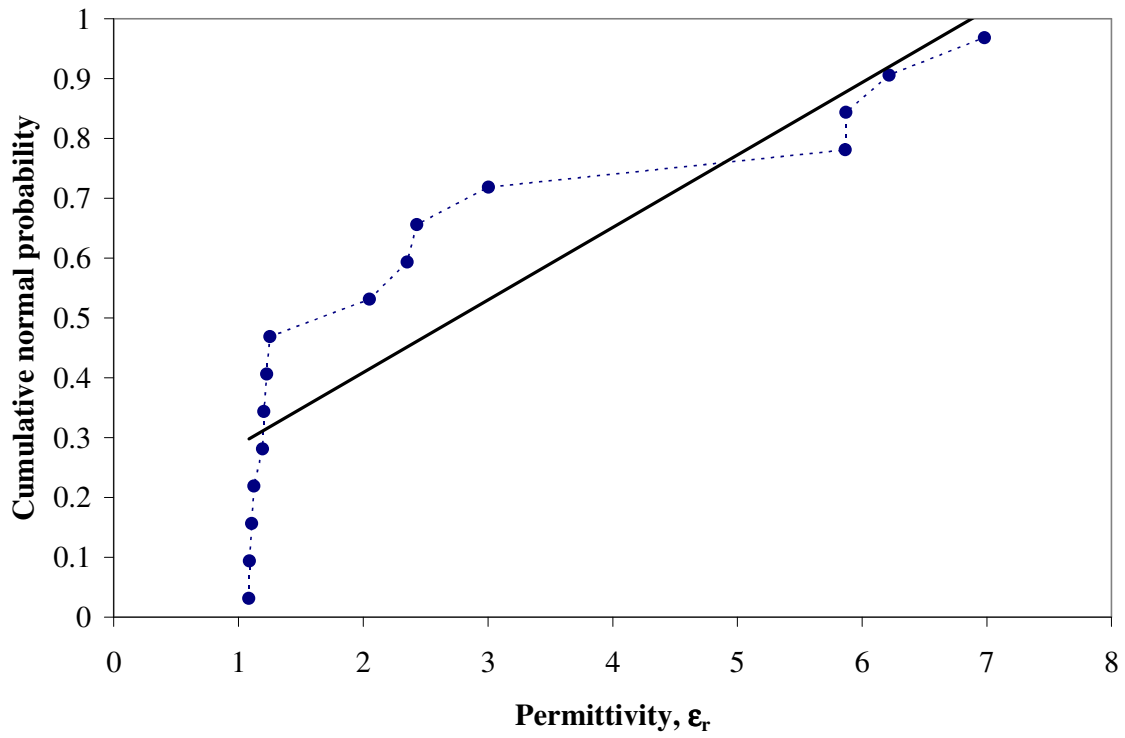
A7 Figure 2 Normal probability plot of permittivity in dry soil contaminated with TCE (5 min).



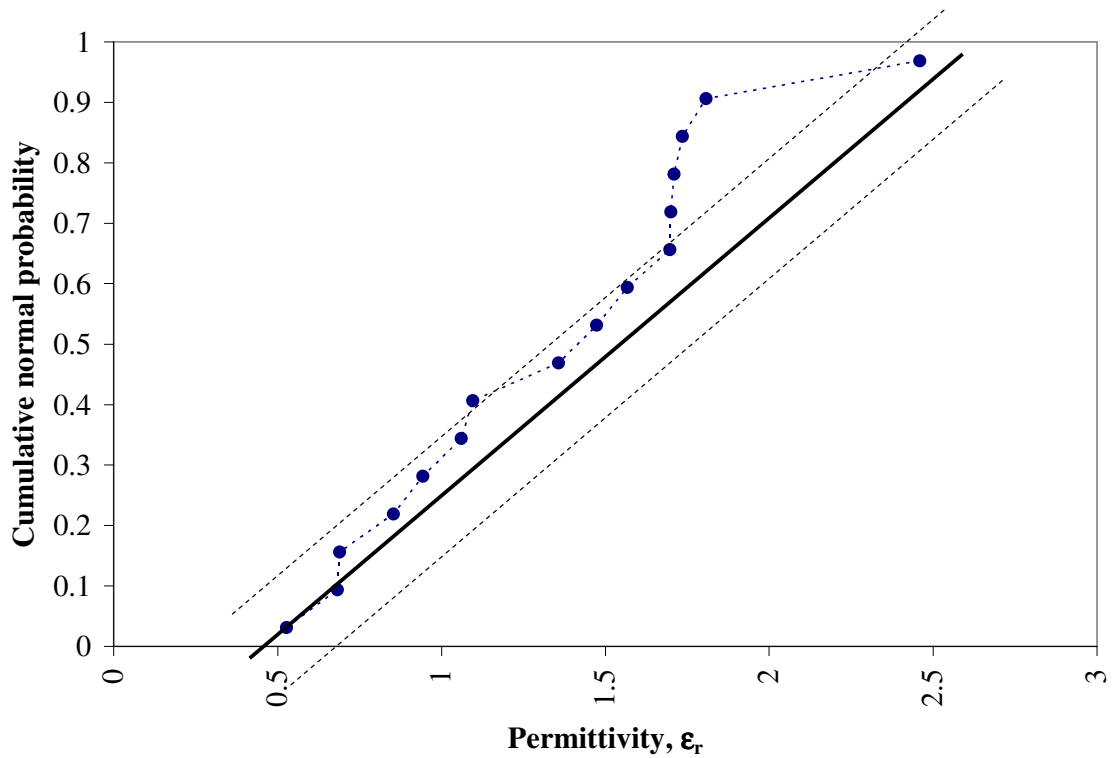
A7 Figure 3 Normal probability plot of permittivity in dry soil contaminated with TCE (10 min).



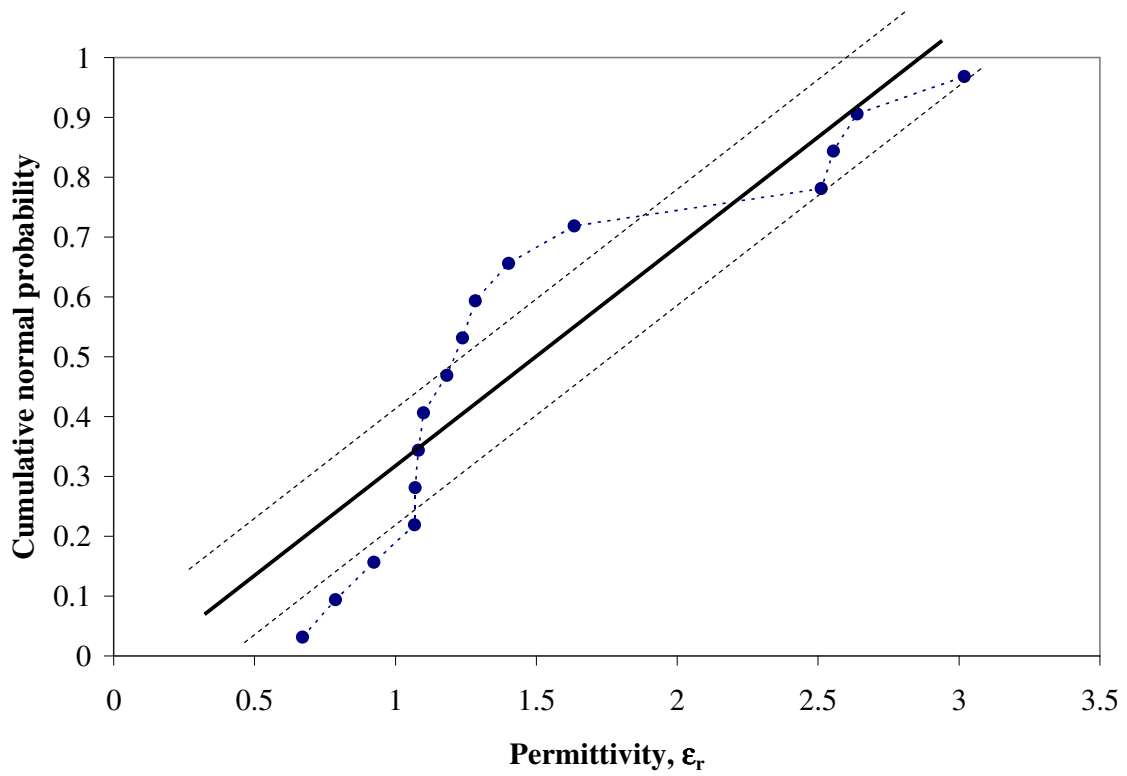
A7 Figure 4 Normal probability plot of permittivity in dry soil contaminated with TCE (30 min).



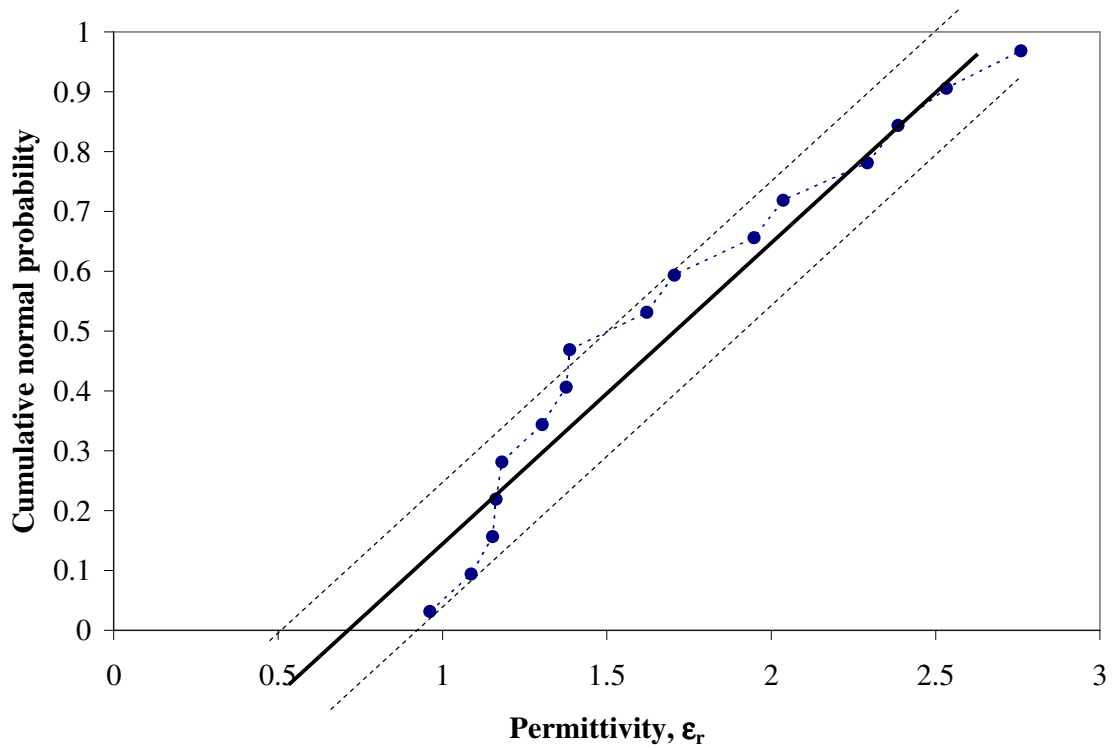
A7 Figure 5 Normal probability plot of permittivity in dry soil contaminated with TCE (42 min).



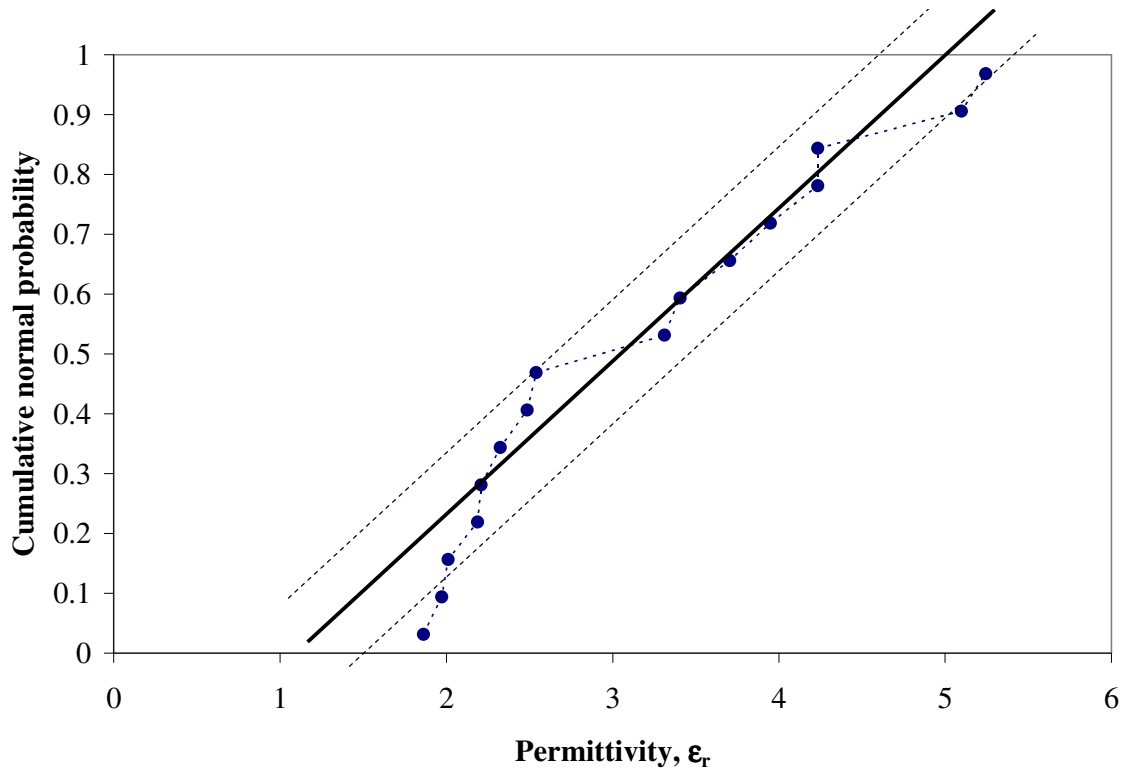
A7 Figure 6 Normal probability plot of permittivity in dry soil – saturated experiments



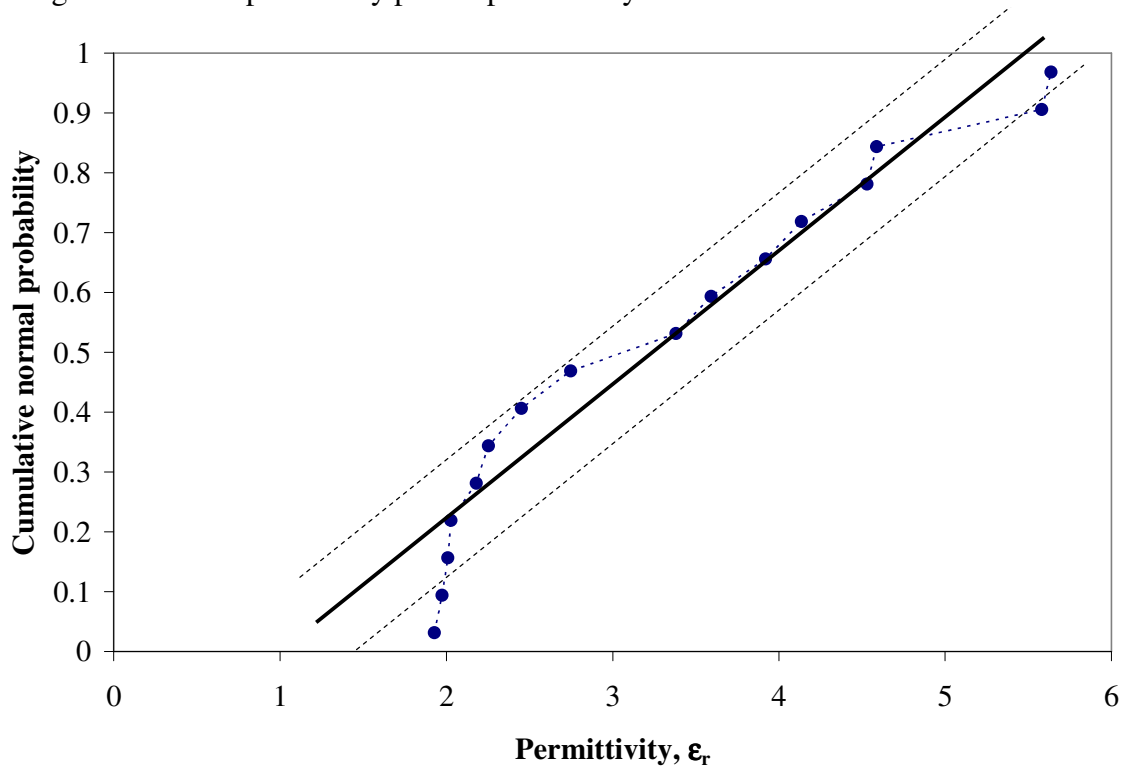
A7 Figure 7 Normal probability plot of permittivity in soil saturated 50%



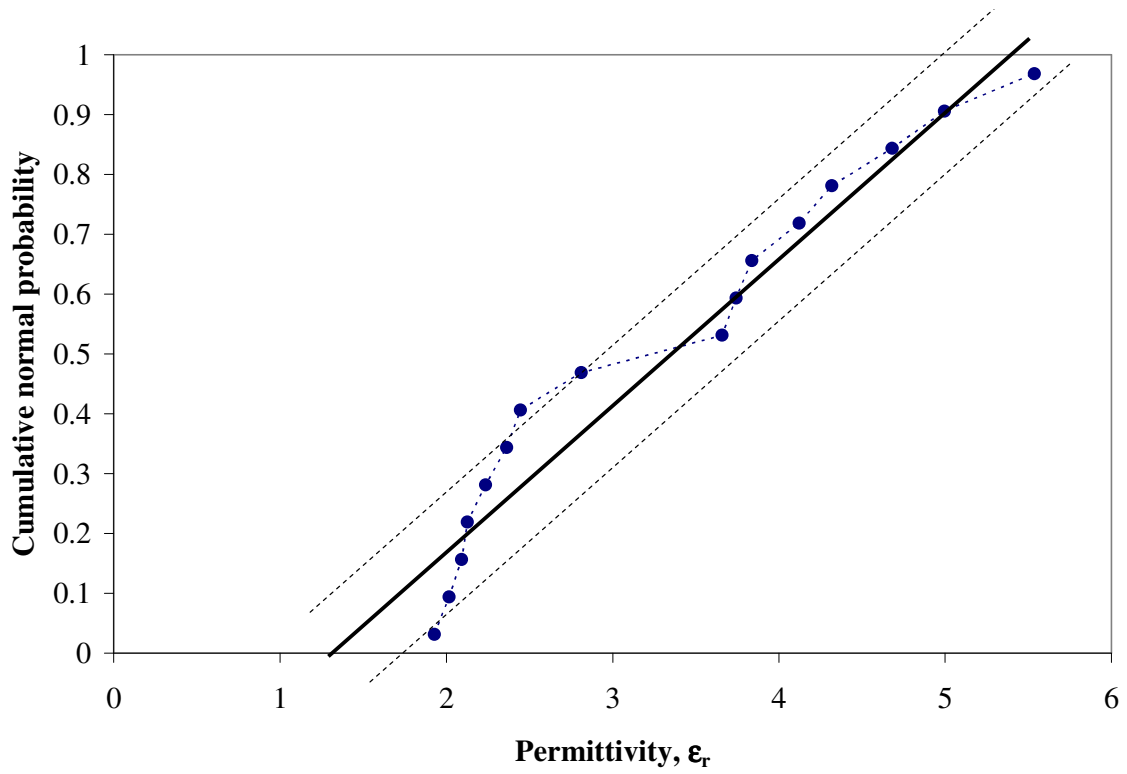
A7 Figure 8 Normal probability plot of permittivity in soil saturated 75%



A7 Figure 9 Normal probability plot of permittivity in soil saturated 100%



A7 Figure 10 Normal probability plot of permittivity in saturated soil 10 min after TCE injection



A7 Figure 11 Normal probability plot of permittivity in saturated soil 45 min after TCE injection

**DRY EXPERIMENTS**

-----  
 StatMost for Windows      Thursday, May 08, 2008    3:19:16 PM  
 -----

\*\*\*\*\* t-Test Analysis Results

\*\*\*\*\*

Confidence Level = 0.95 [Two Tail Test]

Paste\_1 vs. Paste\_2:

	Paste_1	Paste_2	
Sample Size	17	17	
Number of Missings	1	1	
Mean	2.4627	2.3525	Difference = 0.1102
Variance	4.1703	2.8485	Ratio = 1.4640

	t-Value	Probability	DF	Critical t-Value
Paired	0.8433	0.4123	15	2.1314
Co-Variance = 3.3727 , Std Deviation = 0.1307				

Paste\_1 vs. Paste\_3:

	Paste_1	Paste_3	
Sample Size	17	17	
Number of Missings	1	1	
Mean	2.4627	2.4561	Difference = 0.0066
Variance	4.1703	3.5707	Ratio = 1.1679

	t-Value	Probability	DF	Critical t-Value
Paired	0.1371	0.8928	15	2.1314
Co-Variance = 3.8519 , Std Deviation = 0.0482				

Paste\_1 vs. Paste\_4:

	Paste_1	Paste_4	
Sample Size	17	17	
Number of Missings	1	1	
Mean	2.4627	2.4898	Difference = -0.0271
Variance	4.1703	3.8989	Ratio = 1.0696

	t-Value	Probability	DF	Critical t-Value
Paired	-0.6966	0.4967	15	2.1314

Co-Variance = 4.0225 , Std Deviation = 0.0389

Paste\_1 vs. Paste\_5:

	Paste_1	Paste_5	
Sample Size	17	17	
Number of Missings	1	1	
Mean	2.4627	3.1638	Difference = -0.7012
Variance	4.1703	6.2735	Ratio = 0.6647

	t-Value	Probability	DF	Critical t-Value
Paired	-3.4330	0.0037	15	2.1314

Co-Variance = 4.8882 , Std Deviation = 0.2042

Paste\_2 vs. Paste\_3:

	Paste_2	Paste_3	
Sample Size	17	17	
Number of Missings	1	1	
Mean	2.3525	2.4561	Difference = -0.1036
Variance	2.8485	3.5707	Ratio = 0.7977

	t-Value	Probability	DF	Critical t-Value
Paired	-1.1259	0.2779	15	2.1314

Co-Variance = 3.1419 , Std Deviation = 0.0920

Paste\_2 vs. Paste\_4:

	Paste_2	Paste_4	
Sample Size	17	17	
Number of Missings	1	1	
Mean	2.3525	2.4898	Difference = -0.1374
Variance	2.8485	3.8989	Ratio = 0.7306

	t-Value	Probability	DF	Critical t-Value
Paired	-1.3118	0.2093	15	2.1314

Co-Variance = 3.2860 , Std Deviation = 0.1047

Paste\_2 vs. Paste\_5:

	Paste_2	Paste_5
Sample Size	17	17
Number of Missings	1	1

Mean	2.3525	3.1638	Difference = -0.8114
Variance	2.8485	6.2735	Ratio = 0.4540

	t-Value	Probability	DF	Critical t-Value
Paired	-3.1989	0.0060	15	2.1314

Co-Variance = 4.0464 , Std Deviation = 0.2536

Paste\_3 vs. Paste\_4:

	Paste_3	Paste_4	
Sample Size	17	17	
Number of Missings	1	1	
Mean	2.4561	2.4898	Difference = -0.0337
Variance	3.5707	3.8989	Ratio = 0.9158

	t-Value	Probability	DF	Critical t-Value
Paired	-1.4074	0.1797	15	2.1314

Co-Variance = 3.7302 , Std Deviation = 0.0240

Paste\_3 vs. Paste\_5:

	Paste_3	Paste_5	
Sample Size	17	17	
Number of Missings	1	1	
Mean	2.4561	3.1638	Difference = -0.7078
Variance	3.5707	6.2735	Ratio = 0.5692

	t-Value	Probability	DF	Critical t-Value
Paired	-3.1491	0.0066	15	2.1314

Co-Variance = 4.5180 , Std Deviation = 0.2248

Paste\_4 vs. Paste\_5:

	Paste_4	Paste_5	
Sample Size	17	17	
Number of Missings	1	1	
Mean	2.4898	3.1638	Difference = -0.6740
Variance	3.8989	6.2735	Ratio = 0.6215

	t-Value	Probability	DF	Critical t-Value
Paired	-3.0966	0.0074	15	2.1314

Co-Variance = 4.7072 , Std Deviation = 0.2177

## SATURATED EXPERIMENTS

-----  
 StatMost for Windows      Thursday, May 08, 2008    2:55:50 PM  
 -----

\*\*\*\*\* t-Test Analysis Results  
 \*\*\*\*\*

Confidence Level = 0.95 [Two Tail Test]

Paste\_1 vs. Paste\_2:

	Paste_1	Paste_2	
Sample Size	17	17	
Number of Missings	1	1	
Mean	1.3348	1.5098	Difference = -0.1750
Variance	0.2760	0.5477	Ratio = 0.5040

	t-Value	Probability	DF	Critical t-Value
Paired	-0.9765	0.3443	15	2.1314

Co-Variance = 0.1551    ,    Std Deviation = 0.1792

Paste\_1 vs. Paste\_3:

	Paste_1	Paste_3	
Sample Size	17	17	
Number of Missings	1	1	
Mean	1.3348	1.6808	Difference = -0.3459
Variance	0.2760	0.3300	Ratio = 0.8365

	t-Value	Probability	DF	Critical t-Value
Paired	-2.6294	0.0190	15	2.1314

Co-Variance = 0.1646    ,    Std Deviation = 0.1316

Paste\_1 vs. Paste\_4:

	Paste_1	Paste_4	
Sample Size	17	17	
Number of Missings	1	1	
Mean	1.3348	3.1735	Difference = -1.8386
Variance	0.2760	1.2796	Ratio = 0.2157

	t-Value	Probability	DF	Critical t-Value
Paired	-9.9644	5.23652E-008	15	2.1314

Co-Variance = 0.5055 , Std Deviation = 0.1845

Paste\_1 vs. Paste\_5:

	Paste_1	Paste_5	
Sample Size	17	17	
Number of Missings	1	1	
Mean	1.3348	3.3084	Difference = -1.9735
Variance	0.2760	1.6873	Ratio = 0.1636

	t-Value	Probability	DF	Critical t-Value
Paired	-8.6467	3.26407E-007	15	2.1314

Co-Variance = 0.5649 , Std Deviation = 0.2282

Paste\_1 vs. Paste\_6:

	Paste_1	Paste_6	
Sample Size	17	17	
Number of Missings	1	1	
Mean	1.3348	3.3072	Difference = -1.9723
Variance	0.2760	1.4298	Ratio = 0.1931

	t-Value	Probability	DF	Critical t-Value
Paired	-9.3288	1.23652E-007	15	2.1314

Co-Variance = 0.4953 , Std Deviation = 0.2114

Paste\_2 vs. Paste\_3:

	Paste_2	Paste_3	
Sample Size	17	17	
Number of Missings	1	1	
Mean	1.5098	1.6808	Difference = -0.1710
Variance	0.5477	0.3300	Ratio = 1.6598

	t-Value	Probability	DF	Critical t-Value
Paired	-1.4425	0.1697	15	2.1314

Co-Variance = 0.3265 , Std Deviation = 0.1185

Paste\_2 vs. Paste\_4:

	Paste_2	Paste_4	
Sample Size	17	17	
Number of Missings	1	1	
Mean	1.5098	3.1735	Difference = -1.6637
Variance	0.5477	1.2796	Ratio = 0.4280

	t-Value	Probability	DF	Critical t-Value
Paired	-5.3298	8.41446E-005	15	2.1314

Co-Variance = 0.1342 , Std Deviation = 0.3121

Paste\_2 vs. Paste\_5:

	Paste_2	Paste_5	
Sample Size	17	17	
Number of Missings	1	1	
Mean	1.5098	3.3084	Difference = -1.7986
Variance	0.5477	1.6873	Ratio = 0.3246

	t-Value	Probability	DF	Critical t-Value
Paired	-5.1587	0.0001	15	2.1314

Co-Variance = 0.1451 , Std Deviation = 0.3486

Paste\_2 vs. Paste\_6:

	Paste_2	Paste_6	
Sample Size	17	17	
Number of Missings	1	1	
Mean	1.5098	3.3072	Difference = -1.7974
Variance	0.5477	1.4298	Ratio = 0.3831

	t-Value	Probability	DF	Critical t-Value
Paired	-6.1172	1.97036E-005	15	2.1314

Co-Variance = 0.2981 , Std Deviation = 0.2938

Paste\_3 vs. Paste\_4:

	Paste_3	Paste_4	
Sample Size	17	17	
Number of Missings	1	1	
Mean	1.6808	3.1735	Difference = -1.4927
Variance	0.3300	1.2796	Ratio = 0.2579

	t-Value	Probability	DF	Critical t-Value
Paired	-6.1807	1.75910E-005	15	2.1314

Co-Variance = 0.3382 , Std Deviation = 0.2415

Paste\_3 vs. Paste\_5:

	Paste_3	Paste_5	
Sample Size	17	17	
Number of Missings	1	1	
Mean	1.6808	3.3084	Difference = -1.6276

Variance 0.3300 1.6873 Ratio = 0.1956

	t-Value	Probability	DF	Critical t-Value
Paired	-5.8095	3.44042E-005	15	2.1314

Co-Variance = 0.3808 , Std Deviation = 0.2802

Paste\_3 vs. Paste\_6:

	Paste_3	Paste_6	
Sample Size	17	17	
Number of Missings	1	1	
Mean	1.6808	3.3072	Difference = -1.6264
Variance	0.3300	1.4298	Ratio = 0.2308

	t-Value	Probability	DF	Critical t-Value
Paired	-6.8512	5.49477E-006	15	2.1314

Co-Variance = 0.4291 , Std Deviation = 0.2374

Paste\_4 vs. Paste\_5:

	Paste_4	Paste_5	
Sample Size	17	17	
Number of Missings	1	1	
Mean	3.1735	3.3084	Difference = -0.1349
Variance	1.2796	1.6873	Ratio = 0.7584

	t-Value	Probability	DF	Critical t-Value
Paired	-2.4445	0.0273	15	2.1314

Co-Variance = 1.4591 , Std Deviation = 0.0552

Paste\_4 vs. Paste\_6:

	Paste_4	Paste_6	
Sample Size	17	17	
Number of Missings	1	1	
Mean	3.1735	3.3072	Difference = -0.1337
Variance	1.2796	1.4298	Ratio = 0.8950

	t-Value	Probability	DF	Critical t-Value
Paired	-1.3508	0.1968	15	2.1314

Co-Variance = 1.2763 , Std Deviation = 0.0990

Paste\_5 vs. Paste\_6:

	Paste_5	Paste_6
Sample Size	17	17

Number of Missings	1	1	
Mean	3.3084	3.3072	Difference = 0.0012
Variance	1.6873	1.4298	Ratio = 1.1801

	t-Value	Probability	DF	Critical t-Value
Paired	0.0112	0.9912	15	2.1314

Co-Variance = 1.4723 , Std Deviation = 0.1039

---

StatMost Report Created by Eric Harmsen, UPRM

---

#### Reference

Montgomery, D. C. Design and Analysis of Experiments. Wiley, 5<sup>th</sup> edition, New York, 2000.